



**International Committee for Future Accelerators**

Sponsored by the Particles and Fields Commission of IUPAP

# **Beam Dynamics Newsletter**

**No. 54**

**Issue Editor:  
J. Gao**

**Editor in Chief:  
W. Chou**

**April 2011**



## Contents

<b>1</b>	<b>FOREWORD.....</b>	<b>9</b>
1.1	FROM THE CHAIR .....	9
1.2	FROM THE EDITOR .....	11
1.3	FROM THE ILC GDE .....	11
<b>2</b>	<b>POSITRON SOURCE FOR ILC .....</b>	<b>12</b>
2.1	POSITRON SOURCE FOR THE INTERNATIONAL LINEAR COLLIDER .....	12
2.1.1	Introduction .....	12
2.1.1.1	<i>Layout as in RDR Baseline.....</i>	<i>13</i>
2.1.1.2	<i>Layout as in SB2009 Proposal.....</i>	<i>14</i>
2.1.1.3	<i>Critical Components of Undulator Based Positron Source.....</i>	<i>15</i>
2.1.2	The RDR Undulator Based Positron Source .....	20
2.1.3	The SB2009 Undulator Based Positron Source.....	23
2.1.4	High K Short Period Undulator .....	25
2.1.5	References .....	26
<b>3</b>	<b>ILC DAMPING RINGS .....</b>	<b>27</b>
3.1	DAMPING RINGS OVERVIEW .....	27
3.1.1	Introduction .....	27
3.1.2	ILC Damping Ring Design Status .....	28
3.1.3	ILC Damping Ring R&D Status.....	29
3.1.4	References .....	31
3.2	AN UPDATE ON THE CESR TEST ACCELERATOR RESEARCH PROGRAM .....	32
3.2.1	Introduction .....	32
3.2.2	Conversion of CESR to a Damping Ring Test Accelerator Configuration...33	
3.2.3	Electron Cloud Build-Up and Mitigation Studies .....	36
3.2.3.1	<i>EC Mitigation in Dipole Magnets .....</i>	<i>37</i>
3.2.3.2	<i>EC Mitigation in Wiggler Magnets .....</i>	<i>38</i>
3.2.3.3	<i>EC Mitigation in Drift Regions .....</i>	<i>39</i>
3.2.3.4	<i>EC mitigation in Quadrupole Magnets .....</i>	<i>40</i>
3.2.3.5	<i>TE Wave Measurements .....</i>	<i>41</i>
3.2.3.6	<i>Shielded Pickup Measurements.....</i>	<i>41</i>
3.2.4	Low Emittance Tuning.....	42
3.2.5	Studies of EC-induced Beam Dynamics with Low Emittance Beams.....	43
3.2.6	Incorporation of CESR TA Results into the ILC DR Technical Design.....	44
3.2.7	Future Plans .....	45
3.2.8	Acknowledgments .....	45
3.2.9	References .....	45

3.3	RECENT STUDIES IN ATF DAMPING RING .....	47
3.3.1	Introduction.....	47
3.3.2	Low Emittance Tuning in ATF Damping Ring.....	48
3.3.2.1	<i>Beam Based Alignment</i> .....	48
3.3.2.2	<i>Beta-Beat Correction</i> .....	49
3.3.2.3	<i>Orbit Response Matrix Analysis</i> .....	50
3.3.2.4	<i>BPM Electronics Upgrade</i> .....	50
3.3.3	Fast Kicker Test.....	51
3.3.3.1	<i>Beam Extraction Experiment</i> .....	51
3.3.4	References.....	55
3.4	ILC 3.2 KM DAMPING RING DESIGN BASED ON THE FODO CELL .....	56
3.4.1	Introduction.....	56
3.4.2	Global Consideration and Parameter Calculation.....	57
3.4.3	Linear Lattice Design .....	59
3.4.4	Dynamic Aperture .....	60
3.4.5	References.....	62
<b>4</b>	<b>FINAL FOCUS TEST FACILITY FOR ILC AND CLIC.....</b>	<b>62</b>
4.1	ATF2 SUMMARY AND STATUS.....	62
4.1.1	Introduction.....	63
4.1.2	Sub-Systems Hardware.....	66
4.1.2.1	<i>Magnets and Magnet Movers</i> .....	66
4.1.2.2	<i>Beam Position Monitors (BPMs)</i> .....	67
4.1.2.3	<i>IP Beam Size Monitors</i> .....	68
4.1.2.4	<i>EXT Beam Phase-Space Diagnostics (Wire-Scanners and OTRs)</i> .....	68
4.1.2.5	<i>Beam Loss Monitor</i> .....	68
4.1.2.6	<i>Intra-Pulse Feedback</i> .....	69
4.1.2.7	<i>Background Radiation Monitors</i> .....	69
4.1.3	Accelerator Modeling Software.....	69
4.1.3.1	<i>Optics Design and Beam Dynamics Simulations</i> .....	69
4.1.3.2	<i>Online Model and Control System Interface</i> .....	69
4.1.4	Optics Preparation and Beam Dynamics Simulations .....	70
4.1.5	Beam Tuning Procedure .....	72
4.1.5.1	<i>Beam-Based Alignment (BBA)</i> .....	72
4.1.5.2	<i>Orbit Response and Jitter Modelling</i> .....	73
4.1.5.3	<i>Orbit Steering &amp; Feedbacks</i> .....	74
4.1.5.4	<i>Dispersion Measurement and Correction</i> .....	75
4.1.5.5	<i>Twiss Parameters &amp; Coupling Measurement and Correction</i> .....	76
4.1.5.6	<i>IP Vertical Beam Size Tuning</i> .....	77
4.1.6	Summary and Outlook.....	78
4.1.7	References.....	78
4.2	MEASUREMENT OF NANOMETER SCALE BEAM SIZE BY SHINTAKE MONITOR (IPBSM) .....	80
4.2.1	Introduction.....	81
4.2.1.1	<i>Shintake Monitor's Role at ATF2</i> .....	81

4.2.2	Measurement Scheme of Shintake Monitor .....	82
4.2.3	Layout and Structure .....	85
4.2.3.1	<i>Overall Structure</i> .....	85
4.2.3.2	<i>Laser Table and Main Optical Table</i> .....	85
4.2.3.3	<i>Gamma Detector</i> .....	87
4.2.4	Shintake Monitor and Beam Tuning .....	87
4.2.5	Performance .....	88
4.2.5.1	<i>Expectations</i> .....	88
4.2.5.2	<i>Statistical Errors</i> .....	88
4.2.5.3	<i>Systematic Errors</i> .....	90
4.2.6	Status .....	92
4.2.6.1	<i>Previous Run</i> .....	92
4.2.6.2	<i>Most Recent Run (2010 Autumn - 2011 Spring)</i> .....	92
4.2.7	Future Goals .....	93
4.2.7.1	<i>Remaining of Current Run Period</i> .....	93
4.2.7.2	<i>Consequences of the Great Eastern Japan Earthquake</i> .....	94
4.2.7.3	<i>Prospects for Application at ILC</i> .....	94
4.2.8	Footnotes .....	95
4.2.9	References .....	95
4.3	THE MULTI OPTICAL TRANSITION RADIATION SYSTEM .....	96
4.3.1	Introduction .....	96
4.3.2	The Beam Diagnostic Section of the ATF2 Extraction Line: Optics Studies and Beam Spot Size Simulations .....	96
4.3.3	Technical Description: Optical and Mechanical Design .....	98
4.3.4	Software Integration, Beam Spot Size and Emittance Reconstruction Algorithms .....	101
4.3.4.1	<i>Beam Spot Size and Emittance Reconstruction Algorithms</i> .....	103
4.3.5	First Beam Measurements .....	103
4.3.5.1	<i>Fall Run 2010</i> .....	103
4.3.5.2	<i>First Period Run 2011</i> .....	105
4.3.6	Conclusions .....	105
4.3.7	Acknowledgements .....	106
4.3.8	References .....	106
4.4	MICRON SCALE LASER-WIRE SCANNER FOR THE ATF .....	106
4.4.1	Introduction .....	107
4.4.2	Laser-Wire Experiment at the ATF .....	107
4.4.2.1	<i>Hardware</i> .....	107
4.4.2.2	<i>Lens Simulation</i> .....	108
4.4.2.3	<i>Laser-Wire Results</i> .....	109
4.4.3	Laser-Wire Upgrade for the ATF2 .....	110
4.4.3.1	<i>Upgrades</i> .....	110
4.4.3.2	<i>Laser-Wire Results at the ATF2</i> .....	110
4.4.4	Development of a New Fibre Laser Source for Laser-Wire Experiments .....	111
4.4.5	Development of an Electro-Optic Scanner for Fast Laser-Wire Operation .....	112
4.4.6	Conclusions and Future Plans .....	115
4.4.7	References .....	115

<b>5</b>	<b>ACTIVITY REPORTS.....</b>	<b>116</b>
5.1	RECENT LUMINOSITY ENHANCEMENT AT THE BEPCII .....	116
5.1.1	Introduction.....	116
5.1.2	Luminosity Commissioning in 2010 - 2011 .....	117
5.1.3	Future Improvements.....	119
5.1.4	References.....	119
5.2	ACCELERATOR DESIGN OF CHINA SPALLATION NEUTRON SOURCE.....	120
5.2.1	Introduction.....	120
5.2.2	Beam Dynamics Design .....	121
5.2.2.1	<i>Linac</i> .....	121
5.2.2.2	<i>Rapid Cycling Synchrotron</i> .....	122
5.2.2.3	<i>Beam Lines</i> .....	122
5.2.3	Acknowledgements.....	122
5.2.4	References.....	123
5.3	THE ACCELERATOR LAB AT TSINGHUA UNIVERSITY .....	123
5.3.1	Introduction.....	123
5.3.2	Low Energy Linac .....	123
5.3.3	Tsinghua Thomson Scattering X-ray (TTX) Source .....	124
5.3.4	MeV Ultrafast Electron Diffraction Based on Photocathode RF Gun .....	125
5.4	SRF TECHNOLOGY AT PEKING UNIVERSITY .....	127
5.4.1	Introduction.....	127
5.4.2	RF Superconducting Cavities .....	127
5.4.2.1	<i>3.5-Cell Cavity</i> .....	127
5.4.2.2	<i>9-Cell Cavity</i> .....	127
5.4.2.3	<i>QWR and Spoke Cavity</i> .....	128
5.4.3	PKU-SETF.....	128
5.5	NEW LOW CHARGE PARAMETERS FOR ILC.....	129
5.5.1	Introduction.....	129
5.5.2	Main Changes in the New Low Charge Parameters Compared to SB2009131 .....	131
5.5.3	Advantages of the New Low Charge Parameter.....	132
5.5.4	New Design for the Two-Stage Bunch Compressor.....	132
5.5.5	References.....	133
5.6	FIRST BEAM MANIPULATION AND MEASUREMENTS IN THE FINAL FOCUS BEAM LINE AT THE KEK ACCELERATOR TEST FACILITY .....	133
5.6.1	Introduction.....	133
5.6.2	Simulation on Multiknobs Correction .....	134
5.6.2.1	<i>Multiknobs Correction Analysis</i> .....	134
5.6.2.2	<i>Simulation Results on Multiknobs Correction</i> .....	134
5.6.2.3	<i>Summary and Prospects</i> .....	136
5.6.3	Twiss Parameter Estimation .....	136
5.6.3.1	<i>Parametrisation of Beam Sizes Around the IP and Post-IP Waists</i> .....	136
5.6.3.2	<i>Estimation of Twiss Parameters and of Horizontal Emittance</i> ....	137
5.6.3.3	<i>Discussion</i> .....	140

5.6.4	References .....	140
5.7	LINAC BEAM MISMATCH MODES FOR UNEQUAL TRANSVERSE TUNES .....	141
5.7.1	Introduction .....	141
5.7.2	Case of Equal Transverse Tunes .....	142
5.7.3	Instability for Equal Transverse Tunes.....	143
5.7.4	Case of Unequal Transverse Tunes .....	143
5.7.5	Case of Unequal Transverse Tunes and Envelope Equation Non-Linearity.....	144
5.7.6	Inter-Stage Mismatch .....	145
5.7.7	Mismatch Mode Features .....	145
5.7.8	Envelope Modes for an Un-Bunched Beam with Unequal Tunes .....	146
5.7.9	Appendix: Homogeneous Linear Equations for the Mismatch Modes .....	146
5.7.10	References .....	147
5.8	REDUCED EMITTANCE GROWTH IN A LONG MEBT STAGE OF A LINAC.....	148
5.8.1	Introduction .....	148
5.8.2	A 3 MeV, Long MEBT Option for an ISIS Upgrade.....	149
5.8.3	The Basis of the Need for a Second Harmonic Cavity.....	150
5.8.4	Beam Tracking Results for the Modified MEBT .....	151
5.8.5	References .....	152
<b>6</b>	<b>WORKSHOP AND CONFERENCE REPORTS .....</b>	<b>152</b>
6.1	X-BAND STRUCTURES, BEAM DYNAMICS AND SOURCES WORKSHOP (XB-10)....	152
<b>7</b>	<b>RECENT DOCTORIAL THESES.....</b>	<b>155</b>
7.1	ILC PHYSICAL DESIGN AND KEY EXPERIMENTAL STUDY .....	155
7.2	A DAMPED AND DETUNED ACCELERATING STRUCTURE FOR THE MAIN LINACS OF THE COMPACT LINEAR COLLIDER.....	156
<b>8</b>	<b>FORTHCOMING BEAM DYNAMICS EVENTS .....</b>	<b>156</b>
8.1	SIXTH WORKSHOP ON POLARIZED POSITRON BEAMS (POSIPOL 2011).....	156
8.2	SIXTH INTERNATIONAL ACCELERATOR SCHOOL FOR LINEAR COLLIDERS .....	157
8.3	WORKSHOP ON ACCELERATORS FOR HEAVY ION INERTIAL FUSION (HIF2011) ...	162
8.4	SECOND INTERNATIONAL CONFERENCE ON TECHNOLOGY AND INSTRUMENTATION IN PARTICLE PHYSICS (TIPP 2011) .....	164
8.5	15 <sup>TH</sup> INTERNATIONAL CONFERENCE ON RF SUPERCONDUCTIVITY (SRF2011) .....	165
8.6	13 <sup>TH</sup> INTERNATIONAL CONFERENCE ON ACCELERATOR AND LARGE EXPERIMENTAL PHYSICS CONTROL SYSTEMS (ICALEPCS 2011) .....	165
<b>9</b>	<b>ANNOUNCEMENTS OF THE BEAM DYNAMICS PANEL.....</b>	<b>166</b>
9.1	ICFA BEAM DYNAMICS NEWSLETTER.....	166

9.1.1 Aim of the Newsletter.....	166
9.1.2 How to Prepare a Manuscript .....	167
9.1.3 Distribution .....	167
9.1.4 Regular Correspondents.....	168
9.2 ICFA BEAM DYNAMICS PANEL MEMBERS .....	169



# 1 Foreword

## 1.1 From the Chair

Weiren Chou, Fermilab  
Mail to: [chou@fnal.gov](mailto:chou@fnal.gov)

The International Committee for Future Accelerators (ICFA) met on February 17-18, 2011 at IHEP, Beijing, China. Atsuto Suzuki, Director General of KEK and Chair of ICFA, chaired this meeting. The meeting was preceded by an ILC Steering Committee (ILCSC) meeting earlier on February 17 in the same place.

Jonathan Bagger, Chair of ILCSC, reported on the status of the ILC. The R&D on the ILC accelerator and detector designs is progressing well. However, a major question is – what’s next after 2012 when the mandates to the GDE and ILCSC end? Bagger presented criteria for ILC governance past 2012, and the need to integrate the ILC and CLIC communities. He plans to form a working group within the ILCSC to investigate post-2012 possibilities. Bagger’s term will end in 2011. However, since the mandates of GDE and ILCSC will conclude at the end of 2012, ICFA decided that he would remain as ILCSC Chair until the end of 2012.

Atsuto Suzuki reported on the Funding Agencies for Large Collaborations (FALC) meeting in January 2011. FALC liked the suggested multi-lab approach to collaboration on future global projects, believing that it was a natural evolution to the building of large facilities through international cooperation.

Toshiki Tajima, Chair of the International Committee for Ultra Intense Lasers (ICUIL), reported that the joint ICFA-ICUIL task force (formed by ICFA in 2009) is preparing a joint report on particle acceleration by lasers. Future workshops on this topic are planned. The main challenges for the lasers used in particle acceleration are the need for: high average power; high efficiency; high repetition rate; and reasonable cost. The general conclusion is that there are large challenges to developing lasers with the necessary parameters, but no showstoppers.

A long time tradition in the world high-energy community is that the host laboratories do not ask experimental groups to contribute to the running costs of the machines nor the operating costs of the experimental areas. However, since future accelerators will be very large and expensive, ICFA approved the following revised guideline: *“Operating laboratories should not require experimental groups to contribute to the running costs of the accelerators or colliding beam machines nor to the operating costs of their associated experimental areas. However, in particular for a large global facility, allocation of operating costs should be agreed by the project partners before project approval, while still allowing open access for experimental groups.”*

An ICFA Seminar, *“Science Driving Facilities for Particle Physics,”* will take place from October 3-6 this year at CERN. A major objective of the Seminar is to produce a document entitled *“Discovery’s Horizon,”* currently under preparation by Pier Oddone, Joachim Mnich, Sachio Komamiya and members of the InterAction collaboration. The goal is to provide a global picture of particle physics; the audience includes policy

makers, funding agencies, and the media. The key messages are: the compelling science of the field, with new tools providing the opportunity for discoveries not previously possible; accelerators and experiments are beyond the reach of a single region to build and operate; and particle physics research is an outstanding example of international cooperation.

Four ICFA panels (Beam Dynamics, Advanced and Novel Accelerators, Instrumentation, and Interregional Connectivity) presented reports at the meeting. The *EDIT2011 School* organized by the Instrumentation Panel was held at CERN on January 31 to February 10, 2011; it was aimed at final year PhD students and postdocs, most of whom had not previously had hardware experience. The school was very successful. The next *EDIT* school will be at Fermilab.

The Beam Dynamics Panel proposed two ICFA workshops: *FLS2012* at JLab in February 2012, and *HB2012* at IHEP/Beijing in September 2012. Both were approved. ICFA also approved George Neil (JLab) as a new BD panel member to replace Kwang-Je Kim (ANL). I'd like to use this opportunity to thank Kwang-Je for his many years of service on the BD panel. He was the leader of the Future Light Sources Working Group (which will be chaired by George Neil) and has organized a number of ICFA Advanced Beam Dynamics Workshops and mini-workshops. He edited no. 39 of this newsletter with the theme "*Pushing the limits of RF superconductivity*," which was well received by the SRF community. His services were of great value to the world accelerator community. I also want to welcome George, a well-known accelerator physicist and a leader in the FEL field. Under his leadership, we believe the Future Light Sources Working Group will continue to play an important and valued role in the panel.

Reports from 16 laboratory directors and their representatives were presented. A noticeable absence was the directors of Fermilab and SLAC; both were excused due to an emergency meeting at the US DOE because of the US budget situation. CERN was a glamour supernova at the meeting. The LHC run in 2010 was very successful. CERN is promising  $1 \text{ fb}^{-1}$  in 2011 at 7 TeV cm, while hoping for  $3 \text{ fb}^{-1}$ ; this could exclude the Standard Model Higgs at 90/95% to 600 GeV. The LHC will run in 2012 (allowing 3 sigma evidence for the Higgs up to 600 GeV). There will be a 15-month minimum shutdown beginning in 2013.

The host IHEP was another shining star. It reported that it has so many projects (BEPC II, Daya Bay, the Chinese Spallation Neutron Source, the Beijing Advanced Light Source, and the Accelerator-Driven Subcritical System or ADS) that there is a serious shortage of manpower to carry them all out. The IHEP will double its staff from ~1,000 to 2,000 by 2020, in sharp contrast to the current science budget situation in the US.

*The Sixth International Accelerator School for Linear Colliders* will be held from November 6-17, 2011 at the Asilomar Conference Center, Pacific Grove, California, USA. SLAC will host this school. Please see Section 8.2 for the announcement. The school web site is <http://www.linearcollider.org/school/2011/>.

The editor of this issue is Prof. Jie Gao, a panel member and a senior scientist at IHEP, China. Jie collected a number of excellent review articles in the theme sections 2-4 on three important linear collider subsystems – the positron source, the damping rings and the final focus test facility. In this issue there are also eight activity reports, one workshop report, two recent doctoral theses abstracts, and six workshop and school announcements. I thank Jie for editing and producing a newsletter of high quality and great value.

## 1.2 From the Editor

Jie Gao, Institute of High Energy Physics, CAS, China  
Mail to: [gaoj@ihep.ac.cn](mailto:gaoj@ihep.ac.cn)

Seven years ago I edited the ICFA Beam Dynamics Newsletter No. 32, December 2003, which focused on accelerating structures for linear colliders (TESLA, NLC/GLC, CLIC) and on advanced and novel accelerators. Since August 2004, when the International Linear Collider (ILC) was born, enormous progress has been made on ILC by the GDE led by Professor Barry Barish. In this issue, in contrast to No. 32, instead of focusing on accelerator structures, we present material on three key subsystems of the ILC: the polarized positron source, the damping rings and the final focus system (ATF2). These elements are challenged by the design goal requirements, for example, a highly polarized positron beam, and extreme low emittance and extreme small beam size at the IP. Thanks to the three ILC TDR subsystem chairpersons, we have been able to collect high level articles, reflecting the state of the art of the corresponding fields. In the remaining part of this issue, we provide laboratory reports from different accelerator laboratories, mainly from China this time.

In this world, there are many uncertainties, such as the recent enormous earthquake and tsunami in Japan, which not only caused heavy loss of life but also quite extensive perturbations to the facilities at KEK, to which ILC R&D programs are closely related. However, there are also many things which we believe with certainty: Japan will not take too long to recover from this big natural disaster, and KEK will resume soon again its important role in ILC collaboration.

## 1.3 From the ILC GDE

Barry C Barish - CALTECH  
Director – ILC Global Design Effort  
Mail to: [barish@ligo.caltech.edu](mailto:barish@ligo.caltech.edu)

The mandate for the ILC Global Design Effort (GDE) was first to develop an ILC Reference Design Report (RDR), which was produced in 2007 and then to follow-up the ILC Reference Design Report with a more optimized Technical Design Report (TDR) by the end of 2012. The TDR will be based on a more optimized design that will contain all the elements needed to propose the ILC to collaborating governments, including a technical design and implementation plan that are realistic and have been better optimized for performance, cost and risk.

We are on track to develop detailed plans for an ILC, such that once LHC science establishes the main science goals and parameters of the machine, we will be in a good position to make a strong proposal for a new major global project in particle physics. The two overriding issues for the ILC R&D program are to demonstrate that the technical requirements for the accelerator are achievable with practical technologies, and that the ambitious physics goals can be addressed by realistic ILC detectors.

In this issue of the ICFA Beam Dynamics Newsletter we report on the status and advances in three areas: the positron source, the damping rings; and the final focus (ATF2). The main emphasis in the evolving design for the ILC has been a proposal for a series of changes to the ILC baseline. These have been based on the crucial goal of

containing costs as the ILC moves toward becoming a construction project. That important goal is leading to an optimization of the cost, performance and risk.

Four top-level changes have been made in the design resulting in the following important features: 1) the operating gradient of the ILC will be 31.5 MV/m; 2) the conventional facilities will be based on a single tunnel concept; 3) the positron source will be at the end of the linac and the damping ring circumference will be reduced from 6476 m to 3238 m; and 4) the number of bunches will be initially reduced from 2625 to 1312 per bunch.

The changes to the baseline are being made such that the performance of the accelerator will be retained. This requires some innovations in the accelerator design and some of those are covered in this issue. For example, the final focus will include possible stronger focus techniques like the traveling focus scheme. This issue of Beam Dynamics Newsletter has contributions in three crucial areas of the ILC design: positron source and damping rings, the final focus, including the crucial ATF-2 final focus.

I conclude today by stating our full support to our Japanese colleagues, as they recover from the effects of the devastating earthquake. We all hope for a quick recovery, including of course, our work on the ATF-2

## **2 Positron Source for ILC**

### **2.1 Positron Source for the International Linear Collider**

Wanming Liu and Wei Gai, High Energy Physics Div., Argonne National Lab, USA  
Mail to: [wmliu@anl.gov](mailto:wmliu@anl.gov)

#### **2.1.1 Introduction**

The positron source for International Linear Collider (ILC) requires a huge number of positrons to be produced and accepted by damping ring [1]. This requirement is far beyond any existing positron source for linear colliders and brings in a lot of challenges to the designing and realization of ILC positron source.

The ILC baseline positron source is an undulator based positron source. The electron main linac beam passes through a long helical undulator to generate a photon beam with energy from few MeV to several hundreds of MeV which then strikes a thin metal target to generate positrons in an electromagnetic shower. The positrons are captured, accelerated, separated from the shower constituents and unused photon beam and then are transported to the damping ring.

The ILC positron source works in a pulsed mode with a large number of bunches in a pulse at a repetition rate of 5Hz and the repetition rate will be increased to 10Hz for low energy runs as documented recently in SB2009. The 10Hz low energy running scenarios are asserted as a result of insufficient positron yield when the drive beam energy is lower than 150GeV nominal drive beam energy for ILC RDR baseline.

Besides the baseline helical undulator based positron source for ILC, there are other alternative schemes like Laser Compton Scattering based and conventional positron source under R&D in parallel. But here we'll concentrate on the ILC undulator based positron source and discuss about the key elements and parameters.

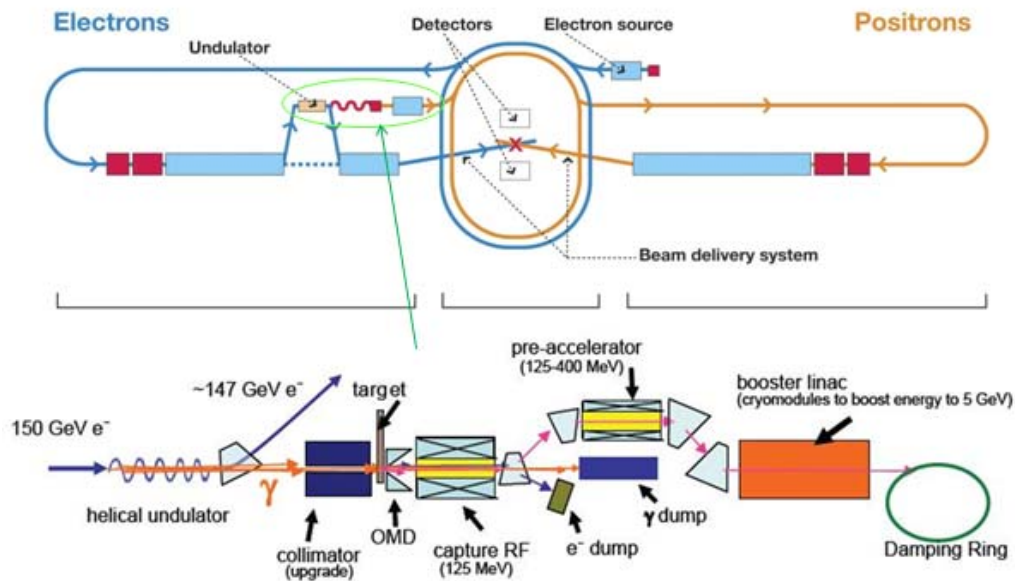


**Figure 1:** Schematic of ILC RDR and undulator based positron source

### 2.1.1.1 Layout as in RDR Baseline

In the RDR baseline [1], the positron source subsystem started with a insertion of an over 100m long of undulator at where the main electron beam is of an energy of 150GeV. The 150GeV main electron beam get bended into the undulator where it will lost about 3GeV of energy into photon beam and then bended back into electron main linac to be accelerated or decelerated to its' desired before get into beam delivery system (BDS). The photon beam produced by the 150GeV drive beam in the ~115m long undulator will bombard into a thin titanium target (0.4 X0) about 400m downstream from the end of undulator. Following immediately after the conversion target, an optical matching device (OMD) is employed to enhance the capture efficiency. The OMD used in RDR baseline is an AMD with a Bz field of 5T on the surface of target and then adiabatically decreased down 0.5T in 20cm. Passing through the OMD, the positrons will then be accelerated up to 125MeV using normal conducting linacs and then separated from electrons and photons. After separation, the positron beam will then be accelerated up to 400MeV in pre-accelerator and then

transported to super conducting booster linac to boost the energy up to 5GeV followed by a bunch compressing and spin rotation before got injected into damping ring.

The detail of the beam line optics for RDR baseline positron source can be found in [2] and [3]. As described in [2], the ILC RDR positron source beam line is divided into the Positron CAPture (PCAP), the Positron Pre-Accelerator (PPA), the Positron Pre-Accelerator To the Electron main Linac tunnel (PPATEL), the Positron TRANsport (PTRAN), the Positron BooSTeR linac (PBSTR) and the Linac To Ring (LTR). In the PCAP, positron produced in the target will be captured and accelerated up to 125MeV. A systematic simulation of positron source from undulator to 5GeV damping ring entrance can be found in [4].

#### ***2.1.1.2 Layout as in SB2009 Proposal***

As shown in figure 2, in SB2009 proposal [5], changes related to positron source in SB2009 include: Undulator-based positron source located at the end of the electron Main Linac (250 GeV), in conjunction with a Quarter-wave transformer as capture device; a lower beam-power parameter set with the number of bunches per pulse reduced by a factor of two ( $n_b = 1312$ ), as compared to the nominal RDR parameter set; reduced circumference Damping Rings ( $\sim 3.2$  km) at 5 GeV with a 6 mm bunch length; integration of the positron and electron sources into a common “central region beam tunnel”, together with the BDS, resulting in an overall simplification of civil construction in the central region.

The change with most significant impact on positron source is to move the undulator based positron source to the end of electron main linac to lower the cost and simplify the civil construction. As a result of such change, the drive beam energy of the undulator based positron source will not be fixed and a study of the performance under different drive beam energies has to be done to understand the risks and solutions.

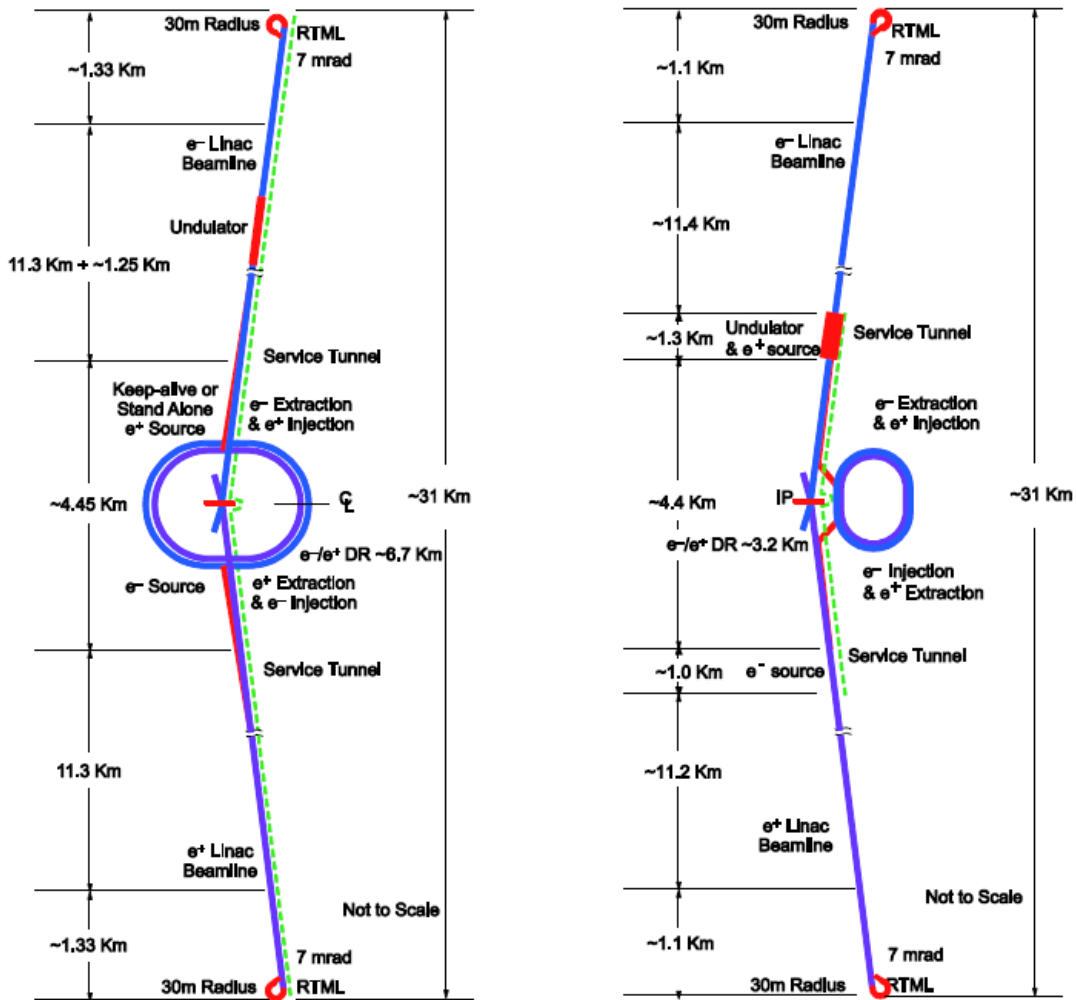


Figure 2: RDR layout and the SB2009 layout

### 2.1.1.3 Critical Components of Undulator Based Positron Source

As mentioned before, the undulator based positron source consists of a long undulator, a thin titanium alloy conversion target, OMD, positron capturing RF linacs, transportation beamline optics, booster linacs, spin rotator and bunch compressor. Among those components, undulator, target, OMD and capturing RF linacs are the most unique and critical components for positron source.

The undulator determines the spectrum of photon radiated for a given electron drive beam. It has great impact on the positron yield and also the polarization property of resulting positron source. The ILC RDR baseline has chosen a baseline of  $K=0.92$  and  $\lambda_u=1.15\text{cm}$ . As shown in figure 3, a 4 meter long cryo-module with two 1.7m long RDR undulator has been completed at STFC/RAL/Daresbury. With 137m RDR undulator, when driven with 150GeV drive beam, the RDR can provide a positron yield of 1.5 with a  $0.4\times 0.4$  Titanium target and an AMD with 5T at the surface of target. When a quarter wave transformer is used in place of AMD, 231m long RDR undulator

is required in order to achieve the 1.5 positron yield. When the drive beam energy is lower or higher as in SB2009, the positron yield can be higher or lower. The detail will be discussed later.

The conversion target is where the positron produced as a result of pair production in the field of a nucleus in the target. Unlike the conventional positron source where the target needs to be 4-6 radiation length thick, the undulator based positron source requires a target of only 0.4-0.5 radiation length. Since the ILC requires about  $5.3 \times 10^{13}$  positrons per RF pulse, thermal stress in the target has to be kept under control in order

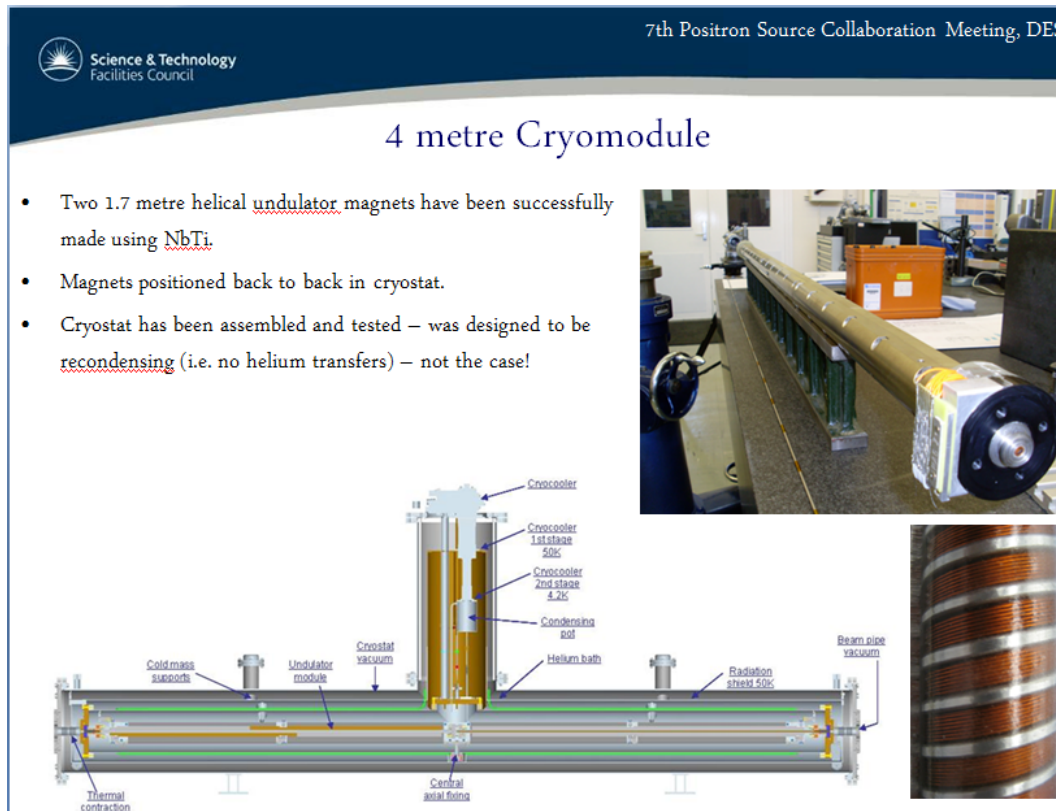


**Figure 3:** 4 meter cryomodule of ILC RDR undulator

to avoid target damage. Low  $Z$  materials have in general a higher heat capacity than high  $Z$  materials. Considering the heat load, low  $Z$  materials are hence preferable as target material. Some studies before shown that at the optimum target thickness of  $0.4X_0$  the yield for a low  $Z$  material as Ti is only about 16% below the yield of an equivalent W target [6]. For ILC RDR baseline and SB2009, the target is a titanium wheel with a diameter of 2 meter and a rim of 2cm wide and 1.4cm thick. In order to take away the heat deposition, a cooling system with rotating vacuum seal for the target is being prototyping and testing for leakage of fluid and vacuum from the effect of vibration and magnetic field at LLNL. Figure 4 shows the vacuum seal test setup at LLNL [7].



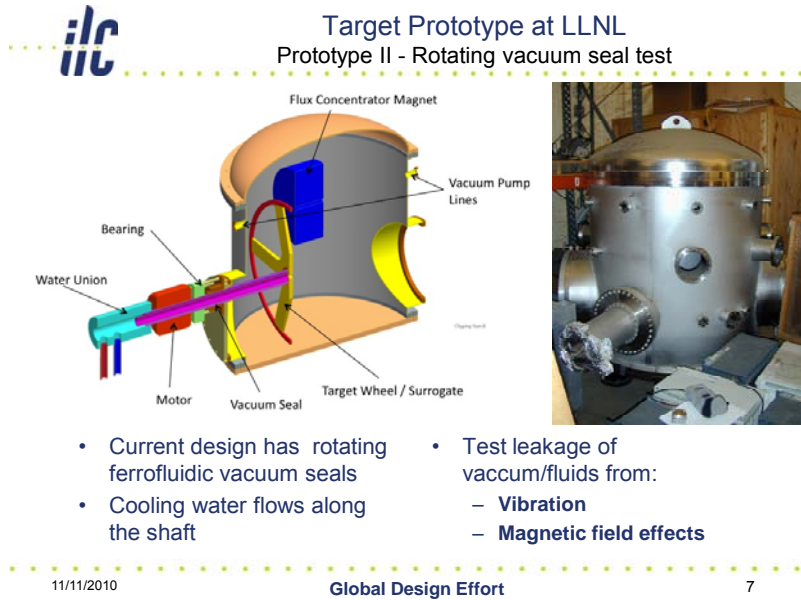


**Figure 4:** Rotating vacuum seal test at LLNL

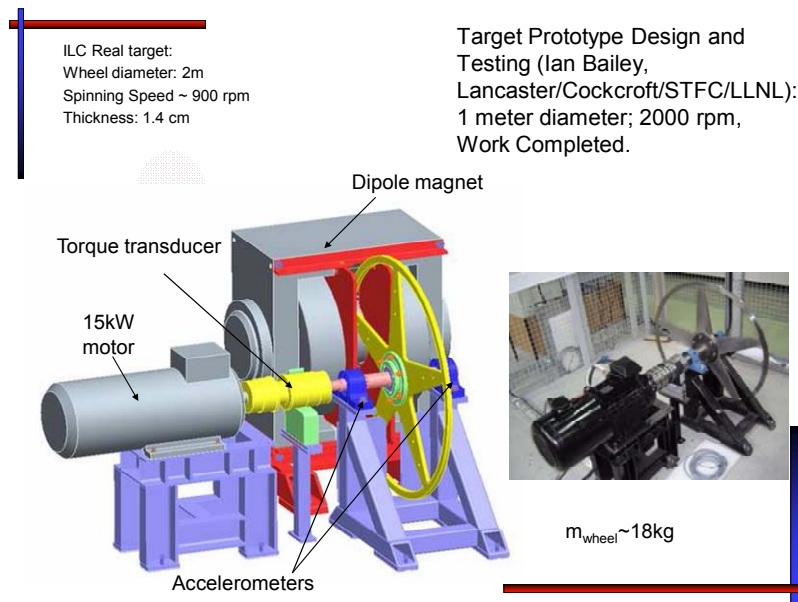


**Figure 5:** Rotating target prototype experiment at STFC

As shown in the schematic layout, target will be followed by an OMD and will be likely exposed to high magnetic field except for cases using lithium lens. The effect from the eddy currents of moving metal objects in magnetic field has also been studied [8] and experiment has been set up and done data taking (STFC/LLNL) [9]. The experiment setup at STFC is showing in Figure 5.

OMD is used to enhance the positron capture efficiency in a positron source and there exist several different type of OMD. Numerical studies have done to compare them under the same conditions, same undulator, target and capturing RF. As shown in table 1, for RDR undulator configuration, both AMD and lithium lens has a capture efficiency of about 30%. But with AMD, the 2 meter diameter target wheel needs to be able rotating at 900RPM in 6T magnetic field which makes it impractical if not impossible. For lithium lens, the performance is about the same of an ideal AMD. But given the beam intensity of ILC positron source, concerns about the survivability of windows need to be answered before it can be seriously considered. To be conservative, the quarter wave transformer is chosen to be used in the RDR baseline and meanwhile, the prototyping of flux concentrator is being carried out at LLNL.

**Table 1:** Capture efficiency of different OMD

OMD	Capture efficiency
Immersed target, AMD (6T-0.5T in 20 cm)	~30%
Non-immersed target, flux concentrator (0-3.5T in 2cm, 3.5T-0.5T 14cm)	~26%
1/4 wave transformer (1T, 2cm)	~15%
0.5T Back ground solenoid only	~10%
Lithium lens	~29%

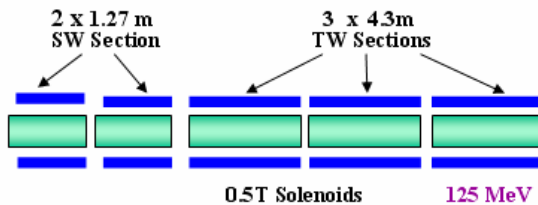


**Figure 6:** Layout of positron capturing region

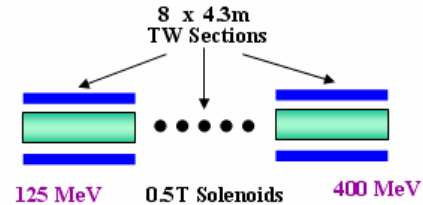


**Figure 7:** Layout of positron Pre-Accelerator

Due to the extremely high energy deposition from positrons, electrons, photons and neutrons behind the positron target, and because a solenoid is required to focus the large emittance positron beam, the 1.3 GHz pre-accelerator has to use normal conducting structures up to energy of 400 MeV. There are many challenges in the design of the normal-conducting portion of the ILC positron injector system such as obtaining high positron yield with required emittance, achieving adequate cooling with the high RF and particle loss heating, and sustaining high accelerator gradients during millisecond-long pulses in a strong magnetic field. Considering issues of feasibility, reliability and cost savings for the ILC, the proposed design for the positron injector contains both

standing-wave (SW) and traveling-wave (TW) L-band accelerator structures. A short version of the new type of the SW section is under fabrication and testing at SLAC[10].

As shown in figure 6, the capture region is composed of two 1.27 m SW accelerator sections at 15 MV/m accelerating gradient and three 4.3 m TW accelerator sections at 8.5 MV/m accelerating gradient in order to capture and accelerate the electron beam to 125 MeV. The positrons are then accelerated from 125 MeV to 400 MeV in a pre-accelerator region, which is composed of eight 4.3 m TW sections at 8.5 MV/m accelerating gradient as shown in figure 7. All accelerator sections are surrounded with 0.5 T solenoids.

The high gradient (15 MV/m) positron capture sections have been designed to be simple  $\pi$  mode 11 cells SW type of accelerator structures. The advantages are a more effective cooling system, higher shunt impedance with larger aperture (60 mm), lower RF pulse heating, apparent simplicity and cost savings. The mode and amplitude stability under various cooling conditions for this type of structure have been theoretically verified. Figure 8 shows a cutaway view of the SW structure and Table 2 gives the important RF parameters.

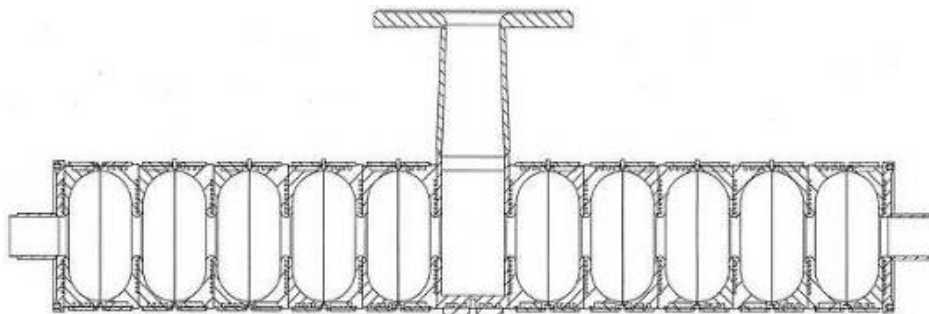


**Figure 8:** 11 Cell  $\pi$  mode SW structure

**Table 2:** Parameters of SW structure.

Structure Type	Simple $\pi$ Mode
Cell Number	11
Aperture $2a$	60 mm
Q	29700
Shunt impedance $r$	34.3 M $\Omega$ /m
$E_0$ (8.6 MW input)	15.2 MV/m

All TW sections are designed to be 4.3 m long,  $3\pi/4$  mode constant gradient accelerator structures. The RF group velocity of traditional  $2\pi/3$  mode traveling wave structures is too high for our larger apertures (the ratio of iris radius with wavelength  $a/\lambda \sim 10\%$ ) to obtain a good RF efficiency. Therefore, to increase the “phase advance per cell” was used to optimize the RF efficiency for designing this type of large aperture TW structure. Compared with standing wave structures, the advantages are lower pulse heating, easy installation for long solenoids, no need to use circulators for RF reflection protection, apparent simplicity and cost saving. Figure 9 shows the shapes for three typical cells and Table 3 gives the important RF parameters.

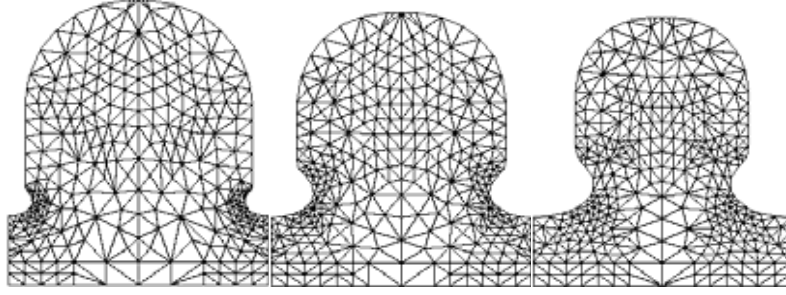


**Figure 9:** Shapes of 3 typical TW structure cell

**Table 3:** RF parameters of TW structure

Structure Type	TW $3\pi/4$ Mode
Cell Number	50
Aperture $2a$	46 mm
Attenuation $\tau$	0.98
Q	24842 - 21676
Group velocity $V_g/c$	0.62% - 0.14%
Shunt impedance $r$	48.60 - 39.45 M $\Omega$ /m
Filling time $T_f$	5.3 $\mu$ s
Power Dissipation	8.2 kW/m
$E_0$ (8.6 MW input)	8.0 MV/m

### 2.1.2 The RDR Undulator Based Positron Source

As mentioned in previous section, the ILC RDR undulator based positron source is consisted of a helical undulator with  $K=0.92$  and  $\lambda_u=1.15\text{cm}$ ; a 2 meter diameter target wheel with a rim of 2cm wide, 1.4cm thick titanium alloy; an AMD with 5T field on target surface and decreased adiabatically down to 0.5T in 20cm followed by capturing RF system, etc. The drive beam is the 150GeV main electron beam. Simulation has shown that for 100m RDR undulator, the positron yield is  $\sim 1.28$  for 100m long RDR undulator without photon collimator and  $\sim 0.7$  for 100m long RDR undulator with photon collimator to enhance the positron beam polarization to  $\sim 60\%$ . In order to achieve a yield of 1.5, one has to increase the length of undulator in both cases. For low polarization source, one will need about 117m long RDR undulator to achieve the 1.5 goal of positron yield. For 60% polarization, one will need  $\sim 215\text{m}$  long RDR undulator.

Showing in figure 10 is photon number spectrum of RDR undulator with 150GeV drive beam. As shown in figure 10, the RDR baseline undulator has a 1<sup>st</sup> harmonic critical energy of  $\sim 10\text{MeV}$ . The contributions to the total number of photons from harmonics are  $\sim 52\%$  for 1<sup>st</sup> harmonic,  $\sim 22\%$  from 2<sup>nd</sup> harmonic, 11% from 3<sup>rd</sup> harmonic, 6% from the 4<sup>th</sup> harmonic, 3.6% from the 5<sup>th</sup> harmonic, 2% from the 6<sup>th</sup> harmonic, 1.2% from the 7<sup>th</sup> harmonic, 0.8% from the 8<sup>th</sup> harmonic. But due to the larger cross section of the positron production from higher energy photons, we found

that these higher harmonics play dominant role in producing positrons in the target, even though their total number is smaller.

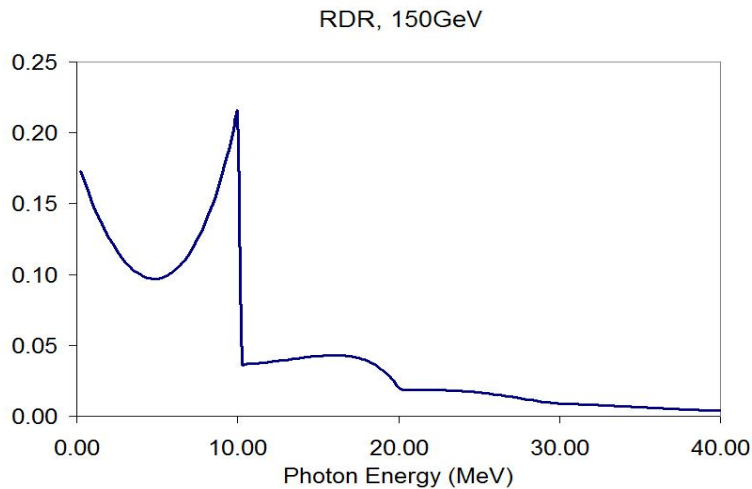


**Figure 10:** Photon number spectrum of RDR undulator with 150GeV drive.

As shown in Figure 11, the partition of yield contribution from harmonics for polarized positron source using undulator with  $K=0.92$   $\lambda_u=1.15\text{cm}$ , the 1st harmonic only contributes  $\sim 6\%$ . The contribution to the captured positron beam is dominated by 2<sup>nd</sup> to 6<sup>th</sup> harmonic.

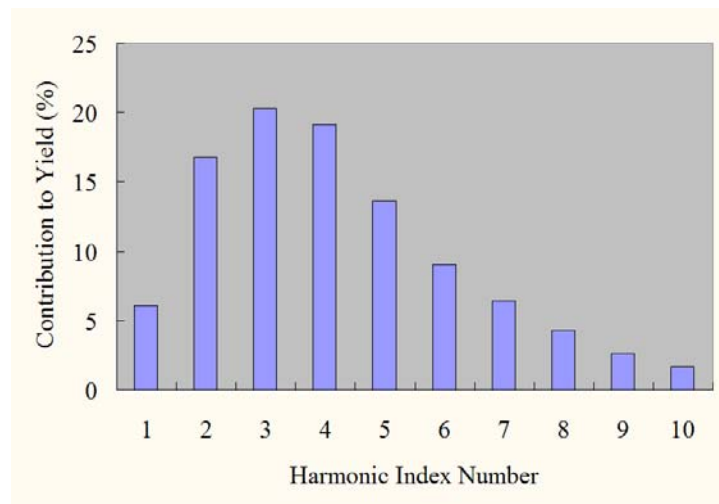


**Figure 11:** Yield contribution from different harmonics of RDR undulator

Showing in Figures 12 and 13 are the initial polarization and energy distribution of positrons of the RDR positron source of all positrons and captured positrons as they exiting the target surface. Assuming the polarization will be preserved, then the polarization of captured positron beam will be  $\sim 25\%$  if OMD is AMD or  $\sim 33\%$  if OMD is FC.

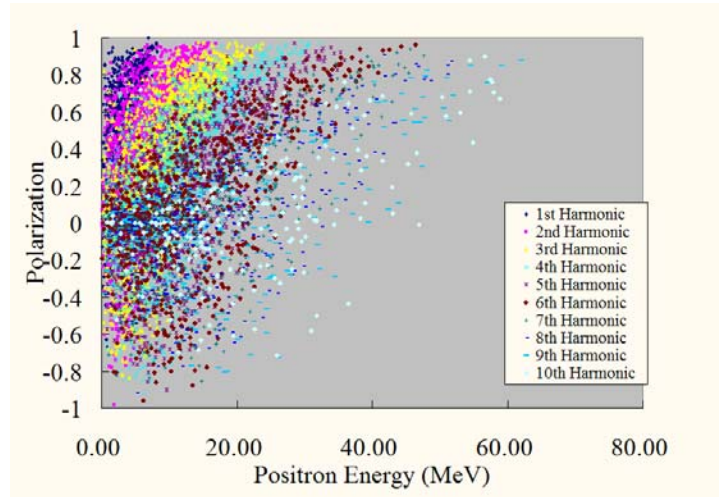


**Figure 12:** Initial positron polarization and energy distribution of RDR positron source exiting the target surface.

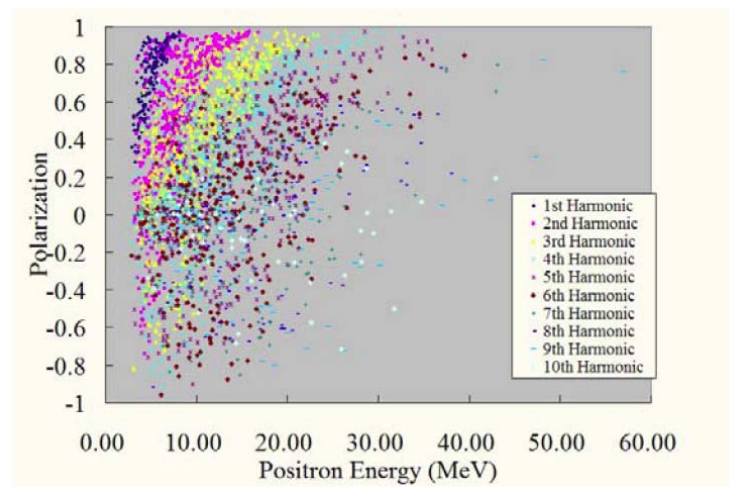


**Figure 13:** Initial positron polarization and energy distribution of RDR positron Source captured positrons.

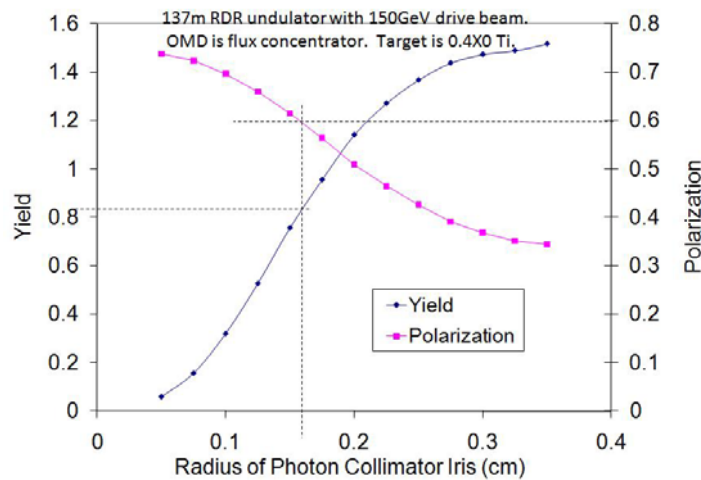


**Figure 14:** Yield and polarization of positron source with 137m RDR undulator using FC as OMD.

Showing in Figure 14 is yield and polarization of positron beam of 137m RDR undulator with FC as function of photon collimator iris. As shown in this figure, 60% polarization can be achieved with a photon collimator of 1.6mm in radius of iris. The yield for 137m RDR undulator will be 0.82 when polarization is 60%. In order to have yield of 1.5 and polarization of 60%, the length of undulator has to be increased to about 256m.

### 2.1.3 The SB2009 Undulator Based Positron Source

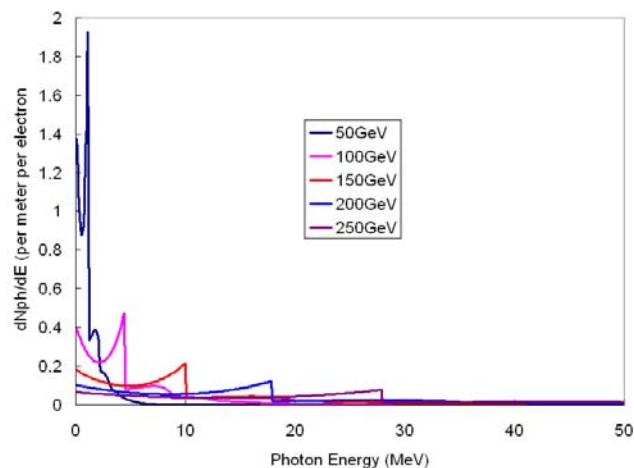


**Figure 15:** Photon number spectrums of RDR undulator with different drive beam energies .

As mentioned before, the undulator of positron source has been relocated to the end of electron main linacs in SB2009 proposal and also a quarter wave transformer has been chosen to be the OMD. As a result of these changes, the drive beam energy of undulator will be varying from 50GeV to 250 GeV for different running scenarios. As

the quarter wave transformer has been used for OMD, in order to achieve the yield of 1.5, the length of undulator is increased to 231m for nominal drive beam energy of 150GeV and thus the heat load in target increased.

As showing in Figure 15, the photon number spectrum of the photon radiation from RDR undulator has a strong dependence on the drive beam energies. The number of photons stays the same for different drive beam energy, but the critical photon energy scales with  $\gamma^2$ . The pair production cross section strongly depends on the photon energy and thus the positron yield also strongly depends on the drive beam energy.

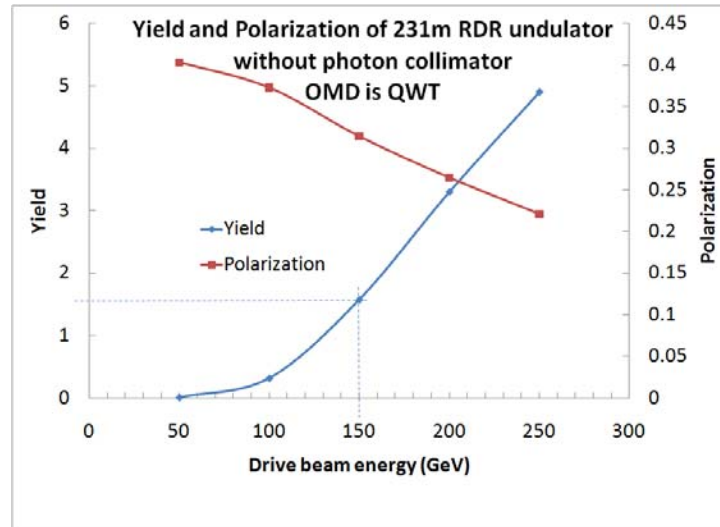


**Figure 16:** Yield and polarization of SB2009 undulator based positron source.

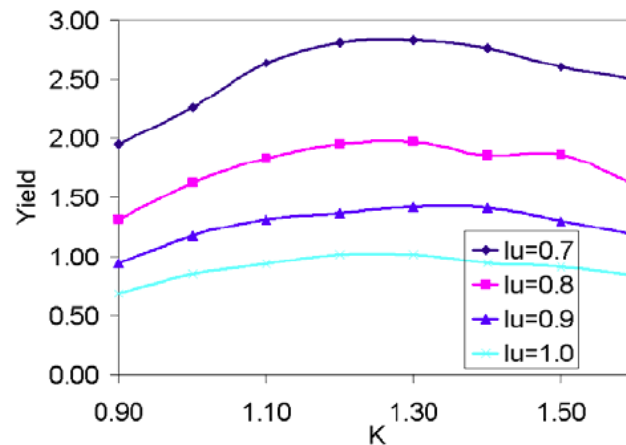
Showing in Figure 16 are the yield and polarization of SB2009 undulator based positron source as a function of drive beam energy. As showing in this figure, the yield is 1.5 for the nominal drive beam energy, 150 GeV and the corresponding polarization is about 30%. The positron yield will drop significantly when drive beam energy goes below 100GeV. In order to maintain the luminosity of the machine at lower energy runs, 10Hz operation is introduced into the SB2009 proposal where 5 pulses will be at 150GeV for positron generation and 5 pulses will be at the lower energy for collision. When the drive beam energy increased, the yield goes up while the polarization goes down. In order to maintain the polarization at about 30%, one can lower the magnetic field of undulator and thus lowered the K and increase the portion of photon from 1<sup>st</sup> harmonic and bring the polarization back. Study has shown that, for 250GeV drive beam and 231m long undulator with  $\lambda u=1.15\text{cm}$ , one can run the undulator at K is about 0.45 to maintain the polarization of captured beam to be 30% while the yield is 1.5.



**Table 4:** Drive beam energy lost for SB2009 undulator based positron source

Drive beam energy	Energy lost per 100m	Energy lost for 1.5 yield
50GeV	~225MeV	N/A
100GeV	~900MeV	~9.9GeV
150GeV	~2GeV	~4.6GeV
200GeV	~3.6GeV	~3.7GeV
250GeV	~5.6GeV	~3.96GeV

Showing in Table 4 are the drive beam energy lost for different drive beam energy passing through SB2009 undulator.

**Figure 17:** Yield of different high K short period undulator with 100 GeV driver beam energy.

#### 2.1.4 High K Short Period Undulator

The current ILC RDR undulator is NbTi based superconducting helical undulator which has a K of 0.92 and period of 1.15cm. With this undulator, when the drive beam energy get lowered down to 100GeV, the positron yield will dropped down to ~0.3 from 1.5 ( 150 GeV drive beam, 137m long undulator, 0.4X0 Ti target and using flux concentrator ). In order to achieve a reasonable yield at lower drive beam energy, it is required to push the period even shorter and keep the K at same level in the same time.

With Nb3Sn superconducting strand, it is possible to have a shorter period and high K in the meantime. The goal set by undulator design group is to reduce the period to ~9mm.

Showing in Figure 17 is a scan of undulator parameter with fixed drive beam energy of 100GeV. The assumptions used in the setup of this set of simulation are as follows:

- Length of undulator: 231m
- Drive beam energy: 100GeV
- Target: 0.4X0, Ti
- Photon Collimation: None
- Drift to target: 400m from end of undulator
- OMD: FC, 14cm long, ramping up from 0.5T to over 3T in 2cm and decrease adiabatically down to 0.5T in 12cm.

As shown in Figure 17, the yield peaks around  $K=1.2$  for all the different period length considered while increasing with the reducing of undulator period. For the nominal targeting parameter of new undulator,  $K=0.9$  and  $\lambda_u=0.9\text{cm}$ , the yield of 231m long such undulator will have a positron yield of about 0.94 which is about twice the value for RDR undulator driven with 100GeV beam with the same length of undulator and capturing optics. From the results shown in figure 10, the advantage of short period and high  $K$  undulator is obvious. Some detail about high  $K$  short period undulator based positron source can found in [11].

### 2.1.5 References

1. International Linear Collider Reference Design Report, Vol. 3, Aug, 2007
2. F. Zhou, etc. Start-to-end beam optics development and multi-particle tracking for the ILC undulator based positron source, SLAC-PUB-12239, Jan. 2007
3. F. Zhou, etc. Transport Optics Design and Multi-Particle Tracking for the ILC Positron source, pp: 3124-3126, Proceedings of PAC07, Albuquerque, New Mexico, USA
4. W. Liu, W. Gai, K.-J. Kim, *Systematic Study of Undulator Based ILC Positron Source: Production and Capture*, PAC07 – Proceedings, Albuquerque, New Mexico, USA, 2007
5. Owen Taylor, *Update on 4m module and generating higher fields*, 7<sup>th</sup> Positron source collaboration meeting, Desy.
6. K. Floettmann, Positron Source Options for Linear Colliders, pp 69-73 , Proceedings of EPAC 2004, Lucerne, Switzerland
7. Jeffrey Gronberg, private communication.
8. S. Antipov, W. Gai, W. Liu, L. Spentzouris. *Numerical Studies of International Linear Collider Positron Target and Optical matching device field effects on Beam*. Published in Appl. Phys. Vol. 102, 014910 (2007)
9. Ian Bailey, *Target eddy current experiment and modeling*, 7<sup>th</sup> Positron source collaboration meeting, Desy.
10. J. W. Wang, etc, Positron Injector Accelerator and RF System for the ILC, SLAC-Pub-12412, 2007
11. W. Liu, W. Gai, Numerical Study on High  $K$ , Short Period Undulator for ILC Positron Source, ILC-NOTE-2011-058.

## 3 ILC Damping Rings

### 3.1 Damping Rings Overview

Susanna Guiducci, LNF/INFN Frascati, Italy  
 Mail to: [susanna.guiducci@lnf.infn.it](mailto:susanna.guiducci@lnf.infn.it)

#### 3.1.1 Introduction

The high luminosity of a linear collider will depend on colliding beams with emittances much smaller than can be produced directly from particle sources. In the case of the positron beam, the vertical emittance must be reduced by five orders of magnitude between the source and the interaction point. Emittance reduction is achieved by the natural synchrotron radiation damping of the beam circulating in a storage ring (damping ring) between machine pulses. The damping ring (DR) requirements are driven by the upstream and downstream systems and principally by the characteristics of the main linac operation. In particular number of bunches, and store time are fixed by the linac pulse time structure: ring circumference, bunch spacing and damping times follow. The ILC [1] and CLIC [2] linear colliders are based on different RF technology and have different pulse length and repetition frequency: 1 ms at 5Hz for ILC and 150 ns at 50Hz for CLIC. The main differences between the damping rings parameters, shown in Table 1, come from that. For getting the high luminosity, ILC requires a higher bunch charge, whereas CLIC targets to much lower emittances.

**Table 1:** ILC and CLIC DRs parameters.

Parameters	ILC	CLIC
Bunch population [ $10^9$ ]	20	4.1
Bunch spacing [ns]	369	0.5
Number of bunches/train	1312	312
Repetition rate [Hz]	5	50
Ex. H/V/L norm. emittances [ $\mu\text{m}, \text{nm}, \text{keV}\cdot\text{m}$ ]	(4.4,20,38)	(0.5,5,6)
Energy [GeV]	5.0	2.86
Circumference [m]	3238	421
Energy loss/turn [MeV]	4.5	4.2
RF voltage [MV]	7.5	4.9
Compaction factor	$1.3 \times 10^{-4}$	$8 \times 10^{-5}$
Damping time x / s [ms]	24 / 12	1.8 / 0.9
Number of arc cells/wigglers	64/32	100/52
Dipole/wiggler field [T]	0.26/1.6	1.4/2.5

Although the different designs, a number of design approaches and challenges still remain common: two stream instabilities due to fast ions in the electron ring and electron cloud in the positron one, ultra low emittance generation, and stringent beam

stability requirements. This paper will describe in more detail the ILC DR design and R&D status; more info on the CLIC DR design can be found in the reference [3].

### 3.1.2 ILC Damping Ring Design Status

The baseline design described in the Reference Design Report [1] is based on a 6.4 km circumference. Since then design changes have been implemented for reduction of cost and technical risk. A racetrack layout has been adopted concentrating the systems that require access in the long straight sections and reducing the large number of access shaft for distributed RF and wigglers. A low and flexible momentum compaction lattice has provided RF system and bunch length optimization. The lattice design named DCO4 is quite mature; it satisfies the main DR requirements and has been the basis of a large amount of technical design work [4].

A new ILC baseline has been proposed for the Technical Design Report due end of 2012. The new parameter set has a number of bunches per pulse reduced by a factor two, and therefore it allows to half the DR circumference keeping the same current. At present different lattices for a 3.2 km ring are under evaluation [5-7], based on the same racetrack design as the DCO4 and with very similar straight sections, in order to take advantage of the technical design already done.

The DR parameters satisfy the requirements for three different operation configurations. The nominal configuration, named “Low power”, with 5Hz repetition frequency and 1312 bunches, shown in Table 1, has been adopted for ILC operation at center of mass energies between 250 and 500 GeV. To increase luminosity at low energy ( $E_{\text{cm}} < 250$  GeV) the design will allow operation at 10Hz repetition rate, which requires a factor of two reduction of the rings damping time. Finally, a configuration with the originally specified 2625 bunches, i.e. twice the beam current (High power) is under study for the energy upgrade.

The main requirements for the DR are transverse and longitudinal acceptances large enough for the injected positron beam and very low emittances for the extracted beam. With respect to the RDR the rms length of extracted bunches has been reduced from 9mm to 6mm to simplify the bunch compressors downstream of the damping rings.

The electron and positron ring are arranged one on top of the other with counter-rotating beams. Injection and extraction for each ring are located in the same straight section. The injection line entering the electron ring is superimposed on the positron extraction line and vice versa. RF cavities and wigglers are in the opposite straight section with respect to injection and extraction. The wiggler straight is located downstream of the RF cavities in order to avoid damage by synchrotron radiation. The RF cavities for each ring are offset from the centre of the straight so that the cavities for the two rings are not superimposed on top of each other. The straight sections also include a phase advance tuning section and a chicane for adjusting the circumference by  $\Delta C/C = \pm 10^{-6}$ .

Due to the circumference reduction, the nominal damping time is obtained with nearly half of the wiggler magnets and RF cavities with respect to the RDR design. For the wigglers we assume to use CESR-c type wigglers at 1.6 T field as in the RDR. A synchrotron radiation absorber placed downstream each wiggler has been designed for the RDR lattice [4]. An optimization of length and period at higher field (2 T) is being studied to increase radiation damping for the 10Hz operation. The design of the

synchrotron radiation absorbers will be modified increasing the length to cope with the highest power and the extra space will be inserted in the lattice.

The RF system is made of 650 MHz superconducting cavities similar to the CESR or KEK-B cavities. The RF section leaves space for a number of cavities sufficient to cover all the options (Low power, 10Hz repetition rate and High power). Since it is an expensive system, cost containment is important. Therefore a low momentum compaction (in the range  $1.7 \cdot 10^{-4} < \alpha_c < 2.7 \cdot 10^{-4}$ ) is preferred in order to achieve the 6mm bunch length with a rather low RF voltage.

At the ALCPG11 workshop a DR session has been dedicated to the lattice evaluation [8]. Three different lattices have been compared: DSB3, based on Super-B arc cell [5], DMC3 FODO-style lattice with  $90^\circ$  phase advance [6], and TME-style lattice [7]. Lattice choices could all potentially satisfy the DR requirements, but none are ready for final down-select. Work is continuing to standardize the straights with the minimum length and to optimize dynamic aperture and momentum compaction choice for lattice selection in June.

### 3.1.3 ILC Damping Ring R&D Status

The main challenges for the damping rings are with the fast kickers, low emittance tuning and controlling collective effects, in particular electron cloud. Two dedicated test facilities were identified for this effort: CEsrTA at Cornell University and ATF at KEK. Both programs have managed large collaborations, with contributors from institutions worldwide working on simulation, experiment and design.

The ATF damping ring achieved a vertical emittance as low as four picometres before the publication of the Reference Design Report and has supported a wide range of important research for many years: low-emittance tuning and intrabeam scattering studies, studies of the fast ion effect and fast kicker tests. Now the damping ring's main focus is the production of an extracted beam with the required characteristics for the ATF2 program and the development and test of low-emittance beam diagnostics. A description of ATF R&D activity on low emittance tuning and multi-bunch extraction test of the fast kicker is reported elsewhere in this issue.

The CESR storage ring has been modified to be used as a test facility for Electron Cloud (EC) studies in low emittance regime. The results from the first 2.5 years of the CESR-TA R&D program are presently being integrated into the ILC DR technical design [9]. A more detailed description of the program is given in a dedicated section in this issue. In particular, tests of electron cloud mitigations as grooved chambers, electron clearing electrodes, and different coating technologies to suppress the secondary emission yield have been carried out. The low-emittance tuning effort provides the foundation for studies of the emittance-diluting effects of the electron cloud in a regime approaching that of the ILC damping rings. A vertical emittance less than 20 picometer has been measured, achieving the goal for the CEsrTA program [10]. The program has covered EC build-up and EC-induced beam dynamics studies for benchmarking the physics models and simulations. Based on these studies, the confidence to make valid projections of the expected ILC positron damping ring performance has been significantly enhanced.

The demonstration of ultra-low emittance was carried out in the framework of the CEsrTA and ATF collaborations, but important results have also come from the synchrotron light sources community. A step forward in the demonstration of very low

vertical emittance has been achieved at some synchrotron light sources, where they operate low-emittance storage rings with characteristics very similar to the ILC damping ring and have developed alignment procedures, machine modeling, tuning algorithms, and orbit stabilization for coupling correction and low-vertical emittance tuning [11]. In particular, Diamond Light Source in the UK, the Swiss Light Source and the Australian Synchrotron storage ring have achieved betatron coupling correction down to 0.1 percent and vertical emittances below two picometers [12-14]. Significant progress has been made in the development of diagnostic systems for the measurement of such small vertical emittances [15-17].

The injection/extraction kickers act as the bunch-by-bunch beam manipulator to compress and decompress the bunch spacing into and from the damping ring. The kickers require high repetition frequency, three megahertz, and very fast rise and fall times of the kicker field: six nanoseconds for the nominal configuration and three nanoseconds for a proposed luminosity upgrade. The tolerance on horizontal beam jitter of the extracted beam is approximately ten percent of the beam size, which requires the extraction kicker amplitude relative stability to be below  $7 \times 10^{-4}$ . A total pulse duration below three nanosecond has been already demonstrated in the ATF using a 30-centimetre long strip-line kicker together with a semiconductor high-voltage pulse source [18]. An ILC-type beam extraction experiment using two strip-line kickers has been carried out successfully at ATF and is described in detail in a dedicated session in this issue.

The design of the new fast strip-line kickers currently used at LNF for the injection of the DAΦNE Φ-factory is based on strip-line tapering to obtain a low beam impedance device and an excellent uniformity of the deflecting field in the transverse plane [19, 20]. After installing the injection system, no instability effects due to the kickers were observed and the DAΦNE broadband impedance, arising from this and other simultaneous vacuum chamber modifications, was reduced by about 50 percent [21]. These characteristics are essential also for the ILC damping ring, and the experience gained with the new DAΦNE injection system will be applied to the damping ring injection system design.

At SLAC two related paths to meet the ILC kicker driver requirements for an ultra fast pulse are being studied: a transmission line adder topology, which combines the output of an array of ultra-fast MOSFET (Metal-Oxide-Semiconductor Field-Effect Transistor) switches and a drift step recovery diode (DSRD) approach. A transmission line adder has been designed based on the ultra-fast hybrid MOSFET/driver switching module. The initial test demonstrated that the adder can combine pulses with 1.4 nanosecond switching time without any degradation [22]. Development of a fully capable DSRD kicker driver is proceeding well, with excellent results obtained from the first commercially produced DSRDs, and from a refined circuit for the MOSFET driver [23]. A prototype with two-nanosecond pulse length and one-megahertz pulse train has been demonstrated. A recent success was to eliminate the post pulse, which is unacceptable for the ILC kicker driver since it affects the bunches adjacent to the kicked bunch [24]. The plan is now to build a demonstration modulator for beam testing at ATF.

### 3.1.4 References

1. N. Phinney, N. Toge, N. Walker, (ed.), "ILC Reference Design Report", Vol. 3 – Accelerator, arXiv:0712.2361, (2007).
2. "The Compact Linear Collider Study", <http://cllc-study.web.cern.ch/CLIC-Study/>
3. Y. Papaphilippou et al., "Design Optimization for the CLIC Damping Rings", proceedings of the 2010 International Particle Accelerator Conference, Kyoto, Japan (2010).
4. A. Wolski et al., "ILC Damping Ring Design Studies at the Cockcroft Institute", ILC-NOTE-2010-057 (2010) <http://ilcdoc.linearcollider.org/record/30937/files/ILC-NOTE-2010-057.pdf>.
5. S. Guiducci, M.E. Biagini, "A Low Emittance Lattice for the ILC 3 km Damping Ring", Proceedings of the 2010 International Particle Accelerator Conference, Kyoto, Japan (2010).
6. D. Wang, J. Gao, Y. Wang, "A New Design for ILC 3.2 km Damping Ring Based on FODO Cell", proceedings of the 2010 International Particle Accelerator Conference, Kyoto, Japan (2010).
7. D. Rubin, "Lattice Studies and Straight Specification" ALCPG11 Workshop at University of Oregon, Eugene, OR, US, March 19-23, 2011. <http://ilcagenda.linearcollider.org/sessionDisplay.py?sessionId=24&confId=4572#20110320>.
8. Damping Ring Lattice Choice Session at ALCPG11 Workshop, University of Oregon, Eugene, OR, US, March 19-23, 2011. <http://ilcagenda.linearcollider.org/contributionDisplay.py?contribId=359&confId=4572>
9. M. Palmer, et al., "CesrTA Preliminary Recommendations for the ILC Positron Damping Ring", to appear in the Proceedings of the ECLLOUD10 Workshop, Ithaca, NY, USA (2010).
10. J. P. Shanks, D. Rubin, D. Sagan, "CesrTA Low Emittance Tuning", Proceedings of IPAC'10, Kyoto, Japan, 2010.
11. R. Bartolini, "Performance and Trends of Storage Ring Light Sources", Proceedings of EPAC08, Genoa, Italy, 2008.
12. R. Bartolini, "Light Sources Trends and Common Design Issues with Low Emittance Rings", LER10, Low Emittance Rings Workshop, CERN 12-15 January 2010. <http://indico.cern.ch/materialDisplay.py?contribId=92&sessionId=21&materialId=paper&confId=74380>
13. M. Böge et al., "The Swiss Light Source a "Test-bed" for Damping Ring Optimization", Proceedings of IPAC10, Kyoto, Japan, 2010
14. R. Dowd, et al., "Emittance Coupling Control at the Australian Synchrotron", Proceedings of PAC09, Vancouver, BC, Canada, 2009.
15. G. Rehm, "Recent Development of Diagnostics on 3rd Generation Light Sources", Proceedings of EPAC08, Genoa, Italy, 2008
16. C. Thomas et al., "X-ray pinhole camera resolution and emittance measurement", PRSTAB, 13, 022805, 2010
17. A. Andersson, et al, "Determination of a small vertical electron beam profile and emittance at the Swiss Light Source" Nucl. Instrum. Methods Phys. Res., Sect. A 591, 437, 2008.
18. T. Naito et al., "Development of a 3ns rise and fall time strip-line kicker for the International Linear Collider", NIM A571(2007) 599-607.
19. D. Alesini et al., "Design and Tests of New Fast Kickers for the DAFNE Collider and the ILC Damping Rings", Proceedings of EPAC 2006, Edinburgh, Scotland, 2006.
20. F. Marcellini, et al., "Tests and Operational Experience with the DAFNE Stripline

- Injection Kicker", Proceedings of PAC09, Vancouver, BC, Canada, 2009.
21. F. Marcellini, et al., "Coupling Impedance of DAFNE Upgraded Vacuum Chamber", Proceedings of EPAC08, Genoa, Italy, 2008.
  22. T. Tang, C. Burkhart, "Development of an Adder-Topology ILC Damping Ring Kicker Modulator", Proceedings of PAC09, Vancouver, BC, Canada
  23. F. Arntz et al., "A Kicker Driver Exploiting Drift Step Recovery Diodes for the International Linear Collider", Proceedings of EPAC08, Genoa, Italy, 2008
  24. C. Burkhart, et al., "Ultra-Fast Damping Ring Kicker Modulator Development at SLAC", IWLC10 Workshop, CERN, October 2010.

## 3.2 An Update on the CESR Test Accelerator Research Program

M.G. Billing, G.F. Dugan, M.A. Palmer and D.L. Rubin  
*for the CESRTA Collaboration*

Cornell University Laboratory for Accelerator-based Sciences and Education  
 (CLASSE), Ithaca, New York 14850, U.S.A.

Mail to: [mark.palmer@cornell.edu](mailto:mark.palmer@cornell.edu)

### 3.2.1 Introduction

The build-up of the electron cloud (EC) in the positron damping ring (DR) of the International Linear Collider (ILC) is one of the principal risk factors for the overall physics performance of the accelerator. In positron storage and damping rings, electrons are produced in the accelerator vacuum chambers through photoemission and secondary emission. Interaction between the resulting EC and the beam can lead to single- and multi-bunch instabilities in the beam. The onset of a single-bunch head-tail instability, which cannot in general be controlled by a conventional feedback system, will lead to emittance growth in the beam. For the ILC DR, which targets a geometric vertical emittance of 2 pm-rad, we must ensure that the machine can be operated safely below this instability threshold. Below the threshold for the onset of single-bunch instabilities, sub-threshold emittance dilution may still occur through the interaction of the beam with the nonlinear fields of the EC. With the ultra low emittance target of the ILC DR, there is little margin for such emittance diluting effects. Hence this area was identified as one requiring further R&D in order to complete the ILC technical design.

The CESRTA research program was approved in late 2007 to carry out electron cloud R&D in support of the ILC technical design. The first dedicated experiments using the Cornell Electron-Positron Storage Ring (CESR) began in March 2008 after the conclusion of 28 years of colliding beam operations for the CLEO experiment [1,2]. Two principal goals were specified for the program. The first was to characterize the build-up of the EC in each of the key magnetic field regions of the accelerator, particularly in the dipoles and wigglers, and to study the most effective methods of suppressing it in each of these regions. This required the design and installation of detectors to study the local build-up of the cloud in each of these environments as well as a supporting simulation program to fully characterize and understand the results. The second goal was to study the impact of the EC on ultra low emittance beams. No positron ring has achieved the 2pm-rad vertical emittance design target of the ILC DR. By benchmarking EC instability and emittance growth simulations in a regime closer to that specified for the DR, confidence in our projections of the final DR performance can be significantly improved. This in turn will determine whether further R&D is required



to reach the design specifications. In order to carry out these measurements, CESR had to be reconfigured as a damping ring and upgraded with the necessary beam instrumentation for low emittance optics correction and characterization of the resulting beams.

### 3.2.2 Conversion of CESR to a Damping Ring Test Accelerator Configuration

Modification of CESR into a damping ring configuration involved three main thrusts:

- Relocation of 6 of the 12 CESR-c damping wigglers [3,4] to the L0 straight which previously supported the CLEO interaction region – this adjustment to the CESR layout provided the capability to place all 12 wigglers in zero dispersion locations for low emittance operation [2];
- Upgrades of the CESR beam instrumentation for low emittance operation and characterization of ultra low emittance beams – in particular, the BPM system was upgraded to provide the necessary measurement resolution along with bunch-by-bunch and turn-by-turn readout capability [5], and a pair of x-ray beam size monitors (xBsMs), also with bunch-by-bunch and turn-by-turn measurement capability, were installed for monitoring of both positron and electron beams [6];
- Addition of vacuum system diagnostics for characterization of local EC growth in a range of vacuum chambers, including those incorporating mitigation techniques that are under consideration for the ILC positron damping ring. Local EC diagnostics deployed around the ring include retarding field analyzers (RFAs) [7,8], TE wave transmission hardware [9], and shielded pickups for time-resolved measurements [10].

Table 1 shows the CESRTA lattice parameters for operation at 2 and 5 GeV. At 2 GeV, 90% of the synchrotron radiation power is provided by the 12 damping wigglers and a natural emittance of 2.6 nm-rad is obtained [11]. During phase I of the CESRTA program, a vertical emittance target of <20 pm-rad (10× the ILC DR vertical emittance target) was specified. A key element of the R&D program is the flexibility of CESR operation. CESR can operate between 1.8 and 5.3 GeV with both positron and electron beams. The ability to operate over a wide range of energies, bunch spacings and bunch intensities enables systematic probes of primary photoelectron and secondary electron contributions to EC build-up in the vacuum chambers which are not feasible at any other facility.

A novel element of the CESRTA upgrade has been the development of a high-resolution x-ray beam size monitor (xBsM) capable of single pass measurements of each bunch in a train [12]. Figure 1 shows a picture of one of the InGaAs detectors wire-bonded to its circuit board along with a single-pass fit of data acquired using pinhole imaging with a 1mA bunch. In addition to pinhole imaging, coded aperture and Fresnel zone plate optics have also been installed in both the positron and electron beam lines. These detectors represent our principal tool for verifying the vertical beam emittance for our ultra low emittance machine optics.

**Table 1:** 2 GeV and 5 GeV lattice parameters for CESRTA.

<b>Energy [GeV]</b>	<b>2.085</b>	<b>5.0</b>
No. Wigglers	12	6
Wiggler Field [T]	1.9	1.9
$Q_x$	14.57	
$Q_y$	9.6	
$Q_z$	0.075	0.043
$V_{RF}$ [MV]	8.1	8
$\epsilon_x$ [nm-rad]	2.6	35
$\tau_{x,y}$ [ms]	57	20
$\alpha_p$	$6.76 \times 10^{-3}$	$6.23 \times 10^{-3}$
$\sigma_1$ [mm]	9.2	15.6
$\sigma_E/E$ [%]	0.81	0.93
$t_b$ [ns]	$\geq 4$ , steps of 2	

Figure 2 shows the layout of the L0 straight after installation of the 6-wiggler string. This region is one of four dedicated CESRTA EC experimental areas. It is equipped with extensive diagnostics to study the growth and mitigation of the EC in wigglers. A second EC experimental straight was installed on the opposite side of CESR in the L3 straight. Figure 3 shows the layout of the L3 region. It supports 4 EC experiments: a large bore quadrupole housing a test chamber; the PEP II chicane, for dipole chamber tests, which was relocated from SLAC after the early termination of PEP II operations; a drift chamber test section presently configured for testing TiZrV (NEG) test chambers; and an in-situ SEY measurement station which supports studies of the processing rates and equilibrium SEY properties of various technical surfaces. In addition to the L0 and L3 experimental regions, two arc sections were configured for flexible installation of experimental drift chambers to study the performance of various mitigations in the photon environment of the CESR arcs.

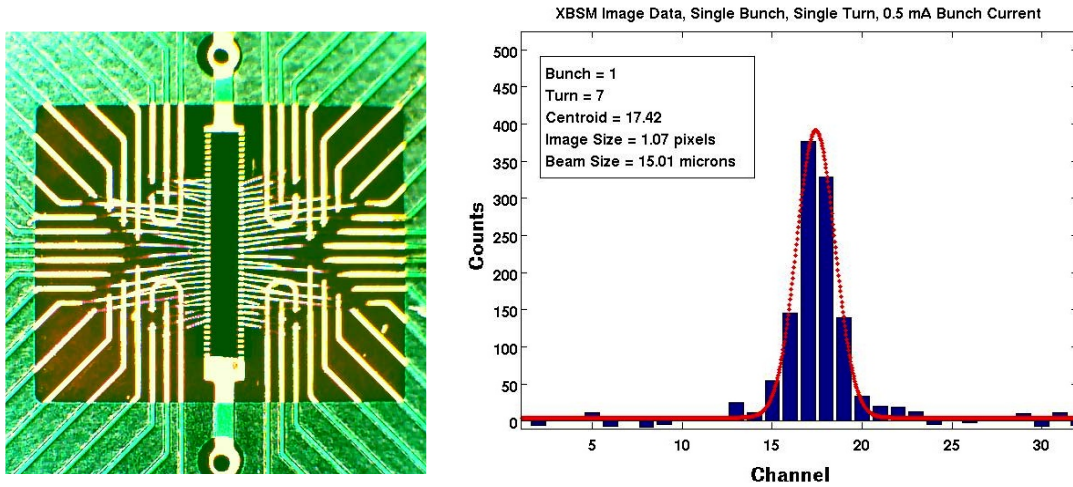


**Figure 1:** Left: image of an xBSM detector, an InGaAs diode array, mounted on its circuit board. 32 diodes of  $400\ \mu\text{m}$  width and  $50\ \mu\text{m}$  pitch are utilized in each detector. Right: a single turn fit to data acquired from a bunch with  $0.8 \times 10^{10}$  particles (at 2.1 GeV beam energy) using a heavy metal slit as the x-ray imaging optic.

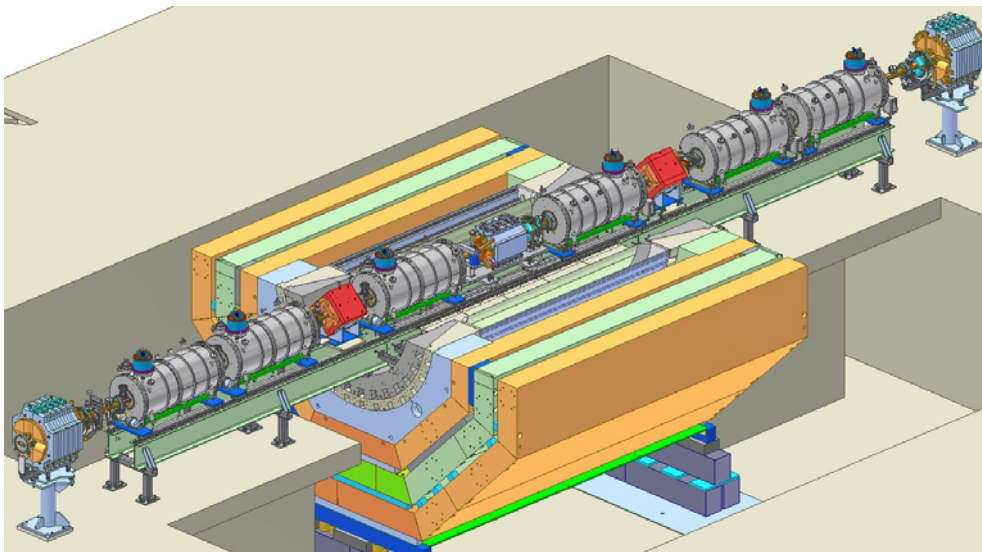


**Figure 2:** Layout of the CESR L0 wiggler straight and EC experimental region with a cutaway view of the CLEO detector. 6 superconducting CESR-c type wigglers are deployed in the straight, which is configured for zero dispersion operation. The straight includes extensive vacuum diagnostics: RFAs, residual gas analyzer, and TE wave measurement hardware.

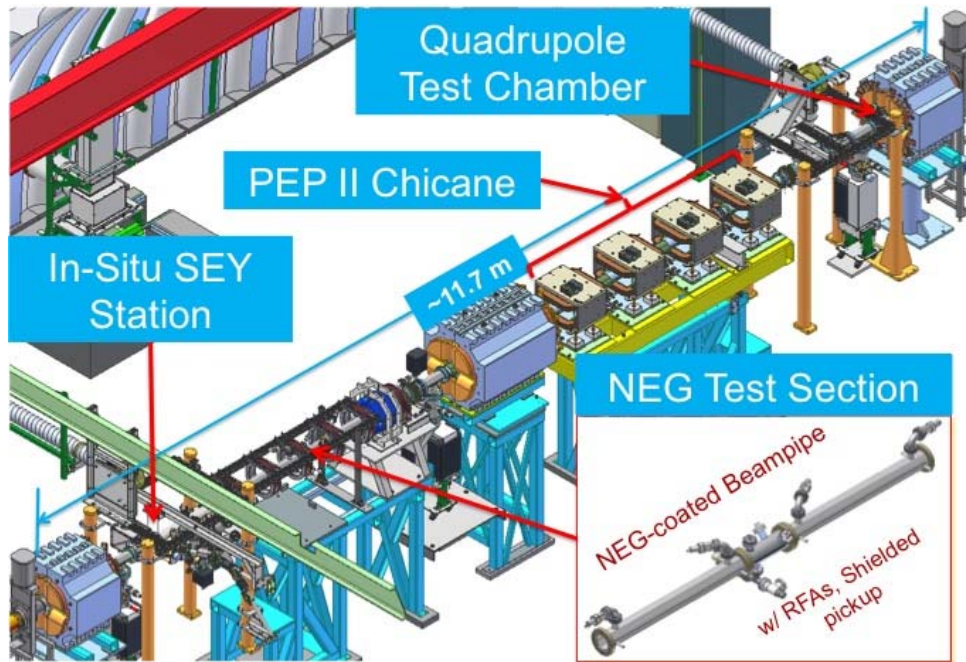


**Figure 3:** Layout of the CESR L3 straight and EC experimental region. Tests of EC mitigations in drift, dipole and quadrupole chambers are possible in this region. Additionally, an in-situ SEY station is also installed which allows characterization of the rate of processing and equilibrium SEY properties of various vacuum system technical surfaces.

### 3.2.3 Electron Cloud Build-Up and Mitigation Studies

RFAs deployed at approximately 30 locations around CESR have enabled the detailed study of local cloud build-up in variety of vacuum chambers under a range of experimental conditions [13, 14]. The RFAs provide a time-averaged current readout at each location. The majority of deployed RFAs utilize a segmented design to provide geometric information about the EC build-up around the azimuth of the vacuum chamber. RFA data taken in vacuum chambers fabricated with EC mitigations provides the foundation for comparison of the efficacy of different EC mitigation methods. An active effort is underway to model this RFA data in order to determine the secondary electron yield (SEY) and photoelectron yield (PEY) parameters of the vacuum chambers treated with mitigations [14-16]. In addition to the RFA studies, TE Wave transmission methods [17] are also being used to characterize the build-up around the ring and a significant simulation effort is underway to take full advantage of these results [18-20]. A final method to study local EC build-up is shielded pickup measurements [21], which are providing additional constraints on the vacuum chamber surface parameters for the chambers in which they're installed. Table 2 summarizes the range of chamber surfaces and mitigation methods that were prepared for testing during Phase I of the CESR TA R&D program.

**Table 2:** Vacuum chambers fabricated for testing during Phase I of the CESR/TA R&D program. Checks indicate chambers for which characterization data has already been acquired while entries with an indicate chambers for which the detailed characterization tests are still in progress.

<b>Mitigation</b>	<b>Drift</b>	<b>Quadrupole</b>	<b>Dipole</b>	<b>Wiggler</b>	<b>Institutions Providing Chambers</b>
Al	☑	☑	☑		CU, SLAC
Cu	☑			☑	CU, KEK, LBNL, SLAC
TiN on Al	☑	☑	☑		CU, SLAC
TiN on Cu	☑			☑	CU, KEK, LBNL, SLAC
Amorphous C on Al	☑				CERN, CU
Diamond-like C on Al	†				CU, KEK
NEG on SS	☑				CU
Solenoid Windings	☑				CU
Fins w/TiN on Al	☑				SLAC
Triangular Grooves on Cu				☑	CU, KEK, LBNL, SLAC
Triangular Grooves w/TiN on Al			☑		CU, SLAC
Triangular Grooves w/TiN on Cu				†	CU, KEK, LBNL, SLAC
Clearing Electrode				☑	CU, KEK, LBNL, SLAC

### 3.2.3.1 EC Mitigation in Dipole Magnets

Figure 4 shows a comparison of the performance of various chamber surfaces in a dipole field along with a plot of the evolution of the transverse distribution of the EC that develops in the dipole chamber as a function beam current. While coating with a low SEY material such as TiN significantly reduces the growth of the EC in this environment, the use of a grooved surface with TiN coating is clearly superior.

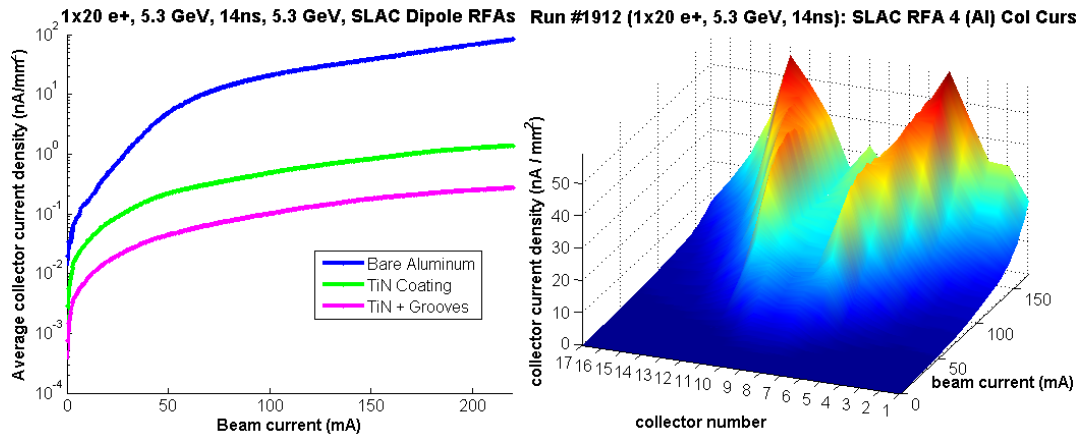


**Figure 4:** Left: the measured RFA current in a dipole versus beam current with a 20 bunch positron train for a bare Al surface, TiN-coated surface and a grooved surface with TiN-coating.

The efficacy of the grooved surface for suppressing the EC is clearly evident. Right: the transverse shape of the EC signal in the dipole RFA (Al chamber surface) as a function of beam current.

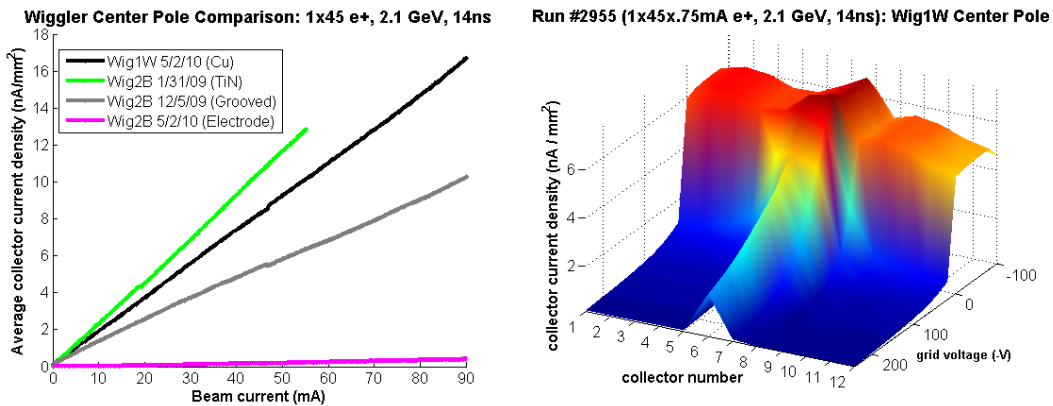
### 3.2.3.2 EC Mitigation in Wiggler Magnets

Figure 5 shows two of the mitigation methods that have been tested in the CESRTA high field damping wigglers: triangular grooves and a clearing electrode. The clearing electrode is a very thin structure based on the design developed at KEK [22] which consists of an  $\sim 0.1$ mm thick tungsten electrode deposited by a thermal spray technique on a  $\sim 0.2$ mm thick  $\text{Al}_2\text{O}_3$  substrate, also deposited by thermal spray. A bare Cu surface and a TiN-coated Cu surface have also been tested.

The left plot in figure 6 shows a comparison of the EC growth as a function of beam current with each of these surfaces. Our observations indicate that the best cloud suppression in the wiggler region is obtained with the clearing electrode. One additional comparison remains, the testing of a grooved surface with TiN coating. This test chamber has recently been installed in CESR and tests will take place over the next few months. The right plot in Figure 6 shows the transverse distribution of the EC present in the vertical field region of the wiggler (Cu surface) as a function of RFA retarding grid voltage, which probes the energy spectrum of the EC.



**Figure 5:** Left: a grooved Cu insert with  $21.8^\circ$  triangular grooves having 1mm pitch for testing in a CESRTA wiggler. Right: a thin clearing electrode applied with a thermal spray method to the bottom half of another CESRTA experimental wiggler chamber.



**Figure 6:** Left: measured RFA current in a wiggler versus beam current with a 20 bunch positron train for a bare Cu surface, TiN-coated Cu surface, and a grooved Cu surface, and a clearing electrode. The efficacy of the clearing electrode for suppressing the EC is clearly evident. Right: the transverse shape of the EC signal in the wiggler RFA as a function of retarding voltage.

### 3.2.3.3 *EC Mitigation in Drift Regions*

EC build-up measurements in drift sections have been used to compare the performance of various coatings. A new coating of significant interest is amorphous carbon coating developed at CERN [23] for use in the SPS. Tests at CESRTA have afforded the opportunity to study the performance of this coating in the presence of synchrotron radiation. Figure 7 shows the relative performance of bare Al, TiN-coated Al, and amorphous C-coated Al surfaces where measurements were made in the same experimental location over successive CESRTA runs. The conclusion is that the mitigation performance of amorphous carbon is quite comparable to that of TiN.

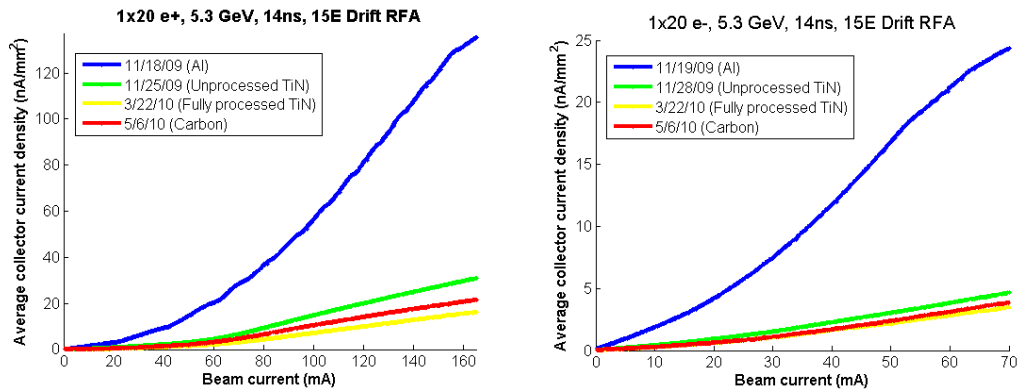


**Figure 7:** Left: measured RFA current in a drift chamber versus beam current with a 20 bunch positron train for a bare Al surface, TiN-coated Al surface, and an amorphous carbon coated Al surface. Right: the same information for an electron beam where response is dominated by photoelectrons. The observed performance of the amorphous carbon and TiN coatings are quite similar in each case.

### 3.2.3.4 EC mitigation in Quadrupole Magnets

EC build-up in quadrupole chambers has also been studied. A quadrupole chamber without mitigation can show quite significant EC build-up. Concerns about long-term trapping of the EC in quadrupole fields [24] require that EC mitigation be incorporated into the ILC DR quadrupole vacuum chambers. Figure 8 shows the effectiveness of TiN coating in this region along with information about the azimuthal distribution of the cloud in the quadrupole vacuum chamber.

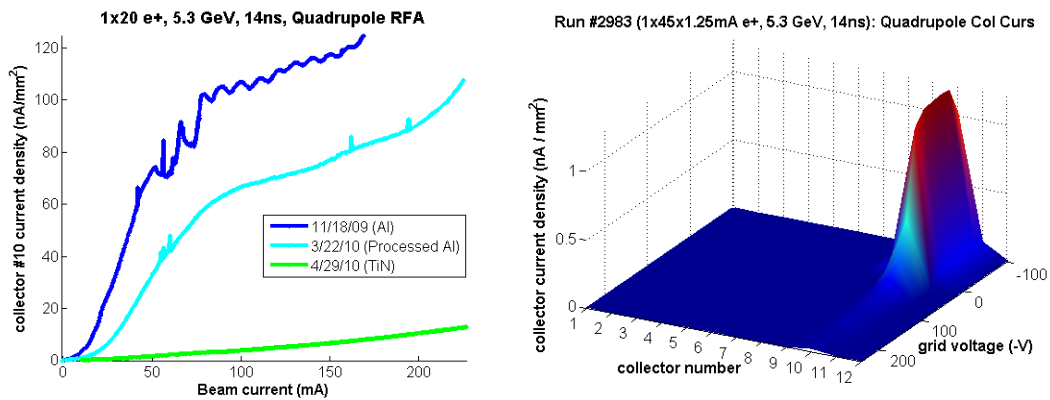


**Figure 8:** Left: the measured RFA current in a quadrupole versus beam current with a 20 bunch positron train for a bare Al surface and a TiN-coated Al surface. The efficacy of the TiN coating for suppressing the EC is clearly evident. Right: the transverse shape of the EC signal in the TiN-coated quadrupole RFA as a function of retarding voltage. The segmented RFA covers approximately  $90^\circ$  of the azimuth and the collector with the peak signal corresponds to the center of the quadrupole pole tip.



### 3.2.3.5 TE Wave Measurements

The transmission of microwaves through an electron plasma results in a phase shift of the signal. This method has been applied to probe the development of the EC in various vacuum chambers in CESR. When compared to other measurement methods, transmission measurements with TE mode waves offer a relatively non-invasive technique because beam buttons which are already in place in most vacuum chambers can be utilized to transmit and receive the signals. The method can also sample the EC throughout a region of vacuum chamber as opposed to being localized to a single measurement location. In figure 9, the left schematics provide an overview of the technique. In addition to transmission within the vacuum chamber, a second method is being developed where a signal below the chamber's cutoff frequency is transmitted and received at the same location, which offers the possibility of more localized measurements with this technique. The plot on the right of figure 9 compares the microwave transmission response for beams of positrons and of electrons. The observed sensitivity of the signal corresponds to roughly  $10^9$  electrons/m<sup>3</sup>.

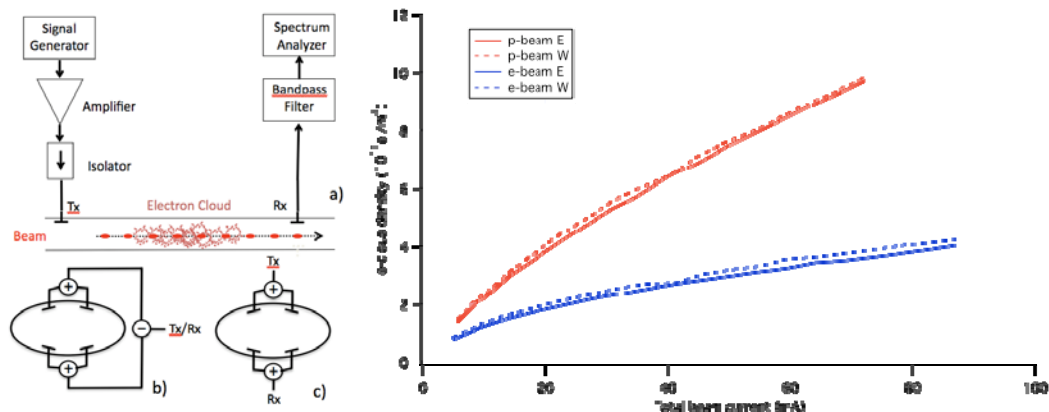


**Figure 9:** Left: Schematic description of the microwave transmission technique utilizing (a) beam buttons at two separated locations on the vacuum chamber. In (b), the configuration of buttons used to send and receive a transmitted signal is shown. An alternate configuration, (c), shows a method where transmission and reception occurs at a single location resulting in an evanescent wave which is localized around the region of the buttons. Right: TE wave response in the L0 straight for electron and positron beams converted to units of EC density needed to induce the observed phase shift. The data was obtained with 45 bunch trains having a bunch spacing of 14 ns.

### 3.2.3.6 Shielded Pickup Measurements

Time-resolved measurements of the build-up of the EC can probe features of the electron cloud build-up and decay that are inaccessible to integrating detectors such as the RFAs. Shielded pickups (SPUs) have been installed in several of the CESRTA experimental chambers. These detectors are similar to those employed at CERN to study the build-up of the cloud [25], however, amplifiers of sufficient bandwidth to study the development of the signal between bunches spaced by as little as 4ns have been employed. The left plot in Figure 10 shows the development of the cloud for a 45-bunch train of positrons with 4ns bunch spacing. The right plot shows results from a “witness” bunch study where a trailing bunch is used to probe the cloud remaining after

the passage of an initial bunch or train. In this case a single initial bunch is employed and the traces from probe bunches located at various delays behind the first bunch are overlaid. Studies of this type allow us to probe the decay of the cloud in the vacuum chamber. The shape and timing of the signal from the first bunch is determined by the geometry of the chamber and the spectrum of the photoelectrons generated on the walls of the vacuum chamber.

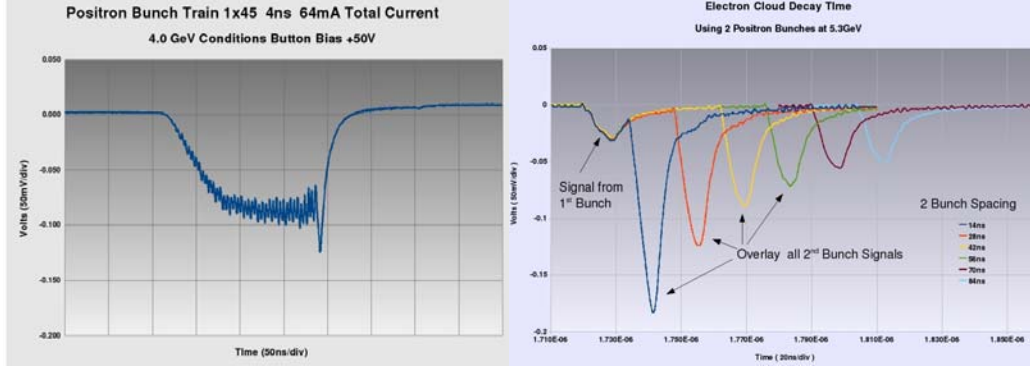


**Figure 10:** Left: SPU signal from a 45 bunch train of positrons with a bunch spacing of 4ns at a beam energy of 4 GeV. Right: Signals observed from a leading bunch with a trailing “witness” bunch to probe the evolution of the cloud in the center of the vacuum chamber. Traces from several witness bunches located at different delay times from the lead bunch.

### 3.2.4 Low Emittance Tuning

The CESRTA low emittance tuning (LET) effort provides the basis for studying the emittance-diluting effects of the EC in a regime approaching that of the ILC damping rings. As of early 2010, the LET program had resulted in reliable operation at or below the Phase I emittance target of  $\varepsilon_y \leq 20\text{pm-rad}$  [26] for both single- and multi-bunch beams as confirmed by xBSM measurements of the vertical beam size [27]. The standard LET procedure to obtain these results is to:

1. Measure and correct the orbit using all vertical (58) and horizontal (55) steering correctors;
2. Measure the betatron phase and transverse coupling at each BPM by resonant excitation of the normal modes. Correct the measured betatron phase using independently powered quadrupoles and correct the measured coupling with 27 skew quadrupoles;
3. Re-measure orbit and transverse coupling and measure the dispersion via resonant excitation of the synchrotron tune. Simultaneously optimize all three using skew quadrupoles and vertical correctors.

The beam size is measured using the xBSM and converted to emittance using the fitted beta and dispersion functions at the source point. Throughout the course of 2010, significant refinements to the methods and instrumental calibrations were implemented. As of the conclusion of 2010, vertical emittances of  $\varepsilon_y < 10\text{pm-rad}$  had been achieved [28, 29].

### 3.2.5 Studies of EC-induced Beam Dynamics with Low Emittance Beams

A number of beam dynamics studies have been conducted in order to fully characterize the impact of the EC on beams in CESR. Measurements of the EC-induced coherent tune shift [30, 31] along trains of electron and positron bunches, as well as for witness bunches at various positions behind a leading train, have provided an important probe of the integrated effect of the cloud around the ring. Systematic measurements over a wide range of beam conditions (varying beam energy, emittance, bunch currents, bunch spacings and train lengths) are being used to obtain information about 6 EC model parameters (the peak SEY value and energy, photon reflectivity, quantum efficiency, re-diffused and elastic yields) for the standard CESR vacuum chambers that cover the vast majority of the ring. These studies are intended to validate more thoroughly our EC models and have led to improved simulations, e.g., for the ring photon propagation model [32], which are now being applied to the ILC DR.

A principal deliverable of the CESRTA program is the characterization of instability thresholds and emittance-diluting effects in the ultra low vertical emittance regime [33-35]. Figure 11 shows the observed beam motion spectrum for each bunch along a train obtained in these conditions. The evolution of the self-excited horizontal and vertical tune lines, denoted by  $F_v$  and  $F_h$ , along the bunch train provides information about the EC density being experienced by each bunch. The development of the  $m=\pm 1$  synchrotron side-bands of the vertical tune, denoted by  $F_v \pm F_s$ , part way along the bunch train indicates where the EC density build-up has become sufficient for a head-tail instability to destabilize the bunches in the beam.

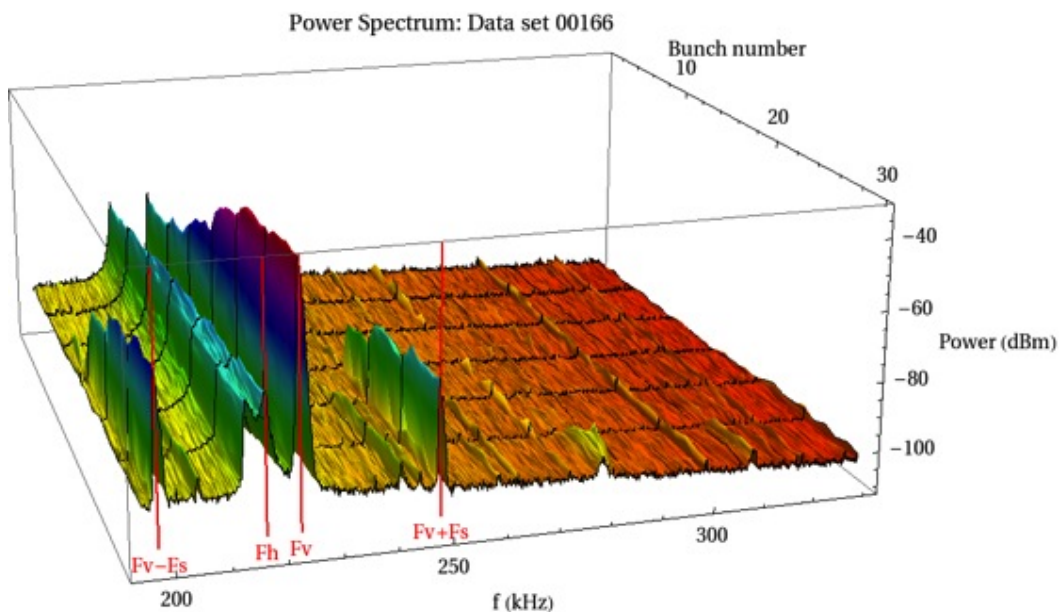


**Figure 11:** Bunch-by-bunch power spectrum for a positron train with a nominal bunch current of 0.75mA/bunch. The horizontal ( $F_h$ ) and vertical ( $F_v$ ) tunes are clearly visible for all bunches with a noticeable bifurcation in the horizontal in the last half of the train. The  $m=\pm 1$  synchrotron sidebands which are consistent with the onset of the head-tail instability appear around bunch 15.

Figure 12 shows bunch-by-bunch beam size development as observed along bunch trains with varying bunch intensities in the ultra low emittance regime. As the bunch current is increased, the bunch in the train at which beam size blow-up occurs moves earlier in the train due to the more rapid build-up of the EC. By studying both the spectral and beam size information as a function of various parameters (eg, bunch intensity, vertical emittance, bunch spacing, chromaticity, feedback conditions, and beam energy) and comparing with simulation [36, 37], we will be able to validate the simulations in a regime approaching that of the ILC DR and ensure that our projections of the expected positron DR performance are accurate.

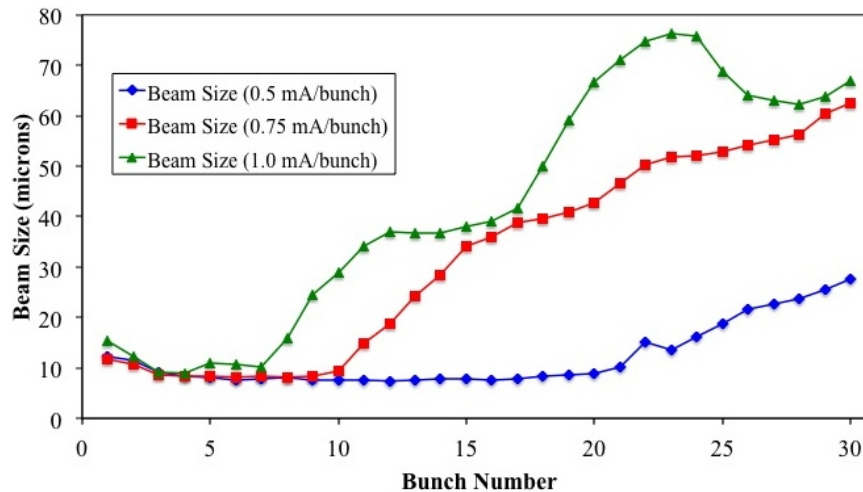


**Figure 12:** Bunch-by-bunch beam sizes based on turn-by-turn fits for each bunch for 30 bunch trains of varying current ( $0.8$ ,  $1.2$ , and  $1.6 \times 10^{10}$  particles/bunch). As the bunch currents are increased, the point in the train at which the EC density is high enough to cause emittance and beam size growth moves to earlier points in the train.

### 3.2.6 Incorporation of CESRTA Results into the ILC DR Technical Design

The results from the first 2.5 years of the CESRTA R&D program are presently being integrated into the ILC DR technical design [38]. In particular, the observed efficacy of grooved chamber surfaces in the dipole dipoles as well as that of the clearing electrode in the high field wigglers provide confidence that practical EC mitigations can be prepared for the arc and wiggler straight regions of the ILC positron damping ring. The importance of EC mitigation in the DR quadrupole chambers has also been demonstrated. New coating technologies to suppress the SEY offer great promise, however, there is still the issue of studying the long-term performance and durability of these coatings – this will be a subject of study during Phase II of the CESRTA program. Perhaps most importantly, the flexibility of CESR operations supports a systematic program of EC build-up and EC-induced beam dynamics studies. By benchmarking our physics models and simulations against these studies, our confidence in being able to make valid projections of the expected ILC positron damping performance has been significantly enhanced.

### 3.2.7 Future Plans

A 3-year extension to the CESRTA experimental program has recently been approved. This extension will allow us to conduct further studies into EC mitigations, in particular, the durability of various coatings that have been tested. With vertical emittances within a factor of a few of the ILC DR specification and with newly developed instrumentation and techniques, CESR is in a unique position to study a range of physics of interest for ultra low emittance machines. We plan to continue our explorations of the EC-induced instabilities and emittance growth along with studies of the fast ion instability and intrabeam scattering. We will also continue to develop the capabilities of our new instrumentation for real-time monitoring of machine parameters.

### 3.2.8 Acknowledgments

The CESRTA program would not have been possible without the participation of a worldwide collaboration [39]. Our colleagues and their institutions have been generous with their time, expertise, and hardware. We have greatly appreciated the chance to work with them during phase I of the program and look forward to a continued fruitful collaboration during the next three years.

We would also like to thank our colleagues in the ILC Global Design Effort and in the Compact Linear Collider (CLIC) for their ongoing support.

Funding for the CESRTA program has been provided by the U.S. National Science Foundation and Department of Energy. Support has also been provided by the Japan/U.S. Cooperation Program.

### 3.2.9 References

1. M.A. Palmer, *et al.*, "Electron Cloud at Low Emittance in CESRTA," Proceedings of IPAC'10, Kyoto, Japan (2010) and references therein.
2. M.A. Palmer, *et al.*, "The Conversion and Operation of the Cornell Electron Storage Ring as a Test Accelerator (CESRTA) for Damping Rings Research and Development," Proc. of PAC09, Vancouver, Canada (2009), and references therein.
3. Y. Li, *et al.*, "CesrTA Vacuum System Modifications," Proceedings of PAC09, Vancouver, British Columbia, Canada (2009).
4. D. Rice, "CESR-c: A Wiggler-dominated Collider," Proceedings of PAC07, Albuquerque, New Mexico, USA (2007).
5. M.A. Palmer, *et al.*, "CESR Beam Position Monitor System Upgrade for CesrTA and CHESS Operations," Proceedings of IPAC10, Kyoto, Japan (2010).
6. J. Alexander, *et al.*, "CesrTA X-Ray Beam Size Monitor Design," Proceedings of PAC09, Vancouver, British Columbia, Canada (2009).
7. M.A. Palmer, *et al.*, "Design, Implementation and First Results of Retarding Field Analyzers Developed for the CesrTA Program," Proceedings of PAC09, Vancouver, British Columbia, Canada (2009).
8. Y. Li, *et al.*, "Design and Implementation of CesrTA Superconducting Wiggler Beampipes with Thin Retarding Field Analyzers," Proceedings of PAC09, Vancouver, British Columbia, Canada (2009).
9. S. De Santis, *et al.*, "The TE Wave Transmission Method for Electron Cloud Measurements at CesrTA," Proceedings of PAC09, Vancouver, British Columbia, Canada (2009).
10. M.G. Billing, *et al.*, "Techniques for Observation of Beam Dynamics in the Presence of

- an Electron Cloud,” Proceedings of IPAC`10, Kyoto, Japan (2010).
11. D. Rubin, *et al.*, “CesrTA Layout and Optics,” Proceedings of PAC09, Vancouver, British Columbia, Canada (2009).
  12. N.T. Rider *et al.*, “Bunch-by-bunch Instrumentation Upgrades for CESR, Based on Requirements for the CESR Test Accelerator Research Program,” to appear in the Proceedings of the ECLLOUD10 Workshop, Ithaca, NY, USA (2011).
  13. J.R. Calvey, *et al.*, “CesrTA Retarding Field Analyzer Measurements in Drifts, Dipoles, Quadrupoles and Wigglers,” Proceedings of IPAC`10, Kyoto, Japan (2010).
  14. J.R. Calvey, *et al.*, “Electron Cloud Mitigation Investigations at CesrTA,” to be published in the proceedings of the ECLLOUD`10 workshop, Ithaca, New York, USA (2011).
  15. J.R. Calvey, *et al.*, “CesrTA Retarding Field Analyzer Modeling Results,” Proceedings of IPAC`10, Kyoto, Japan (2010).
  16. J.R. Calvey, *et al.*, “Methods for Quantitative Interpretation of Retarding Field Analyzer Data,” to appear in the Proceedings of the ECLLOUD10 Workshop, Ithaca, New York, USA (2011).
  17. S. De Santiset *et al.*, “Characterization of Electron Clouds in the Cornell Electron Storage Ring Test Accelerator using TE-Wave Transmission,” Phys. Rev. ST Accel. Beams 13:071002 (2010).
  18. G. Penn, J-L. Vay, “Theoretical Studies of TE-Wave Propagation as a Diagnostic for Electron Cloud,” Proceedings of IPAC`10, Kyoto, Japan (2010).
  19. K. Sonnad, *et al.*, “Simulations Using VORPAL on the Effect of Imperfections and Nonuniformities in TE Wave Propagation Through Electron Clouds,” to appear in the Proceedings of the ECLLOUD10 Workshop, Ithaca, NY, USA (2011).
  20. S. Veitzer, *et al.*, “Modeling Electron Cloud Buildup and Microwave Diagnostics Using Vorpall,” to appear in the Proceedings of the ECLLOUD10 Workshop, Ithaca, NY, USA (2011).
  21. J. Crittenden, *et al.*, “Electron Cloud Modeling Results for Time-resolved Shielded Pickup Measurements at CesrTA,” to appear in the Proceedings of the ECLLOUD10 Workshop, Ithaca, NY, USA (2011).
  22. Y. Suetsugu, *et al.*, “Demonstration of Electron Clearing Effect by Means of Clearing Electrodes and Groove Structures in High-Intensity Positron Ring,” proc. of PAC09, Vancouver, Canada(2009).
  23. C. Yin Vallgren, *et al.*, “Amorphous Carbon Coatings for Mitigation of Electron Cloud in the Cern SPS,” Proceedings of IPAC`10, Kyoto, Japan (2010).
  24. L. Wang and M.T.F. Pivi, “Electron Trapping in Wiggler and Quadrupole Magnets of CesrTA,” Proceedings of IPAC`10, Kyoto, Japan (2010).
  25. E.Mahner, *et al.*, “Electron cloud detection and characterization in the CERN Proton Synchrotron,” PRSTAB 11 094401 (2008)
  26. J.P. Shanks, *et al.*, “CesrTA Low Emittance Tuning,” Proceedings of IPAC`10, Kyoto, Japan (2010).
  27. D.P. Peterson, *et al.*, “CesrTA X-Ray Beam Size Monitor Operation,” Proceedings of IPAC`10, Kyoto, Japan (2010).
  28. D.L. Rubin, *et al.*, “CesrTA Low Emittance Tuning,” to appear in the Proceedings of the ECLLOUD10 Workshop, Ithaca, NY, USA (2011).
  29. J. Shanks, *et al.*, “Status of Low Emittance Tuning at CesrTA,” to appear in the Proceedings of PAC11, New York, NY, USA (2011).
  30. J. Crittenden, *et al.*, “Studies of the Effects of Electron Cloud Formation on Beam Dynamics at CesrTA,” Proceedings of PAC09, Vancouver, British Columbia, CA (2009).
  31. J. Crittenden, *et al.*, “Progress in Studies of Electron Cloud –Induced Optics Distortions at CesrTA,” Proceedings of IPAC`10, Kyoto, Japan (2010).
  32. G. F.Dugan, *et al.*, “Synrad3D Photon Propagation and Scattering Simulation,” to

- appear in the Proceedings of the ELOUD10 Workshop, Ithaca, NY, USA (2011).
33. G.F.Dugan, *et al.*, “CesrTA EC-Induced Beam Dynamics,” to appear in the Proceedings of the ELOUD10 Workshop, Ithaca, NY, USA (2011).
  34. J.W. Flanagan, *et al.*, “Measurement of Low-Emittance Beam with Coded Aperture X Ray Optics at CesrTA,” Proceedings of IPAC’10, Kyoto, Japan (2010).
  35. J.W. Flanagan, *et al.*, “xBSM Bunch-by-Bunch Measurements in EC Conditions at CesrTA,” to appear in the Proceedings of the ELOUD10 Workshop, Ithaca, NY, USA (2011).
  36. K. Ohmi, *et al.*, “Electron Instability in Low Emittance Rings, CesrTA and SuperKEKB,” to appear in the Proceedings of the ELOUD10 Workshop, Ithaca, NY, USA (2011).
  37. M.T.F. Pivi, *et al.*, “ILC Damping Ring Electron Cloud R&D Effort and Single-Bunch Instability Simulations Using CMAD,” to appear in the Proceedings of the ELOUD10 Workshop, Ithaca, NY, USA (2011).
  38. M. Palmer, *et al.*, “CesrTA Preliminary Recommendations for the ILC Positron Damping Ring,” to appear in the Proceedings of the ELOUD10 Workshop, Ithaca, NY, USA (2011).
  39. The CESR/TA Collaboration includes senior researchers from the following institutions: ANL, Australian Synchrotron, BNL, California Polytechnic State Univ., Carleton Univ., CERN, the Cockcroft Institute, FNAL, INFN-LNF, KEK, LBNL, Purdue University, SLAC and Technion-Haifa.

### 3.3 Recent Studies in ATF Damping Ring

S. Araki, H. Hayano, K. Kubo, S. Kuroda, T. Naito, T. Okugi, N. Terunuma and  
J. Urakawa, KEK, Tsukuba, Japan

M.D. Woodley, SLAC, Menlo Park, CA, USA

A. Wolski and K. Panagiotidis, Univ. of Liverpool and the Cockcroft Institute, UK

Mail to: [junji.urakawa@kek.jp](mailto:junji.urakawa@kek.jp)

#### *Abstract:*

The damping ring of the Accelerator Test Facility (ATF) at KEK is designed to produce an extremely small vertical emittance beam as a test accelerator for future linear colliders. Development of various system and components for ILC (International Linear Collider) is also an important purpose of this facility. Though most of the beam time of ATF is dedicated to the final focus test project (ATF2), some studies have been performed in the damping ring. Here we report recent effort of low emittance tuning and multi-bunch extraction test of the fast kicker.

#### 3.3.1 Introduction

The damping ring of the Accelerator Test Facility (ATF) at KEK is designed to produce an extremely small vertical emittance beam as a test accelerator for future linear colliders. Development of various system and components for ILC (International Linear Collider) is also an important purpose of this facility. Though most of the beam time of ATF is dedicated to the final focus test project (ATF2), some studies have been performed in the damping ring.

Here we report recent effort of low emittance tuning and multi-bunch extraction test of the fast kicker.

### 3.3.2 Low Emittance Tuning in ATF Damping Ring

The damping ring has two straight sections and two arc sections. Each arc is 41.7 m and each straight section is 27.6 m in length; the total circumference of the ring is 138.6 m. There are 48 horizontal and 50 vertical steering magnets for the orbit correction, and 96 beam position monitors (BPMs) in each plane. There are 34 focusing and 34 defocusing sextupole magnets in the arc sections. For the purpose of coupling correction, the trim windings of all 68 sextupole magnets have been arranged to produce skew quadrupole fields. There are no skew correctors in the dispersion free straight sections.

The usual tuning procedure for low emittance in the ATF damping ring consists of three consecutive corrections: orbit correction, vertical orbit-dispersion correction, and coupling correction. In the orbit correction, the readings of the BPMs are minimized using steering magnets. In the vertical-dispersion correction, dispersion and orbit are minimized simultaneously (with certain relative weights) using steering magnets, where dispersion is obtained as the difference of orbits measured with different frequencies of the RF accelerating cavities. In the coupling correction, we measure the vertical orbit response to a pair of horizontal steering magnets. Then, the responses are minimized using skew correctors. The performance of the tuning with misalignment of magnets and errors in the BPMs was studied by simulations [1].

The tuning procedure is usually performed every one or two weeks; the vertical emittance after tuning is typically less than 10 pm. Some results were reported in references [2], [3] and [4]. Here we report some of the recent efforts to tune for lower emittance related to beam measurements.

#### 3.3.2.1 Beam Based Alignment

For reducing the offset errors of BPMs with respect to the nearest magnet field center (magnet to BPM offset), we perform beam based alignment (BBA) for each quadrupole (or sextupole) magnet with the nearest BPM.

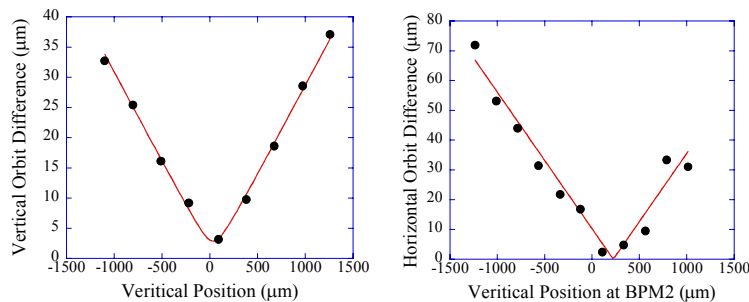
For each quadrupole–BPM pair, vertical local orbit bumps of several different amplitudes are set, where the beam position change at the magnet should be the same as at the BPM. Then for each bump setting, the response of the vertical orbit in the whole ring (beam position at all BPMs) to the strength change of the magnet is measured. If the beam is at the field center of the magnet, there should be no orbit response. The procedure is similar for a sextupole magnet–BPM pair. Each sextupole magnet has trim windings to produce a skew quadrupole field, and BBA is performed using the skew quadrupole field.

Figure 1 shows an example of the measurements, orbit change (RMS of position changes at many BPMs) as a function of vertical bump amplitude, for one quadrupole and one sextupole magnet. The typical error of the offset, estimated from fluctuations of the BPMs, is about 30 microns for quadrupole magnets and about 80 microns for sextupole magnets.

In April 2009, we performed BBA for all the main quadrupole magnets in the arc sections and for all of one family of sextupole magnets. We also performed BBA for the same set of quadrupole magnets in April 2008. The differences between the two sets of



measurements are significant compared with the estimated measurement errors for most of the magnets. This suggests that BBA should be performed more frequently.



**Figure 1:** Examples of BBA data analysis. Orbit change (RMS of position changes at many BPMs) as a function of vertical bump amplitude. Left: quadrupole magnet, Right: sextupole magnet (skew quadrupole field).

### 3.3.2.2 *Beta-Beat Correction*

Simulations have also shown that optics matching (i.e. minimising the beta-beat in arc sections) can be important for achieving low emittance. We have studied the effects of optics mismatch by applying the same simulation to different matching conditions. The results suggest that a mismatch will enhance the sensitivity to errors (magnet misalignment).

Beta-function at every quadrupole magnet is measured from the tune dependence on the strength change of each quadrupole magnet. We tried to correct the residual beta-beat, fitting the strengths of the quadrupole magnets to reproduce the measured beta-function. Then, the strength of each magnet was changed by an amount given by the difference between the fitted strength and the strength in the design optics. However, we found that the fitted model was not good enough for predicting the beta function after the correction. For a precise beta-beat correction, more careful study will be necessary.

We still could reduce the beta-beat by a somewhat empirical technique, though the results are not completely satisfactory. In this correction, we concentrated on the beta function at magnets of one family in the arc sections (magnets named QF1R) and looked for several quadrupole magnets whose change would partly correct the beta-beat in that region. Figure 2 shows, as an example of the correction, the vertical beta function at all the quadrupole magnets of one family in the arc sections, before and after the correction. For matched optics, the line should be flat.

More systematic methods of beta-beat correction and the effect of such corrections on the performance of low emittance tuning are still under investigation.

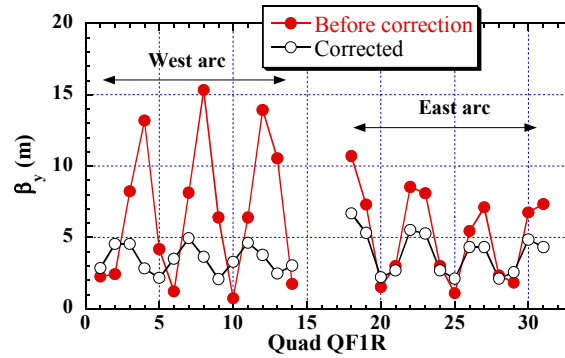


**Figure 2:** Example of a set of measured vertical beta function at all quadrupole magnets of one family in the arc sections, before and after a beta-beat correction. For matched optics, the line should be flat.

### 3.3.2.3 Orbit Response Matrix Analysis

Orbit response matrix (ORM) analysis is a well established technique for identifying and correcting optics errors in storage rings [5-6]. Briefly, one measures changes in the closed orbit with respect to changes in strength of a number of orbit correctors, and then fits a machine model to the data, by adjusting parameters such as quadrupole strengths, BPM gains and couplings, and corrector magnet strengths and tilts. At ATF, the orbit response matrix is measured using all BPMs in each plane, and all steering magnets. The data are fitted using parameters including the strengths of 34 skew quadrupoles distributed through the arcs. This procedure effectively projects the betatron coupling sources onto the skew quadrupoles, and thus allows the determination of skew quadrupole strengths required to cancel the coupling sources.

Unfortunately, we have not been able to confirm any additional significant reduction in the vertical emittance (after the usual tuning procedure) using the skew quadrupole strengths determined from ORM analysis. The reasons for this lack of success are not completely clear, but it is possible that a poor orbit may play a role. Another possible limitation on the effectiveness of ORM analysis is the possibility of degeneracy between errors that cause coupling (such as quadrupole tilts or sextupole alignment errors) and errors in the diagnostics that only give the appearance of coupling in the ORM data (such as BPM couplings or corrector magnet tilts). These degeneracies have been investigated in simulation [7], and it is possible that they may limit the vertical emittance that can be achieved at the ATF using ORM analysis to around 5 pm.

### 3.3.2.4 BPM Electronics Upgrade

Recently, the electronics and data taking system of all BPMs in the DR have been replaced [8]. Two major improvements of this upgrade relevant to low emittance tuning are: (a) better resolution of closed orbit by averaging positions of many (some 1000s) turns; and (b) turn-by-turn position measurement at all BPMs. The improvement (a) obviously should improve performance of the usual tuning procedure, which fully depends on closed orbit measurement. The improvement (b) will make possible new methods of low emittance tuning. One possibility would be to identify the two separate eigen-modes of betatron oscillations at all BPMs, providing accurate information for coupling correction.

Unfortunately we have not yet had sufficient beam operation time with good conditions for performing low emittance tuning making full use of the functions of the new BPM system, though the system itself has been established. Confirmation of the effects of the upgrade is expected from beam operation in the near future.

### 3.3.3 Fast Kicker Test

In the Damping Rings (DR) of the International Linear Collider (ILC), “fast kickers”, kickers with very short rise and fall time, are required for beam injection and extraction. A bunch train in the ILC Main Linac (ML) consists of 1320 - 5120 bunches with 189 - 480 ns bunch spacing. Each bunch train is over 200 km long. For reasonable DR circumference, the bunch spacing must be much shorter, 3 - 9 ns in the ILC baseline design [9]. The parameters are specified as ranges because the resulting flexibility allows difficulties in achieving design performance in one area to be compensated by changing operating parameters in another [9]. The injection/extraction kickers act as a bunch-by-bunch beam manipulator to compress and decompress the bunch spacing as bunch trains enter/exit the DR. The kicker field must affect only the deflecting bunch without affecting previous/subsequent bunches. Thus, a high repetition frequency of 6 (to 2) MHz (corresponding to the ML bunch spacing) and a very fast rise/fall time of 3 (to 9) ns (corresponding to the DR bunch spacing) are required for the kickers. Among candidate technologies, a system using multiple strip-line kickers appears to be the most likely to realize the required performance [10-13]. Multi-bunch beam extraction experiments at the ATF DR using a prototype strip-line kicker have been performed successfully; some past results are reported in [14]. Here, results of a recent experiment are reported [15].

#### 3.3.3.1 *Beam Extraction Experiment*

In the experiment, 3 bunch trains spaced by 103.6 ns were stored in the DR. Each train, which is injected in a single cycle of the injection linac, consists of 10 bunches with a bunch spacing of 5.6 ns (for a total of 30 bunches stored). The strip-line kicker deflects the last bunch of each train into the extraction channel at an interval of 308 ns. The interval is changed to 302.4 ns on every third pulse to extract the next bunch of the train. The injection rate is 1.5 Hz (one train) and the extraction rate is 0.5 Hz. Figure 3 shows the bunch structure in the DR and the order of the extracted bunches in the extraction line.

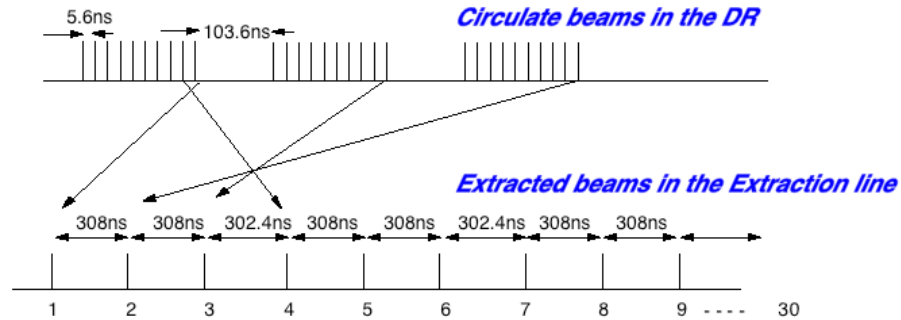


**Figure 3:** Bunch structure in the DR and in the Extraction line: The stored bunch in the DR is three trains and each train consists of 10 bunches with 5.6ns bunch spacing. The beam is extracted bunch-by-bunch from the last bunch of each train with 308ns spacing. The bunch spacing change to 302.4 ns after every three bunches extraction.

Two strip-line kickers were installed in the DR, each consisting of a pair of strip-lines with 60 cm length. One kicker has a 9 mm gap and the other has an 11 mm gap. The length of each is limited by the required short rise time of the kick field (see below). The gaps are determined by considering the aperture for the injecting beam and by the kick angle. The downstream strip-line, where the orbit difference between the circulating beam and the extracted beam is larger, has a wider gap. Pulsers for the kickers are located outside of the shielding; 6 m long coaxial cables are used for the high voltage pulse transmission. The trigger timing for the two pairs of pulsers are independently controlled by four delay circuits. Figure 4 shows a pair of the strip-line electrodes.

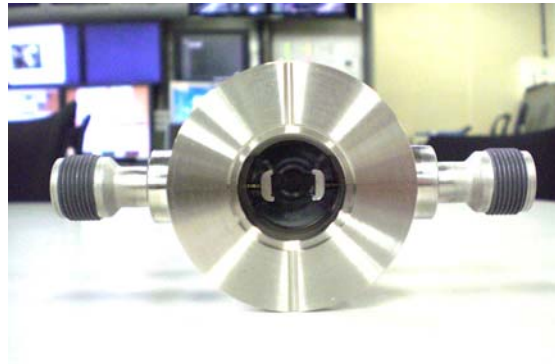


**Figure 4:** Photograph of the strip-line electrodes

Two pairs of FPG10-3000KN pulsers (fabricated by FID Co., Ltd. [16]) are used. The main parameters of the pulsers are: peak amplitude 10 kV, rise time 1.5 ns, repetition rate 3.3 MHz (burst), and bursts of up to 60 pulses at 1 Hz. Figure 5 shows a single pulse waveform and Figure 6 shows the burst pulse waveform for the first 48 pulses. The last 30 pulses, where the amplitude and timing are most stable, are used to kick the beam. The length of the strip-line electrode increases the effective rise/fall time of the kick field. The electric and magnetic fields of the kicker pulse are transmitted at the speed of light in the strip-line electrodes, and the beam travels in the opposite

direction. The kick field applied to the beam is determined by integrating the voltage waveform from the pulser. The time profile of the kick field is shown in Figure 7. The rise time of the kick field is less than 5 ns. The estimated kick angles are 1.8 mrad for 9 mm gap strip-line and 1.5 mrad for 11 mm gap strip-line, without accounting for cable loss and the reflection coming from impedance mismatch at the strip-line. With these effects accounted for, the angle can be approximately 10% lower than the estimated value. When two 60 cm long strip-lines with  $\pm 10$  kV pulsers are used, the resulting total kick angle is 3 mrad.

Figure 8(a) shows three trains of 10 bunches stored in the DR; Figure 8(b) shows the extracted train of 30 bunches.

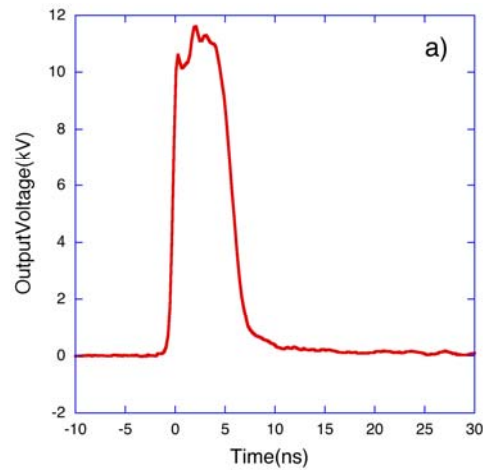


**Figure 5:** The waveform of the kicker pulse (positive polarity)

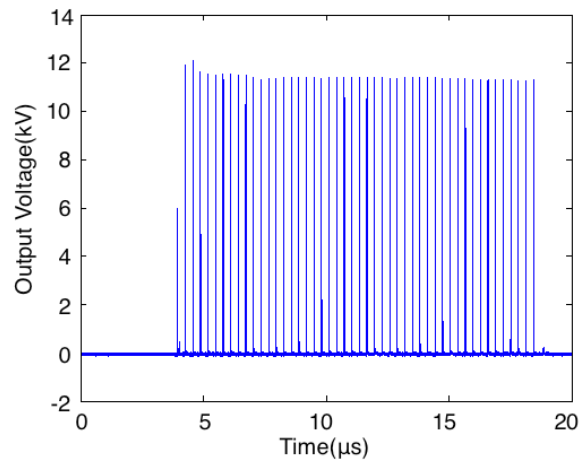


**Figure 6:** Burst pulse waveform of FPG10-3000KN.

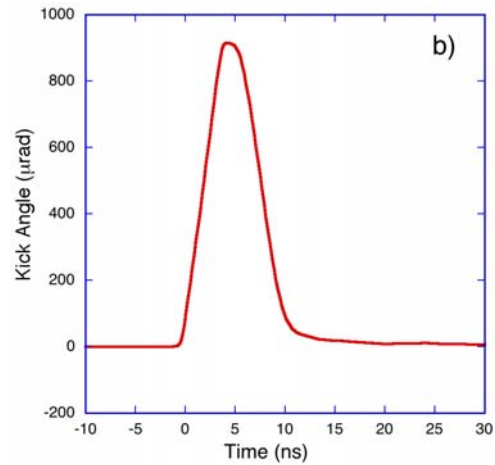


**Figure 7:** Evaluated kick field when the kicker pulse is applied to a 60 cm long strip-line.

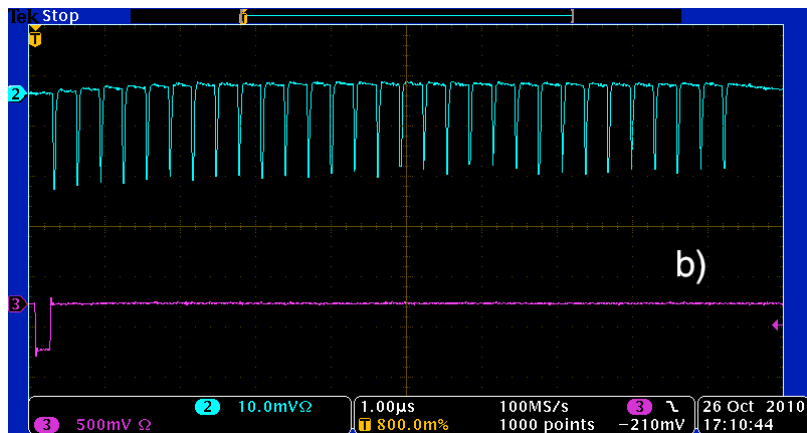
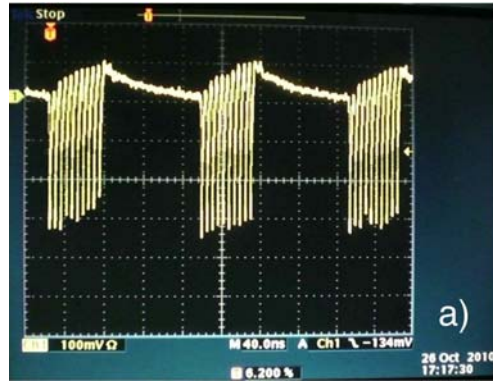


**Figure 8:** (a) Stored bunch current in the DR, measured with a wall current monitor, after three 10-bunch train injections. Bunch spacing in each train is 5.6 ns. (b) The blue trace shows the extracted multi-bunch beam signal, measured by a current transformer located in the middle of the extraction line. The bunch spacing is 308 ns (302.4 ns for every third bunch). The bunch-to-bunch intensity variation comes from stored beam current variations in the DR.

Temperature changes inside the pulsers make a 400 - 600 ps per day timing drift in the output timing, which is characteristic of the pulser used. Using a timing feedback system to adjust fine delays, the timing could be kept stable within the range of 200 ps.

We also observed timing shifts in the burst pulse of the pulsers. We therefore avoided using the first 18 pulses (no bunches circulating in the DR when these are applied to the strip-lines), after which the timing is stable. In addition, we introduced a trigger timing circuit to cancel the predictable timing changes. The resultant pulse timing stability within the range of 200 ps is acceptable for multi-bunch beam extraction.

We estimated the kick angle stability for a single extracted bunch from the orbit jitter in the extraction line. The kick angle on each pulse is evaluated from measured beam positions using 19 beam position monitors (BPMs) assuming design beamline optics. Figure 9 shows the kick angle distribution for 400 shots. The measured angle jitter was  $1.3 \mu\text{rad}$ , which is  $3.5 \times 10^{-4}$  of the total kick angle. These results indicate that the strip-line kicker has a good stability, comparable to that of the double kicker system presently in use [17]. The timing jitter of the kicker pulse is considered to be the dominant source of kick angle jitter. The estimated kick angle jitter, assuming 200 ps timing jitter, is about  $3.3 \times 10^{-4}$ , in agreement with the measurement.

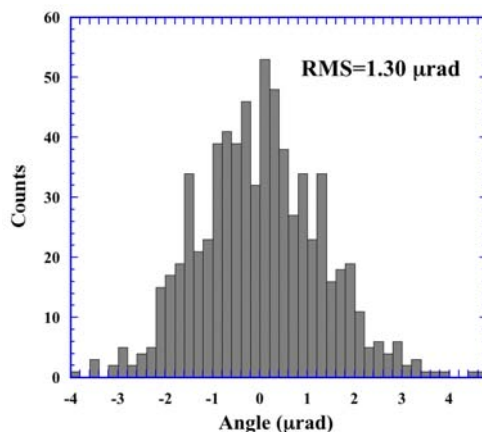


**Figure 9:** Kick angle jitter distribution, deduced from measured pulse-to-pulse horizontal beam position variations at 19 extraction line BPMs using design R12 transport matrix elements.

The kick angle and angle jitter for the multi-bunch beam were also measured. The average kick angles are different bunch-by-bunch at the level of 1%. The bunch-by-bunch relative angle jitter was distributed from  $1-4 \times 10^{-3}$ . These results were worse than the single bunch case because individual fine timing adjustment of all pulses was difficult. Note that the requirement for the angle jitter and the bunch-by-bunch angle difference of the kicker system can be loosened by the use of downstream feedback and/or feed-forward systems [18-19].

### 3.3.4 References

1. K. Kubo, "Simulation study of low emittance tuning of the Accelerator Test Facility damping ring at KEK" Physical Review ST-AB, vol. 6, 092801 (2003)
2. ATF Collaboration, "Extremely low vertical emittance beam in accelerator test facility at KEK", Phys. Rev. Lett. 88:194801, 2002.

3. Y. Honda et al., “Achievement of ultralow emittance beam in the ATF damping ring”, Phys. Rev. Lett. 92:054802, 2004.
4. K. Kubo, et. al., Proceedings of PAC09, Vancouver, BC, Canada (2009), paper ID FR1RAC05.
5. J. Safranek, “Experimental determination of storage ring optics using orbit response measurements,” Nuclear Instruments and Methods in Physics Research A 388 (1997) 27-36.
6. A. Wolski, M.D. Woodley, J. Nelson, M.C. Ross, “Analysis of KEK-ATF optics and coupling using LOCO,” proceedings of EPAC 2004, Lucerne, Switzerland.
7. K. Panagiotidis, A. Wolski, “Possible limitations in coupling correction using orbit response matrix analysis,” Proceedings of PAC09, Vancouver, BC, Canada (2009).
8. P. Priet, et al., “High resolution upgrade of the ATF damping ring BPM system”, Presented at 13th Beam Instrumentation Workshop (BIW08), Lake Tahoe, California, May 2008.
9. ILC Global Design Effort and World Wide Study, “ILC Reference Design Report”, <http://www.linearcollider.org>, Aug 2007
10. T. Naito et. al., “Development of the Strip-line Kicker System for ILC Damping Ring”, Proceedings of PAC07, Albuquerque, New Mexico, USA, pp2772-2274.
11. T. Naito et. al., “Development of a 3ns rise and fall time strip-line kicker for the International Linear Collider”, NIM A571 (2007) pp599-607
12. B.I. Grishanov et al., “Very Fast Kicker for Accelerator applications”, NIM A 396 28-34, 1997
13. D. Alesini et al., “Design, test, and operation of new tapered stripline injection kickers for the e+e- collider DAΦNE”, PRST-AB 13, 1110002, 2010
14. T. Naito et. al., “BEAM EXTRACTION USING STRIP-LINE KICKER AT KEK-ATF”, Proceedings of PAC09, Vancouver, Canada, pp1620-1622
15. Naito et. al., “Multi-bunch beam extraction using strip-line kicker at the KEK Accelerator Test Facility”, submitted to PR-STAB.
16. <http://www.fidtechnology.com/products/fpg-nanosecond.html> The modified version (repetition rate and burst mode) is used in this report.
17. T. Imai et al., “Highly Stable Beam Extraction by Double Kicker system”, KEK-Preprint 2002-16, May 2002
18. R. Apsimon et al., “LATEST BEAM TEST RESULTS FROM ATF2 WITH THE FONT ILC PROTOTYPE INTRA-TRAIN BEAM FEEDBACK SYSTEM”, Proceedings of IPAC10, 2010, Kyoto, Japan, pp2788-2790
19. A. Kalinin et al., “TURNROUD FEED-FORWARD CORRECTION AT THE ILC”, Proceedings of PAC07, 2007, Albuquerque, New Mexico, USA, pp. 419-421

### 3.4 ILC 3.2 km Damping Ring Design Based on the FODO Cell

Dou Wang, Jie Gao, Gang Xu and Yiwei Wang, IHEP, Beijing 100049, China

Mail to: [wangdou@ihep.ac.cn](mailto:wangdou@ihep.ac.cn), [gaoj@ihep.ac.cn](mailto:gaoj@ihep.ac.cn), [xug@ihep.ac.cn](mailto:xug@ihep.ac.cn),  
[wangyw@ihep.ac.cn](mailto:wangyw@ihep.ac.cn)

#### 3.4.1 Introduction

Within the ILC, the damping rings are one of the most important subsystems because they must accept the  $e^-$  and  $e^+$  beams with large transverse and longitudinal emittances and reduce the emittances to the required level within a 200 ms interval between the machine pulses. In addition, the relatively large bunch separation in the



main linac beams means that the damping ring must be capable of injecting and extracting individual bunches without affecting the stored bunches.

The design study of the ILC 6 km damping ring started very early and went through intense competition. Older versions of the ILC damping rings (OCS) [1] had used TME (theoretical minimum emittance) arc cells and had 6 arc sections. As early as 2005, the Chinese ILC group began using FODO cells in its design [2]. FODO structures have since replaced TME cells in the ILC damping design based on greater flexibility and large dynamic aperture. The 6.4 km DCO4 [1] based on FODO arc cells is the latest version adopted by RDR baseline in 2008.

After the ILC had entered the Technical Design Phase 1 at the end of 2008, the Minimum Machine Study [3] based on RDR baseline was launched essentially with the premise to find cost-reductions. The term “minimum machine”, while reflecting the need to redesign the machine, did not refer to any definable true minimum, but instead was a euphemism for higher-level alternative-design concepts that could promise significant cost-reduction while maintaining machine performance. With the new machine parameters, a reduction in the number of bunches by a factor of two allowed a reduction by the same factor in the circumference of the damping ring, while keeping the current (bunch spacing) in the rings constant. This could result in a reduction in damping ring cost by almost a factor of two. From 2009, we participated the studies for the 3.2 km ring. Considering the advantages of FODO lattices, such as fewer numbers of quadrupoles and sextupoles per cell, freely tunable momentum compaction, and a better dynamic aperture, we redesigned the smaller ring using FODO arc cells that can satisfy all the requirements for the ILC damping ring. For brevity, we term the new design DMC (Damping Ring-Minimum Machine-China).

### **3.4.2 Global Consideration and Parameter Calculation**

The basic requirements for the damping ring relate to damping time, normalized horizontal emittance, bunch length, sufficient aperture for injecting a large emittance positron beam and sufficiently large and flexible momentum compaction factor to maintain single bunch stability. In our design, we adopted the racetrack structure similar to the 6.4 km baseline design (DCO4). The layout of the 3.2 km damping ring is shown in Figure 1 with the electron and positron beams counter-rotating in their respective rings. The advantage of this kind of structure is that the injection and extraction beam lines for the  $e^+$  and  $e^-$  rings can be located in the same tunnel. Also, the RF section and wigglers are located near each other to minimize cryogenic transfer lines, while the RF section must be upstream to avoid radiation damage.

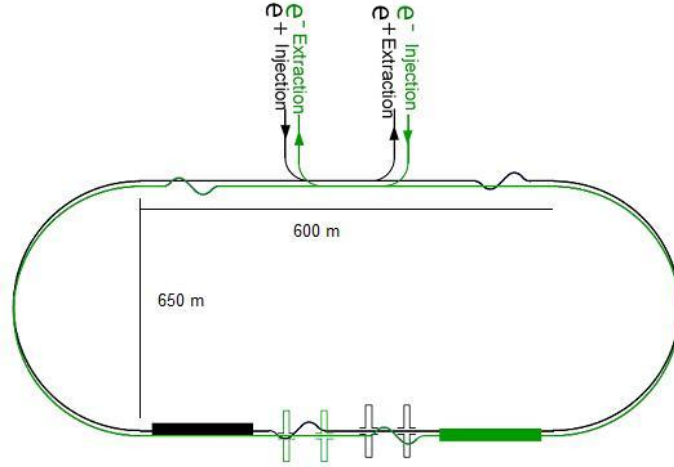


**Figure 1:** A rotational transformation and layout of the 3.2 km ILC damping ring.

The first parameter that should be considered before the lattice design is the damping time. The ILC damping ring has a very fast damping time (about 25 ms) which is dictated by the 5 Hz machine repetition rate. The damping time for a damping ring is given by [4]

$$\tau = \frac{2E_0 T_0}{U_0} \quad (1)$$

$$U_0 = U_{0,arc} + U_{0,w} \quad (2)$$

$$U_{0,arc} = \frac{C_\gamma}{2\pi} E_0^4 I_{2,arc} = \frac{C_\gamma}{2\pi} E_0^4 \left( \int \frac{ds}{\rho^2} \right) \approx C_\gamma E_0^4 \frac{B_{arc}}{(B\rho)} \propto B_{arc} \quad (3)$$

$$U_{0,w} = \frac{C_\gamma}{2\pi} E_0^4 I_{2,w} = \frac{C_\gamma}{4\pi} E_0^4 \frac{B_w^2 L_w}{(B\rho)^2} \propto L_w \quad (4)$$

where  $C_\gamma = 8.846 \times 10^{-5} \text{ m/GeV}^3$ ,  $U_0$  is the total energy loss from synchrotron radiation per turn,  $T_0$  is the circling period,  $U_{0,arc}$  and  $U_{0,w}$  are the energy loss in the arcs and wigglers respectively,  $I_2$  is the second synchrotron integral for storage ring,  $B_{arc}$  and  $B_w$  are the magnetic strength for the arc dipoles and wigglers, and  $L_w$  is the total length of wigglers. Because the circling period is decreased by a half, the total energy loss per turn should be decreased by a half to maintain a constant damping time. We need to consider how to allot the energy loss in arcs and wigglers while maintaining total energy losses reduced by a half.

Next, we will consider the horizontal emittance of a damping ring. The formulae for equilibrium emittance are as follows [4]:

$$\varepsilon_0 = \varepsilon_{0,arc} \frac{1}{1+F_w} + \varepsilon_{0,w} \frac{F_w}{1+F_w} \quad (F_w = \frac{U_{0,w}}{U_{0,arc}}) \quad (5)$$

$$\varepsilon_{0,arc} = \frac{F}{12\sqrt{15}} C_q \gamma^2 \frac{\theta^3}{J_x} \quad (F \approx 100 \text{ for the normal FODO cell}), \quad (6)$$

$$\varepsilon_{0,w} = \frac{8}{15\pi} C_q \gamma^2 \frac{\langle \beta_x \rangle B_w^3}{(B\rho)^3 k_w^2} \quad (7)$$

where  $C_q=3.84 \times 10^{-13}$  m,  $\varepsilon_{0,arc}$  and  $\varepsilon_{0,w}$  are the equilibrium emittance contributions from the arcs and wigglers,  $F_w$  is the ratio of energy losses in the wigglers and arcs, and  $\theta$  is the bending angle in each arc dipole. We find that the emittance contribution from the wigglers depends only on the peak magnetic strength but not related to their total length. If we choose the same wiggler as the baseline design,  $\varepsilon_{0,w}$  will not change. In ILC 6.4 km damping ring, although  $\varepsilon_{0,arc}$  is larger than  $\varepsilon_{0,w}$  by one order of magnitude, the equilibrium emittance can be controlled at the required value by increasing the wiggler's contribution ( $F_w \approx 10$ ). For the smaller ring, we elect for the same  $F_w$  value to satisfy the emittance requirements. Combined with eqs. (3) and (4), both the arc dipole strength  $B_{arc}$  and the total wiggler length  $L_w$  should be reduced by a half so that the ratio of the energy losses from arcs and wigglers is constant.

In the ILC, the energy spread in the beam extracted from the damping ring is also an important parameter for the bunch compressors: the larger the energy spread, the more difficult the design and operation of the bunch compressors becomes. In the damping rings, the natural energy spread is essentially determined by the wiggler [4]:

$$\sigma_\delta^2 \approx \frac{4}{3\pi} \frac{e}{mc} C_q \gamma B_w \quad (8)$$

Thus, the natural energy spread will be same as DCO4 (about 0.13% with beam energy of 5 GeV and wiggler field of 1.6 T).

For the momentum compaction factor,

$$\alpha_p = \frac{1}{C_0} \oint \frac{D_x}{\rho} ds = \frac{D_{x,dipole}}{C_0} \oint \frac{1}{\rho} ds = \frac{2\pi D_{x,dipole}}{C_0} \quad (9)$$

where  $D_{x,dipole}$  denotes the horizontal dispersion function in the dipole magnets. If we want to keep the momentum compaction factor at the same order as the 6 km ring, we have to reduce the horizontal dispersion in the dipoles by approximately half. In addition, the uncertainty in the impedance and instability estimation requires some flexibility in the momentum compaction factor and this can be realized by changing the phase advance of each FODO arc cell.

### 3.4.3 Linear Lattice Design

We use MAD [5] to aid in the lattice design. There are 166 arc cells in total in our damping ring design. Therefore, including the dispersion suppressor, each dipole magnet provides a bending angle of  $2\pi/340$  for the beam. By tuning the power supply of the quadrupoles in the arc cell, then adjusting the strength of the magnets in the dispersion suppressor, and finally matching sections, we can tune the momentum compaction from  $2.77 \times 10^{-4}$  to  $6.19 \times 10^{-4}$ , while the whole lattice design remains unchanged. The major parameters of our design are shown in Tables 1. Meanwhile the magnet details are shown in Table 2.

**Table 1:** Major parameters for DMC3.

<b>Parameter</b>	<b>Value</b>		
Beam energy	5.0 GeV		
Circumference	3258.68 m		
RF frequency	650 MHz		
Harmonic number	7065		
Transverse damping time	23 ms		
Natural bunch length	6 mm		
Natural energy spread	$1.26 \times 10^{-3}$		
Phase advance per FODO cell	60°	75°	90°
Momentum compaction factor	$6.19 \times 10^{-4}$	$4.04 \times 10^{-4}$	$2.77 \times 10^{-4}$
Normalized natural emittance	6.27 $\mu\text{m}$	4.45 $\mu\text{m}$	3.58 $\mu\text{m}$
RF voltage	33.0 MV	21.84 MV	15.36 MV
RF acceptance	2.75%	2.58%	2.38%
Synchrotron tune	0.067	0.044	0.03
Working point x/y	38.28/36.21	44.35/42.30	51.23/49.36
Natural chromaticity x/y	-42.3/-41.5	-51.2/-49.9	-63.7/-61.7

**Table 2:** Magnet parameters.

<b>Parameter</b>	<b>Value</b>		
	DMC3	DSB3	DCO4
Arc dipole length	2.0 m	2.7 m	2.0 m
Arc dipole field	0.154 T	0.26/0.36T	0.27 T
Number of arc dipoles	344	128	200
Chicane dipole length	1.50 m	1.0 m	1.0 m
Chicane dipole field	0.1 T	0.27 T	0.27 T
Number of chicane dipoles	32	48	48
Quadrupole length	0.40 m	0.6/0.3 m	0.3 m
Total number of quadrupoles	474	590	692
Maximum quadrupole gradient	11.3 T/m	7.5 T/m	12.0 T/m
Sextupole length	0.25 m		0.25 m
Total number of sextupoles	332	192	392
Maximum sextupole gradient	151 T/m <sup>2</sup>	145 T/m <sup>2</sup>	215 T/m <sup>2</sup>

### 3.4.4 Dynamic Aperture

The dynamic aperture should ensure efficient acceptance of the large emittance for the positron beam. The required value is 3 times the injected e<sup>+</sup> beam size. For our design, we use one focusing sextupole and one defocusing sextupole per arc cell to correct the first order chromaticity to zero. The results of DA tracking (300 turns) are shown in Figure 2.

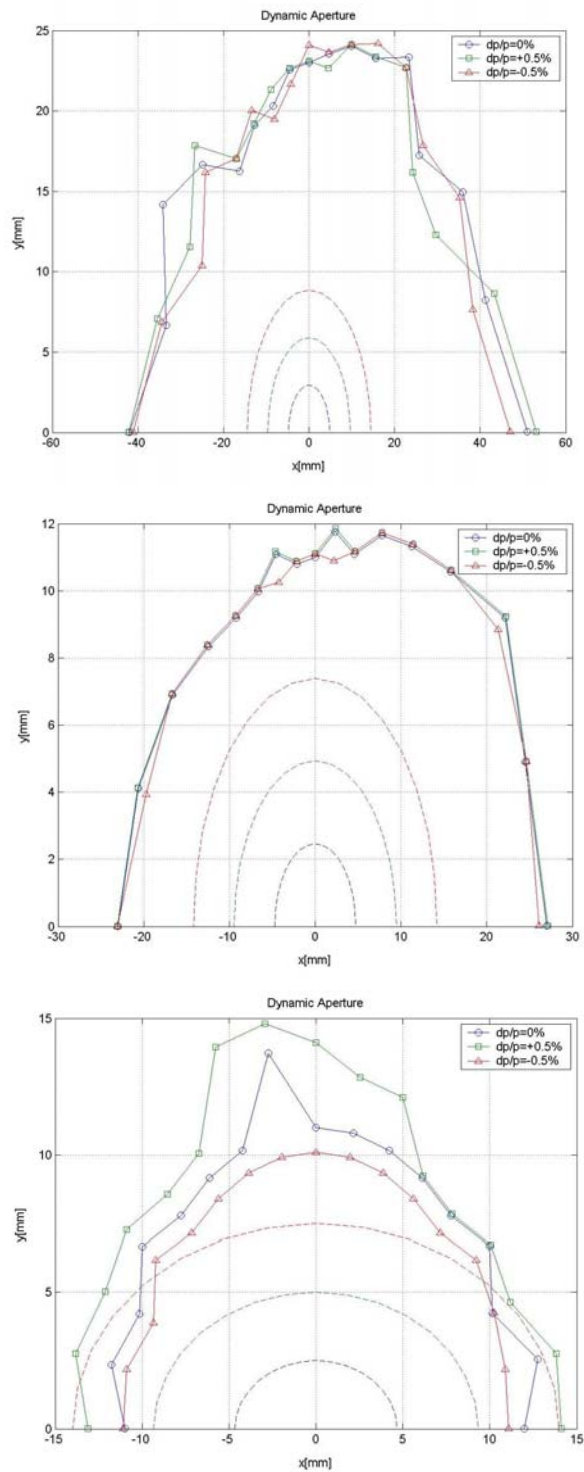


**Figure 2:** DMC3 dynamic aperture. (Top: 60°, middle: 75°, bottom: 90°. The three dashed ellipses correspond to single, double, and triple injected positron beam sizes respectively.)

### 3.4.5 References

1. ILC damping ring working group, Cornell ILC Wiki, [https://wiki.lepp.cornell.edu/ilc/bin/view/Public/DampingRings/WebHome#Damping\\_Rings\\_Parameters\\_and\\_Lat](https://wiki.lepp.cornell.edu/ilc/bin/view/Public/DampingRings/WebHome#Damping_Rings_Parameters_and_Lat).
2. Sun Y P, Gao J, Guo Z Y, et al., “International linear collider damping ring lattice design based on modified FODO arc cells”, Phys Rev ST Accel Beams, 11, 061001:1-91, 2008.
3. ILC GDE, “ILC minimum machine study proposal”, Technical Report, ILC-EDMS Doc 865085, January 2009.
4. A. Wolski, “Damping ring for linear collider”, Lecture for the 4th ILC school, Huai Rou, Beijing, 2009.
5. Grote H., Iselin F, “The MAD program”, CERN/SL/90-13 (AP) (Rev. 5), CERN, 1996.

## 4 Final Focus Test Facility for ILC and CLIC

### 4.1 ATF2 Summary and Status

ATF Collaboration:

J. Alabau Gonzalvo,<sup>2</sup> M. Alabau Pons,<sup>10</sup> J. Amann,<sup>3</sup> D. Angal-Kalinin,<sup>4</sup> R. Apsimon,<sup>5</sup> S. Araki,<sup>6</sup> A. Aryshev,<sup>6</sup> S. Bai,<sup>7</sup> P. Bambade,<sup>1,6</sup> P. Bellomo,<sup>3</sup> D. Bett,<sup>5</sup> G. Blair,<sup>9</sup> C. Blanch,<sup>2</sup> B. Bolzon,<sup>10</sup> S. Boogert,<sup>9</sup> G. Boorman,<sup>9</sup> P. Burrows,<sup>5</sup> G. Christian,<sup>5</sup> P. Coe,<sup>5</sup> B. Constance,<sup>5</sup> L. Corner,<sup>5</sup> M. Davis,<sup>5</sup> J.-P. Delahaye,<sup>10</sup> L. Deacon,<sup>9</sup> E. Elsen,<sup>11</sup> A. Faus-Golfe,<sup>2</sup> J. Frisch,<sup>3</sup> M. Fukuda,<sup>6</sup> J. Gao,<sup>7</sup> N. Geffroy,<sup>8</sup> E. Gianfelice-Wendt,<sup>12</sup> H. Guler,<sup>13</sup> H. Hayano,<sup>6</sup> A.-Y. Heo,<sup>14</sup> Y. Honda,<sup>6</sup> J.Y. Huang,<sup>15</sup> W.H. Hwang,<sup>15</sup> Y. Iwashita,<sup>16</sup> A. Jeremie,<sup>8</sup> J. Jones,<sup>4</sup> Y. Kamiya,<sup>17</sup> P. Karataev,<sup>9</sup> E.-S. Kim,<sup>14</sup> H.-S. Kim,<sup>14</sup> S.H. Kim,<sup>15</sup> Y.I. Kim,<sup>14</sup> S. Komamiya,<sup>17</sup> K. Kubo,<sup>6</sup> T. Kume,<sup>6</sup> S. Kuroda,<sup>6</sup> B. Lam,<sup>3</sup> A. Lyapin,<sup>18</sup> M. Masuzawa,<sup>6</sup> D. McCormick,<sup>3</sup> S. Molloy,<sup>9</sup> T. Naito,<sup>6</sup> T. Nakamura,<sup>17</sup> J. Nelson,<sup>3</sup> L. Nevay,<sup>5</sup> D. Okamoto,<sup>19</sup> T. Okugi,<sup>6</sup> M. Oroku,<sup>17</sup> Y.J. Park,<sup>15</sup> B. Parker,<sup>20</sup> E. Paterson,<sup>3</sup> C. Perry,<sup>5</sup> M. Pivi,<sup>3</sup> T. Raubenheimer,<sup>3</sup> Y. Renier,<sup>10</sup> J. Resta-Lopez,<sup>5</sup> C. Rimbault,<sup>1</sup> M. Ross,<sup>12</sup> T. Sanuki,<sup>19</sup> A. Scarfe,<sup>21</sup> D. Schulte,<sup>10</sup> A. Seryi,<sup>5</sup> T. Smith,<sup>3</sup> S. Smith,<sup>3</sup> C. Spencer,<sup>3</sup> T. Suehara,<sup>17</sup> R. Sugahara,<sup>6</sup> C. Swinson,<sup>5</sup> T. Takahashi,<sup>22</sup> T. Tauchi,<sup>6</sup> N. Terunuma,<sup>6</sup> R. Tomas,<sup>10</sup> J. Urakawa,<sup>6</sup> D. Uner,<sup>5</sup> M. Verderi,<sup>13</sup> R. Walczak,<sup>5</sup> D. Wang,<sup>7</sup> M.-H. Wang,<sup>3</sup> M. Warden,<sup>5</sup> M. Wendt,<sup>12</sup> G. White,<sup>3</sup> W. Wittmer,<sup>3</sup> A. Wolski,<sup>23</sup> M. Woodley,<sup>3</sup> Y. Yamaguchi,<sup>17</sup> T. Yamanaka,<sup>17</sup> Y. Yan,<sup>17</sup> H. Yoda,<sup>17</sup> K. Yokoya,<sup>6</sup> F. Zhou<sup>3</sup> and F. Zimmermann<sup>10</sup>

<sup>1</sup>LAL, Universite´ Paris-Sud, CNRS/IN2P3, Orsay, France

<sup>2</sup>Instituto de Fisica Corpuscular (CSIC–University of Valencia), Valencia, Spain

<sup>3</sup>SLAC National Accelerator Laboratory, Menlo Park, California 94025, USA

<sup>4</sup>Cockcroft Institute, STFC, Daresbury Laboratory, United Kingdom

<sup>5</sup>John Adams Institute, Oxford, United Kingdom

<sup>6</sup>High Energy Accelerator Research Organization, Tsukuba, Japan

<sup>7</sup>Institute of High Energy Physics, Beijing China

<sup>8</sup>LAPP, Universite´ de Savoie, CNRS/IN2P3, Annecy-le-Vieux, France

- <sup>9</sup>John Adams Institute, Royal Holloway, United Kingdom  
<sup>10</sup>European Organization for Nuclear Research, Geneva, Switzerland  
<sup>11</sup>Deutsches Elektronen-Synchrotron, Hamburg, Germany  
<sup>12</sup>Fermi National Accelerator Laboratory, Batavia, Illinois 60510-5011, USA  
<sup>13</sup>Laboratoire Leprince-Ringuet, CNRS/IN2P3, Ecole Polytechnique, Palaiseau, France  
<sup>14</sup>Kyungpook National University, Korea  
<sup>15</sup>PAL, Korea  
<sup>16</sup>Kyoto ICR, Japan  
<sup>17</sup>The University of Tokyo, Japan  
<sup>18</sup>UCL, London, United Kingdom  
<sup>19</sup>Tohoku University, Japan  
<sup>20</sup>Brookhaven National Laboratory, Upton, New York 11973-5000, USA  
<sup>21</sup>Cockcroft Institute, University of Manchester, United Kingdom  
<sup>22</sup>Hiroshima University, Japan  
<sup>23</sup>Cockcroft Institute, University of Liverpool, United Kingdom

Mail to: [toshiaki.tauchi@kek.jp](mailto:toshiaki.tauchi@kek.jp)

#### 4.1.1 Introduction

The Accelerator Test Facility (ATF) [1] at KEK was originally constructed as a Damping Ring (DR) demonstration facility for the next generation of electron linear colliders. It consists of a 1.3 GeV s-band linac and a 136m circumference damping ring which can routinely generate 1.6 nC electron bunches with very small vertical emittances ( $<10\text{pm}\cdot\text{rad}$ ). Completed in December of 2008, a new extraction line and final focus optics was built, this is referred to as ATF2 [2]. The location of ATF in relation to the KEK site can be seen in Figure 1.

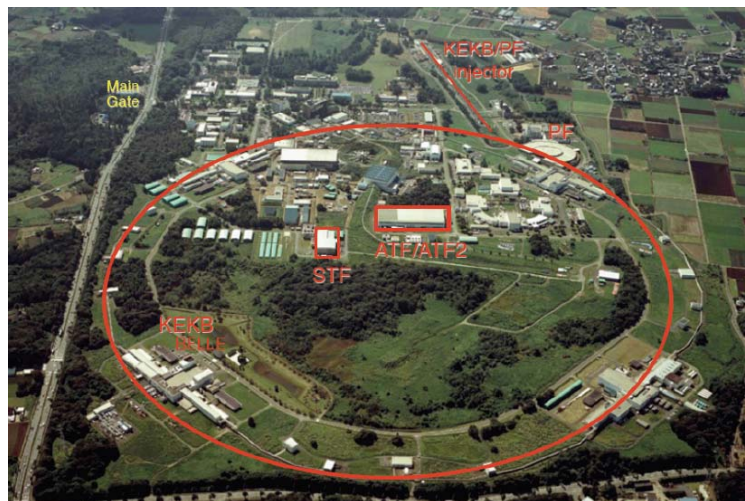


**Figure 1:** Location of ATF accelerator building at KEK, Tsukuba, Japan.

ATF is a general-purpose facility for accelerator physics related R&D activities, with approximately 50% of the available beam time currently devoted to the ATF2

program. The ATF2 extraction line (EXT) and final focus system (FFS) extends about 90 meters from the DR extraction point, a sketch of this system can be seen in figure 2, along with the location of key instrumentation. The primary purpose of the ATF2 beam line is to demonstrate a new style of magnetic focusing optics intended for use at future linear colliders, such as ILC [3] or CLIC [4] based on a local chromaticity correction scheme [7]. The primary goal of the collaboration is to demonstrate the ability of this optics to focus an electron beam of similar emittance to the ILC using a FFS of the same design chromaticity. A comparison of some of the ATF2 design parameters with those of the ILC and CLIC are shown in table 1. With the 1.3 GeV beam energy of ATF2, the target spot size to prove the operability of this optics for ILC is 37nm. This is referred to as “Goal 1”. In addition, Goal 1 requires the demonstration of stable operations with such a beam size at the Interaction Point (IP)<sup>1</sup>. “Goal 2” is to demonstrate nm-level stability with respect to the IP beam monitors, such as is required for stable beam collisions at ILC or CLIC. A further goal is to attempt to increase the chromaticity of the final focus optics, reducing the IP beta functions to a level where the system more closely resembles the CLIC FFS [8], and also for some of the newly proposed ILC parameters. It is anticipated that the difficulty of successfully tuning the FFS to deliver design IP beam spot sizes scales with the chromaticity of the system. The design of the achromatic focusing system involves fine cancelation of first, second and third order aberrations at the IP. One needs more accurate cancelation the tighter one attempts to focus the beam, also including more higher order terms. By gradually pushing the system to smaller IP beta functions and higher chromaticity we hope to learn what the limits of such a design are when applied practically. This will give confidence in the design philosophy behind future high-luminosity colliders and in the simulations used to predict their behaviour.

**Table 1:** Selection of beam parameters for ATF2, the ILC (Reference Design Report) and CLIC (1.5 TeV)

<i>Parameters</i>	<i>ATF2</i>	<i>ILC (RDR)</i>	<i>CLIC</i>
Beam energy [GeV]	1.3	250	1500
$L^*$ [m]	1	3.5-4.5	3.5
$\gamma\epsilon_{x/y}$ [m.rad]	$5 \times 10^{-6} / 3 \times 10^{-8}$	$1 \times 10^{-5} / 4 \times 10^{-8}$	$6.6 \times 10^{-7} / 2 \times 10^{-8}$
IP $\beta_{x/y}$ [mm]	4 / 0.1	21 / 0.4	6.9 / 0.07
IP $\eta'$ [rad]	0.14	0.0094	0.00144
$\sigma_E$ [%]	0.1	0.1	0.3
Chromaticity	$1 \times 10^4$	$1 \times 10^4$	$5 \times 10^4$
Number of bunches	1-3 (Goal 1)	2820	312
Number of bunches	3-30 (Goal 2)	2820	312
Bunch population	$1 \times 10^{10}$	$2 \times 10^{10}$	$3.7 \times 10^9$
IP $\sigma_y$ [nm]	37	5.7	0.7

The commissioning of ATF2 began in December 2008. During 2009, we commissioned the various hardware diagnostic systems whilst commissioning the beam line with a relaxed optics configuration (10mm vertical IP beta function). The relaxed

<sup>1</sup> Although there is no interacting beam at ATF2, the waist where the beam is brought to minimum size vertically and horizontally is referred to as the IP. In a linear collider, this is where the beam collisions take place.



optics configuration was intended to allow for simplified checkout of the linear optics as the reduced chromaticity of the FFS at this level of focusing did not require the chromaticity compensation sextupoles to be switched on. It also provided for a small enough beam ( $\sim 1\mu\text{m}$  vertical IP size) to commission the initial mode of the IP beam size monitor (IPBSM). Some more details of this initial commissioning phase can be seen in [5]. During 2010 we switched to a more aggressive optics (1mm vertical IP beta function), switched on the FFS sextupoles and tuned the beam size below 1mm for the first time, with a smallest recorded spot size by the IPBSM of 310 nm [6]. Then starting in the autumn runs of 2010 and going into 2011, we switched to the nominal vertical focusing optics, whilst keeping the horizontal beta function at 2.5 times nominal for reasons explained below. We expected to start tuning work towards obtaining the nominal vertical IP spot size during the spring of 2011. However, due to a fire in the modulator supplying power to the klystron generating RF for the gun, the program was put back 3 weeks, and then ATF suffered damage during the great Eastern Japanese M9.0 earthquake, March 11. At the time of writing, work is still ongoing to repair the damages before a restart of the ATF can be attempted.

In the rest of this section we summarise the key hardware systems required for ATF2 operation, the theoretical tuning studies which underpin the tuning algorithms used to tune the IP beam spot size, and also describe the software environment and applications used during ATF2 operations.

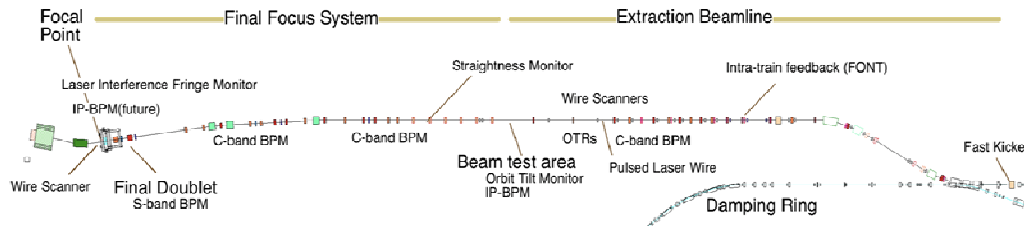


**Figure 2:** The extraction line and final focus section of ATF2 after extraction from the damping ring, showing the location of key ATF2 diagnostic systems.

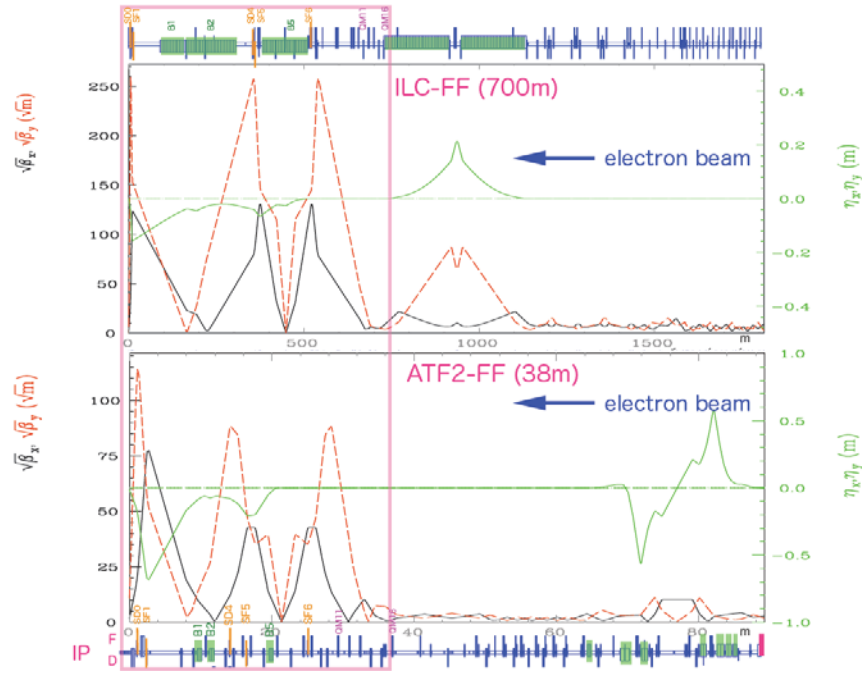


**Figure 3:** The betatron functions and design dispersion of the ATF2 and ILC FFS's. The ATF2 FFS is a scale test of the ILC optics, much shorter due to the 1.3 GeV vs. 250 GeV beam energy.

## 4.1.2 Sub-Systems Hardware

### 4.1.2.1 Magnets and Magnet Movers

The ATF2 beam line contains seven dipole, three septum, 49 quadrupole, five sextupole, one skew-sextupole and 25 corrector magnets. The quadrupoles and dipole bends for the main part of the FFS were purpose designed and built for ATF2, whilst the other magnets were re-used from the old ATF extraction line and from the FFTB experiment at SLAC. [9]

Amongst the re-used magnets are the 2 final doublet (FD) quadrupoles. A lot of work was done to measure, and through the use of shims, reduce the magnitude of higher order multipole components of the FD quadrupole fields. Even so, the tolerances on the skew multipole components for the QF1FF magnet are very tight due to the huge horizontal beta function at the entrance to this magnet ( $\sim 2.3\text{km}$ ). A small amount of coupling generated here causes significant vertical beam size degradation. It proved impossible to remove all multipole components to a level that satisfied the beam dynamics requirements, a non-linear re-matching procedure was developed which ameliorates this and other multipole defects, outlined in a later section. A proposed future upgrade to ATF2 is a test of a prototype ILC-style final doublet superconducting quadrupole magnet [10]. Such a magnet is being prepared at BNL. Due to the unique direct-wind technology used to manufacture this magnet it has been made with very small multipolar field components, well below the tolerance specifications for the QF1FF quadrupole. Together with adjustments to the layout of other quadrupole magnets, this may allow the original optics to be tried in future. Also under test is a prototype of a high-field permanent FD quadrupole magnet [11].

In addition to requiring pure magnetic fields, the final doublet system (comprising the 2 final focus quadrupoles and their associated local chromatic correction sextupoles) also needs to be very stable with respect to vibration between the magnetic elements and the IP beam waist. To operate the IP beam size monitor (IPBSM) at its highest level of precision, the beam jitter with respect to the monitor's laser fringes has to be of order 10nm RMS or better (pulse-pulse, where ATF2 typically operates at 1.56Hz). This translates to a vibration tolerance with respect to the IP of 7 and 20 nm (integrated above 0.2Hz) for QD0FF and QF1FF respectively. The floor of ATF has been specially prepared, with deep concrete piles, to be vibrationally stable and has a very good coherence length, ~4m. In addition, much work has been undertaken to ensure the stability of the FD support table [12]. The FD elements are attached to a rigid honeycomb block and bolted to the floor, using a thin layer of beeswax between the steel plate support at the base of the block and the floor to ensure good mechanical coupling. Measurements were made in September 2008 that showed the relative vibrations between QF1FF, QD0FF and the IP were below tolerance. Measurements were also made to show the coolant flowing through the magnets does not introduce a significant level of vibration [13].

The magnets in the FFS have particularly tight main field tolerances (see [2]). With this in mind and to provide a test of the type of redundant power supply modules required for future colliders containing many thousands of magnets, a high accuracy, high availability power supply system was provided [14].

Each quadrupole and sextupole magnet in the FFS is mounted on a 3-axis mover system (horizontal, vertical and roll motion capable). This system is used to align the FFS to a high degree of precision using the beam which can be done repeatedly as required to counter thermal drift, long-period ground motion etc. It is also used to calibrate the high-precision cavity BPMs attached to the magnets and to determine the offset of the beam with respect to the cavity BPM readout centres. The magnet movers were relocated to the ATF from FFTB [15, 16]. Each mover system consists of three camshafts that provide the capability of moving the heavy magnets. They have a dynamic range of about 2mm/1.5mm/5mrad in x/y/roll. The precision of the system is about 1-2 $\mu$ m in the horizontal and vertical and about 10 $\mu$ rad in roll.

#### **4.1.2.2 Beam Position Monitors (BPMs)**

There are a total of 37 c-band and 4 s-band high-resolution cavity BPMs and 13 striplineBPMs in use at ATF2. The cavity BPMs [17] are capable of operating with <200nm resolution or down to about 20nm with maximum gain (minimum dynamic range). The stripline BPM system [18], mainly in the extraction line section (EXT), received an upgrade of its processing electronics and readout system in the spring of 2010 and now operates with a resolution <10 $\mu$ m with good charge-level independence and has a self-calibration system. The cavity BPM system includes a specially designed doublet of c-band cavities that are installed inside the IP vacuum chamber to provide IP position information. The goal resolution of this system is <2nm and represents an ongoing area of study [19]. For the tuning program presented here, the key properties of these systems are high resolution, charge independence and gain stability. Details of the BPM systems are included elsewhere in this publication.

#### 4.1.2.3 *IP Beam Size Monitors*

The suite of IP beam measurement devices installed at ATF2 allows for measurement of both the horizontal and vertical beam spot sizes at the focused waist for tuning and verification of goal 1 [20]. The vertical spot size can be measured from several 10's of micro-metres down to the goal spot size of 37nm, and down further to a resolution limit of about 22nm. For the larger spot sizes there are 2 wirescanner systems 42cm downstream from the nominal IP with 10um tungsten and 5um carbon horizontal, vertical, 45-degree (tungsten) and 10-degree (carbon) wires. In 2011, a 5um carbon wire scanner was also installed as part of the main IP assembly. There is also a "Shintake Monitor" installation [21] that measures the IP vertical beam size based on inverse Compton scattering between the incident electron beam and a laser interference pattern. There are different crossing angle modes of the interfering laser beams that provide interference patterns of differing pitch. The pattern is scanned across the beam, typically in 90 steps, whilst recording the Compton signal registered in the downstream calorimeter at each step. The beam size is inferred from the modulation depth of the recorded signal. The four crossing angle modes give differing beam size sensitivity from about 3 um, down to the resolution limit of about 22 nm in the 174-degree measurement mode. More details on this system are presented elsewhere in this publication.

#### 4.1.2.4 *EXT Beam Phase-Space Diagnostics (Wire-Scanners and OTRs)*

The mainstay of the ATF EXT beam measurement system has been a system of 5 wirescanner stations equipped with horizontal, vertical and 45-degree 10um tungsten wires. These have been used to measure the emittance and Twiss parameters of the beam after DR extraction and to correct coupling (e.g. [22,23]). Installed in the autumn of 2010, four new optical transition radiation (OTR) detectors were installed into the EXT at locations close to the wirescanner stations [24]. These are capable of directly imaging the 2D ellipse of the beam and can perform the emittance and Twiss measurements in a much shorter time than the wirescanner system (under 2 minutes, as opposed to well over an hour due to the low rep-rate of the ATF2 beam). This system is also described in more detail elsewhere in this publication.

#### 4.1.2.5 *Beam Loss Monitor*

An optical fibre has been strung along the complete length of the ATF2 EXT and FFS beam lines. The PMT readout is digitised and made available to the control system for monitoring of potential beam losses throughout the ATF2 beamline. This is especially useful for initial beam steering before the application of beam-based alignment.

The Japanese company Toray makes the fibre. It has a 960um core<sup>2</sup>(PMMA), 1000um cladding(Fluorinated Polymer) and a 2.2mm black colour jacket. The sensitivity of the fibre is better than gas filled PLIC [47] cables, and has faster rise and fall times which makes separating discrete losses easier.

---

<sup>2</sup> A fiber with a 2mm core diameter is available and provides about 4 times the sensitivity of the smaller fiber if greater sensitivity is required.

#### **4.1.2.6 *Intra-Pulse Feedback***

Specialised hardware is installed and under test in the EXT beam diagnostic region to demonstrate the feasibility of a multi-MHz feedback system capable of stabilising the tail of the bunch train pulse to a few nm [25]. Full details of this system are provided elsewhere in the publication.

#### **4.1.2.7 *Background Radiation Monitors***

Achieving good signal: background levels in the IPBSM Compton photon detector are critical to the primary goal of ATF2. In addition to the background monitor integral to the IPBSM system, the photon detectors for wirescanner detectors and the fibre beam loss monitor system, there is a study group devoted to measuring, and understanding through modeling, the background sources. They deploy multiple independent calorimetric detectors around the ATF2 beam lines to study the background and possible sources [46].

### **4.1.3 Accelerator Modeling Software**

#### **4.1.3.1 *Optics Design and Beam Dynamics Simulations***

A number of different software packages are used and have been developed for the purposes of initial optics design, lattice description and modeling, and for beam dynamics simulations to develop and test tuning algorithms. The original design of the ATF2 optics, starting with an energy-scaled version of the ILC FFS optics was performed according to the prescription detailed here [27], using a combination of MAD [29], TURTLE [30] and Matlab [31] scripts. The lattice description is maintained in XSIF [32] format from where it is ported to other software as required through the use of XSIF parsers and manual conversions scripts. Due to the non-linear nature of the FFS optics, multi macro-particle tracking software has been used to test the performance of the optics and to develop beam-tuning algorithms and to test their robustness under realistic error conditions. This has been done independently with multiple codes, which provide a useful crosscheck of the methods used and the tracking software in the different codes themselves. Codes used for these studies are Lucretia [33], SAD [34], MADX (MAPCLASS) [35] and PLACET [36].

#### **4.1.3.2 *Online Model and Control System Interface***

The existing core controls infrastructure for ATF/ATF2 is built upon a VSYSTEM [37] database and graphical interface [26]. New devices, especially systems contributed from outside-KEK institutes are now based upon an EPICS [38] interface. An existing online model exists based on the SAD modeling code with inbuilt links to the VSYSTEM control structure. A new online model and controls interface was introduced in addition to this based on Lucretia and a Matlab-based extension to Lucretia which gives it the ability to control accelerator systems through the EPICS interface. Where control of a VSYSTEM device is required, an EPICS->VSYSTEM controls bridge was written that allows access to VSYSTEM database structures through an EPICS ‘soft IOC’. This online model and control platform is packaged together with a simulated EPICS layer that contains simulated EPICS Process Variables (PVs) for most ATF2

control elements. This total package is known as the “ATF2 Flight Simulator” [38]. One of the important aspects of the Flight Simulator is the ability to code and test algorithms offsite and deploy the same code at ATF2 proper with no transitional steps required. As many of the tuning algorithms for ATF2 were developed by collaborators at foreign institutes this has been a very useful tool.

#### 4.1.4 Optics Preparation and Beam Dynamics Simulations

The ATF2 FFS incorporates non-linear optics to achieve very tight focusing of the beam at the IP. It is very sensitive to many different sources of errors (for example see analyses in [39-40]) and has uniquely tight tolerances not found in previous accelerator designs. Hence, in addition to the classical FFS tuning procedure developed for ILC, three different analyses environments were constructed based on MADX, SAD and Lucretia. These are able to re-match the FFS optics and study effects of errors using macro-particle tracking through the model lattice together with the application of all envisaged error sources.

One such error source was discovered after construction was complete: the higher-order multipolar components of many of the quadrupole and dipole magnets in the EXT and FFS were large enough to generate aberrations at the IP which noticeably increase the expected vertical spot size. Measurements of the normal and skew multipole components of these magnets were made at KEK and at SLAC and inserted into the models. It was found that multipole components up to octupole, and in the case of the final doublet, up to 12-pole were important. After carefully checking the modeling of these multipole components in the various simulation codes, the expected beam sizes obtained by multi-particle tracking are shown in table 2. When the beam becomes significantly non-gaussian, the method by which the beam size is calculated is important. The entries in the table show the calculated beam sizes for an RMS value and from fitting a Gaussian function to the core of the beam. This last method de-weights the effects of the large non-gaussian tails of the beam distribution caused by the multipoles. A simulation of the way in which the IPBSM calculates the beam size based on its measurement method was also included. This measures a value which is somewhere between the RMS and Gaussian fit methods. It should be noted that the number most relevant for ILC operations would be the core fit method that more closely reflects the expected luminosity. There are some differences between the simulation results, partly due to the different statistics in modeling the beam and partly due to differences in the modeling of the multipoles in the different models. The details behind these differences were not studied in detail at this time. These expected beam sizes are considerably larger than the goal vertical beam size of 37nm (RMS). To try and recover the design beam size closer to the goal a study was performed to try and re-match the optics to mitigate the effects induced by the measured multipoles. This was done using MADX and the MAPCLASS re-matching code in addition to a separate analysis with SAD. The result of this process is shown in figure 4. By increasing the horizontal beta function at the IP by a factor of 2.5 to 10mm, and thus reducing the horizontal beam size in the QF1FF aperture and other sensitive apertures, the effect of the various skew multipole components was mitigated somewhat. Additionally by introducing a skew-sextupole magnet into the beamline, the beam size was further improved by compensating for the skew-sextupole multipoles. Realising this, a skew sextupole magnet was sourced at KEK and installed into the beam line at the beginning of 2011

and is now available for use. Taking this, and in conjunction fine-tuning the settings of the standard chromaticity and geometric correction sextupoles, a beam size at the IP close to the goal was shown to be achievable in simulation.

**Table 2:** Simulated vertical beam sizes at IP including measured multipoles.

Vertical beam size measurement type	MADX	SAD	Lucretia
RMS / nm	175	278	220
Shintake Monitor / nm	100		
Gaussian Core Fit / nm	50	60	65

Notice that the vertical beam size scales noticeably with horizontal emittance. This is due to the sampling of more of the skew multipole fields at larger horizontal beam sizes at the high beta points. The normal horizontal emittance achieved is about  $5\mu\text{m}\cdot\text{urad}$  (normalised), but has been measured lower at lower bunch charge (due to collective effects in the damping ring).

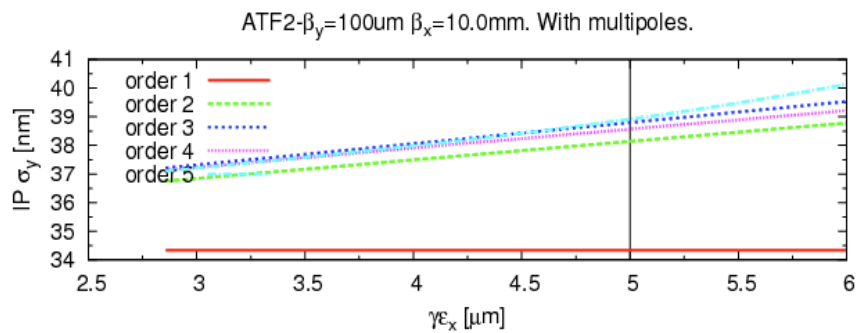


**Figure 4:** Re-tuned IP vertical beam spot size as a function of input horizontal emittance, with 2.5 times nominal IP horizontal beta function.

This result is brand new at the time of writing and has not been confirmed yet by other tracking codes, although previous re-matching studies have compared favourably across the three codes in use at the 10% level and we expect the same in this case.

After generating the desired lattice as above, we simulate the expected performance of the accelerator in the presence of all expected error conditions (e.g. survey alignment tolerances, magnet field strength errors, BPM errors, ground motion, beam size measurement errors etc). This has been done using a Monte Carlo approach whereby 100 random distributions of error conditions are generated and the full tuning procedure is applied to each seed. The mean and spread in the final results represents our best guess of the expected performance of the machine and an estimate as to our uncertainty in the results based on the level of knowledge of the expected error sources. These simulations also provide the basis for developing and testing different tuning algorithms and techniques. Figure 5 shows the results of one such simulation, where the initial beam sizes are expected to be of the order of about  $1\text{-}3\mu\text{m}$  and can be tuned down to within 20% of the nominal beam size in about 12 steps. At each step the range of dominant aberrations at the IP (up to third order) are examined. The most common aberration at each step is then targeted across all Monte Carlo seeds. This then forms the basis for the tuning procedure to be applied to the real accelerator. It has also been

shown that further iterations of the tuning knobs produces a final beam spot size within about 10% of the design goal after a few hours of tuning. This simulation has been performed additionally in MADX and PLACET with similar results. However, more work is required to get the desired level of agreement that will take more time due to the complexity of the simulations.

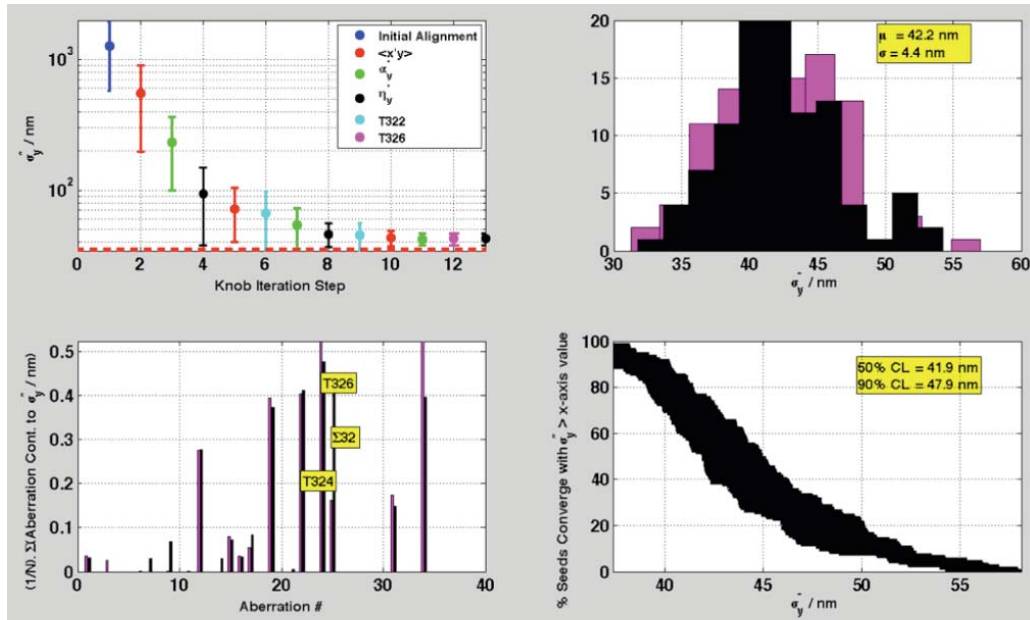


**Figure 5:** Lucretia tuning simulation results for the first 12 tuning steps. The bottom left plot shows the contributions to the beam size from different aberration terms. The bounds of the bottom right plot are the RMS and “gaussian-fit to the core” methods of determining the vertical beam spot size.

#### 4.1.5 Beam Tuning Procedure

We present here some details regarding the steps followed during ATF2 tuning shifts to prepare and tune the electron beam down to small vertical sizes at the IP.

##### 4.1.5.1 Beam-Based Alignment (BBA)

It is of importance for the goals of the ATF2 project to generate and maintain a well aligned beam trajectory through the EXT and FFS magnets for two principal reasons: backgrounds and beam quality. The IPBSM requires large signal:background ratios in its Compton photon detector. The level of backgrounds was found to correlate strongly with the amplitude of the orbit; maintaining the beam centroid within 500um of the centres of the magnets keeps the halo-generated backgrounds reaching the IP detectors small enough for normal operations. The basis of beam steering algorithms is the BPM system and knowing the offsets of the BPM’s electrical readout centres to the magnetic field centres of the magnets.

For quadrupoles the BBA is performed by changing the main field strength by 20% (this value is used as it is small enough to allow the nominal field to be restored afterwards without re-standardising and large enough to produce an observable effect) and observing the change in downstream orbit. The change in orbit is determined either



using downstream BPMs or more manually using a screen where the phase advance to downstream BPMs is not so favourable. The orbit in the magnet under BBA is then changed either using a dipole corrector based orbit bump or using a magnet mover if available. Using several different beam positions in the magnet under BBA with 2 field strength settings it is possible to read off the beam alignment [39].

For sextupole magnets, one moves the magnet across the beam trajectory and finds the alignment point between BPM reading and sextupole field centre using a parabolic fit to the downstream BPMs, the alignment is the zero-gradient point of the fit. The strength of the sextupoles needs to be set to maximum (50A for the first three, 10A for the final, downstream two) to produce a detectable parabolic BPM response. For the final two, this was found to not be enough; the downstream (horizontal) response was lost in the pulse-pulse noise (this region has large design horizontal dispersion). To enhance the signal, an SVD technique was employed to fit out the common incoming energy and position related jitter (similar to MIA techniques [41]). At the time of writing we are also testing similar jitter subtraction code to enhance the resolution of the quadrupole BBA technique that currently provides 10-50  $\mu\text{m}$  alignment accuracy. The approximate accuracy of the sextupole alignment is currently 10-20  $\mu\text{m}$ .

More work is envisioned in this area to test the reproducibility of the procedure through repeated measurements and to try and find ways of automating and speeding up the procedures.

#### ***4.1.5.2 Orbit Response and Jitter Modelling***

Before the rest of the tuning procedure can be embarked upon, we need to be sure that we have a good current online model. This is important, as the cavity BPM system requires periodic re-calibration and the ATF2 optics are frequently changed for other research programs. To determine the BPMs are well enough calibrated, that there are no optics anomalies etc we adopt a single, fast measurement check at the start of all ATF2 tuning shifts as shown in figure 6.

During 2011, new monitoring software was put in place based on an SVD analysis of the past few hundred BPM readings in the storage buffer. By pulling out the energy mode from the dispersive BPMs in the EXT, FFS and also the last turn of the DR in the arc sections, it is possible to calculate the relative pulse-pulse energy change and thus produce a running display of dispersion throughout the beam line. This together with the monitoring of the incoming orbit jitter parameters allows for us to check for any change in beam conditions that could fight the ongoing tuning process at the IP.

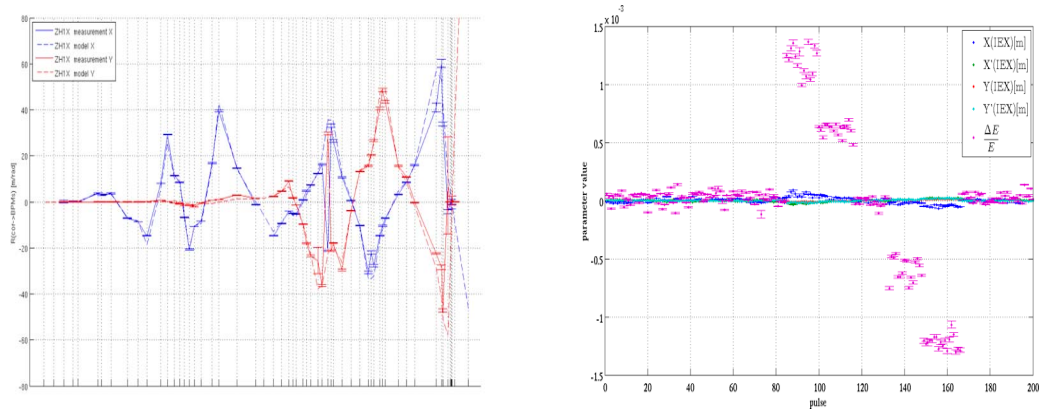


**Figure 6:** Left plot: measured and model response to kick in first horizontal dipole corrector (with energised skew quads producing expected coupling). Right plot: multi-pulse reconstruction of 5D incoming beam jitter.

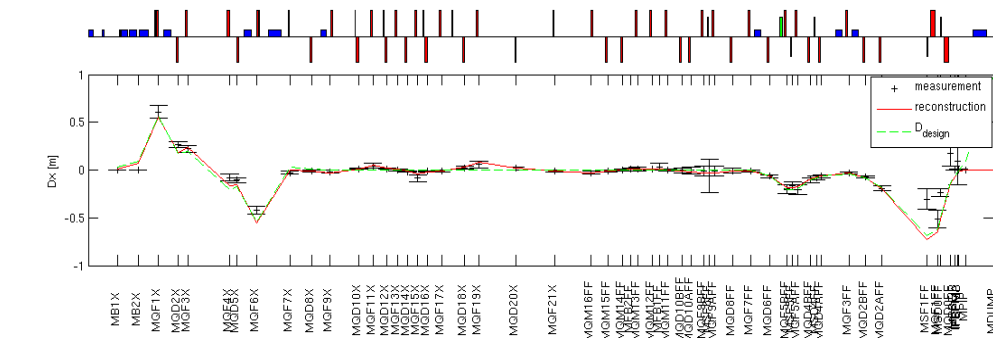


**Figure 7:** Reconstructed horizontal dispersion function from an SVD analysis of pulse-pulse jitter.

#### 4.1.5.3 Orbit Steering & Feedbacks

With well calibrated and aligned BPMs we put the beam through the EXT and FFS magnet field centres using a ‘1-1’ style steering algorithm in two stages (such a system was studied in simulation here [42]). First the EXT orbit and launch into the FFS is corrected using all the BPMs and the 25 horizontal and vertical dipole corrector magnets. Then the FFS section is steered flat using the FFS magnet movers and the BPMs attached to each magnet. Weighting is applied to the steering algorithm to force the position and angle at the IP to be that required to send Compton photons to the IPBSM detector.

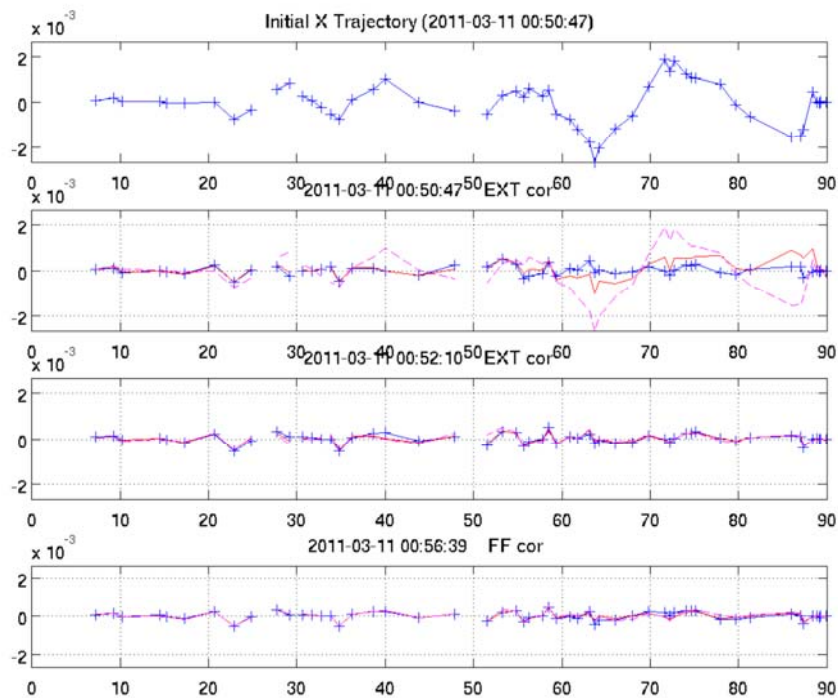


**Figure 8:** Orbit steering through EXT and FFS sections. Top plot is original orbit, next is after 1 EXT correction, then another EXT correction, then FFS correction.

#### 4.1.5.4 Dispersion Measurement and Correction

Dispersion generated in the EXT and FFS optics (through position and roll misalignments of magnets), and to some extent the residual dispersion leakage out of the DR, is measured and corrected in the EXT before IP beam tuning. The dispersion is measured by changing the energy in the DR by changing the DR RF frequency and recording the resultant change in BPM readings in the EXT and FFS. Horizontal dispersion correction is achieved using a pair of quadrupole magnets in the extraction inflector section immediately after DR extraction where large horizontal dispersion is present (in equal and opposite amounts at each magnet, QF1X & QF6X). Vertical correction is achieved using a pair of skew quadrupole magnets in similar locations, where they are powered as a pair, generating dispersion and angular dispersion with a minimal amount of coupling, as shown in figure 9. For no incoming vertical dispersion, this “sum” knob is able to correct both vertical dispersion and angular dispersion to zero. For finite incoming dispersion, both phases of dispersion cannot be simultaneously corrected. In these instances, a correction value is set such that the measured dispersion at the IP is within a correctable range for the IP tuning knobs and the values in the FFS (mostly 90 degrees out of IP phase) are as small as possible. When large amounts of incoming dispersion are observed from the DR, the correction needs to be performed inside the DR itself.

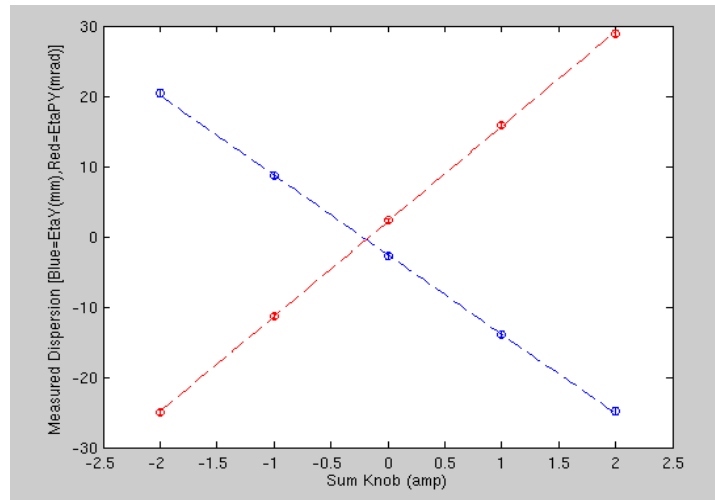


**Figure 9:** Fitted dispersion at match point within the EXT from measured values in EXT and FFS BPMs.

#### 4.1.5.5 Twiss Parameters & Coupling Measurement and Correction

In the past the twiss parameters and coupling parameters have successfully been calculated using the five wire scanners in the EXT [22-23]. The coupling has then been corrected by minimising the vertical projected emittance through successive scans of the four skew quadrupoles (QK1X – QK4X) in the EXT. This is a slow process and thus the correction is prone to errors from drifting beam conditions throughout the measurement and correction process. To speed up the process, and thus to allow for more parameters to be scanned against emittance, a multi-OTR system was installed which allows for sub-2 minute emittance measurements [24].

The betatron mismatch into the EXT is always measured to be very small; typical BMAG [43] values of  $<1.05$  in the vertical and horizontal planes are measured. In principle the six matching quadrupoles at the beginning of the FFS can be used to rematch the beam to the IP in the case of strong mismatch. In practice this has not been required; simulations show that the beam can be tuned down to goal levels with the measured matching conditions. An approximate check of the linear matching directly at the IP has been performed with relaxed beta optics [44] using the IP wire scanners. This is done either by measuring the change in measured beam size as the waist is moved by changing the strength of the final quadrupole magnet (QD0FF), or by sequential measurements of the beam size at the IP and Post-IP wire scanner locations.

Prior to March of 2010, we experienced a large (factor 2-3) vertical emittance growth from the DR into the EXT [45]. A number of factors were expected to be responsible for this, and many improvements were made in the previous couple of years. The beam is extracted at a large radius in one of the ring quadrupoles (QM7), sextupolar fields in this region were suspected and the magnet was exchanged for one with larger aperture. In the early part of 2010 a large roll in the third extraction septum was discovered and fixed. Also a program of survey, physical and beam-based alignment in the DR was undertaken. After this, sub 12pm vertical projected emittances were measured in the EXT. However, since Dec 2010 we have not been able to correct the extracted emittance to below  $\sim 27$ pm (with  $\sim 10$ pm measured in the DR). At the time

of writing, the source of this has not yet been discovered, although we are hopeful that with the help of fast emittance measurements from the OTR system the source of this can be found.

#### 4.1.5.6 IP Vertical Beam Size Tuning

After initial tuning steps have been completed as summarised above, residual aberrations still remain at the IP that cause the vertical profile of the beam at the waist to be significantly larger than the design value. The principal aberrations present are expected to be horizontal angle – vertical position coupling, vertical waist shift and vertical dispersion. To cancel these, approximately orthogonal knobs have been calculated using tracking simulations. The five FFS sextupole magnets are deliberately offset using their respective magnet mover systems to generate the required correction terms at the IP. Due to the non-precise orthogonality of these knobs, iteration is required to reduce the beam size below 100nm. Beyond this level higher order terms start to become important. Knobs for the expected dominant terms have also been generated.

During tuning shifts, the beam has been brought down to about 300nm in vertical size. This is the resolution limit of the 8-degree mode of the IPBSM. To progress further requires the use of the 30-degree mode of operation of this device; this is the highest priority task once ATF2 beam operations resume. Figure 10 shows the simulation results of the tuning process (upper and lower 1 sigma bounds from 100 Monte Carlo seeds) and the results from ATF2 tuning shifts. The tuning behaviour down to the 300nm level is about consistent with the expectation from the simulations. One extra tuning step required that was not simulated is the  $\langle xy \rangle$  coupling term correction. This is done using an orthogonal knob generated with the four EXT skew quadrupole magnets. None of the FFS magnets should generate significant quantities of this coupling term. It is suspected that this is due to a physical rotation of the IPBSM laser fringe system with respect to the FFS alignment frame.

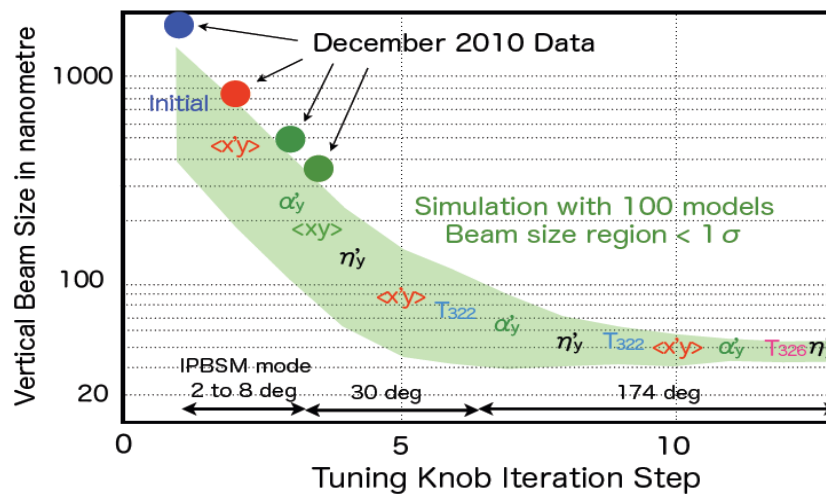


**Figure 10:** IP vertical beam size tuning; experimental results and simulation. Shown are the data points from Dec 2010, the  $\pm 1$  sigma curves from the Monte Carlo model, the tuning steps are indicated in text. The required operation mode of the IPBSM is also indicated for each relevant section of the plot.

#### 4.1.6 Summary and Outlook

All the tuning tools to reach goal 1 of ATF2 are in place and in most cases have been tested and repeatedly used during dedicated tuning shifts by the worldwide ATF2 collaboration. So far a vertical beamsizes of about 300 nm has been achieved on two separate occasions following the tuning procedure outlined here (May and December 2010), see IPBSM section in this publication for details. It was our intention of commissioning the final two stages of the IPBSM system during the spring of 2011 and demonstrating close to design vertical IP beam spot sizes. Unfortunately due to the great Eastern Japanese earthquake, March 11 2011, we will have an interruption of unknown length until the damage to KEK and ATF can be assessed and fixed. We look forward to resuming beam operations and completing the demonstration of a 37nm beam as soon as repairs can be made. The intention then is to demonstrate reliable 37nm beam operations with few-nm stability by the end of Japanese fiscal year 2012. Longer term, more tentative plans being discussed include, after 2012, the pushing of the FFS focusing harder to explore its limitations and applicability to correcting for the levels of chromaticity pertinent to the CLIC collider designs, and also for some of the newly proposed ILC parameters. Beyond that, tests of a prototype design for the ILC superconducting final doublet quadrupole currently under construction at Brookhaven National Laboratory are being considered as well as possible provision of a photon facility with laser and optical cavities. Together with the unique electron beam provided by the ATF accelerator, strong QED experiments with laser intensities of  $> 10^{22}$  W/cm<sup>2</sup> could be considered, e.g. to pursue experimental studies of the predicted phenomenon of Unruh radiation.

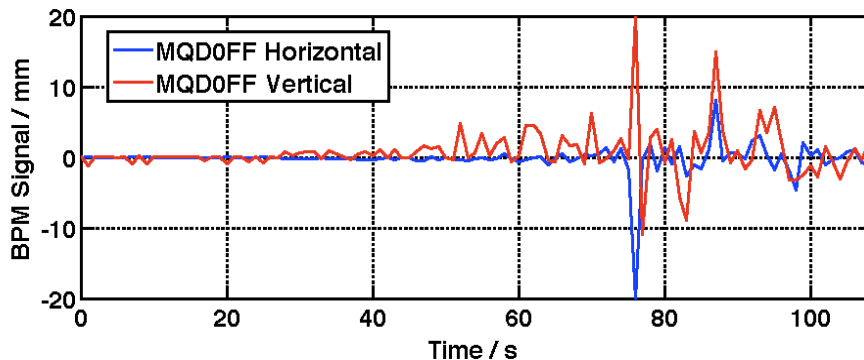


**Figure 10:** Archived BPM readings from the last quadrupole magnet BPM in the ATF2 FFS during the Eastern Japan M9.0 earthquake, March 11, 2011, at about 14:46 local time. Data from just before the onset of the earthquake until the beam was aborted a few seconds after is shown.

#### 4.1.7 References

1. J. Urakawa et al. (ATF Collaboration), <http://atf.kek.jp/collab/ap/>.
2. ATF2 Proposal, Report No. SLAC-R-771, 2005.
3. GDE (Global Design Effort) and WWS (World Wide Study), ILC RDR, ILC-REPORT-2007-001.
4. R. Tomas, Phys. Rev. STAccel. Beams 13, 014801 (2010), and references therein.
5. Present status and first results of the final focus beam line at the KEK Accelerator Test

- Facility. P. Bambade et al., Apr 1, 2010. Phys.Rev.STAccel.Beams 13:042801, 2010.
6. Operational Experiences Tuning the ATF2 Final Focus Optics Towards Obtaining a 37nm Electron Beam IP Spot Size. Glen White et al. IPAC-2010-WEOBMH01, May 2010.
  7. P. Raimondi and A. Seryi, Phys. Rev. Lett. 86, 3779 (2001).
  8. Scenarios for the ATF2 Ultra-Low Betas Proposal. Eduardo Marin et al. IPAC-2010-THPE020, May 2010.
  9. A Project to Design and Build the Magnets for a New Test Beamline, the ATF2, at KEK. C. M. Spencer et al, SLAC-PUB-14339, Oct 2010. Presented at 21st International Conference on Magnet Technology (MT-21), Hefei, China, 18-23 Oct 2009.
  10. A Superconducting Magnet Upgrade of the ATF2 Final Focus. Brett Parker *et al.* IPAC-2010-WEPE041, May 2010.
  11. Beam Test Plan of Permanent Magnet Quadrupole Lens at ATF2. Yoshihisa Iwashita et al., IPAC-2010-WEPE017, May 2010.
  12. ATF2 Project: Final doublet support studies at LAPP. B. Bolzon. LCWS-2007-ATF201, May 2007.
  13. B. Bolzon et al. ATF-Report No. 09-01.
  14. ATF2 High Availability Power Supplies. A Bellomo et al., EPAC08-THPP127, SLAC-PUB-13278, Jun 27, 2008. 3pp.
  15. V. Balakin et al., Phys. Rev. Lett. 74, 2479 (1995).
  16. Precision Magnet Movers for the Final Focus Test Beam, G. Bowden et al., SLAC-PUB-95-6132, June 1995.
  17. Cavity Beam Position Monitor System for ATF2. S. Boogert *et al.* IPAC-2010-MOPE070, May 2010.
  18. New Beam Monitoring Instrumentation at ATF2, KEK.G. White et. al., TUPSM027 BIW2010.
  19. Development of Electronics for the ATF2 Interaction Point Region Beam Position Monitor. Y. Kim et al., IPAC-2010-MOPE035, May 2010.
  20. A nanometer beam size monitor for ATF2. Taikan Suehara et al. 2010. Nucl.Instrum.Meth.A616:1-8, 2010.
  21. T. Shintake, Nucl. Instrum. Methods Phys. Res., Sect. A311, 453 (1992).
  22. Coupling Measurements in ATF2 Extraction Line. C.Rimbault, IPAC-2010-THPD080, May 2010. IPAC'10, Kyoto, May 2010.
  23. 4D Emittance Measurements Using Multiple Wire and Waist Scan Methods in the ATF Extraction Line. C. Rimbault, EPAC08-TUPC087, Jun 24, 2008. EPAC 08, Genoa, Italy, 23-27 Jun 2008.
  24. Multi Optical Transition Radiation System for ATF2. J.Alabau-Gonzalvoet. al., 2010-MOPE050, May 2010. IPAC'10, Kyoto, Japan, May 2010.
  25. Latest Beam Test Results from ATF2 with the Font ILC Prototype Intra-train Beam Feedback Systems. P. Burrows et al., IPAC-2010-WEPEB044, Kyoto, Japan, May 2010.
  26. Control system of the ATF. N. Terunuma et al. International Workshop on Controls for Small and Medium Scale Accelerators (IWCSMSA 96), Tsukuba, Japan, Nov 1996.
  27. Design of the Beam Delivery System for the International Linear Collider. A.Seryi et al. PAC07-WEOCAB01, Aug 2007. PAC 07, Albuquerque, New Mexico, 25-29 Jun 2007.
  28. H. Grote and F. C. Iselin (CERN Report No. SL-90-13-AP-REV.2, 1991).
  29. TURTLE (trace unlimited rays through lumped elements): A Computer program for simulating charged particle beam transport systems. David C. Carey, FERMILAB-NAL-064, Dec 1971.
  30. <http://www.mathworks.com/products/matlab/>
  31. Guide to LIBXSIF, a Library for Parsing the Extended Standard Input Format of Accelerated Beamlines. P. Tenenbaum, SLAC-TN-03-063, July 2003.
  32. Lucretia: A Matlab-Based Toolbox for the Modelling and Simulation of Single-Pass Electron Beam Transport Systems. P. Tenenbaum, PAC05, Knoxville, Tennessee,

- Knoxville, Tennessee, May 2005, pp 4197.*
33. K. Hirata (CERN Report No. 88-04, 1988), <http://accphysics.kek.jp/SAD/>.
  34. R. Tomas, “MAPCLASS: a code to optimize high order aberrations” CERN AB-Note-2006-017 (ABP), and “Nonlinear Optimization of Beam Lines”, Phys. Rev. ST Accel.Beams 9, 081001 (2006).
  35. D. Schulte (CERN Report No. PS-2000-028-AE, 2000),  
<https://savannah.cern.ch/projects/placet/> .
  36. <http://www.vista-control.com/vsystem.htm> .
  37. <http://www.aps.anl.gov/epics/> .
  38. A Flight Simulator for ATF2: A Mechanism for International Collaboration in the Writing and Deployment of Online Beam Dynamics Algorithms. Glen White et al., EPAC08-TUPP016 Genoa, Italy, Jun 2008.
  39. Beam-Based Alignment, Tuning and Beam Dynamics Studies for the ATF2 Extraction Line and Final Focus System. G. White et al., EPAC08-MOPP039, SLAC-PUB-13303, Jul 25, 2008.
  40. Simulation of beam size multiknobs correction at the Accelerator Test Facility 2 at KEK. ShaBai et al., Chinese Physics C 2011 Vol. 35 (4): 397-401.
  41. Model-Independent Analysis with BPM Correlation Matrices. J. Irwin et al., SLAC-PUB-7863, June 1998.
  42. Orbit reconstruction, correction, stabilization and monitoring in the ATF2 extraction line. Y. Renier et al. PAC09, Vancouver, Canada. July 2009.
  43. M. Sands (Report No. SLAC-AP-85, 1991); P. Bambade (Report No. SLAC-CN-367, 1988).
  44. First beam waist measurements in the final focus beam line at the KEK Accelerator Test Facility. ShaBai et al., PRSTAB 13, 092804 (2010)
  45. Study of Abnormal Vertical Emittance Growth in ATF Extraction Line. M. Alabau et al. EPAC08-MOPP003, EPAC08, Genoa, Italy, Jun 2008.
  46. What can we learn at ATF2 concerning ILC backgrounds? H. Guler, M. Verderi. Jul 2010. e-Print: arXiv:1007.3671 [physics.ins-det]
  47. Long ion chamber systems for the SLC. J. Rolfe et al. Proceedings of the 1989 Particle Accelerator Conference, Chicago, March 1989.

## 4.2 Measurement of Nanometer Scale Beam Size by Shintake Monitor (IPBSM)

Jacqueline Yan<sup>a</sup>, Masahiro Oroku<sup>a</sup>, Youhei Yamaguchi<sup>a</sup>, Takashi Yamanaka<sup>a</sup>, Yoshio Kamiya<sup>b</sup>, Taikan Suehara<sup>b</sup>, Sachio Komamiya<sup>a</sup>, Toshiyuki Okugi<sup>c</sup>, Nobuhiro Terunuma<sup>c</sup>, Toshiaki Tauchi<sup>d</sup>, Sakae Araki<sup>c</sup>, Junji Urakawa<sup>d</sup>  
 Mail to: [jackie@icepp.s.u-tokyo.ac.jp](mailto:jackie@icepp.s.u-tokyo.ac.jp)

<sup>a</sup>Department of Physics, University of Tokyo, 7-3-1, Bunkyo District,  
 Tokyo, 113-0033, Japan

<sup>b</sup>ICEPP, University of Tokyo

<sup>c</sup>Accelerator Laboratory, KEK, 1-1 Oho, Tsukuba, Ibaraki 305-0801, Japan

<sup>d</sup>Institute of Particle and Nuclear Studies, KEK

### *Abstract:*

The Shintake Monitor (IPBSM) has been developed at ATF2, a final focus test facility for ILC, to measure nanometer scale beam sizes. It plays a crucial role as a beam tuning device in achieving and verifying ATF2's 37nm design vertical beam size



at its virtual interaction point (IP). A laser interference fringe is formed as a scattering target with the electron beam. The resulting signal photons are detected and separated from background (BG) in a downstream detector. Modulation depth of the signal is measured, from which beam size is calculated. The monitor is capable of measuring beam sizes in the range of 25 nm – 6 μm, with resolution better than 10%. A vertical beam size of 310 nm has been measured. This section of the paper describes Shintake Monitor's purpose, design, measurement scheme, expected performance, status, and further goals.

## 4.2.1 Introduction

### 4.2.1.1 *Shintake Monitor's Role at ATF2*

The ILC (International Linear Collider) holds great potential for the detection and detailed study of new physics beyond the Standard Model. Collision of electrons and positrons, elementary particles without inner structures, enables clean and precise observations of the most fundamental processes, in which sense surpasses the LHC (Large Hadron Collider), where separation of signal from backgrounds due to complex proton – proton collisions is a challenge. However, a linear collider, while relieved from synchrotron radiation loss, has only one chance for collision, thus accumulation of statistics poses stringent requirements on power and luminosity.

$$\text{Luminosity is expressed as : } L = \frac{n_b N^2 f_{rep}}{4\pi\sigma_x\sigma_y} H_D \dots\dots\dots(1-1)$$

$n_b$  : No. of bunches,  $N$  : particles/bunch,  $f_{rep}$  : repetition rate,  $H_D$  : disruption parameter

Assuming Gaussian beam distribution, the denominator represents beam cross section. Apparently beam focusing is essential for realization of ILC.

The design beam size at the ILC interaction point ("IP") is 640 nm in the horizontal (x) and 5.7 nm in the vertical (y) direction<sup>1</sup> [1]. Constructed downstream of ATF (Accelerator Test Facility) is ATF2, a final focus test facility to realize nm focusing of the ultra low emittance ATF beam, as well as demonstrate Local Chromaticity Correction. ATF's beam energy is 1.3 GeV, as opposed to ILC's 500GeV. Thus design IP beam size is scaled down accordingly at ATF2 to 37 nm in vertical and 2.8 μm in horizontal.

ATF2's goals are: (1) to achieve 37 nm y beam size by applying the Local Chromaticity Correction. (2) beam position stabilization of 2 nm precision with an ILC-like beam<sup>3</sup>. Shintake Monitor, installed at the virtual IP<sup>2</sup> of ATF2, is designed for goal (1), the crucial task of measuring ATF2's nanometer scale beam sizes<sup>4</sup>. It is the only system at present capable of measuring a beam size as small as 37 nm, surpassing traditional systems such as wire scanners and laserwire modes. Shintake Monitor's outcomes are crucial to ATF2, which in turn affect directly the likelihood of ILC being realized.

#### 4.2.2 Measurement Scheme of Shintake Monitor

Fig. 1 and Fig. 2 show Shintake Monitor's overall structure. [1,5] The laser introduced to IP in pulses (synchronized with electron beam pulses) is split into two paths by a half mirror. The two paths are intersected by optics to create a interference fringe. Compton scattering take place as the electron beam traverses the fringe perpendicularly at IP. The released photons are detected in a downstream gamma detector.

What is actually measured as the standing wave fringe's phase is scanned across the beam is the variation in number of scattered photons, or the modulation depth ("M"). The modulation spectrum is indeed a plot of Compton signal strengths at different fringe phases for different beam bunches. Each point on the plot stands for the signal intensity in a particular bunch. Also reflected are measurement errors such as fluctuation of laser power, phase and BG levels. To maintain high modulation quality and thus good beam size measurement resolution, we must suppress these errors. This will be discussed in further detail later on.

M is large for well focused beams, and small for dispersed beams (see Figure 3 [3]).

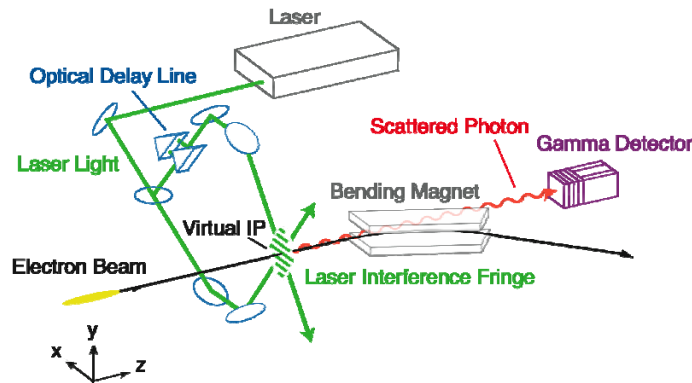


Figure 1: Schematic layout of Shintake monitor.

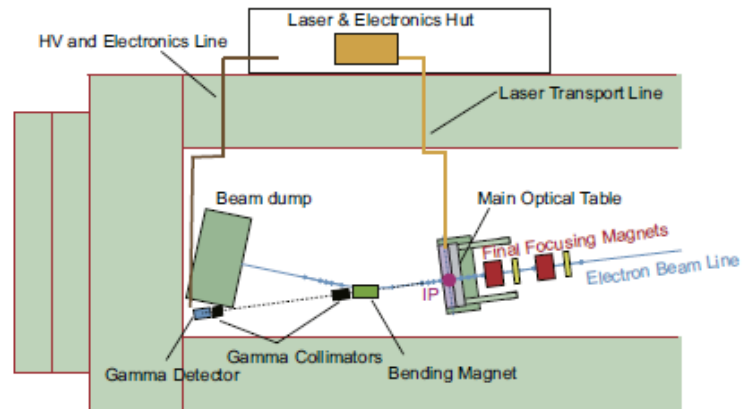
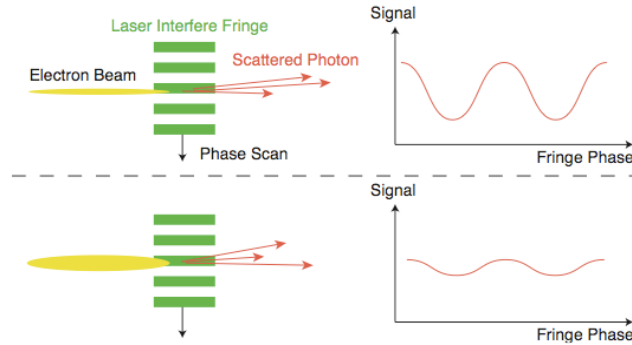


Figure 2: Amore realistic view of the IP area. (Note: not to scale)



**Figure 3:** Relationship between beam size and modulation.

Fringe phase is opposite for magnetic and electric field, thus the modulation peak correspond to where the two are perpendicular to each other. However if we choose the magnetic field direction as perpendicular to the beam direction, cross section would depend solely on the magnetic field for relativistic energy beams [1].

Averaging over time the magnetic field strength gives:

$$B_x^2 + B_y^2 = B^2 (1 + \cos 2\phi \cos 2k_y y) \quad (2-1)$$

Here, x and y are horizontal and vertical directions perpendicular to the beam.  $\phi$  is half laser crossing angle  $\theta$ .  $k_y = k \sin \phi$  is wave number component normal to the fringe.

Assuming Gaussian beam distribution,  $N$ , the number of Compton signal photons, is related to the beam's center position  $y_0$ , and the vertical beam spread  $\sigma_y$  as

$$N \propto \int_{-\infty}^{\infty} \frac{1}{\sqrt{2\pi}\sigma_y} \exp\left(-\frac{(y-y_0)^2}{2\sigma_y^2}\right) (B_x^2 + B_y^2) dy \quad (2-2)$$

$$\Rightarrow N = \frac{N_0}{2} [1 + \cos(2k_y y_0) \cos(2\phi) \exp(-2(k_y \sigma_y)^2)]$$

$M$  is related to  $N_+$  and  $N_-$ , maximum and minimum, respectively, of signal intensity as:

$$M = \frac{N_+ - N_-}{N_+ + N_-} = |\cos(2\phi) \exp(-2(k_y \sigma_y)^2)| \quad (2-3)$$

$$N_+ = \frac{N_0}{2} [1 + \cos(2\phi) \exp(-2(k_y \sigma_y)^2)] \quad N_- = \frac{N_0}{2} [1 - \cos(2\phi) \exp(-2(k_y \sigma_y)^2)]$$

The actually measured  $M = \text{amplitude} / \text{average}$ . is obtained by fitting signal variation with a cosine curve. From eq. (2-3),  $\sigma_y^*$  is related to  $M$  and  $d$ , laser fringe "pitch" as [2]

$$\sigma_y = \frac{d}{2\pi} \sqrt{2 \ln \left( \frac{|\cos(2\phi)|}{M} \right)} \dots \dots (2.4)$$

$$d = \frac{\pi}{k_y} = \frac{\lambda}{2 \sin(\phi)} \dots \dots (2.5) \quad (\lambda : \text{laser wave length} = 532 \text{ nm for ATF2})$$

**Table 1:** Accurately observable beam sizes vary with design values of fringe pitch, which is determined by laser wavelength and crossing angle (Eq (2-5)).

Crossing angle $\theta$	174 deg	30 deg	8 deg	2 deg
Fringe pitch $d$	266 nm	1.028 $\mu\text{m}$	3.81 $\mu\text{m}$	15.2 $\mu\text{m}$
Measurable $\sigma_y$	25 ~ 100 nm	100 ~ 360 nm	360 nm ~ 1.4 $\mu\text{m}$	1.4 ~ 6 $\mu\text{m}$

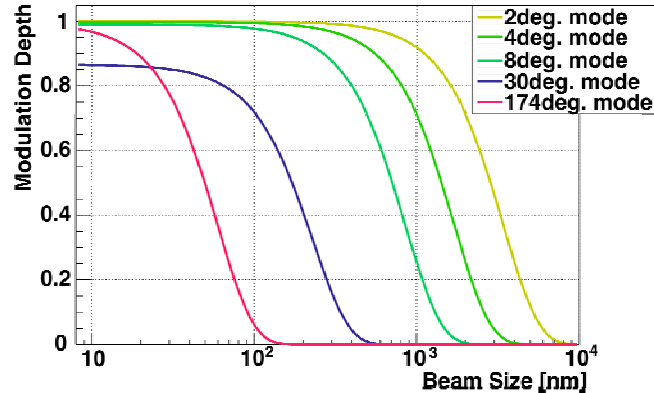


**Figure 4:** Relationship between  $M$  and beam size for each mode from plotting Eq. (2-3) [3-4].

#### ***Comparison with Shintake Monitor at FFTB:***

The Shintake Monitor, invented by Dr T. Shintake, was first used at FFTB (Final Focus Test Beam), at SLAC, where it succeeded in measuring a  $y$  beam size of 70 nm with 10% resolution, whereas the design size was 60 nm. Since then the University of Tokyo has upgraded it for usage at ATF2 to measure the even smaller beam sizes to be available there. Table 2 compares ATF2's parameters with those at FFTB [1,3].

The major upgrades points are the following:

- Laser wavelength has been shortened from 1064 nm to 532 nm (YAG 2nd harmonics) to accommodate smaller beam sizes down to 25 nm.
- Our monitor is capable of measuring a wider range of beam sizes than FFTB's, due to newly designed laser optics. Continuously adjustable modes (with mover stages) between 2 to 8 degrees, are added to enable measurement of  $y$  beam sizes as large as several  $\mu\text{m}$ s, which overlaps ranges and thus can be compared for consistency with traditional wire scanners. Also implemented was a laser wire scheme, which uses only one laser path, to measure the even larger  $x$  beam size.
- A phase control system was improvised in which the optical delay line functions with one prism fixed and another moved step by step on a piezo stage. In this way, the laser fringe is being scanned, instead of the beam (as at FFTB), eliminating beam instability factors and contributing to higher measurement accuracy.
- The gamma detector has been newly designed. It is calorimeter-type made of CsI(Tl) and separated into multi layers. It takes advantage of the difference in energy spectrum, and thus shower development to separate BG from Compton signal. This scheme alleviates BG energy fluctuation effects.

### 4.2.3 Layout and Structure

#### 4.2.3.1 Overall Structure

The Shintake Monitor system consists of a laser table located in a laser and electronics hut, linked to a main optical table, a gamma detector behind collimators, and control electronics. Laser is transported from the laser table via a transport line to the IP area, where it forms interference fringes upon the main optical table. The electron beam is focused at IP by final focusing magnets in order to collide precisely with the laser fringe. Then it is bent out of Compton photons' path by a bend dipole and disposed safely into a dump. On the other hand Compton photons proceed straight to the gamma detector through collimator apertures.

#### 4.2.3.2 Laser Table and Main Optical Table

High laser density at IP is needed to obtain enough Compton photons. We use a Q-switched pulsed laser with peak power 140 MW. Its 8 nsec (FWHM) pulse length is much longer than the electron bunch length of 17 psec. Laser output is triggered by an upstream kicker magnet signal.

Figure 5 shows layout of the laser table [3]. There, the 532 nm wavelength monochromatic laser is created by the source, and its properties are monitored and adjusted for transportation to the main optical table. An attenuator is inserted and ejected to switch between low power for laser path alignment, and high power for interference mode. An “expander”, made up of a pair of convex and concave lenses, magnifies the laser spot size two-folds prior to transportation to prevent dispersion throughout the 20 m transport line. Spot size will be restored after transportation and continuously adjustable by a “reducer” of a similar pair lens structure. Other optical components monitor laser timing, power, profile, and position, shot by shot.

**Table 2:** Electron beam and Shintake Monitor parameters: ATF2 vs FFTB.

	FFTB	ATF2
Beam energy	46.6 GeV	1.3 GeV
Repetition rate	30 Hz	1.56 Hz (3 Hz)
Electrons / bunch	$1 \times 10^{10}$	$0.5 \times 10^{10}$
Bunch length	3 ps	16 ps
Design beam size at IP	X : 900 nm Y: 60 nm	X: 2.8 $\mu$ m Y: 37 nm
Mode 1	174 deg	174 deg
Fringe pitch d	0.53 $\mu$ m	0.27 $\mu$ m
Measurable beam sizes	40 ~ 180 nm	25 ~ 100 nm
Mode 2	30 deg	30 deg
Fringe pitch d	2.1 $\mu$ m	1.028 $\mu$ m
Measurable beam sizes	160 ~ 720 nm	100 ~ 360 nm
Mode 3	6 deg (horizontal)	2 ~ 8 deg (continuous)
Fringe pitch d	10.2 $\mu$ m	3.81 ~ 15.2 $\mu$ m
Measurable beam sizes	760 nm ~ 3.4 $\mu$ m	360 nm ~ 6 $\mu$ m
Laser wire mode (single pass)	None	174 deg (horizontal) > 30 $\mu$ m

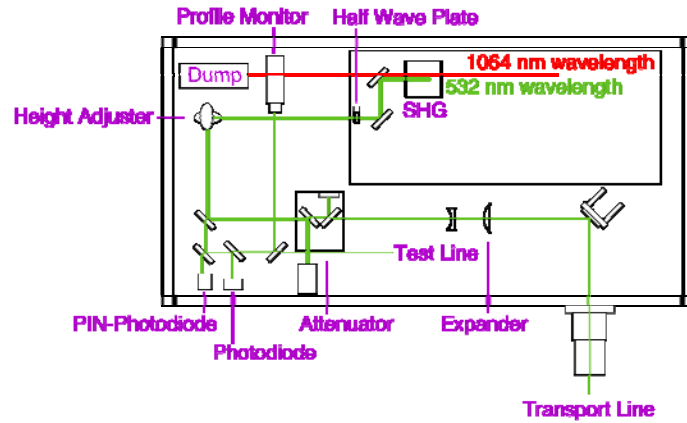


Figure 5: Layout of the laser table.



Figure 6: Main (or “vertical”) optical table at IP area.

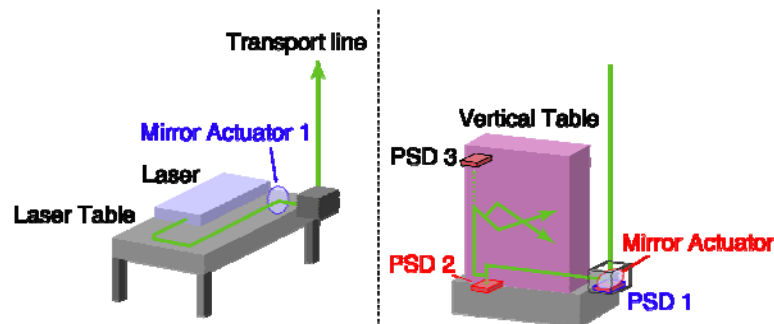


Figure 7: Link between laser table (laser hut) and vertical table (IP) [3].

The upright main optical (or “vertical”) table (Fig. 6) [3] is made of steel honeycomb and supported by a rigid frame which suppresses vibration relative to the electron beam. Its movements have been confirmed to be synchronized with ground motion.

The laser beam delivered via the transport line emerges from the bottom-right corner. After spot size is restored by the reducer, it passes through a 95% reflection

mirror. The reflected (95% energy) beam advances to a 50% beam splitter, which divides it into upper and lower paths to be intersected at IP. Actuator-attached mirrors placed in both paths produce the crossing angles for each mode, as well as stabilize laser beam position. These rotate by stages to enable mechanical switching among  $2^\circ$  to  $8^\circ$  (continuously),  $30^\circ$ , and  $174^\circ$ , depending the beam size targeted for a particular beam tuning stage. The laser wire mode for horizontal sizes is selected similarly. These laser beams are focused at IP by final focusing lenses to achieve high photon density.

The transmitted (5% energy) laser is admitted to a diagnostic section occupying the right side of the table. Here, phase monitors, position sensitive detector (PSD)s, photodiode (PD)s, and high response PIN-PDs oversee alignment, position feedback, and intensity jitter correction. Special PSDs and PDs are installed for enhanced stabilization when measuring the smallest sizes with 174 deg mode.

#### 4.2.3.3 *Gamma Detector*

Shintake Monitor's gamma detector is calorimeter-type made of multi-layered CsI(Tl). The forward 40 mm part, out of a total thickness of 330 mm, is divided into four 10 mm layers. This is followed by a 290 mm thickness bulk divided into three sections in the width direction. Two to four PMTs (12 in total) are attached to each layer. It distinguishes between signal and BG by taking advantage of their difference in energy spectrum, i.e. shower development. Average energy is 14.7 MeV for signal and 53.0 GeV for BG. Collimators are installed in post-IP beam line sections to cut BG.

#### 4.2.4 **Shintake Monitor and Beam Tuning**

Beam size at IP is determined by combined effects of betatron oscillation and momentum spread. Beam tuning is carried out to satisfy requirements on beam size and stability. Precise adjustments are made for beam position (trajectory) and intensity, as well as for electromagnet strength, especially the "final doublet", located 1 m upstream of IP. Below explains procedures for applying Shintake Monitor as a beam tuning tool.

- (1) Laser must be constantly kept under precise alignment and feedback system in order to achieve high quality interference fringe scan. However with an oversized beam hinders signal modulation, and we would be conducting "blind" alignment. Thus for best beam time efficiency,  $\sigma_y^*$  must first be tuned below  $4.5 \mu\text{m}$  [3] (confirmable by wire scanners) before commencing usage of our monitor.
- (2) Beam tuning involves adjusting magnets' current and their movers' positions, causing shifts in trajectory or emittance. Energy deposit in the detector will change if gamma rays strike the collimator apertures. The same applies to BG energy deposit if its source changes. These reduce our multilayered detector's resolution, which depends on signal – BG energy spectrum separation. First of all, we conduct "collimator scan", to confirm that the beam is deviated far from the center of a  $10 \text{ mm}\varnothing$  collimator' inserted especially for this scan. Then, the reference shower expansion applied as the detector 's fitting function is checked every time the actual shower changes. Inconsistency between reference shower and the actual shower expansion would cause signal evaluation errors<sup>6</sup>.
- (3) Laser Q-switch timing is adjusted to beam timing with precise digital modules.
- (4) Laser position alignment: First laser path(s) are overlapped at low power with the

beam on a 10  $\mu\text{m}$  precision screen monitor installed at IP. Then comes the “laserwire scan”, in which laser position is scanned using mirror actuators at high power in the transverse direction to locate the Compton signal peak. Additional lens and fringe angle adjustment is necessary for the sensitive 174 deg mode.

- (5) Interference fringe wouldn't form if the two laser paths are offset in the beam direction, even if laser – beam collision occurs. Thus longitudinal alignment is conducted through “interference scan”. A single path is scanned longitudinally to locate the position that renders the sharpest fringe and deepest modulation.

Having completed all alignments and preparations, we are ready to measure beam sizes with interference mode and the results are fed back to the beam tuning process.

## 4.2.5 Performance

### 4.2.5.1 Expectations

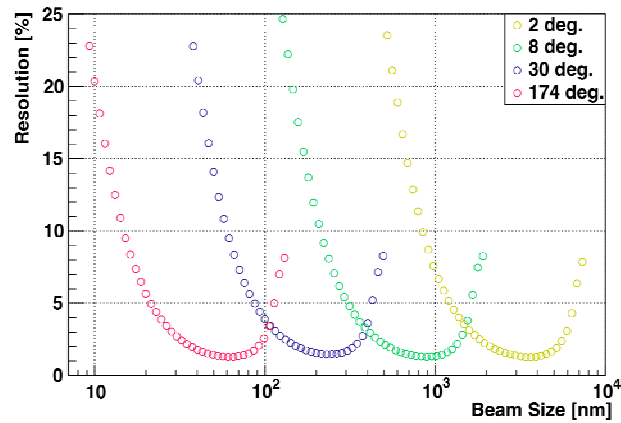


**Figure 8:**  $\sigma_y^*$  measurement resolution for each crossing angle mode [3, 4].

Shintake Monitor is capable of 25 nm - 6  $\mu\text{m}$  measurement in 90 bunches with better than 10% resolution (see Fig. 8). This comes from simulation under conditions of  $S/N = 3.5$  and 50 % bunch-by-bunch BG fluctuation. Harsh BG conditions were selected when simulating measurement of 37 nm design beam size. The expected accuracy is [3]

$$37 \pm 2 \text{ (stat.)}_{-0}^{+4} \text{ (sys.) nm}$$

Although the detector functions very near design expectations, it is not void of errors related to the actually measured  $M_{\text{meas}}$ , which are conveyed directly to beam size accuracy. These are divided into statistical errors, due to inadequate detector resolution in signal/BG separation, beam current jitter, and laser power jitter, and systematic errors, which degrade fringe contrast and reduce modulation depth.

### 4.2.5.2 Statistical Errors

Statistical errors relate to signal strength, and consequently become the error bars when fitting each gamma signal point upon the modulation curve. Statistical errors have



been alleviated from 12% to 10% for 90 bunch measurements of beam sizes of 25 nm - 6  $\mu$ m, owing to efforts to raise laser intensity and S/N. However more stringent S/N is to be encountered as beam sizes decrease, since defocusing by QF1 of the final doublet becomes abrupt, increasing background due to collision between beam pipe and beam halo. Also, with a smaller beam size beam position jitter, and thus error from relative beam-fringe position jitter takes on heavier effects. This section describes various causes of statistical errors.

**Detector Resolution:** Inconsistency between reality and the reference shower applied to our detector (see 3.4) lead to signal evaluation errors. This is especially a concern under high BG conditions. A few causes are suspected. Gain or PMT output of each calorimeter layer may have changed over time. Gain monitors are used to investigate this effect. Beam trajectory shifts cause intensity fluctuation of major BG sources, as well as collision of gamma signal against collimators, which alters energy spectrum. Number of BG photons hitting collimators should not vary greatly provided no significant change in angular distribution. Thus both signal and BG reference showers should remain consistent as long as signal is made to fit within collimator apertures. This is achievable 99% of the time by beam orbit adjustments. We frequently check the reference shower, which takes merely a few minutes, especially after beam trajectory shift. If BG energy alters in a way to approach signal energy, detector resolution will worsen even with accurate reference shower. However this is quite rare.

**Relative position jitter:** Interference fringe phase jitter causes laser intensity felt by the beam to vary shot-by-shot. This jitters the number of Compton photons. The same goes for beam position jitter, since interference fringe phase is scanned relative to the beam. These also cause systematic errors by reducing modulation.

Signal jitter due to relative position jitter is small when the beam collide with the fringe's peak or valley, and large when it collide elsewhere in between these regions. The jitter size takes on a periodic function comparable with that of the fringe phase.

**Laser timing instabilities:** Interaction between beam and laser can be interpreted as collision of beam in 16 ps pulses against the much longer 8 ns pulsed laser. Thus a few ns change in laser timing will cause fluctuation in number of Compton photons. Laser timing, monitored by high response PIN-PDs and beam timing taken from an upstream timing BPM are matched by inputting them into a TDC.

**Laser power instabilities:** Laser power is monitored by PDs on the vertical table. Signal jitter from laser power fluctuation (relative to intensity) is evaluated to be 0.86%.

**ICT monitor Resolution:** The amount of gamma signal, which produces the modulation depth, should be proportional to the number of electrons in a single bunch. In order to cancel effects from beam current jitter, signal energy is normalized by the beam charge (current), measurable by the "ICT monitor". This can suppress errors from beam current jitter down to the ICT monitor's resolution, which is constant regardless of current. Resolution could be degraded by amplifier noise, or by noise from nearby high voltage devices, i.e. kicker magnets. ICT monitor resolution was evaluated to be 2-5 - 5%, and the "ICT-corrected" signal fluctuation was evaluated to be  $\Delta S_{CT} = 2.5\%$ .

#### 4.2.5.3 Systematic Errors

Systematic errors cause reduction of modulation depth. 6 % of modulation reduction corresponds to 2.9 nm error for 37 nm beam size. The measured modulation  $M_{meas}$  can be written as

$$M_{meas} = C_{\alpha}C_{\beta}.....M_{ideal} \quad (5-1)$$

Each modulation reduction factor  $C_i$ , ( $< 1$ ),  $i = \alpha, \beta, \dots$ , represent the error source. A part of these independent sources degrade the interference fringe's contrast [5, 6].

$$\begin{aligned} \left| \overline{B_x + B_y} \right|_{meas}^2 &= B^2 \left( 1 + \left( \prod_i C_i \right) \cos \theta \cos(2k_y y + \alpha) \right) \quad \dots\dots(5-2) \\ &= B^2 \left( 1 + \frac{M_{meas}}{M_{ideal}} \cos \theta \cos(2k_y y + \alpha) \right) \end{aligned}$$

Comparing Eq (5-2) with the ideal case Eq (3-1), and the  $\sigma_y^*$  from Eqs (3-2) ~ (3-4), one can see that when  $M_{meas} < M_{ideal}$ , bias factors cause “systematic” over-evaluation.

Some systematic errors arise from the laser optics, such as laser path misalignment, difference in polarization and intensity between the two paths, degraded spatial and temporal coherence, tilt and spherical effects of the fringe. Others come from the beam's condition, such as beam position jitter. Because most systematic errors are independent from beam size,  $C_i$  is a suitable estimation of bias effects.  $C_i$  has been evaluated for ATF2's Shintake Monitor for a variety of error sources. However we can only obtain the lower limits for most of these. Below describes a few in details [3].

**Laser position misalignment:** Realistically, the laser profile possesses a finite Gaussian spread. If differences in profile or spot size between the two paths are comparable in scale to the beam size, fringe contrast will be degraded, causing systematic beam size evaluation. These can arise from misalignment of focusing lenses or from laser beam emerging unparallel (or dispersed) from the reducer. These can be resolved by adjusting the reducer and lens set-up.

Misalignment also causes laser position to deviates from that of the electron beam. These produce uneven interference fringes, and the beam traversing it will “see” different intensities at different locations, thus degrading contrast.

Mirror actuators with better than 50 nm precision are used to suppress systematic errors due to laser misalignment. However we must repeatedly realign during beam tuning when beam position shifts significantly, or under turbulent beam conditions. The electron beam passage point is aligned with the laser intersection to within 1/2 of laser spot size for rough tuning, and 1/10 of laser spot size for finer tuning. Taking the latter, reduction factor due to laser misalignment is evaluated in the beam direction as  $C_{z,pos} > 99.5\%$ , and in the transverse plane as  $C_{t,pos} = 100\%$ .

**Relative position jitter between beam and laser fringe:** Jitter in laser fringe phase or beam position smear the cosine-like modulation curve, reduce amplitude, and cause beam sizes to be “seen” larger than actual. Laser phase jitter arise from slight optical components vibrations, and alters optical paths. Beam position jitter come from magnet vibrations, or unstable extraction from the damping ring. Beam position is

measured by beam position monitors (BPMs). Feedback correction using BPM data can suppress errors due to beam position jitter down to 0.5% ( $\sim$  BPM resolution).

**Offset between beam and laser fringe axis:** If the plane upon which interference fringe forms is not exactly perpendicular to the beam direction, beam size will be measured larger than actual. This “tilt” effect occurs in both transverse and longitudinal directions. As systematic errors are independent from beam size, the 174 deg mode, which measures the smallest sizes, receives the heaviest effect.

Even if the beam passes straight as a whole, individual particles within a single bunch possess approximately 0.4 mrad angular spread in longitudinal direction for 37 nm measurement. This causes approximately 99.6% of modulation depth reduction, corresponding to 2 nm beam size over-evaluation.

**Spherical wavefront effects:** The laser waist is spherically in shape. Curvature is infinite at the focal point, where planary wave approximations are valid. However the focal point is off from IP, or from crossing point of the two laser beams, we can no longer ignore spherical effects that cause the beam to feel “distorted” fringes. Design values  $\sigma_x=2.2\mu\text{m}$ , Raleigh length  $z_R=1.2\text{mm}$  are used to evaluate this effect in terms of the heaviest affected 174 deg mode. which results at  $C_{\text{spherical}} > 99.7\%$ .

**Change of beam size within fringe:** The beam waist is tuned to land upon IP. However the laser fringe’s finite spread in the z direction is unavoidable, and interaction occurring where beam isn’t exactly at its waist produce errors accordingly. Beam size fluctuates in vicinity of IP by an amount depending on emittance and the beta function at IP. Modulation reduction factor here is evaluated as  $C_{\text{growth}} > 99.7\%$ .

**Table 3:** (upper limits of) modulation reduction factors  $C_i$  for each systematic error type for [1] design size 37 nm with 174 deg mode, and [2] 300 nm size with 8 deg mode. While some errors, such as spherical wavefronts, affect only the sensitive 174 deg mode, others, such as power and phase jitter seriously degrade modulation, regardless of beam size.

Modulation reduction factor	300 nm at 8 deg	37 nm at 174 deg
Total power	$97.8 \pm 1.8 \%$	$99.8 \pm 0.1\%$
Alignment (z: longitudinal)	$> 99.1\%$	$> 99.1\%$
Alignment (t: transverse)	$> 99.6\%$	$> 99.6\%$
Spatial coherence	$> 99.9\%$	$> 99.9\%$
Fringe phase / beam position jitter	$> 98.0\%$	$> 98.0\%$
Fringe tilt (longitudinal)	$> 98.2\%$	[99.3% : 99.6%]
Fringe tilt (transverse)	$> 99.9\%$	$> 99.9\%$
Spherical wavefronts	100%	$> 99.7\%$
Beam size growth within fringe	100%	99.7%
Total : $\prod_i C_i$	$> 91.1\%$	[95.1% : 95.4%]

## 4.2.6 Status

### 4.2.6.1 Previous Run

Due to tentative tuning issues, a special “10 x beta“ beam condition had been implemented during the continuous run of spring, 2010. The vertical beta function at IP was increased to 1 mm, 10 times of the nominal value. This resulted in an exceptionally low BG averaging at 15 GeV. Signal was much higher, thus S/N exceeded 10. The theoretical size under this optics was 100 nm.

Usage of Shintake Monitor commenced after beam size cleared 1 $\mu$ m. As beam tuning proceeded, operation mode was changed from 2 deg to 4 deg, then finally to 8 deg. Accuracy in beam size measurement, as well as consistency between various modes were confirmed at each point. Fig.9 (below) shows the smallest beam size measured by Shintake Monitor for this run, in May, 2010 at 7.96 deg mode [5, 6].

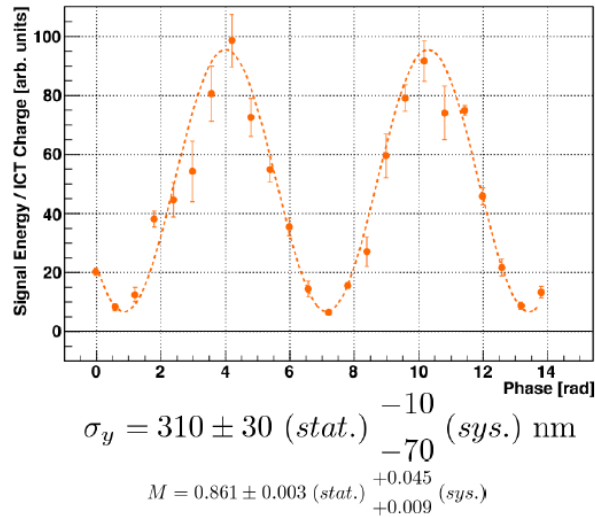


**Figure 9:** Results for  $\sigma_y^*$  and modulation are:

$$\sigma_y = 310 \pm 30 \text{ (stat.)} \begin{matrix} -10 \\ -70 \end{matrix} \text{ (sys.) nm} \quad M = 0.861 \pm 0.003 \text{ (stat.)} \begin{matrix} +0.045 \\ +0.009 \end{matrix} \text{ (sys.)}$$

Statistical error is from deviation calculated for repeated measurements under consistent conditions. Systematic error is evaluated by contrast degradation.

### 4.2.6.2 Most Recent Run (2010 Autumn - 2011 Spring)

For the most recent run period, optics has been returned to nominal, with IP beta at 0.1 mm. As expected, BG levels rose significantly from May, 2010, typically ranging from 40 GeV to as high as over 100 GeV. Shintake Monitor was proven in May's run to fulfill expectations provided BG is low. However with high BG, its accuracy decreases for regions of slight signal variation, which makes low S/N a major concern.

The smallest beam sizes measured by Shintake Monitor during this run were at 280  $\pm$  90 nm (stat. errors only) at 5.96 deg. Figure 10 shows one such example.

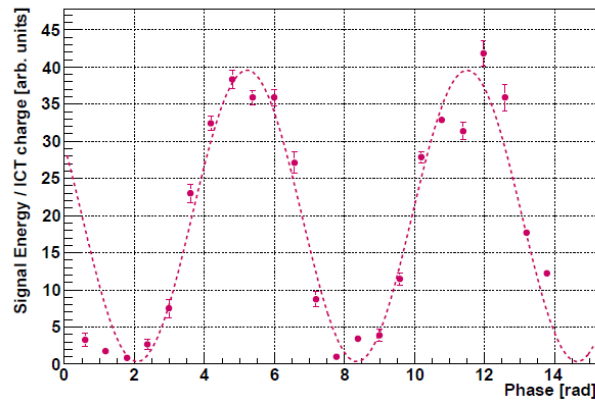


**Figure 10:** Interference scan plot for one of the smallest beam sizes measured on Dec 16, 2010,  $\sigma_y^* = 280 \pm 90$  nm

After this we switched on to 30 deg in pursuit of smaller sizes, but encountered difficulties. Signal peak was low, and S/N was only 1/5 to 1/2. We observed signal jitters, which reduce precision. These arise from fluctuation in trajectory and BG levels, as well as unstable laser beam position. BG studies are undergoing to improve S/N. The laser itself is also under investigation whether or not its quality deteriorated over time.

We are currently under commissioning of 30 deg mode and 174 deg mode.

## 4.2.7 Future Goals

### 4.2.7.1 Remaining of Current Run Period

As a vital beam tuning and R&D tool, Shintake Monitor is on its way to measure the 37 nm vertical beam size. This demands favorable experiment conditions for both beam (BG levels, trajectory, current) and laser system. Laser path stability must be controlled over long time periods with a feedback system consisting of PSDs and mirror actuators.

Since Shintake Monitor was first upgraded at ATF2, we have focused on developing hardware, detector resolution simulations, and evaluation of systematic and statistical errors. At present we are confident of its abilities to meet standards in measuring beam sizes above 300 nm. To further suppress systematic errors below 10% for 37 nm measurement, the following hardware improvements are being carried out.

**IP-BPM:** A high precision BPM expected to have approximately 8 nm resolution has been installed at IP, It is currently under alignment and electronics commissioning, after which its contribution to beam position jitter correction is highly anticipated.

**Focal point scanner:** A focal point scanner consisting of lens positioned upon a moving stage was installed at IP to prevent spherical wave front bias in the case of beam offset from laser focus point. We are expecting to align focal point of the final focusing lenses with IP within 100  $\mu\text{m}$  precision during 174 deg mode.

**Tilt monitor:** A profile monitor downstream from IP observes the laser with PSDs and a CCD camera in order to evaluate systematic effects of fringe tilt relative to the beam axis. Specially arranged PSDs are responsible for the 174 deg mode.

**Background studies:** An ultra-focused 37 nm beam receives abrupt defocusing from QF1, and even the slightest trajectory shift will sharply increase BG. Low S/N worsens detector resolution and casts measurement limits. BG level was confirmed to be within detector tolerance under nominal optics of Dec, 2010. However S/N (often < 0.5) was an obstacle to commissioning of higher modes. Through collaboration with ATF2's beam tuning team, we conducted studies aimed at investigating possible new BG sources. Intermediate collimators were added to further suppress BG.

**Laser position stabilization enhancement:** To stabilize laser position at IP, a mirror actuator followed by a PSD have been newly installed in a box at the transport line exit. Another actuator in a downstream laser table section contributes to remote control of laser path during beam time. As the laser system is keen to temperature fluctuation, temperature monitoring of laser hut and cooling water have been reinforced.

#### ***4.2.7.2 Consequences of the Great Eastern Japan Earthquake***

The first draft of this IPBSM section had actually been completed on March 10, 2011, just one day before an immense earthquake of magnitude 9.0 shook eastern Japan on March 11, 2011. Up until that point, we had set clear goals to complete commissioning of the remaining 30 deg and 174 deg modes, and anticipated reaching vicinity of the 37 nm goal by spring of 2011.

However, ATF, along with rest of KEK, suffered damage from the earthquake, which takes time to assess and repair. Furthermore the serious long term electricity deficit accompanying this natural disaster will prolong interruption, exactly how long no one can be certain about at the present. As we eagerly await operations to resume, we are devising ideas for improving the laser optics, and working on more accurate analysis of past data. These are positive steps to take during this interval, and will contribute to speedier achievement of a reliable 37nm beam once ATF operation resumes.

#### ***4.2.7.3 Prospects for Application at ILC***

Basic capability for Shintake Monitor's utilization at the real ILC a beam tuning device should be confirmed following the success of measuring ATF2's 37nm beam size. However, several issues must first be resolved:

- (1) Reinforced shielding against the harsher radiation from ILC's high beam energy.
- (2) A nanometer beam size monitor is essential for commissioning of the ILC beamline. However space is limited at ILC's IP owing to collision detectors. One possibility is that Shintake Monitor could be upgraded for primary ILC beamline commissioning, then be replaced by "pair monitors" [3] when e+ e- collision actually commences.
- (3) Since ILC operates at a much higher energy, total scattering cross section will be reduced to as low as 1/3 of ATF's (assuming 250 GeV for ILC and 1.3 GeV for ATF). This will further decrease as a shorter laser wavelength is used. A high

intensity laser is required to overcome this obstacle and maintain adequate number of Compton photons,

- (4) A shorter laser wavelength is required for the smaller fringe pitches to measure ILC's 5.8 nm vertical beam sizes. An intense UV laser is the most likely candidate. For example, ArF excimer lasers of wavelength 193 nm and F2 excimer lasers of wavelength 157 nm yield M of 0.93 and 0.89, respectively [3]. They possess excellent BPMs and are capable of nearly 100% fringe contrast. However they must be kept stable even when spot sizes are focused below the vertical IP beta function.
- (5) ILC's signal photon energy will approach that of the beam's, which is beneficial from S/N's standpoint. However this also means that signal will approach BG in energy, erasing the advantage of the current detector's multilayer scheme. Thus a new detector needs to be designed for the Shintake Monitor at ILC.

Although ATF2 is a scaled down version, its outcomes and results are directly applicable to ILC. In any case, Shintake Monitor's soon to come success in measuring ATF2's 37 nm beam size, and its evaluation of phenomena pertaining to ultra-small beam sizes, will be very valuable towards designing, realizing, and developing ILC.

#### 4.2.8 Footnotes

- <sup>1</sup> The two dimensions are quite different in beam size requirements due to the reason that a "flat" beam prevents beam – beam effects during acceleration.
- <sup>2</sup> It is actually only a virtual IP, with an electron beam travelling in one direction.
- <sup>3</sup> These two goals are planned to achieve separately, because we need alternative monitors at the interaction point (IP).
- <sup>4</sup> IP-BPM meant for (2) is also contributes to (1) by correcting beam position jitter.
- <sup>5</sup> Evaluated using data from May 2010. Beam current was at  $1 \times 10^9$  e-/ bunch,
- <sup>6</sup> In the "shot-by-shot" method, BG shower is taken with the laser off, while signal shower is derived by subtracting BG events from data taken with the laser on.

#### 4.2.9 References

1. T. Suehara, et al: "A nanometer beam size monitor for ATF2" in Nuclear Instruments and Methods in Physics Research A 616 (2010) 1–8
2. M. Oroku, master thesis, Graduate School of Science, University of Tokyo (2009).
3. Y. Yamaguchi, master thesis, Graduate School of Science, University of Tokyo (2010).
4. M.Oroku, J.Yan, Y.Yamaguchi et al:" IP-BSM Status and Plan", "IP-BSM Operation", 11th ATF2 Project Meeting . (Jan. 13-14, 2011) SLAC
5. M.Oroku et al: "The Nanometer Beam Size Monitor (Shintake Monitor) at ATF2" IEEE Proceeding (2010)
6. M.Oroku et al: "Measurement of Nanometer Scale Bam Size by the Shintake Monitor" : International Conference on Physics in Intense Fields (PIF 2010), KEK, Japan, Proceedings and poster session (2010)

### 4.3 The Multi Optical Transition Radiation System

A. Faus-Golfe, J. Alabau Gonzalvo and C. Blanch Gutierrez  
 Instituto de Fisica Corpuscular (CSIC-UV) Spain

D. McCormick, J. Cruz, M. Woodley and G. White, SLAC, USA

Mail to: [Angeles.Faus-Golfe@uv.es](mailto:Angeles.Faus-Golfe@uv.es)

#### 4.3.1 Introduction

The determination and monitoring of the transverse phase space in ATF2 is crucial in order to meet their performances specifications. Since the beam sizes at the Interaction Point (IP) depend strongly on the aberrations in the Final Focus System (FFS), accurate measurement upstream of the FFS is required to tune the beam sizes at the IP. The beam sizes as well as the emittance are measured in several locations in the beam diagnostic section of the Extraction Line (EXT line) of ATF2. The vertical beam sizes in the diagnostic section are of the order of 10  $\mu\text{m}$  this means that the devices have to image spot sizes as small as 5  $\mu\text{m}$ , with 10% accuracy a 2  $\mu\text{m}$  resolution device is necessary. The ATF2 EXT line is a beam line with low power and low repetition rate that make usable devices using solid targets.

In contrast to a ring machine, where an individual bunch can be measured many times as it passes around the ring, the beam size and the emittance measurement in the LC or in the beam lines have to be performed in a single pass. This requires that the wire scan device types (laser or solid) sample across successive bunches within a train, often with an over-estimation of the beam size due to beam position and intensity jitter, and can take up to half a minute to complete the measurement. Although some of these effects could be corrected, as the jitter effect could be subtracted by using the nearby BPMs signals, this can be avoided by using Optical Transition Radiation (OTR) Monitors. These monitors are based on the transition radiation effect, a light cone emitted when the charged particle crosses a metallic interface. This light is emitted in a specular fashion so it can be focused on to a CCD and produces an image of the beam. OTRs are able to take many fast measurements and therefore to measure the emittance with high statistics, giving a low error and a good understanding of the emittance jitter.

In this article, simulations of the expected beam sizes and emittance, along with a technical description of the system, its hardware and software implementation are described. Additionally first measurement of the beam size and emittance of the Multi Optical Transition Radiation System located in the Extraction Line of ATF2 are presented.

#### 4.3.2 The Beam Diagnostic Section of the ATF2 Extraction Line: Optics Studies and Beam Spot Size Simulations

The transport beam line from the Damping Ring (DR) to the FFS of ATF2 is called the EXT line [1]. The ATF2 EXT line is divided in three regions as shown in Figure 1: the first section or extraction part shared with the DR, the matching section and the diagnostic section. Instrumentation equipment such as: Button Beam Position Monitors



(BPM), Strip-line BPMs, Beam Current Monitors (BCM) and filament Wire Scanners (WS) from ATF are re-used in the new ATF2 EXT line. Furthermore four OTRs (labelled as OTR0, OTR1, OTR2 and OTR3) have been installed close to the five WS (labelled as MW0X, MW1X, MW2X, MW3X and MW4X). These four OTRs are known as the multi-OTR system.

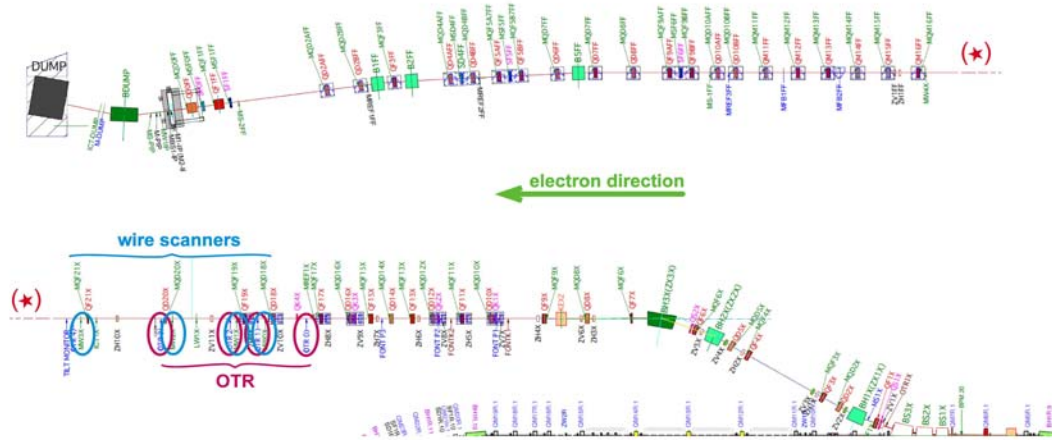


**Figure 1:** Layout of ATF2 EXT line.

The measurement of beam sizes and emittances of the extracted beam from the DR is made by means of the WSs and the multi-OTR system. Moreover, the proximity to the WS will be a definitive test of the OTR as a beam diagnostic device.

Optics studies and tracking simulations with MAD8 program [5] have been made. The beam spots calculated from the optics are big enough not to damage the target and they are comparable to these on the WS. Comparisons with the WS beam spot sizes are found in Table 1. The beam spots from tracking simulations are shown in figure 2. The input beam for the MAD8 simulations was 50000 particles with Gaussian distribution in  $x$ ,  $y$  and energy, and with energy spread of  $8.00 \times 10^{-4}$ .

**Table 1:** Beam size comparison in OTR and WS locations.

Label	Unit	OTR		WS	
		$\sigma_x$	$\sigma_y$	$\sigma_x$	$\sigma_y$
0	$\mu\text{m}$	118	9	82	11
1	$\mu\text{m}$	148	8	157	7
2	$\mu\text{m}$	92	12	88	13
3	$\mu\text{m}$	144	7	151	6

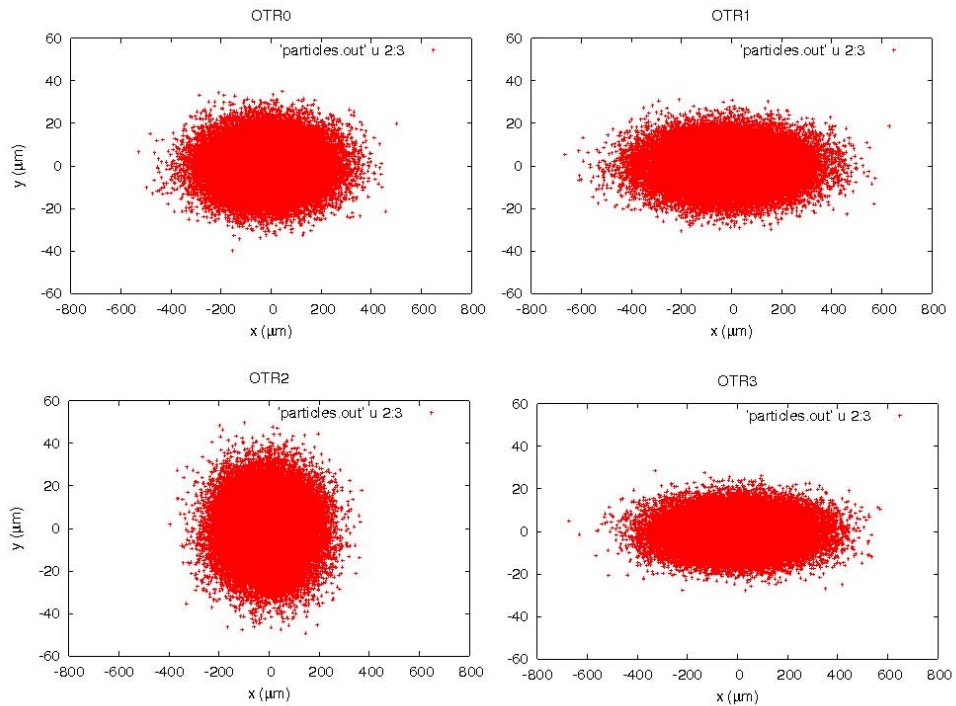


**Figure 2:** Tracking spotsizes at the OTR locations.

Furthermore tracking simulations have been made comparing the sizes in the OTR locations obtained with the codes MAD8 and LUCRETIA [6] and the simulation of the CCD image obtained using LUCRETIA obtaining in all the cases similar results.

### 4.3.3 Technical Description: Optical and Mechanical Design

The design of the new OTRs is based on the OTR1X, which was previously installed in the ATF EXT line, but it has several modifications. Its original purpose was to demonstrate that this device could measure the small beam sizes that would be found after a linear collider DR and evaluate target materials for the currents and spot sizes most likely to be encountered [3]. Since its reinstallation in 2007 in the ATF EXT line, the OTR1X has been used to measure the beam sizes and the projected vertical emittance at the entrance of the ATF EXT line. In 2007 and 2008 an experimental study of the vertical emittance growth in the ATF EXT line versus vertical bumps in the DR and in the ATF EXT line demonstrated the usefulness of the OTR1X for measuring the beam sizes and projected vertical emittance in the ATF EXT line [8]. This study has been the seed for the multi-OTR system in the ATF2 EXT line.

Operationally the OTR monitor inserts a metallic foil target in the beam pipe at a 20-degree angle with respect to the beam. An optical system at the angle of reflection to the incoming beam gathers the light emitted when the beam passes through the target. A pneumatic actuator inserts the target and repeatability of the target position is assured by a stainless steel ball at the end of the actuator shaft that is pushed into a titanium conical receiver inside the OTR body. Figure 3 shows the latest version of the OTR design, with the beam moving from left to right. In the beams direction, on the right side of the pipe is the optical system: a Mitutoyo lens, a 12bit Prosilica camera and a

Newport focus adjuster. A pair of Newport stages is used to move the optical system vertically and horizontally over the target. This makes the set up easier and in the case of target damage, allows different areas of the target to be viewed. The top of figure 3 shows the target pneumatic actuator and in the bottom, a horizontal and vertical mover. These two remote controlled movers move the whole system vertically and horizontally. With these movers is possible to search for the beam for measurements or to leave a clear space for normal beam operations.

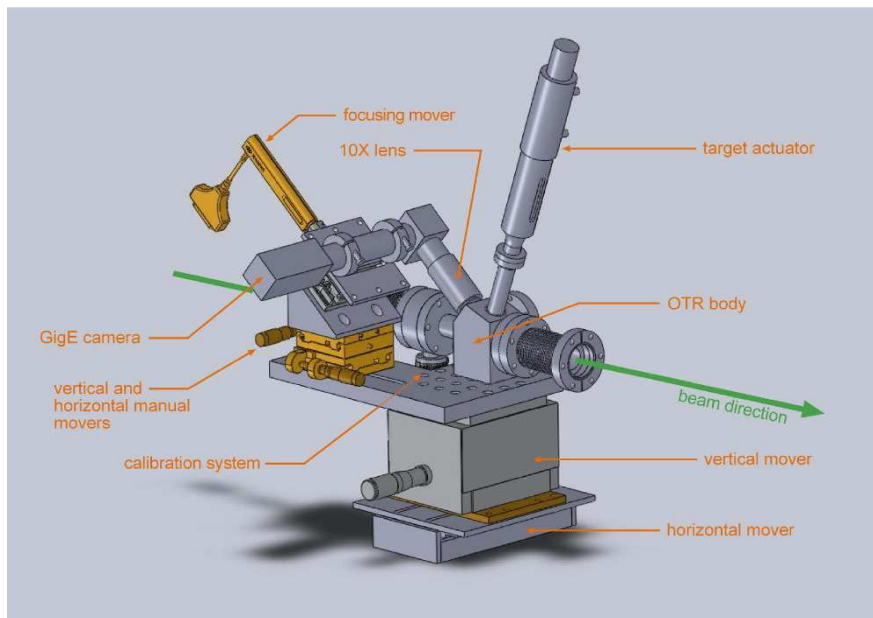


**Figure 3: OTR Design**

The new design's calibration system includes a scribed target and a small lamp that can be pushed into the beam pipe to illuminate the target when there is no beam. The target scribe marks are well illuminated and the stages supporting the camera are used to move the camera precisely over the scribe marks. This produces the required pixels/micron calibration. The total beam line footprint was reduced with respect to the old one by nearly half and now the overall length is less than 30cm.

A goal of the original OTR design was to find the damage threshold for various target materials [3]. A goal of ATF2 is to get  $2 \times 10^{10}$  electrons in a single bunch and to do multi-bunch experiments with over  $2 \times 10^{11}$  in a train. With these levels of currents too small spot sizes cannot be allowed with OTR operations. During the original damage tests, round spots of about  $5 \mu\text{m}$  were reached. Copper and even beryllium targets were damaged with around  $2 \times 10^{10}$ . With current beam aspect ratios of around 50 times larger than during the original damage tests, damage will be much less of a problem but multi-bunch operation will still not be possible without risking target damage. If currents are too low and spots are too large it will be difficult to get enough light output to have a good signal to noise. Taking in account these constraints the ideal spot size would be somewhere around  $20 \mu\text{m}$  in y and  $200 \mu\text{m}$  in x. The tracking simulations shown above indicate that installed locations will nearly ideal for the OTRs

For the new design an extremely thin aluminized Mylar target was tested in the OTR1X and figure 4 shows an OTR capture of the beam taken with the new Mylar target during November 2009. The spot sizes estimated for the four new OTR locations will be larger than before so no target damage problems are expected.

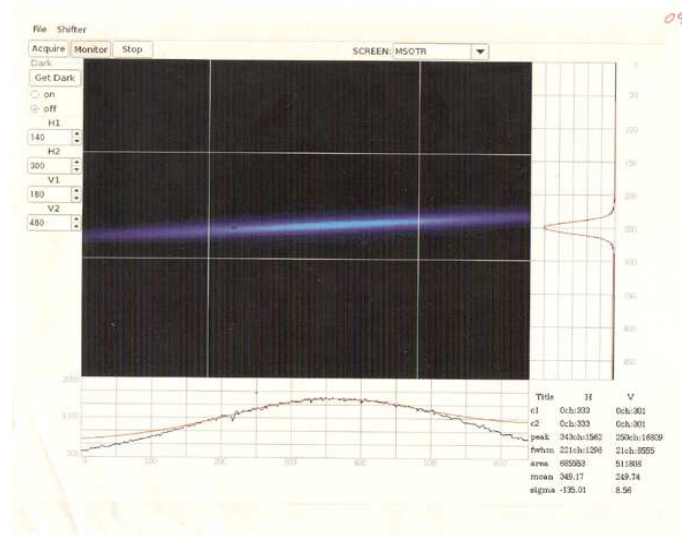


**Figure 4:** Test of the new target at OTR1X in November 2009.

New targets and targets holders were installed in November 2010. The new targets are made of Aluminum coated Kapton for OTRs2 and 3 and 1  $\mu\text{m}$  Aluminum foils for OTRs 0 and 1. These targets have withstood beam currents of  $1 \times 10^{10}$  at near normal beam sizes for several minutes without being damaged.

The target holders have been modified to hold a wire card that has four 10  $\mu\text{m}$  tungsten wires. There is a single vertical, and, horizontal, wire plus two wires tilted at  $\pm 10$  deg shown in Figure 5. By using the vertical and horizontal movers each OTR can be used as a WS. The normal step size in the vertical plane is 2 mm and in the horizontal 10 mm. This permits a comparison between the size measured by the wire and the size measure by the OTR. Both measurements will be in the exact same location so the calibration process is easier and precise.

The optical system is based around a commercial long working distance microscope objective. It uses a 10X lens with Numerical Aperture of 0.28 and 1  $\mu\text{m}$  resolving power. The working distance of the lens is about 34 mm, which requires a thin compact non-distorting vacuum window. ZEMAX calculations indicated that a 1mm thick 7 mm diameter fused silica window with a  $\lambda/4$  surface flatness would produce small enough distortions so that the lenses' resolving power was minimally affected. This window is vacuum-sealed with an indium washer and a threaded ring. It was recognized in the old design there were problems with depth of field. It is planned to tilt the camera so that the CCD is parallel to the OTR target, and it is expected that this will reduce the need to adjust the focus when the beam moves vertically on the target.



**Figure 5:** Target holders and wire cards with the targets.

The optics is folded in order to make it easier to shield the camera from radiation damage. Since target thickness is reduced, the radiation from the beam target interaction is going to be lower and less lens darkening is expected. In October 2010 after some running time the CCDs were protected with lead blocks to reduce the pixel damage due to radiation.

In order to facilitate initially finding the beam a de-magnifier system will be installed soon. Figure 5 shows one of the OTRs installed in ATF2 EXT line.



**Figure 6:** OTR with the calibration system installed at ATF2.

#### **4.3.4 Software Integration, Beam Spot Size and Emittance Reconstruction Algorithms**

The measurement of the beam sizes and the emittance is completely integrated in the ATF2 control system. First Graphic User Interface (GUI) tests and some initial calibrations using IPBSM were made in November 2010 and have been improved

during the first running period of 2011. Figure 7 shows the image of main start panel, the single OTR panel for beam size measurement and the emittance measurement panel using the beam sizes measured in the OTRs as seen in the ATF2 control room.

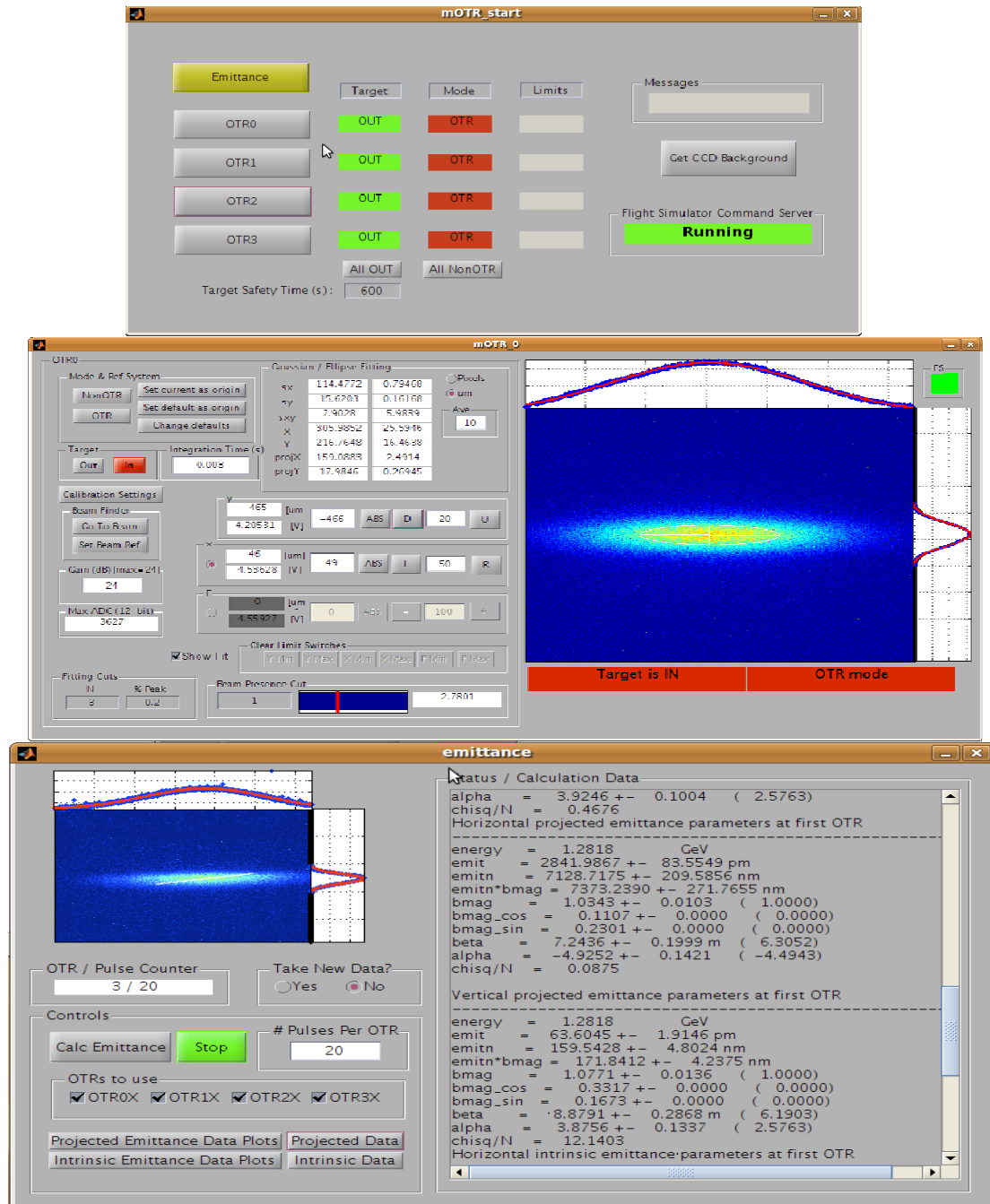


**Figure 7:** Main start panel, beam size and emittance measurement in OTR0 as seen in the ATF2 control room.

The high level control software and the user interface are being developed in Matlab. It includes basic control commands like the movement of the devices, taking the target

in and out, OTR status, machine global protection alarms as well as single-OTR data analysis functions for beam size measurement. Proper multi-OTR functions use near simultaneous information of the four OTRs to perform algorithms in order to calculate the emittance value. The software uses labCA to send EPICS commands to the IOC software and it is integrated in the on-line Flight Simulator [8]. Because of this, the auto-tracking of the beam can be implemented in the future by receiving information from nearby Beam Position Monitors so the four targets will be automatically positioned. All useful data is stored in EPICS PVs and archived in the EPICS archival system.

#### 4.3.4.1 Beam Spot Size and Emittance Reconstruction Algorithms

The projected beam size and their rms errors is calculated by using a Gaussian fits to projections and a statistical rms of measured beam sizes over a certain number of pulses at each OTR, as shown in Figure 7.

The emittance reconstruction is made using the standard approach to reconstructing the 2D (projected emittance) and the 4D (intrinsic emittance) coupled beam matrix with the least squares fit method [9]. In the presence of coupling the emittance reconstruction falls with the beam size measurement error [10-12]. Figure 8 shows the ratio of no real emittance values as a function of the size measurement error in simulated reconstructions. Real systematic measurements will be made to determine the real rejection ratio. A criterion to reduce the imaginary values in the intrinsic emittance is being developed.

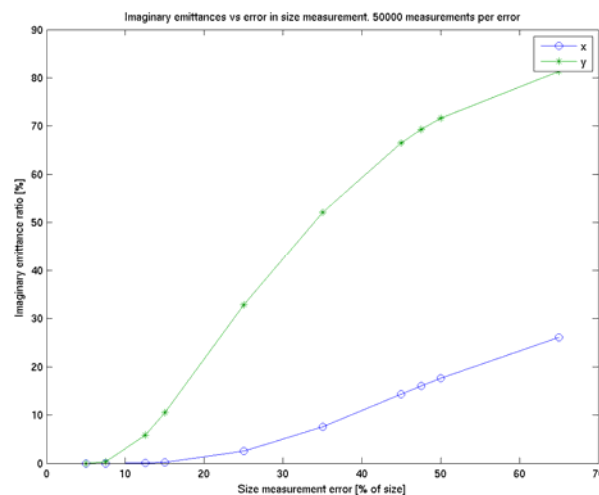


**Figure 8:** Ratio of imaginary emittances as a function of measurement error.

### 4.3.5 First Beam Measurements

#### 4.3.5.1 Fall Run 2010

In November 2010 we made the first GUI tests and some initial calibrations using IPBSM (IP Beam Size Monitors) were made for each OTR. New targets behave very well.

In the last week of November 2010 a vacuum leak was detected in the camera window of OTR2. It was repaired during the first week of December 2010 and we could continue with the measurements using all the OTRs. One of the first tests was the OTR wire scans versus the signal in the IPBSM background detector. The measurement was made to cross check wire scans with observed beam sizes. The measures agree within the fit errors. Afterwards we perform the vertical scale calibration for all the OTRs to get the factor  $\mu\text{m}$  versus pixel. This was made by scanning the vertical mover stage and recording the motion of the observed beam centroid. The calibration is shown in Figure 9. To test the calibration an upstream corrector is scanned and the response in observed the OTR. To test roll alignment (of the OTR CCDs) we have to look for no motion in the opposite plane.

Furthermore a coupling correction in the EXT line is achieved by scanning each of the four EXT skew quads. For each scan the quantity  $(\gamma\varepsilon_y * \text{BMAGY})$  versus the strength of the skew quad is plotted and taken the optimal from a parabolic fit, as shown in Figure 10.

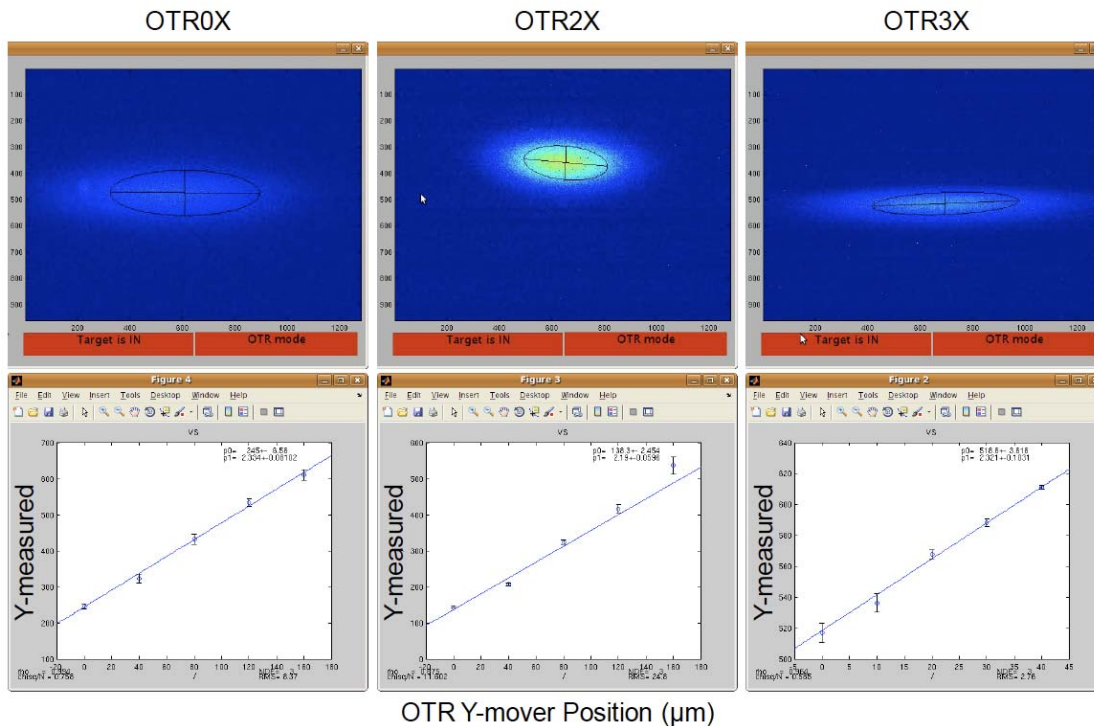


**Figure 9:** Vertical scale calibration where the factor  $\mu\text{m}/\text{pixel}$  is obtained.



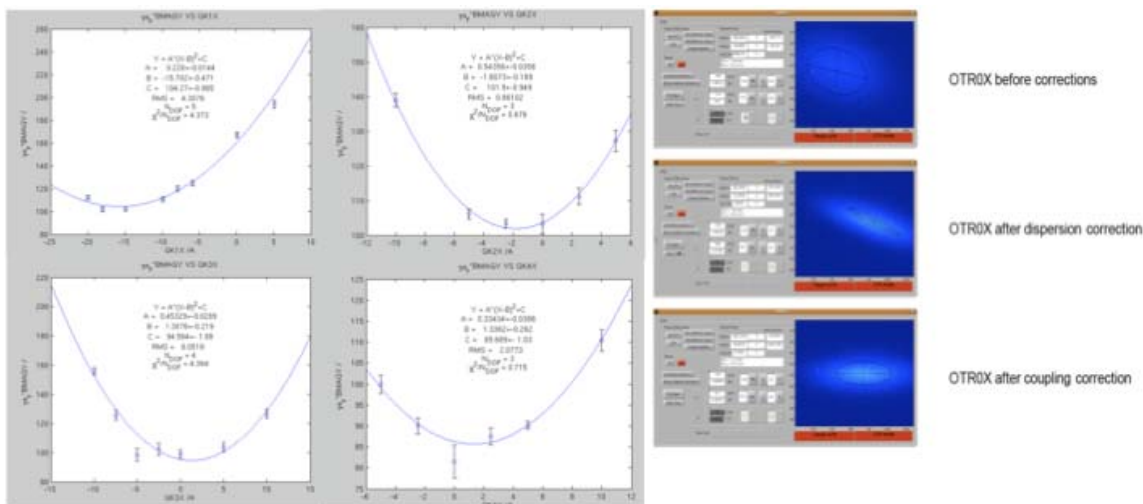


**Figure 10:** Coupling correction of the ATF2 EXT line by using the OTRs.

#### 4.3.5.2 First Period Run 2011

Some sets of measurements were done in the first trimester of 2011 to test the algorithms. Figure 11 shows a sequence of consecutive  $x$  and  $y$  projected size measurements on the four OTRs. The size measurement behaves as expected from one bunch to next one. Since it is possible to measure single bunch position jitter studies can be performed as well. The method has been tested qualitatively and it works properly but a campaign of systematic measurements has to be done in order to make a detailed comparison with the WS results and the simulation results. This will give us a confirmation of the whole system as an emittance measurement device.

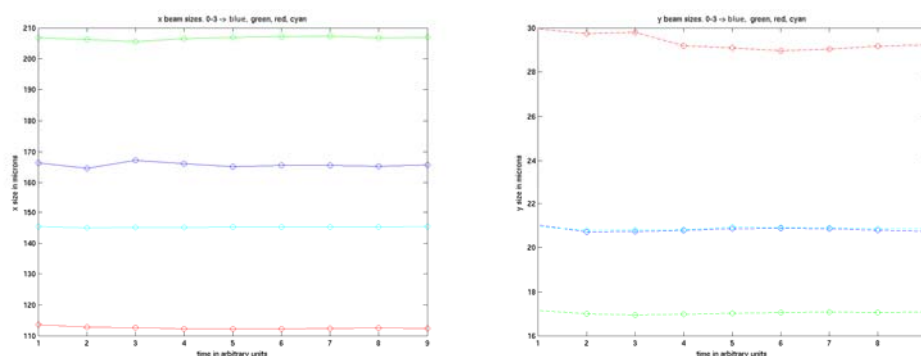


**Figure 11:** Set of consecutive projected size measurements.

#### 4.3.6 Conclusions

A Multi-OTR system has been installed in the EXT line of ATF2 during 2010 and it is operative from last period of 2010. Since 2011 a systematic measurement campaign has been carried out.

The results of the measurements with OTR monitors will help to understand emittance jitter in the line and its success will definitely confirm the OTR as an emittance diagnostic device.

#### 4.3.7 Acknowledgements

We would like to thank the ATF group at KEK for all the support, especially N. Terunuma for his continuous help on the installation.

#### 4.3.8 References

1. ATF2 Group, "ATF2 Proposal Vol.1, CERN-AB-2005-035", (August 11, 2005).
2. J. Bossler et al, "Optical transition radiation proton beam profile monitor", Nuclear Instruments and Methods in Physics Research A238, (1985), 45-52.
3. M. Ross et al, "A very high resolution optical transition radiation beam profile monitor", SLAC-PUB-9280, (2002).
4. H. Hayano, "Wire Scanners for Small Emittance Beam Measurement in ATF", XX International Linac Conference (2000).
5. H. Grote and C. Iselin, "The MAD Program (Methodical Accelerator Design)", CERN SL 90-13 (AP) <http://mad.home.cern.ch/mad/mad8web/mad8.html>
6. The LUCRETIA Project, <http://www.slac.stanford.edu/accel/ilc/codes/Lucretia/>
7. G. White et al, "A flight simulator for ATF2: A mechanism for international collaboration in the writing and deployment of online beam dynamics algorithms", EPAC08, Genoa, TUPP016, (2002).
8. C. Alabau Pons et al, "Experimental Studies and Analysis of the Vertical Emittance Growth in the ATF Extraction Line in 2007-2008" ATF-08-15 (2009).
9. M. Minty and F. Zimmermann, "Measurement and Control of Charged particle Beams", Springer, Berlin 2003.
10. M. Woodley, "Simulations of intrinsic emittance measurements in an ideal 4D diagnostic section: coupled input beam", ATF 99-07.
11. M. Woodley, "Simulations of intrinsic emittance measurements in ATF EXT line", ATF 99-08.
12. I. Agapov et al, "Beam emittance measurements with laser wire scanners in the International Linear Collider" Physical Review Special Topics – Accelerators and Beams 10, 112801 (2007).

#### 4.4 Micron Scale Laser-Wire Scanner for the ATF

L. Corner, N. Delerue, B. Foster, D. Howell, M. Newman, L.J. Nevay, R. Senanayake, R. Walczak and F. Ganaway,  
John Adams Institute at Oxford University, Denys Wilkinson Building, Keble Road,  
Oxford OX1 3RH, UK

S.T. Boogert, G.A. Blair, G. Boorman, A. Bosco, L.C. Deacon and P. Karataev,  
John Adams Institute at Royal Holloway, Egham, Surrey TW20 0EX, UK

A. Aryshev, M. Fukuda, N. Terunuma and J. Urakawa,  
KEK, 1-1 Oho, Tsukuba, Ibaraki 305-0801, Japan

Mail to: [l.corner1@physics.ox.ac.uk](mailto:l.corner1@physics.ox.ac.uk)

#### 4.4.1 Introduction

This article describes the development of the laser-wire experiment at the Accelerator Test Facility (ATF) at KEK in Tsukuba, Japan. This is a project to develop a reliable method for rapidly measuring electron beam sizes with sub-micron resolution. A laser-wire scanner [1, 2, 3] uses a focused laser pulse that scatters from an electron beam producing higher energy Compton photons nearly parallel to the electrons. Scanning the laser pulse across the electron beam while monitoring the number of scattered photons provides a measurement of the transverse electron beam density.

#### 4.4.2 Laser-Wire Experiment at the ATF

##### 4.4.2.1 Hardware

The laser-wire experimental system consists of a high power pulsed laser, laser focusing optics, interaction region chamber and Compton photon detectors. The interaction region is shown schematically in figure 1. Full details of the laser-wire installation and experiments at the ATF may be found in [4].

The laser system is located in a temperature controlled room on top of the shielding blocks of the ATF. It consists of a Nd: VAN seed laser producing 1064nm, 20ps pulses with an average output of 600mW. It is frequency locked to an external 357MHz signal derived from the ATF rf system. Two Pockels cells are used to pick pulses at the ATF repetition rate of 1.56Hz, which are injected into an Nd: YAG regenerative amplifier where they are stretched to  $\sim 110$ ps and amplified to 15mJ. These pulses are further amplified in two single pass Nd: YAG amplifiers to a typical energy of 900mJ. The pulses are frequency doubled in a KDP crystal to 532nm with a maximum pulse energy of 400mJ. The laser beam is transported 9m to an optical table next to the ATF extraction line where it is steered onto the final lens and focused inside the interaction chamber to the laser-wire interaction point (LWIP).

The final focus lens is custom made from fused silica for radiation hardness and designed to be corrected for spherical aberrations. It consists of 2 curved elements and the vacuum window which is an integral part of the design. All the elements are coated with a high damage threshold antireflection coating. The lens has a focal length of 56.6mm and a spectral acceptance bandwidth of 1nm. It is fixed to the vacuum chamber which can be moved horizontally and vertically to allow the laser beam to be scanned over the electron beam. To aid the alignment of the laser and electron beams a 300 $\mu$ m thick gold coated silicon knife edge is mounted on a translator in the interaction chamber. After exiting the chamber the laser is recollimated with another lens and directed onto an energy meter.

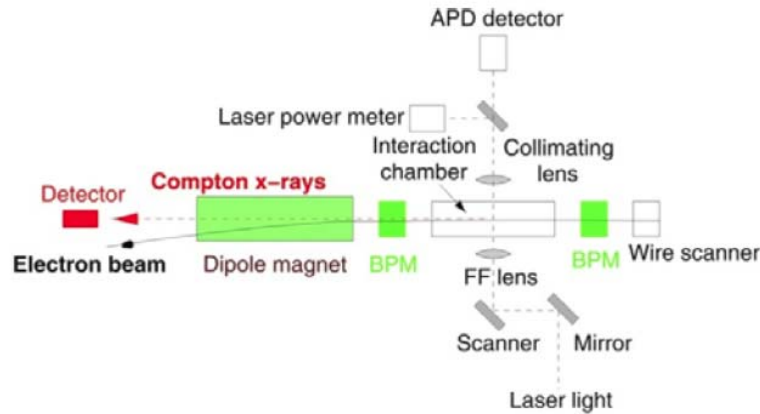


**Figure 1:** Schematic of the laser-wire interaction region

The photons scattered at the interaction point exit the beampipe through a 1mm thick aluminium window after being separated from the electron beam in a dipole magnet. They then travel a further 7.7m in air to the detector system. The primary detector is an aerogel Cherenkov detector. The photons are converted into electron-positron pairs using 7.35mm of lead and then produce Cherenkov radiation in 5.5cm of Matsushita Denshi SP-15 aerogel with an area perpendicular to the beam of  $10 \times 10$ cm. The Cherenkov radiation is guided to a PMT placed at floor level to reduce the background. The secondary detector is a calorimeter made of a single  $110\text{mm} \times 120\text{mm} \times 360\text{mm}$  lead glass crystal placed directly behind the aerogel and coupled to a PMT. It measures the photons unconverted by the lead plate, approximately 85% of the total. The two detectors are complementary, the Cherenkov detector counting the photons generated and the calorimeter measuring the total energy.

#### 4.4.2.2 Lens Simulation

A ZEMAX simulation of the final focus lens was performed to find the focused laser spot size at the LWIP as a function of the input Gaussian beam size on the lens.

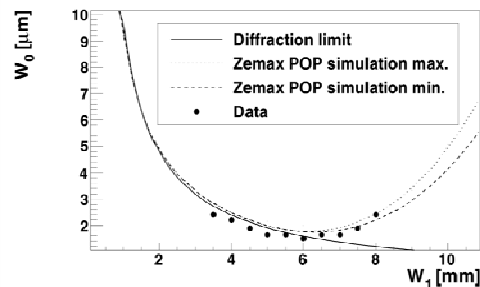


**Figure 2:** ZEMAX simulation and data of the focused spot size  $W_0$  as a function of input size  $W_1$

ZEMAX uses a model called physical optics propagation (POP) to compute the laser intensity distribution in the focal plane of the lens on a 2-dimensional grid. The calculated focused spot depends slightly on the size of the grid. This is illustrated in

figure 2, which shows the focused spot size  $W_0$  plotted against the input beam  $W_1$ . The dashed and dotted lines show the minimum and maximum values of  $W_0$  calculated using the different grid sizes. The data points were taken with a beam profiler to measure the focused spot size after the lens using a cw laser with excellent spatial quality. The data show excellent agreement with the simulation, validating the modeling and allowing the optimum  $W_1$  for the smallest laser focus to be found.

#### 4.4.2.3 Laser-Wire Results

The laser and electron beams were overlapped with each other by initially using a low power cw laser with the knife edge to determine the position of the laser focus within the chamber. Then the pulsed laser was set to low power and the knife edge brought into the electron beam where optical transition radiation (OTR) is produced. The laser pulse and OTR were monitored on an avalanche photodiode (APD) placed behind the chamber and the timing of the laser pulse adjusted until it overlapped the OTR. Then the laser beam was moved so that it was obscured by the knife edge just above the electron beam and translated downwards until a laser signal was observed on the APD, which guaranteed that both beams were just below the knife edge. Finally removing the knife edge and turning the laser up to full power resulted in an observable Compton signal on the detector.

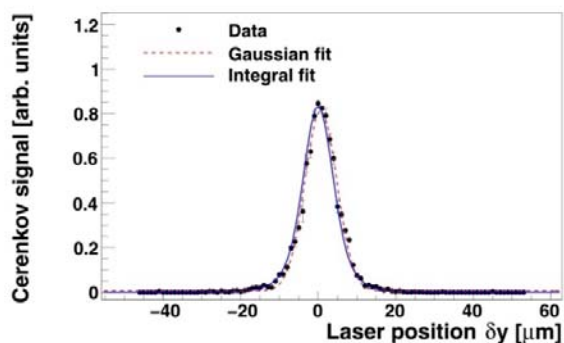


Figure 3: Smallest rms  $\sigma_s$  laser-wire scan

The laser-wire scan with the smallest convoluted rms size  $\sigma_s = 5.4 \pm 0.1 \mu\text{m}$  is shown in figure 3. This result was taken after aligning the system carefully and then optimizing the upstream quadrupoles QD4X and QS1X to reduce the vertical electron beam size. The laser spot size for this scan was estimated to be  $2.54 \pm 0.49 \mu\text{m}$  so the minimum measured rms electron beam size was  $4.8 \pm 0.3 \mu\text{m}$ . Figure 3 also shows the scan fitted with a Gaussian and a fit generated using an overlap integral between the laser and electron beams. There are shoulders on the data and it is not well fitted by a Gaussian, indicating the effect of the limited Rayleigh range of the laser. This can be accounted for using the overlap integral approach, but this requires knowledge of the horizontal size of the electron beam which was unknown in our experiment so the rms method was considered the most reliable quantitative measure of the scan size. Further details of this analysis can be found in [4].

### 4.4.3 Laser-Wire Upgrade for the ATF2

#### 4.4.3.1 Upgrades

The upgrade to the ATF2 enabled major improvements to be made to the laser-wire experiment. These included building a new laser room, relocation of the laser system, vacuum chamber and detector, redesign, modelling and installation of a new laser transport line and diagnostics and changes to the laser optics to achieve  $1\mu\text{m}$  resolution.

A new experimental hut with improved air conditioning and temperature control for the laser-wire laser systems, computers and DAQ has been built and the laser installed on a new optical table with an aperture enabling the light beam to be directed via a periscope to the accelerator tunnel. The laser beam is then transported approximately 17m to the LWIP which is now situated between QF19X and QD20X as shown in figure 4. To enable remote alignment of the laser, at two places along the beam in the tunnel low reflectivity beam splitters have been installed on translation stages which can be moved into the beam and direct light through a lens onto a camera. These can be used to correct the laser position for optimum alignment by feeding back to actuators on the mirrors directing the laser to the LWIP [5]. The optics upstairs in the laser room have been improved to include a telescope to alter the beam size of the laser on the final focus lens, which our previous measurements had shown not to be optimized for the smallest focused laser spot [4].

The detector has been moved to just after BF55, approximately 22m from the LWIP. It is closer to the extraction line beampipe than before so the aerogel has been modified by cutting it down to an area of  $4 \times 4\text{cm}$  to reduce the background. As the detector is considerably further away from the LWIP than in the previous installation its alignment is critical. To align the electron beam and the detector correctly during the summer shutdown the beampipe was opened up and an alignment laser directed from upstream through the LWIP centrally onto the detector. The position of the laser beam on either side of the LWIP was measured with wire scanners MW1X and MW2X and we were able to use this to define a trajectory of the electron beam through the LWIP that was aligned with the detector.

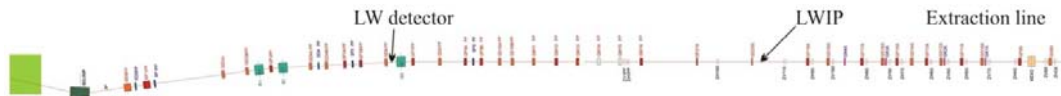


**Figure 4:** ATF2 extraction line showing the position of the laser-wire IP and detector.

#### 4.4.3.2 Laser-Wire Results at the ATF2

The nominal optics for the ATF2 extraction line produce an electron beam size at the LWIP which is too large to be easily measured using this laser-wire. A special set of laser-wire optics have been developed with the aim of producing a small beam size at the LWIP which should be rematched into the extraction line downstream of the laser-wire and enable it to run with the minimum spot size at the ATF2 IP. The first laser-wire data with the upgraded system was taken in November 2010. Two laser-wire scans of the vertical beam size are shown in figure 5. Figure 5a shows an initial scan before

beam tuning fitted with a Gaussian with a convoluted size of  $\sigma_s = 19.2 \pm 0.2 \mu\text{m}$ . After the beam was corrected for dispersion and X-Y coupling the scan size was reduced to  $\sigma_s = 8.1 \pm 0.1 \mu\text{m}$  as shown in figure 5b, clearly showing the effect of the beam tuning. These data were taken with a laser energy of 110mJ and a bunch charge  $\sim 0.2 \times 10^{10} e$ . The non-destructive nature of the laser-wire scanner was demonstrated by the fact that another experimental group was working with a laser-wire scanner in the beam at the ATF2 IP at the same time as this data was being taken.

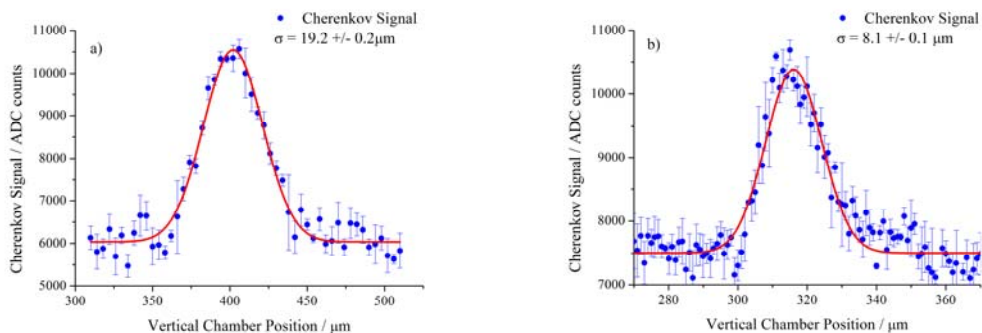


**Figure 5:** a) Laser-wire scan before beam tuning; b) Smallest laser-wire scan.

#### 4.4.4 Development of a New Fibre Laser Source for Laser-Wire Experiments

In parallel with the development of the high resolution laser-wire experiment we have been developing novel fibre lasers as a potential replacement for the current solid state laser systems. Fibre lasers have many advantages over more conventional technologies, particularly their small size, efficiency (60 – 85%), simplicity (no water cooling of the lasing medium) and economical pump sources (high brightness diode bars). They also have excellent single mode spatial quality and beam pointing stability due to their waveguide structure. These properties make them ideally suited for the laser-wire experiment.

The fibre laser developed for the ATF2 laser-wire project is designed to work in burst mode with a pulse spacing of 154 ns (6.49 MHz) to match ATF multi-bunch operation to reduce the time required for a laser-wire scan. The output specifications for the laser are a pulse energy of 50 μJ in the green (100 μJ at a wavelength of 1 μm) with a pulse duration of 1 – 10 ps. The final laser architecture is a commercial system (Amplitude Systèmes, Bordeaux) which is then amplified in rod-type ytterbium (Yb) doped photonic crystal fibre (PCF). The commercial laser consists of a Yb: KYW oscillator at 1035 nm with an output power of > 1W which can be locked to an external frequency reference at ~ 52 MHz. The oscillator pulses are stretched to ~ 200 ps in a grating stretcher and then pass through an AOM to reduce the pulse rate to 6.49 MHz. They are then amplified in Yb doped fibre to reach a final pulse energy of > 1 μJ. The system also contains an EOM after the power amplifier to enable bursts of pulses to be produced.

The seed output of the commercial system is transmitted through an optical isolator and coupled via a series of lenses and a dichroic mirror into the core of the PCF, as shown schematically in figure 6. The 70cm long single mode polarization maintaining

PCF (DC-200/70-PM-Yb-ROD, NKT Photonics) has a core diameter of 70 $\mu\text{m}$  and pump absorption at 976nm of 30dB/m. It is supported in a metal V groove and has no water or forced air cooling. The pump is a specially developed 400W fibre-coupled diode laser bar (Spectra-Newport) which is designed to emit at 976nm in both pulsed and cw modes. It is coupled into the 200 $\mu\text{m}$  diameter inner cladding in a counter propagating geometry to aid alignment and increase efficiency and the amplified seed and pump are separated using a second dichroic mirror.

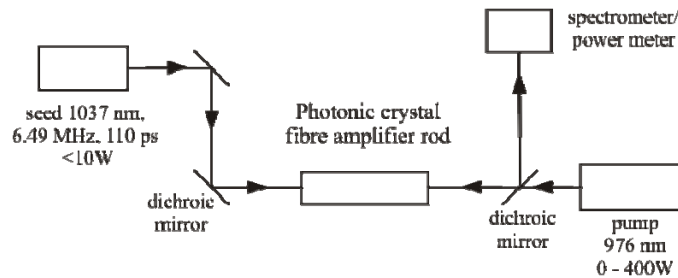


**Figure 6:** Schematic arrangement of fibre amplification experiment

The high gain required to amplify the seed pulses to  $> 100\mu\text{J}$  will be achieved by operating the amplifier in burst mode, where the pump is turned on before the seed to build up a large population inversion in the PCF. This means that the first few seed pulses in a burst see a high transient gain and will be amplified to high energies.

#### 4.4.5 Development of an Electro-Optic Scanner for Fast Laser-Wire Operation

The development of a laser as described in the previous section with a repetition rate matching the electron multi-bunch timing structure in the accelerator will increase the collision rate to 100%. In order to fully exploit this and ultimately improve the capabilities of the laser-wire scanner to perform intra-train scans, a scanning technique different from the mechanical translation currently in use must be employed. The shortest laser-wire scan durations achieved using electro-mechanical scanners such as step motors or piezo-electric deflectors are of the order of 10 – 100 seconds [4].

Electro-optic (EO) techniques are promising for fast laser beam scanning because they can achieve spatial displacement in very short timescales (1-100 $\mu\text{s}$ ), are very repeatable and because of the availability of very high quality EO crystals. Based on this choice of scanning technique, we have designed and realized an EO scanning device capable of making full laser-wire scans in 253ms using a laser with 130kHz repetition rate [6].



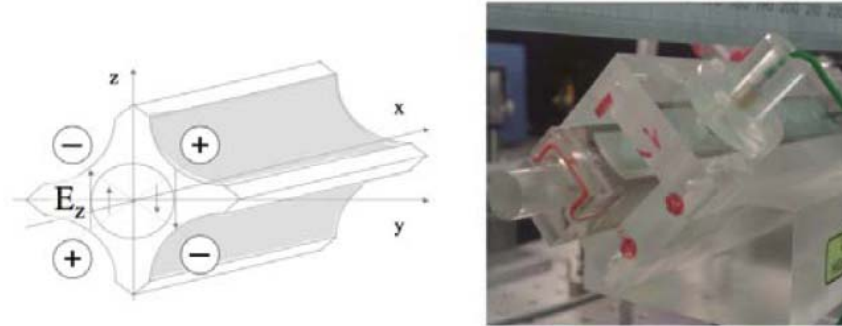


**Figure 7:** a) Schematic of the EO scanner; b) Photo of the device.

The operating principle of the device is illustrated in Fig. 7a. A linear gradient of the refractive index across the crystal is generated by the EO effect which deflects the laser beam. The active material used for our device is MgO doped LiNbO<sub>3</sub> (MgO:LNB), an easily available material with high EO coefficients.

The arrangement of hyperbolically shaped electrodes shown in figure 7a generates an electric field whose components along the y and z coordinates increase linearly from the centre with alternate signs. Due to the EO coupling between the component  $E_z$  and the optical properties of the crystal, the refractive index will be modulated. The effect of such modulation on a laser beam that propagates through the crystal will be that the right side will travel at a different speed than the left one. Thus the laser beam will be deflected by an amount proportional to the refractive index difference between the two sides and the propagation length in the crystal.

The standard design of an EO scanner, in which the electrodes are placed directly onto the crystal, restricts the optical aperture and hence the laser energy that can be transmitted without damaging the crystal. In order to overcome this problem, we have developed a new hybrid solution in which the electrodes are attached to a holder made of a common polymer. A picture of the device is shown in figure 7b. Two cylindrically shaped MgO:LNB crystals with diameter 8.6 mm and length 45 mm were inserted in the centre of the holder for a total active length of 90 mm. This means that a Gaussian beam with a diameter of 5.5mm can be deflected with this scanner.

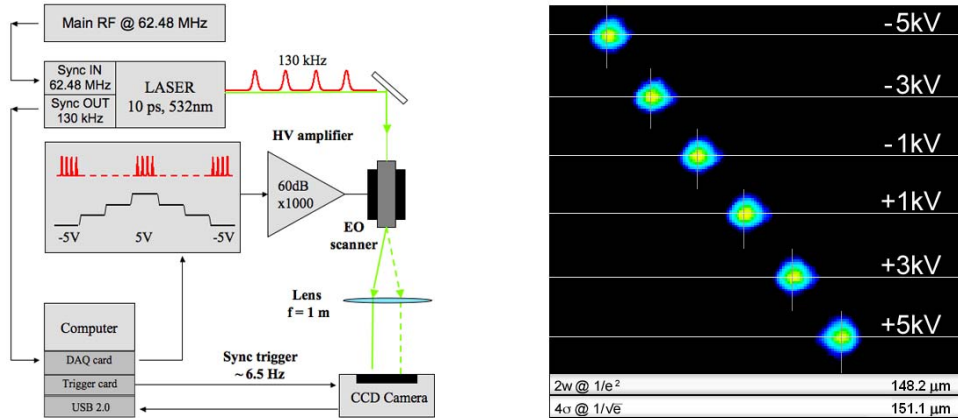


**Figure 8:** a) Layout of the experimental setup; b) Images of the laser profiles against voltage.

The experimental setup used to test the device is shown in figure 8a. The laser used for these tests was a frequency doubled mode-locked Nd:YVO<sub>4</sub> laser emitting 10ps pulses at 532nm with a repetition rate of 130 kHz. The laser beam propagating through the deflector was collimated to a spot size  $2w = 5.4 \text{ mm}$  and images of the laser after being transmitted through the scanner were recorded by a CCD camera. Figure 8b shows the laser profile and its deflection during scanning. The complete scan from -5kV to +5kV took 253ms and the total angular deflection obtained was 1.2mrad.

The linearity of the deflection against voltage is excellent, as shown in figure 9a. From figure 8b it is possible to see that the laser beam also maintains an excellent spatial profile. A measurement of the laser quality factor  $M^2$  after propagation through the scanner at maximum deflection angle is shown in figure 9b. The laser has an  $M^2$  of 1.05 which is increased to only 1.09 after the crystal, showing that the scanner affects the beam quality by less than 4%.

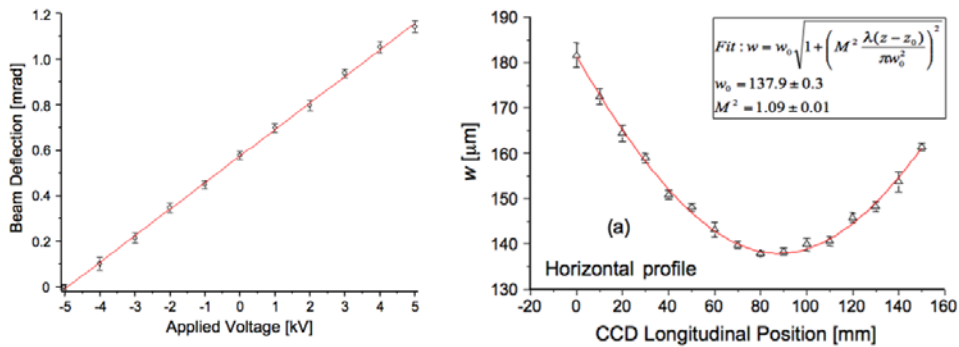


**Figure 9:** a) Plot of the deflection vs voltage; b)  $M^2$  measurement.

This prototype of an EO deflector should be suitable for applications where high power lasers are involved. The deflection obtained could be improved by up to a factor of 5 by choosing materials with better dielectric matching and the scan time can be shortened using a higher bandwidth high voltage amplifier.

#### 4.4.6 Conclusions and Future Plans

The laser-wire experiment at the ATF has taken data measuring electron beam sizes of  $\sim 5\mu\text{m}$ , with no indication that this is the limit of the resolution of the method. We have successfully upgraded the experiment for the ATF2 and completed the initial commissioning to take data in November 2010. This upgraded system has measured a convoluted scan size of  $8.1\mu\text{m}$  and is not yet fully optimized. In the future we plan to completely tune the electron beam size and reduce the laser focus by adjusting the spot size on the final lens. A full analysis of the signal dependence on beam charge and laser energy is planned in order to establish the minimum laser energy required to perform a laser-wire scan. This will enable further development of the fibre laser system in preparation for its installation at the ATF2. We also aim to achieve intratrain scanning using the new electro-optic scanner.

#### 4.4.7 References

1. R. Alley, D. Arnett, E. Bong, W. Colocho, J. Frisch, S. Horton-Smith, W. Inman, K. Jobe, T. Kotseroglou, D. McCormick, J. Nelson, M. Scheeff, S. Wagner and M.C. Roass, 'A laser-based beam profile monitor for the SCL/SLD interaction region', *Nuclear Instruments and Methods in Physics Research A* 379, 363 (1996).
2. I. Agapov, G.A. Blair and M. Woodley, 'Beam emittance measurement with laser wire scanners in the International Linear Collider beam delivery system', *Physical Review Special Topics – Accelerators and Beams* 10, 112801 (2007).
3. A. Bosco, M.T. Price, G.A. Blair, G. Boorman, S. Malton, C. Driouichi, T. Kamps, F. Poirier, K. Balewski, E. Elsen, V. Charibyan, H-C. Lewin, S. Schreiber, N. Walker and K. Wittenburg, 'A two-dimensional laser-wire scanner for electron accelerators', *Nuclear Instruments and Methods in Physics Research a* 592, 162 (2008).
4. Stewart T. Boogert, Grahame A. Blair, Gary Boorman, Alessio Bosco, Lawrence C. Deacon, Pavel Karataev, Alexander Aryshev, Masafumi Fukuda, Nobuhiro Terunuma, Junji Urakawa, Laura Corner, Nicolas Delerue, Brian Foster, David Howell, Myriam Newman, Rohan Senanayake, Roman Walczak and Fred Ganaway, 'Micron-scale laser-wire scanner for the KEK Accelerator Test Facility extraction line', *Physical Review Special Topics – Accelerators and Beams* 13, 122801 (2010).
5. A. Aryshev, H. Hayano, N. Terunuma, J. Urakawa, G.A. Blair, S.T. Boogert, G. Boorman, A. Bosco, L. Deacon, P. Karataev, D. Howell, L.J. Nevay, L. Corner, N. Delerue, B. Foster, F. Ganaway, M. Newman, R. Senanayake and R. Walczak, 'Micron size laser-wire system at the ATF extraction line, recent results and ATF-II upgrade', *Proceedings of the 2009 Particle Accelerator Conference, Vancouver, Canada* (2009).
6. A. Bosco, G.A. Blair, S.T. Boogert and G. Boorman, 'An electro-optic scanner for a fast laser-wire scanner', *Proceedings of the 2008 European Particle Accelerator Conference, Genoa, Italy* (2008).

## 5 Activity Reports

### 5.1 Recent Luminosity Enhancement at the BEPCII

Qing Qin, IHEP, P.O. Box 918-9, Beijing 100049, P.R. China  
Mail to: [qing@ihep.ac.cn](mailto:qing@ihep.ac.cn)

#### 5.1.1 Introduction

The Upgrade Project of Beijing Electron Positron Collider (BEPCII) is a factory like double-ring collider, working at the  $\tau$ -charm energy region. Same as its predecessor, the design of BEPCII kept the key philosophy of “one machine, two purposes”, which means to deliver beams to both high energy physics (HEP) experiments and synchrotron radiation (SR) users [1, 2]. Figure 1 shows the layout of the whole machine and the storage rings with beam lines of synchrotron radiation. Two parallel placed rings can accommodate electron and positron beams as a collider, and each outer half of each ring consists of the third ring, SR ring, which is a bit bigger than the collision ring and can be operated dedicatedly only with electron beam to SR users at the energy of 2.5 GeV. Table 1 lists the main design parameters of the BEPCII.

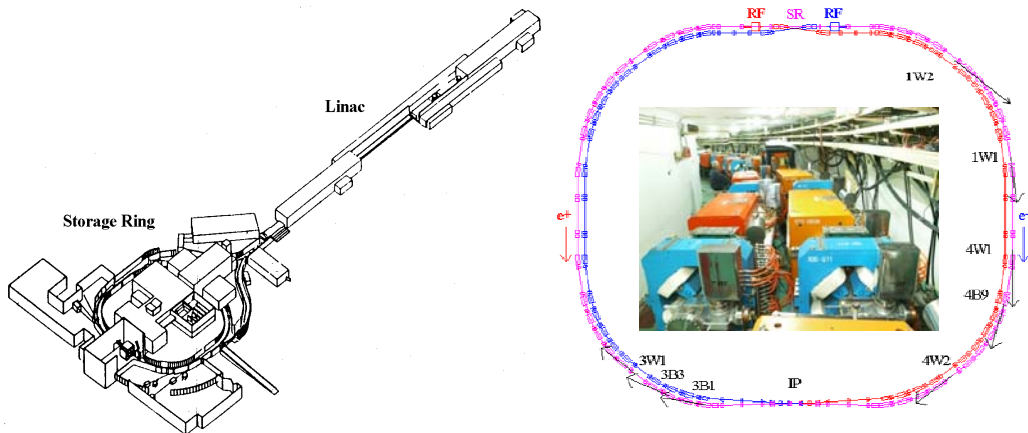


**Figure 1:** Layout of the BEPCII. Left: whole machine; Right: storage rings with beam line ports and tunnel view.

**Table 1:** Main design parameters of the BEPCII.

Energy for collision	GeV	1.89
Beam current in collision	mA	910
Energy for SR	GeV	2.5
Beam current in SR	mA	250
Injection energy	GeV	1.89 – 2.5
Injection rate ( $e^+$ , $e^-$ )	mA/min	50, 200
Luminosity	$\text{cm}^{-2}\text{s}^{-1}$	$1 \times 10^{33}$

The construction of the project was finished in the July of 2008, symbolized by the first hadron event observed at the detector, BESIII. Since Nov. 2006, three phases of beam and collision commissioning had been carried out, covering from beam accumulation, beam optics correction, detector solenoid compensation, beam instability cure, luminosity tuning, etc [3, 4, 5]. Moreover, several runs to provide beam to SR users were fulfilled, 168  $\text{pb}^{-1}$  of  $\psi'$  events, and 84  $\text{pb}^{-1}$  of  $J/\psi$  events were taken within 39 and 46 days, respectively, during these three phases of commissioning. Being passed the national test in the mid of July, 2009, with a peak luminosity of  $3.3 \times 10^{32} \text{cm}^{-2}\text{s}^{-1}$ , which is about one third of the design value, the BEPCII started to perform as a user facility, delivering beams regularly to HEP and SR users.

### 5.1.2 Luminosity Commissioning in 2010 - 2011

At the beginning of 2010, two sets of longitudinal feedback system were installed in both electron and positron rings to cure the instabilities observed one year ago. The instability happened as the single bunch current increased, and resulted as a luminosity reduction along the bunch trains. A dipolar longitudinal oscillation was clearly observed with oscilloscope and from the BPM signals induced by beam [5]. Figure 2 shows the bunch distributions of two rings and the bunch-by-bunch luminosity before and after the longitudinal feedback systems applied.

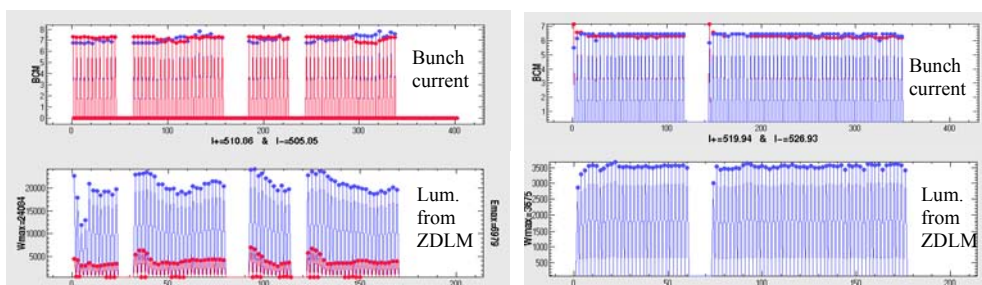


**Figure 2:** Bunch current and bunch-by-bunch luminosity along bunch trains Left: without longitudinal feedback; Right: with longitudinal feedback.

With the longitudinal feedback systems in both rings, the luminosity at the beam energy of 1.89 GeV during the data taking of the detector increased from  $2 \times 10^{32} \text{cm}^{-2}\text{s}^{-1}$  to  $3.2 \times 10^{32} \text{cm}^{-2}\text{s}^{-1}$  from Feb. to May, 2010. The highest luminosity was got at the design transverse tune of  $\nu_x \sim 6.53$ . When we tried to move the horizontal tune to the

half integer resonance line, we found a big rise of the background of detector. This background blocked the data taking, though the luminosity was higher than that in the region of  $\nu_x \sim 6.53$ .

During the machine shutdown last summer, a survey and alignment of the magnets around the storage rings were done carefully, especially the superconducting quadrupole near the interaction point. It was thought to be helpful on the background reduction of the detector.

In the new run for HEP experiments started from last Dec., we first corrected all the Twiss parameters and closed orbit distortions around the rings to theoretical values, with the method of response matrix. Then the luminosity was finely tuned via the displacement and divergence offsets at the IP, working points scanning,  $\beta$ -waist optimization, correcting x-y coupling at the IP, filling pattern determination, etc. The luminosity increased quickly and surpassed the best value in the first half year of 2010.

A luminosity enhancement came from the horizontal tune being shifted to  $\sim 6.51$ , where a higher dark current on the detector occurred. After optimizing the beam orbits, and the collimators' aperture near the interaction region to reduce the background of the detector, we finally operated the machine at the working point of  $\nu_x \sim 6.506$ , with a luminosity increase of about 20% compared to the previous horizontal tune. Figure 3 shows the luminosity evolution from last Dec. to the end of Feb. 2011. The newest luminosity record is  $5.94 \times 10^{32} \text{ cm}^{-2} \text{ s}^{-1}$ , at which the detector was run for data taking with an acceptable background level.

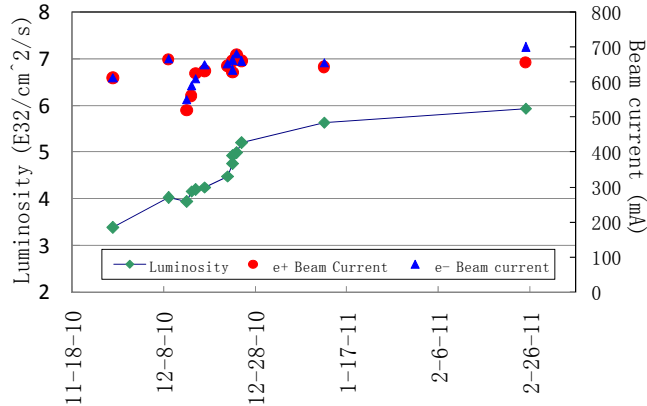


**Figure 3:** Luminosity evolution from Dec. 2010 to Feb. 2011.

From Fig. 3, we can see that as the luminosity goes up, the beam currents are not increased as the same scale of luminosity. It owes to the decrease of the transverse coupling of two beams. Figure 4 shows the luminosity got in routing operation (left) and comparison with the simulation results at different beam parameters (right).

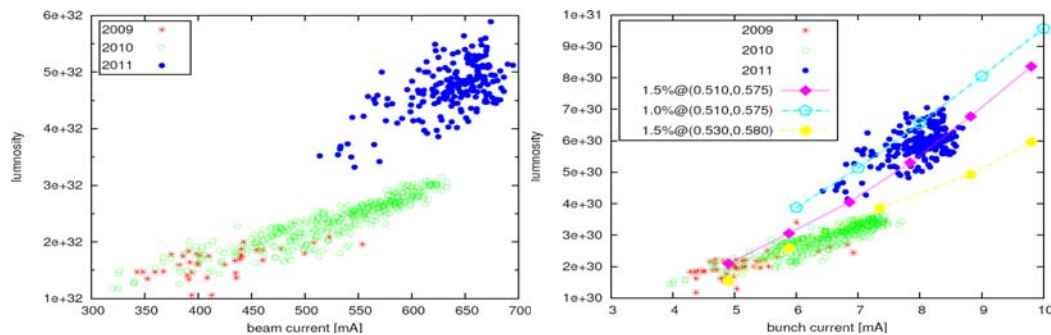


**Figure 4:** Luminosity vs. beam current (left), and with different coupling and tunes (right).  
(Courtesy Y. Zhang)

### 5.1.3 Future Improvements

With the efforts from accelerator team, the luminosity of BEPCII reached about 60% of its original design value. The integrated luminosity is already about 70 times than the BEPC machine due to the improved hardware systems. The further luminosity enhancement includes shortening bunch spacing to accommodate more bunches, increasing bunch and beam current, and squeezing the  $\beta_y$  at IP. Some of these measures to increase luminosity will be tried during the coming machine study in the following month. The feedback systems will also be checked with higher beam current and increased bunch number. The possible beam instabilities, such as ECI, will be the potential of degrading luminosity. Furthermore, the crab-waist scheme [6], which was realized at DAΦNE, will be another possible option for higher luminosity. But it needs a lot of simulation and experimental studies.

### 5.1.4 References

1. P.D. Gu, Y. Luo, Q. Qin, J.Q. Wang, S. Wang, G. Xu, C.H. Yu, Accelerator physics design of BEPCII, ICFA Beam Dynamics Newsletter 31: 32-41, 2003.
2. BEPCII Team, BEPCII design book—storage ring, IHEP-BEPCII-SB-03-3, 2003.
3. L. Ma, J.Q. Wang, C. Zhang, The BEPCII: Status and Early Commissioning, Proc. of PAC'07, Albuquerque, New Mexico, 2007.
4. J.Q. Wang, L. Ma, C. Zhang, Commissioning of BEPCII, Proc. of EPAC'08, Genoa, Italy, 2008.
5. Q. Qin, L. Ma, J.Q. Wang, C. Zhang, Status and Performance of BEPCII, Proc. of IPAC'10, Kyoto, Japan, 2010.
6. P. Raimondi, Proceedings of the 2<sup>nd</sup> Super B Workshop, Frascati, March 2006.

## 5.2 Accelerator Design of China Spallation Neutron Source

Shinian Fu, Jingyu Tang, Sheng Wang and Li Ma, IHEP, CAS, Beijing 100049

Mail to: [fusn@ihep.ac.cn](mailto:fusn@ihep.ac.cn)

### 5.2.1 Introduction

The China Spallation Neutron Source (CSNS) [1-3] provides a multidisciplinary platform for scientific research and applications by scientific institutions, universities, and industries. The high-flux pulsed neutrons from CSNS will compliment CW neutrons from nuclear reactors and X-rays from synchrotron radiation facilities. Strongly advocated by the user groups, the CSNS project was approved by the Chinese central government in 2008 and will start construction in June 2011. It is scheduled to be completed in 2017 at the site in Guangdong province. The CSNS accelerator is the first large-scale, high-power proton accelerator project to be constructed in China. In the CSNS design proton beam pulses are accelerated to 1.6 GeV kinetic energy at 25 Hz repetition rate, and then strike a tungsten target to produce spallation neutrons. The accelerator provides a beam power of 100 kW on the target in the first phase and then 200 kW in the second phase by raising the linac output energy from 80 MeV to 132 MeV and doubling the average beam current. The accelerator part has even the reserved potential to be upgraded to 500 kW. A schematic layout of CSNS complex in phase-I is shown in Figure 1. In the accelerator design, some conservative redundancy has been taken into account. So the designed beam current and thus beam power is higher than the nominal value. The major nominal parameters of the CSNS accelerator complex are listed in Table 1. In phase-I, an  $H^-$  ion source produces a peak current of 25 mA  $H^-$  beam. RFQ linac bunches and accelerates  $H^-$  beam to 3 MeV. DTL linac raises the beam energy to 80 MeV in phase-I and 132 MeV in phase-II. After  $H^-$  beam is converted to proton beam via a stripping foil at the injection, RCS accumulates and accelerates the proton beam to 1.6 GeV before extracting it to the target.

**Table I:** CSNS Design Parameters

<b>Project Phase</b>	<b>I</b>	<b>II</b>
Beam Power on target [kW]	100	200
Proton energy t [GeV]	1.6	1.6
Average beam current [ $\mu$ A]	62.5	125
Pulse repetition rate [Hz]	25	25
Linac energy [MeV]	80	132
Linac type	DTL	DTL
Linac RF frequency [MHz]	324	324
Macropulse. ave current [mA]	15	30
Macropulse duty factor	1.05	1.05
RCS circumference [m]	228	228
RCS filling time [ms]	0.42	0.42
RCS harmonic number	2	2
RCS RF frequency [MHz]	1-2.4	1.3-2.4
RCS Acceptance [ $\pi$ mm-mrad]	540	540



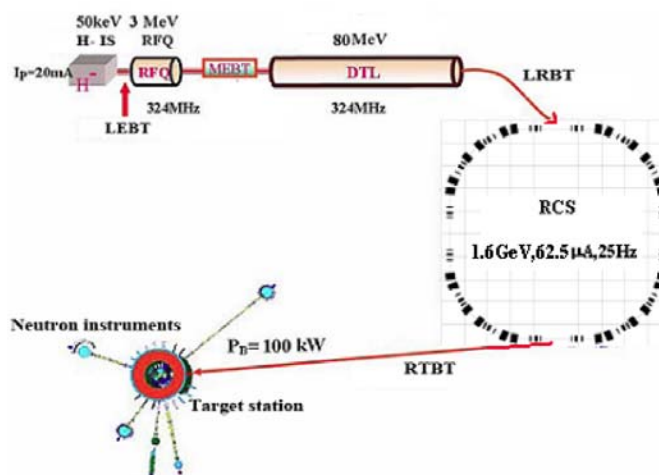


Figure 1: Schematics of the CSNS complex

## 5.2.2 Beam Dynamics Design

### 5.2.2.1 Linac

A four-vane type RFQ is adopted, with total length of 3.62 m, which consists of four segments. RFQ accelerates  $H^-$  beam from 50 keV to 3 MeV, with duty factor of 1.05%. The selection of 3 MeV output energy is a compromise between the chopper design in MEBT and injection energy of DTL.

The MEBT matches the  $H^-$  beam from RFQ to DTL in 6-dimensional phase space, and chops beam with a fast ( $\sim 10$  ns) rise time. The total length of MEBT is 3 m, including eight magnets, two bunchers and two J-PARC type RF choppers. MEBT is found to be the major contributor to the emittance growth in the linac.

The DTL accelerates the 3 MeV beam from the RFQ to 80 MeV. To reach high effective shunt impedance, the cell shape and size are tuned with  $\beta$  stepwise in the low  $\beta$  segment, and keeping the maximum surface field below 1.3 times the Kilpatrick limit. The FD focusing lattice is used in the dynamic design with equal-partitioning as a design goal for a tight control of beam emittance growth [4]. Figure 2 plots the zero-current phase advance in transverse and longitudinal directions, respectively.

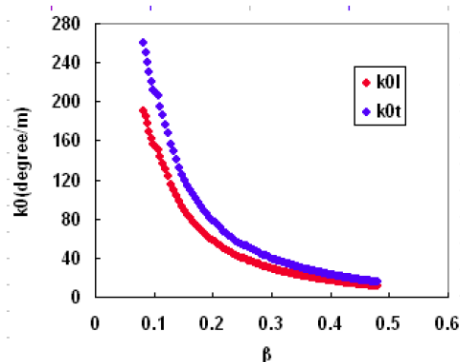
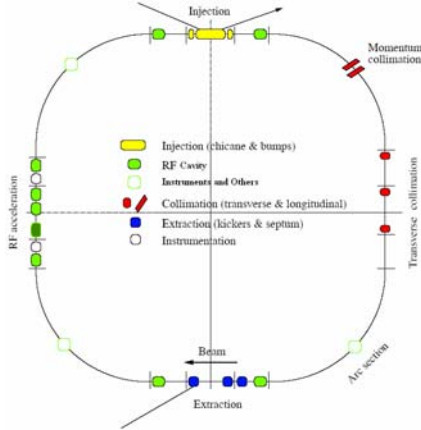


Figure 2: Zero current phase advance per meter in CSNS DTL.

### 5.2.2.2 Rapid Cycling Synchrotron

A Four-fold structure RCS is schematically shown in Figure 3 with major functional components in the four long-straight sections. The lattice is based on triplet focusing structure, and the whole ring consists of sixteen triplet cells, with circumference of 228 m. In each super-period, an 11 m long drift space is left, and this uninterrupted long space is very good for allocation of injection, extraction, RF acceleration and transverse collimation systems.



**Figure 3:** Schematics of RCS

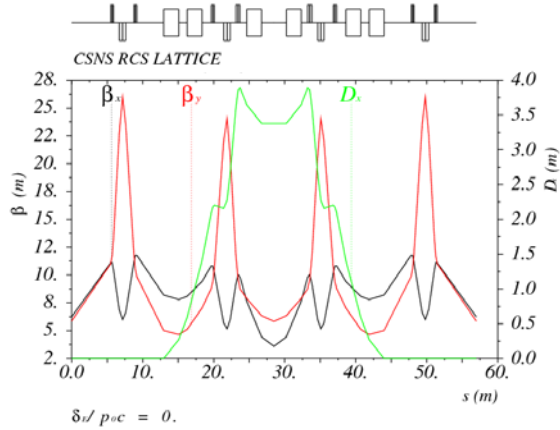


**Figure 4:** Twiss parameters in one super-period

The Twiss parameters of one super-period are plotted in Figure 4. The maximum beta function is less than 26 m, and the maximum dispersion function is less than 4 m. Space charge effects in the RCS have been studying by using ORBIT and SIMPSONS codes [5]. This includes both transverse and longitudinal space charge effects in the injection painting process, RF capture and acceleration. The working point, injection painting scheme and RF voltage pattern have been selected based on the simulations. The longitudinal painting by using off-momentum injection helps reducing the tune shift/spread. The maximum Laslett tune shift for CSNS-I is about -0.3. The transverse emittance growth due to the space charge is the most important source of beam losses. Based on the detailed study, anti-correlated painting scheme has been selected for controlling the emittance growth [6].

### 5.2.2.3 Beam Lines

There are two beam transport lines: LRBT and RTBT. LRBT transports  $H^-$  beam to the RCS, and transverse and momentum collimators are designed to scrape the halo particles. The debuncher is used in the LRBT to decrease momentum spread. RTBT transports extracted beam from the RCS to the target. The beam loss due to malfunction of kickers is minimized in the design. Collimation system is designed at RTBT for protection of the target and shielding of back scattering neutrons.

### 5.2.3 Acknowledgements

The CSNS accelerator is designed with the generous support from and the collaboration with many institutes including the Rutherford-Appleton Laboratory of UK, the KEK/JAEA and the J-PARC Project of Japan, the Brookhaven National

Laboratory, the Oak Ridge National Laboratory, the Argonne National Laboratory, the Los Alamos National Laboratory, and the PEPF Project of Korea. The authors also thank the accelerator team members of the CSNS project for their devotion and hard work.

#### 5.2.4 References

1. S. X. Fang, S. N. Fu, Q. Qin, J. Y. Tang, S. Wang, J. Wei, and C. Zhang, *J. Korean Phys.*, 48 (4), 697 (2006)
2. Shinian Fu, Hesheng Chen, et al., Status of the China Spallation Neutron Source Project, Proc. of PAC09, May, 2009, Vancouver, Canada (2009).
3. Wei Jie, Fu Shi-Nian, Tang Jing-Yu, et. al., China Spallation Neutron Source-an overview of application prospects, *Chinese Physics C* 2009 33 (11): 1033—1042.
4. X.J. Yin, S.N. Fu and J. Peng, Emittance coupling driven by space charge in the CSNS linac, *Chinese Physics C*, 2009, 33 (9): 811-814
5. S.Y. Xu, S.X. Fang, S. Wang, The study of the space charge effects for CSNS, Proc. of HB2010, 2010.
6. Jing-Yu Tang, Shi-Nian Fu, Li Ma, High intensity aspects of the CSNS accelerators, Proc. of HB2010, 2010.

### 5.3 The Accelerator Lab at Tsinghua University

Chuanxiang Tang, Wenhui Huang, Huaibi Chen, Yingchao Du and Renkai Li  
 Accelerator Laboratory, Department of Engineering Physics and  
 Key Laboratory of Particle and Radiation Imaging of Ministry of Education  
 Tsinghua University, Beijing 100084, China  
 Mail to: [Tang.xuh@tsinghua.edu.cn](mailto:Tang.xuh@tsinghua.edu.cn)

#### 5.3.1 Introduction

The main focuses of accelerator lab of Tsinghua University are given to the research on the accelerating structure, the application of low-energy linac, the high-brightness electron injector, the X-ray source based on Thomson scattering, etc. Some works are being given in the rest part.

#### 5.3.2 Low Energy Linac

China's first linac for medical applications, first linac for irradiation and first linac for dosage benchmarking were designed and manufactured in the accelerator lab of Tsinghua University. The energy switcher for medical therapy SW linac and. KV/MV homologous dual-beam acceleration tube were invented in the accelerator lab of Tsinghua University. More than three hundreds of S-band linac tubes were developed for Non Destructive Testing and radiotherapy. Besides the extensive research in S-band linac, the lab also devoted much effort in designing and manufacturing C-band, L-band and X-band linac tubes.



**Figure 1:** Different linac tubes produced by the accelerator lab of Tsinghua University.

### 5.3.3 Tsinghua Thomson Scattering X-ray (TTX) Source

Compact Thomson scattering X-ray sources supply monochromatic and tunable X-rays, which can be served as the X-ray sources for the ultra-fast science studies, medical and industrial applications. Studies on Thomson scattering X-ray sources at Tsinghua University started in 2001. A preliminary experiment using a 16MeV backward traveling wave (BTW) linac and a YAG laser was carried out during 2001–2006 collaborating with the Chinese Academy of Engineering Physics (CAEP). The Tsinghua Thomson scattering X-ray (TTX) source, as shown in Figure 2, which consists of a photocathode RF electron injector and a femtosecond terawatt laser system, will be served as a tunable monochromatic X-ray source for advanced X-ray imaging applications.

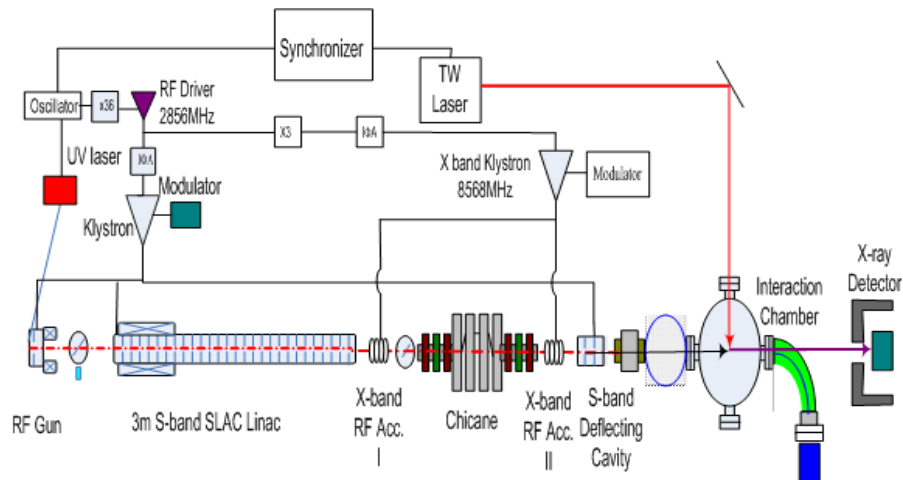


**Figure 2:** Schematic of the Tsinghua Thomson scattering X-ray (TTX) source.

Before installation of booster linac of photoinjector at TTX, a soft X-ray pulse is generated through Thomson scattering in the head-on collision between the 3-MeV

electron beam from a photocathode RF gun and a terawatt femtosecond laser beam. The maximum energy, pulse duration, and number of generated X-rays are estimated to be 290.4eV, 1ps, and  $6.4 \times 10^3$ /pulse, respectively.

In order to increase the energy and flux of the scattered photons, we are increasing the electron energy to more than 40MeV with a 3-m SLAC-type traveling wave accelerating section, as shown in Figure 3, and also enhancing the power of the laser for scattering up to 600 mJ/pulse. Experiments to utilize this X-ray pulse in practical applications will be undertaken recently.

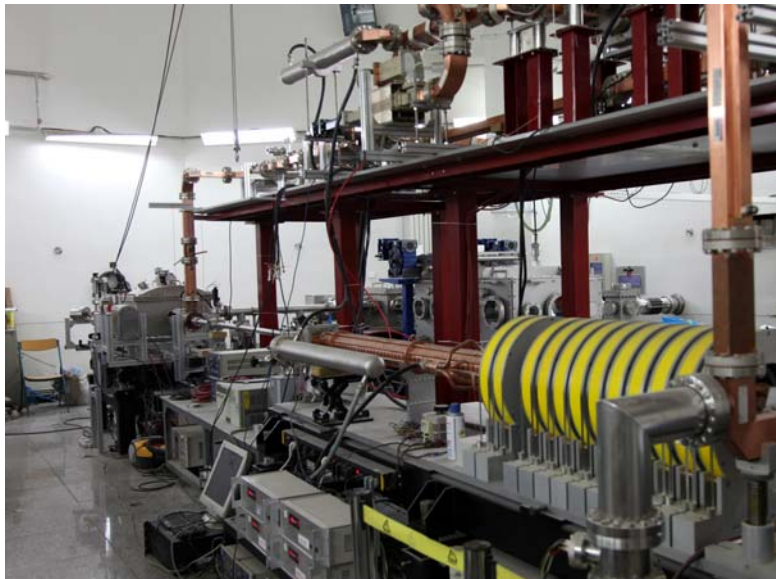


**Figure 3:** Layout of the Tsinghua Thomson scattering X-ray (TTX) source

### 5.3.4 MeV Ultrafast Electron Diffraction Based on Photocathode RF Gun

Recently, there are urgent demands on high brightness electron bunch emerge in China. The research related to photocathode RF gun is carried out at Tsinghua University since 2001, several S-band photocathode RF guns have been developed at Tsinghua University for Tsinghua Thomson scattering X-ray (TTX) source, Shanghai Institute of Applied Physics, Brookhaven National Laboratory, University of Science and Technology of China. For mitigating the space-charge forces, we also explore the using of MeV electron beam generated by a photocathode rf gun for ultrafast electron diffractions (UED) recently.

Using ultrashort high quality electron pulses from an S-band photocathode rf gun and a polycrystalline aluminium foil as the sample, we experimentally demonstrated a single-shot improved spatial resolution of MeV UED, as shown in Figure 4, in which the Debye–Scherrer rings of the (111) and (200) planes were clearly resolved. This result showed that MeV UED is capable to achieve an atomic level spatial resolution and a  $\sim 100$  fs temporal resolution simultaneously, and will be a unique tool for ultrafast structural dynamics studies.

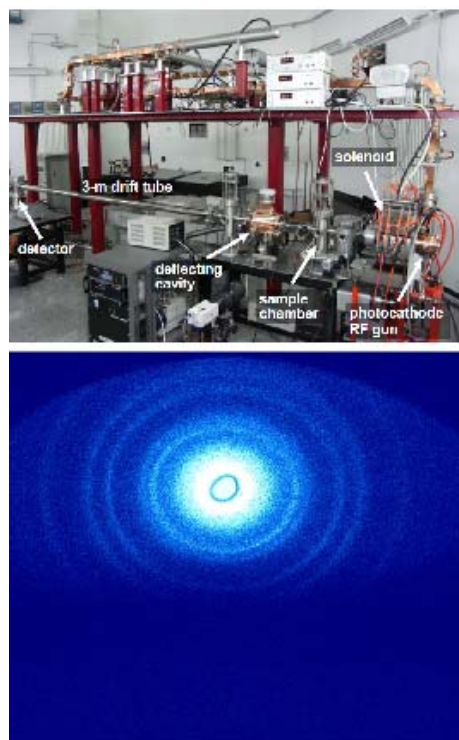


**Figure 4:** Layout of MeV UED and Measured diffraction pattern

We also have demonstrated single-shot continuously time-resolved MeV ultrafast electron diffraction using a static single crystal gold sample. As shown in Figure 5, an MeV high density electron pulse was used to probe the sample and then streaked by an rf deflecting cavity. The single-shot, high quality, streaked diffraction pattern allowed structural information within several picoseconds to be continuously temporally resolved with a  $\sim 200$  fs resolution. The temporal resolution can be straightforwardly improved to 100 fs by increasing the streaking strength. We are now developing the MeV UED facility at Tsinghua and foresee that this facility would become a powerful tool for ultrafast structural dynamics studies.

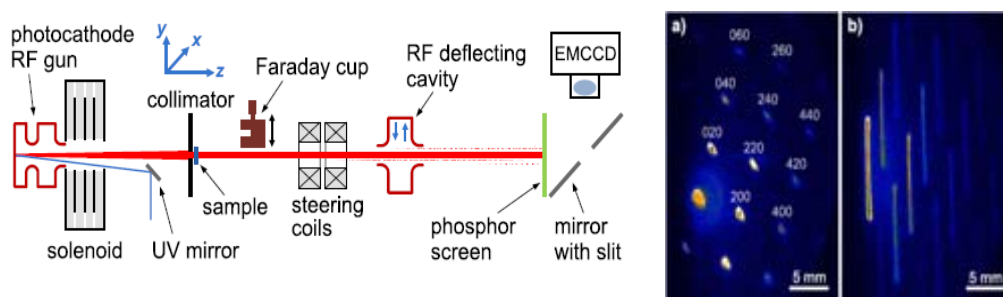


**Figure 5:** Schematic of a continuously time-resolved MeV UED system and measured diffraction pattern.

## 5.4 SRF Technology at Peking University

K. Liu, K. Zhao and J.E. Chen  
Institute of Heavy Ion Physics, Peking University, Beijing 100871, China  
Mail to: [kxliu@pku.edu.cn](mailto:kxliu@pku.edu.cn)

### 5.4.1 Introduction

RF superconducting technology has been developed at Peking University since 1988. At the early stage, a series of cavity was made mainly for research purpose. Recently we have designed and fabricated multi cell TESLA type superconducting cavities which are used in our DC-SRF photocathode injector, superconducting accelerator modules and other purposes. Except to develop cavity technology, we plan to build a SRF Energy Recovery Linac test facility (PKU-SETF) to provide coherent radiations.

### 5.4.2 RF Superconducting Cavities

2-cell, 3.5-cell, 5-cell and 9-cell TESLA type superconducting cavities have been made for different purposes. 3.5-cell and 9-cell cavities with end groups are typical ones. We have also developed QWR cavity and Spoke cavity for proton acceleration.

#### 5.4.2.1 3.5-Cell Cavity

The specially designed 3.5-cell cavity is made of large grain Nb. To compensate the deformation caused by Lorentz force and tuning, special reinforced stiffening ring is applied to the first cell, especially the first half cell so that the field flatness change within the  $\pm 200\text{KHz}$  tuning range is less than 3%. Simulations of various parameters have also been made to see the possible field of multipacting in the first cavity so as to ensure that no multipacting would occur at the operating field gradient. Because of the compact structure of the special end group, the possible cross talk between main coupler and pick up was also examined and it can be neglected at the SRF status. 3.5-cell cavity has been constructed under strict quality control, and the gradient reached 23.5 MV/m. (Fig.1) The field in the first half cell is actually the limiting factor of the field gradient.

#### 5.4.2.2 9-Cell Cavity

We have made three 9-cell TESLA cavities. Two of them has acceleration gradient of about 23MV/m and one reaches 28.6MV/m (Fig.2). This cavity is the first 9-cell cavity with end groups in China reaching a gradient usable for the ILC. The cavity is made of high purity niobium from Orient Tantalum Industry Corp. (OTIC), Ningxia. Successful bulk electro-polishing (EP) of PKU3 was made for this cavity and furnace vacuum heat treatment was applied to the cavity at 800°C for 2 hours. The field flatness was tuned to 97.9%. The Q slope might be due to the field emission by the sharp edges in the iris EBW regions. The cavity will be re-inspected for further improvement.

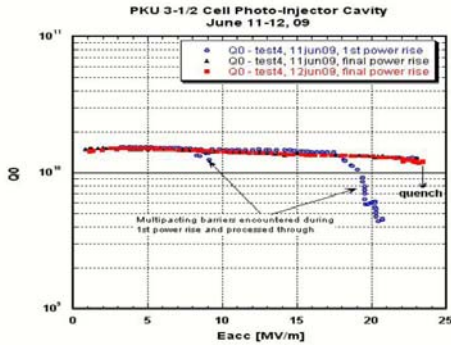


Figure 1: RF Test of 3.5-cell cavity at J-Lab

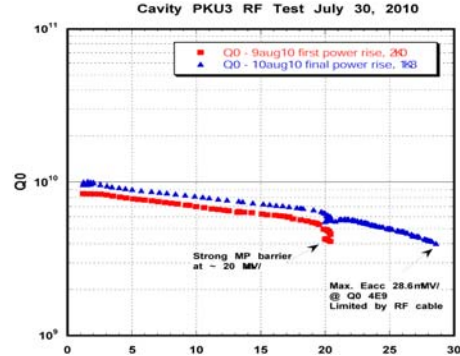


Figure 2: RF Test of 9-cell cavity at J-Lab

### 5.4.2.3 QWR and Spoke Cavity

A QWR superconductor cavity using sputtered niobium on copper was designed and manufactured. Acceleration gradient is about 3MV/m and proton beam was accelerated by this cavity with an energy gain of 500keV. A Spoke test cavity was also designed and fabricated recently and the preliminary RF test showed the acceleration gradient is about 3.4MV/m.

### 5.4.3 PKU-SETF

The PKU-SETF consists of mainly a 5 MeV DC-SRF injector and a cryomodule of 9-cell TESLA cavity working at 2k for accelerating electrons to 15-20 MeV. An energy recovery beam transport ring with two arcs is designed to match with the main accelerator. An undulator and a chicane are inserted in the ring to produce 4-8 micron laser light. The PKU-SETF will be implemented in about 3 steps. For the first step, the 5 MeV beam from the DC-SRF injector will be injected directly to an undulator to produce THz radiation. After the main accelerator and the energy recovery ring being commissioned, an ERL-CBS device will be constructed to produce high flux X-ray of ~10 keV. Finally with an 11.5 m long optical cavity, the IR laser light can be produced so that PKU-SETF can provide users with various kinds of radiations according to their needs (Fig.3). To realize these goals, cryomodule of DC-SF injector and the main accelerator have been constructed (Fig.4).

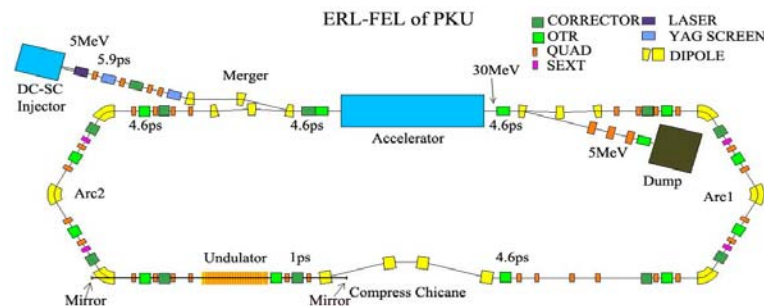


Figure 3: The PKU Energy Recovery Linac Test Facility





**Figure 4:** Cryomodule of DC-SF injector and the main accelerator

Great efforts have been made to reconstruct the old building into a new SRF Experimental Hall to house the PKU-SETF and related beam lines, control room, laser room, cleaning rooms for processing, assembling and tuning of SRF cavities as well as the whole cryogenic system so as to enable the DC-SRF injector and the accelerating cryomodule working under 2K for a number of applications. For this purpose the L-140 Helium liquefier and related cryogenic facility produced by the Linde Company have been installed and commissioned in the new SRF Hall. It can provide 120l/hr liquid He and about 60W cryogenic capability at 2K temperature.

## 5.5 New Low Charge Parameters for ILC

Dou Wang and Jie Gao, IHEP, Beijing 100049, China  
 Mail to: [wangdou@ihep.ac.cn](mailto:wangdou@ihep.ac.cn), [gaoj@ihep.ac.cn](mailto:gaoj@ihep.ac.cn)

Kiyoshi Kubo, KEK, 1-1 Oho, Tsukuba, Ibaraki 305-0801, Japan  
 Mail to: [kiyoshi.kubo@kek.jp](mailto:kiyoshi.kubo@kek.jp)

### 5.5.1 Introduction

The International Linear Collider (ILC) has been proposed to be a 500 GeV centre-of-mass electron-positron collider with a peak luminosity of  $2 \times 10^{34} \text{ cm}^{-2}\text{s}^{-1}$ . For the first time, the Reference Design Report (RDR) [1] gave a thorough description of ILC in 2007 (Table 1). The design in the RDR is based on 1.3 GHz superconducting RF cavities operating at a gradient of 31.5MV/m. The collider operates at a repetition rate of 5 Hz with a beam pulse length of roughly 1 msec. The site length is 31 km for the energy of 500 GeV and would have to be extended to reach 1 TeV. The beams are prepared in low energy damping rings that operate at 5 GeV and are 6.7 km in circumference. They are then accelerated in the main linacs which are about 12 km per side. Finally, they are focused down to very small spot sizes at the collision point with

an elaborated beam delivery system. The ILC outlined in the RDR design stands for a legacy of over fifteen-years R&D.

After the publication of RDR, ILC entered into the Technical Design Phase. With more consideration of cost issue except for machine performance in this new step, SB2009 [2] design began to be studied. The key parameters for SB2009 are also listed in Table 1. The major changes to the RDR baseline are summarised as follows:

- The number of bunches per pulse is reduced by a factor of two ( $n_b = 1312$ ) compared to the nominal RDR parameter set ( $n_b = 2625$ ) while keeping the same pulse length.
- The circumference of damping ring is reduced by a half ( $\sim 3.2\text{km}$ ).
- Undulator-based positron source is moved to the end of the electron Main Linac (250 GeV), in conjunction with a Quarter-wave transformer as capture device.
- A single-tunnel solution for the Main Linacs and RTML can be accepted.
- The simpler single-stage bunch compressor with a compression ratio of 20 is used instead of the original two-stage bunch compressor.

The advantages of this low beam-power parameter set are apparent. Total number of klystrons and modulators in Main Linacs and the AC power both for beam and refrigerators are reduced obviously. Also, the requirements for source are loosened because of lower beam power. All the modifications and simplifications for the machine were aim to cost efficiency.

Except for the merit of SB2009, we see some risks of this low power parameter. For example, collision stability may become a problem with the 38.4 disruption. Large photon (1.74) and hadron (3.6) production will make the noise background level in the detector much higher than the RDR design, and also the large beamstrahlung energy spread will enlarge the uncertainty of the physics experiments. In addition, the large disruption angle (0.48 mrad) may interfere with the detection of small-angle events. In order to mitigate the strong beam-beam effects and keep IP physics qualities, a new low charge parameter is proposed in the beginning of 2011 (see Table 1) [3]. For this report we will focus on the main modifications and the impact of this new parameter.

**Table 1:** New low charge parameters compared to the RDR and SB2009 parameter set.

<i>Parameter</i>	<i>Nominal RDR</i>	<i>SB2009</i>	<i>RDR Low charge</i>	<i>New low charge</i>
$E_{cm}$ (GeV)	500	500	500	500
Ne	$2 \times 10^{10}$	$2 \times 10^{10}$	$1.0 \times 10^{10}$	$1.0 \times 10^{10}$
$F_{rep}$ (Hz)	5	5	5	5
$N_b$	2625	1320	5640	2625
$P_b$ (MW)	10.5	5.3	11.3	5.37
$\beta_x$ (mm)	20	11	12	8
$\beta_y$ ( $\mu\text{m}$ )	400	200	200	166
$\gamma\epsilon_x$ ( $\mu\text{m}$ )	10	10	10	10
$\gamma\epsilon_y$ (nm)	40	36	30	10
$\sigma_x$ (nm)	639	474	495	404
$\sigma_y$ (nm)	5.7	3.8	3.5	2.0
$\sigma_z$ ( $\mu\text{m}$ )	300	300	150	166
$\delta_B$	0.031	0.056	0.026	0.0241
$n_\gamma$	1.3	1.74	0.832	1.01
Dy	19.0	38.4	10.0	24.0
$H_D$	1.74	1.63	1.56	1.6
$\theta$ (rad)	0.00036	0.00048	0.00023	0.00029
$N_{had}$	1.1	3.6	0.21	0.66
Trav. focus	No	Yes	No	No/Yes
$L_0$ ( $\text{cm}^{-2}\text{s}^{-1}$ )	$2.0 \times 10^{34}$	$1.9 \times 10^{34}$	$2.0 \times 10^{34}$	$2.0 \times 10^{34} / 2.4 \times 10^{34}$
Bunch separation (ns)	356	680	178	356
$I_b$ (mA)	9	4.7	9	4.6
Efficiency form RF to beam	61%	44%	63%	44%
AC power for beam (MW)	108	76	112	76
AC power for refrigerators (MW)	9	13	10	13
Total AC power (MW)	117	89	122	89

### 5.5.2 Main Changes in the New Low Charge Parameters Compared to SB2009

As we known, SB2009 has strong beam-beam effects so that the IP physics qualities may be degraded. Since the aim of the machine construction is to realize good physics experiments, we should not sacrifice the physics qualities for cost reduction. Meanwhile, we still have some potential difficulties to produce the polarized positron with  $2 \times 10^{10}$  bunch charge. So, in order to keep the qualities of IP physics experiments and balance the technical difficulties for all the subsystems, we decrease the bunch charge from  $2 \times 10^{10}$  to  $1 \times 10^{10}$ .

Because of reducing the bunch charge by a half, the bunch number per train can be increased twice assuming the same 3.2 km damping ring as SB2009.

Besides the changes of bunch charge and bunch number, the bunch length at the collision point is reduced from original 300  $\mu\text{m}$  to 166  $\mu\text{m}$ . So the two-stage bunch

compressor will be needed and a new design for bunch compressor to get 160  $\mu\text{m}$  is inevitable.

### 5.5.3 Advantages of the New Low Charge Parameter

- The beam-beam effects are reduced significantly compared to SB2009. The IP physics qualities are even better than the RDR design.
- Reducing the bunch charge by a half will mitigate the difficulties for source further especially for the positron source.
- The highlight of low beam power and low AC power in SB2009 is kept.
- Emittance preservation in RTML and ML will be easier with the low charge parameter.
- Two-stage bunch compressor gives more flexibility to the whole machine.
- Travelling focus is not needed as SB2009. But travelling focus is still good for option. With this technique we can upgrade the luminosity to  $2.4 \times 10^{34} \text{ cm}^{-2}\text{s}^{-1}$ .

The new low charge parameter assumes to use the same damping ring (3.2 km) layout as SB2009. Because the beam current is same as SB2009 but the bunch density is lower, the performance of damping ring should be a little better than SB2009 parameter (1310 bunches and  $2.0 \times 10^{10}$  particles per bunch). The new low charge parameter needs 10 nm IP vertical emittance so that the extract vertical emittance from damping ring should be about 5 nm. Then the transverse damping time for the damping ring should be decreased from 23 ms to 17 ms. The modification of damping ring compared to SB2009 will be only strengthen the wigglers a little or lengthen them by 35%. The production of ultra-low vertical emittance still is an issue to be confirmed.

One thing we want to emphasize is that the two-stage bunch compressor is a better choice than the single-stage at the primary phase of machine construction. It will be difficult for one-stage bunch compressor to get the bunch length shorter than 300  $\mu\text{m}$ . With the two-stage bunch compressor, we have a spring to transfer technical difficulty from one subsystem to another without compromising IP physics qualities. Since the cost saving by one-stage bunch compressor is very limited, we don't need to shrink the bunch compressor and sacrifice the machine flexibility.

### 5.5.4 New Design for the Two-Stage Bunch Compressor

According to the new low charge parameter, we made a new design for the two-stage bunch compressor to get the 166  $\mu\text{m}$  bunch length. From table 2, we can see that all the requirements for ILC bunch compressor can be achieved. Also we can see that the average energy spread in the bunch compressor is much smaller than the RDR parameter. So it will be expected emittance preservation in bunch compressor is even better than RDR design.

**Table 2:** New design of two-stage bunch compressor for ILC new low charge parameter.

<i>Parameter</i>	<i>BC1</i>	<i>BC2</i>
Initial energy (GeV)	5	4.95
Initial energy spread (%)	0.13	0.8
Initial bunch length (mm)	6	0.95
RF voltage (GV)	0.25	13.66
RF Phase (Deg)	-101	-43
$R_{56}$ (mm)	-738	-60
Final energy (GeV)	4.95	15
Final energy spread (%)	0.8	1.6
Final bunch length (mm)	0.95	0.16

### 5.5.5 References

1. ILC GDE, “International Linear Collider Reference Design Report”, August 2007.
2. ILC GDE, “SB2009 Proposal Document”, Release 1.1, December 2009.
3. D. Wang, J. Gao, K. Kubo, “New Low Charge Parameters for ILC”, 2nd Baseline Assessment Workshop, SLAC, January 2011.

## 5.6 First Beam Manipulation and Measurements in the Final Focus Beam Line at the KEK Accelerator Test Facility

Sha Bai for the ILC group, IHEP, Beijing, China  
P. Bambade, LAL, Orsay, France  
Mail to: [baisha@ihep.ac.cn](mailto:baisha@ihep.ac.cn)

### 5.6.1 Introduction

The Accelerator Test Facility 2 (ATF2) [1,2] is the test facility with an International Linear Collider (ILC) [3] type final focus line, to reach a final beam size of 37 nm at the optical focal point (hereafter referred to as IP, interaction point, by analogy to the linear collider collision point). How to tune this small nanometer beam size in both simulation and experiment is a crucial point. During the initial commissioning, from November 2008 to March 2009, we used a large  $\beta$  optics with 20 times  $\beta_x$  (0.08m) and 800 times  $\beta_y$  (0.08m) at the IP and turned off all the five sextupoles in ATF2 line to reduce the high-order optical aberrations [4]. In April 2009, we started using 20 times  $\beta_x$  (0.08m) and 100 times  $\beta_y$  (0.01m) (see Table 1). For the optical correction methods which are planned for the designed optics ( $\beta_y=0.0001\text{m}$ ), sextupole multiknobs are used; while for the initial commissioning, we needed something different for rough adjustments in the large  $\beta$  optics mode. During the commissioning, to measure such a small beam size at the IP, a “Shintake” monitor [5] based on colliding the beam with the interference pattern from lasers is used [6]. In addition, wire scanners with diameters 10 and 5 $\mu\text{m}$ , respectively in tungsten and carbon, are placed 40cm behind the IP to measure the beam sizes during initial tuning, with resolutions of about 2.5 and 1.25 $\mu\text{m}$ . When these wire scanners were used, the waists in both planes were moved to the post-

IP location by readjusting the currents of the final doublet QD0 and QF1 quadrupole magnets [7].

In this paper, the simulation results of the beam size correction and some further work needed for the practical implementation of waist scan, dispersion, coupling and  $\beta$  function multiknobs during commissioning is first outlined. Then since the first complete beam waist measurements at the ATF2 IP were done during the Spring commissioning in 2009, these measurements were used to provide first estimates of Twiss parameters at the IP and of the horizontal emittance, before implementing systematic optical corrections. The results obtained, using two analysis methods, are described in this paper.

**Table 1:** Beam parameters with Nominal and Large  $\beta$  Optics.

	<b>Large <math>\beta</math> optics</b>		<b>Nominal <math>\beta</math> optics</b>	
	<b>Nominal IP</b>	<b>Wire scanner</b>	<b>Nominal IP</b>	<b>Wire scanner</b>
<b><math>\beta_x(\text{cm})</math></b>	8.0	9.90	0.4	0.495
<b><math>\beta_y(\text{cm})</math></b>	1.0	1.84	0.01	0.0184
<b><math>\sigma_x(\mu\text{m})</math></b>	12.7	14.1	2.80	3.15
<b><math>\sigma_y(\mu\text{m})</math></b>	0.343	0.466	0.0343	0.0466
<b>QD0 current(A)</b>	130.34	105.24	130.34	105.24
<b>QF1 current(A)</b>	70.84	66.87	70.84	66.87

## 5.6.2 Simulation on Multiknobs Correction

### 5.6.2.1 Multiknobs Correction Analysis

Since the beam line is not perfect, there are various kinds of strength errors of the magnets and also alignments, rotation errors, etc... Thus, when the beam goes through the beam line with these imperfect magnets, particle orbits will be different from the ideal ones, as a result, a larger than the nominal beam size is got at the IP, which is beyond our expectation. In order to train correcting those imperfections or errors of the beam line, we choose 1mrad rotation errors and 1% strength errors at all quadrupoles in ATF2 line to see obvious effect and simulate the scanning of the minimum vertical beam size using the coupling and dispersion corrections with skew quadrupoles, the  $\alpha$  waist scan knobs with final doublet (QD0 and QF1 - a pair of quadrupoles which are at the end of the ATF2 beam line just before the IP) and the  $\beta_y$  knob with one matching quadrupole - QM12 which is located at the beginning of the final focus line.

### 5.6.2.2 Simulation Results on Multiknobs Correction

Simulation to scan the minimum vertical beam size (tracking in MAD with energy spread 0.0008) using the coupling and dispersion corrections with skew quadrupoles,  $\alpha$  waist scan knobs with final doublet and the  $\beta_y$  knob with QM12 were done at the Post-IP. We choose first to scan in only a single iteration step by step within the strength limits of all the magnets. Fig. 1 shows the results after the multiknobs correction. The histograms show the vertical beam sizes distribution after successive multiknobs scans

to find the minimum values, while the left dashed and right solid lines show the ideal beam size and average beam size after correction respectively.

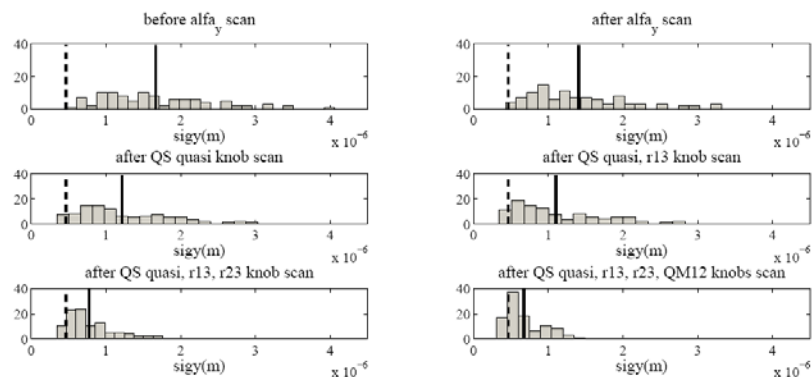


**Figure 1:** After multiknobs correction to find the minimum vertical beam size at Post-IP

The vertical beam size goes down to  $6.7e-7\text{m}$  which is close to the ideal vertical beam size  $4.67e-7\text{m}$ , but at around 1 micron, there are some badly corrected seeds, amounting to about 15% of the total. After analysis of the phase space of these abnormal seeds, obvious correlation can be seen and some coupling still remained. It means that another iteration of the multiknobs scan is needed. A simulation study with the multiknobs scan correction another two times is shown in Figure 2, which indicates that after the two another iterations, the vertical beam size goes down to very close to the ideal beam size.

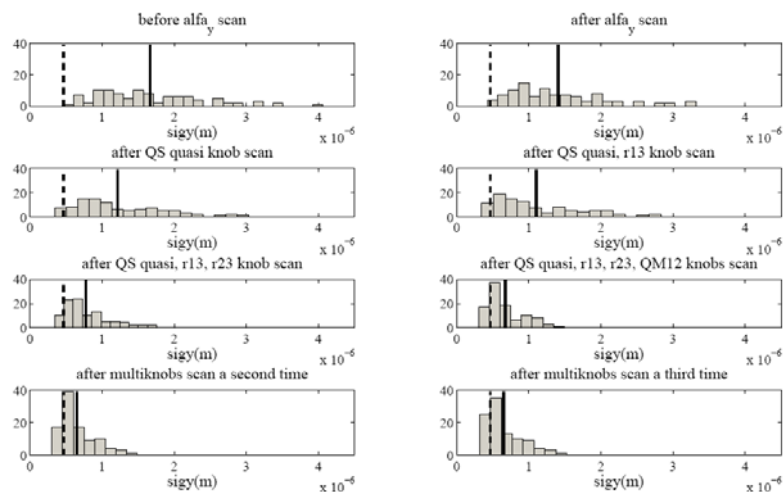


**Figure 2:** After multiknobs scan correction another two times to find the minimum vertical beam size at Post-IP.

When shifting back from the Post-IP to IP, the vertical beam size simulated is preserved which can be seen from Figure 3. Thus, since the Shintake monitor that installed at the IP is still under preparation for nanometer measurement resolution, the simulation study of beam size multiknobs correction in this paper makes tuning at the Post-IP feasible to prepare the beam for the Shintake monitor.

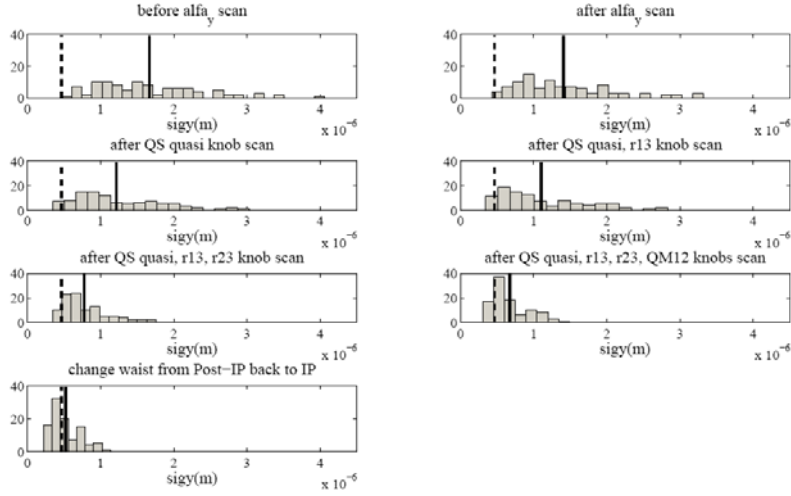


**Figure 3:** Results after shifting back to IP.

As stated before, the simulation is scanned in all the magnet strength limits, but there is an exception. The QK2X, QK3X which have the strength limit 5 amperes before were found not big enough for the scan. So the power supplies of the skew quadrupoles QK1X, QK2X, QK3X, and QK4X were changed to 20 amperes at KEK to match the requirements [8].

### 5.6.2.3 Summary and Prospects

Large  $\beta$  optics mode has been chosen for the initial commissioning, and in this optics mode, a simulation of coupling, dispersion, waist scans and  $\beta$  function correction multiknobs was done in the presence of magnet strength and roll errors. A vertical beam size which is very close to the ideal beam size was obtained. In the ATF2 commissioning, a reasonable initial correction of the beam size could be realized by setting these knobs in a single iteration according to this procedure and can be improved in several iterations.

## 5.6.3 Twiss Parameter Estimation

### 5.6.3.1 Parametrisation of Beam Sizes Around the IP and Post-IP Waists

The measurements consisted in varying the QD0 magnet current and recording horizontal and vertical beam sizes with the post-IP wire scanners. In the vicinity of the IP waists, the beam sizes  $\sigma_x$  and  $\sigma_y$  can be shown to depend on beam parameters and on the longitudinal displacement  $\Delta f_{x,y}$  of each waist from the nominal location according to [9]:

$$s_{x,y}^2 = e_{x,y} b_{x,y} + \frac{e_{x,y}}{b_{x,y}} Df_{x,y}^2 \quad (1)$$

where  $\beta_{x,y}$  and  $\epsilon_{x,y}$  are the horizontal and vertical  $\beta$  functions and emittances, respectively. By fitting parabolic dependencies to the measured data as function of the QD0 magnet currents, the parameters in (1) could be determined. For both the emittance and  $\beta$  function to be determined simultaneously, it is essential that the minimum beam



size at the waist be resolved. This was the case in the horizontal but not in the vertical plane. For the latter, estimates of the  $\beta$  function could still be inferred from the second term in (1), without requiring the minimum beam size to be resolved, by using values for the emittance measured upstream, for example, after extraction from the damping ring or within the damping ring.

As explained, the square of the beam size in the vicinity of the IP or post-IP has a parabolic dependence with the longitudinal waist displacements  $\Delta f_{x,y}$ , see Equation (1). For small variations  $\Delta Q$  of the QD0 quadrupole magnet integrated strength, Equation (1) can be approximated by:

$$s_{x,y}^2 = e_{x,y} b_{x,y} + \frac{e_{x,y}}{b_{x,y}} (DQ \times a_{x,y})^2 \quad (2)$$

where  $a_{x,y}$  are constants determined from the optical lattice using simulation<sup>3</sup>. When the optics is set to focus the beam to a waist at the post-IP wire scanner,  $a_{x,y} = 3.43, 2.23$  square meters. The variations of the beam sizes with QD0 strength are shown for illustration in Figure 4 from the simulation, when setting the optics to focus the beam to a waist at either the IP or post-IP locations.

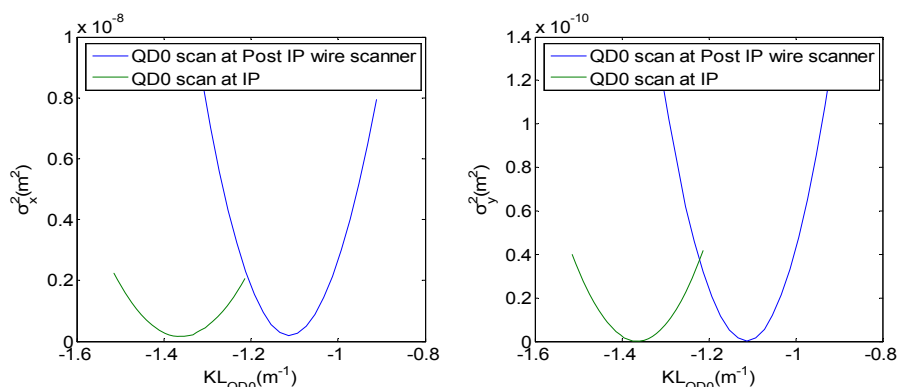


**Figure 4:** Simulated beam size squared with respect to QD0 strength in the  $\beta_{x,y} = 0.08/0.01\text{m}$  ATF2 optics, when focusing the beam to a waist at the IP (green curves) or post-IP (blue curve) locations.

### 5.6.3.2 Estimation of Twiss Parameters and of Horizontal Emittance

Using the corrected beam sizes, parabolas of form  $\sigma^2(KL_{QD0}) = A(KL_{QD0} - B)^2 + C$  were fitted to the data taking into account the measurement errors, using the GNU PLOT software. The results are displayed in Table 2 and in Figures 5 and 6, where the green and red lines correspond, respectively, to the data corrected only for the wire size or corrected for both the wire size and dispersion.

<sup>3</sup> Variations in  $\beta_{x,y}$  as the integrated strength of the QD0 quadrupole magnet is changed, of order  $\Delta f_{x,y}/L^* \sim \beta_{x,y}/L^*$ , where  $L^* = 1$  meter is the distance between the exit of the final doublet and the IP, are neglected in (2). The induced biases, amounting to less than a few per mil in the nominal  $\beta$  optics and a few percent in the present large  $\beta$  configuration, are neglected in the following.

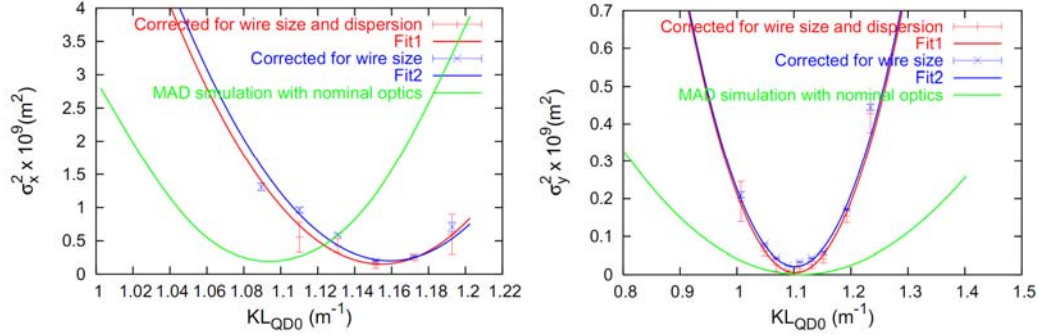


**Figure 5:** Squares of horizontal and vertical beam sizes (upper plot) as a function of QD0 magnet strength on May 20 compared to the predictions from the optics simulation for the design large  $\beta$  optics.  $KL_{QD0}$  are the integrated QD0 magnet strengths, which are computed from the power supply currents using relations based on the magnetic measurement data [10].

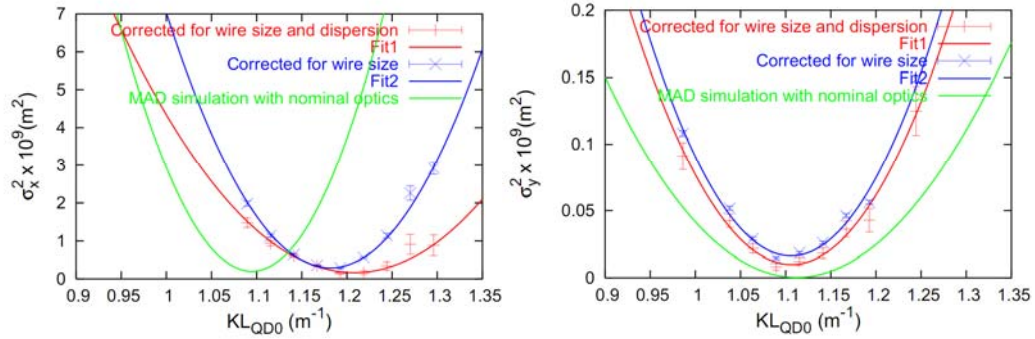


**Figure 6:** Squares of horizontal and vertical beam sizes (lower plot) as a function of QD0 magnet strength on May 28 compared to the predictions from the optics simulation for the design large  $\beta$  optics.  $KL_{QD0}$  are the integrated QD0 magnet strengths, which are computed from the power supply currents using relations based on the magnetic measurement data [10].

**Table 2:** Results of fitting parabolas to the squares of the horizontal and vertical beam sizes.

	$A[m^4]$	$B[m^{-1}]$	$C[m^2]$	$Cov(A,C)$
<b>May 20 X</b>	$(2.97 \pm 0.94)e-7$	$1.154 \pm 0.003$	$(1.49 \pm 0.38)e-10$	-0.605
<b>May 20 Y</b>	$(1.97 \pm 0.18)e-8$	$1.102 \pm 0.003$	$(4.96 \pm 3.57)e-12$	-0.502
<b>May 28 X</b>	$(9.64 \pm 0.91)e-8$	$1.208 \pm 0.004$	$(1.61 \pm 0.22)e-10$	0.161
<b>May 28 Y</b>	$(5.92 \pm 0.49)e-9$	$1.106 \pm 0.003$	$(9.80 \pm 1.57)e-12$	-0.495

Two methods were used to estimate the Twiss parameters and emittance from the parameters of these parabolas.

The first method, referred to as *method 1*, consists in evaluating the  $\beta$  parameter at the waist from the angular divergence contribution in the second term on the right hand side of Equation (2), using as input the emittance measured upstream, e.g. in the ATF2 diagnostic section (using methods described in [11]) or in the damping ring [12]. Equating the parabolic form fitted to the data with Equation (2) then yields:

$$\begin{aligned}
s^2 &= e_{EXT} b (1 + a^2 DQ^2 / b^2) \\
&= A(KL_{QD0} - B)^2 + C \\
&= ADQ^2 + C
\end{aligned}$$

One gets:

$$\begin{aligned}
A &= e_{EXT} a^2 / b \\
b &= e_{EXT} a^2 / A
\end{aligned} \tag{3}$$

where  $\varepsilon_{EXT}$  is the emittance used as input based on upstream measurements.

The second method, referred to as *method 2*, exploits the full information in the parabolic fit to infer both the  $\beta$  parameter and the emittance at the waist, by equating:

$$A = ea^2 / b \quad C = eb \tag{4}$$

One gets:

$$e = a^{-1} \sqrt{AC} \quad b = a \sqrt{\frac{C}{A}} \tag{5}$$

It should be noted that *method 2* is affected by large biases when the minimum of the parabola is smaller than the instrumental resolution, as is the case in the vertical plane, or when it includes significant residual optical aberrations, such as residual dispersion, cross-plane coupling effects or chromaticity. This method was therefore only used to analyze parameters in the horizontal plane, while *method 1* could be used for both sets of measurements.

It is important in both methods to include measurements far enough on both sides of the minimum of the parabola, such that the quadratic term in equation (2) is well fitted. In practice, beam sizes at least two or three times the minimum are sufficient.

The horizontal and vertical Twiss parameters and the horizontal emittance obtained applying both methods to the data collected on May 20 and 28 are listed in Table 3. The horizontal and vertical emittances used as inputs for *method 1* were 1.86nm and 20pm for the data collected on May 20, and 1.7nm and 11.5pm for those collected on May 28, based on measurements in the diagnostic section earlier in each of the two shifts.

**Table 3:** Twiss parameters and horizontal emittance computed from post-IP wire scanner measurements, compared with nominal values. The listed uncertainties result from propagating the errors in Equation (2), taking into account the measured beam size statistical fit errors in Table 2, the measured dispersion errors and a 7% uncertainty from the finite wire size correction.

		$\varepsilon_x$ [m.rad]	$\beta_x$ [m]	$\alpha_x$	$\varepsilon_y$ [m.rad]	$\beta_y$ [m]	$\alpha_y$
<b>Nominal values</b>		2.0 e-9	0.099	0	1.2 e-11	0.018	0
<b>May 20</b>	<b>Method 1</b>	1.86 e-9	0.074 ± 0.023	-2.40	2 e-11	0.0051 ± 0.0001	-0.205
	<b>Method 2</b>	(1.94 ± 0.25) e-9	0.076 ± 0.019	-2.40			
<b>May 28</b>	<b>Method 1</b>	1.7 e-9	0.21 ± 0.02	-1.744	1.15 e-11	0.0096 ± 0.0001	0.816
	<b>Method 2</b>	(1.15 ± 0.10) e-9	0.14 ± 0.01	-1.744			

### 5.6.3.3 Discussion

The consistency of the results from *methods 1* and *2* was good for the horizontal emittance and  $\beta$  function using the data set from May 20 and agreed reasonably well with the nominal values. The results using the data set on May 28 showed discrepancies at the 50 percent level, indicating that input matching conditions of the beam had probably changed.

On the other hand, in both data sets the dispersion and  $\alpha_x$  Twiss parameter were mismatched in similar ways, and the estimated vertical  $\beta$  functions were also distorted.

Since these first measurements were performed before implementing optical corrections systematically, uncertainties in the input emittances used in *method 1* could not be properly accounted for. The beam intensity during the data taking on May 20 and 28 was recorded to be about  $4 \times 10^9$  particles per bunch. For such intensity, the expected horizontal emittance is about 1.4nm [13]. Using this value rather than that which was measured in the diagnostic section on May 28 (1.7nm) would yield a somewhat improved agreement. Similarly, for the vertical  $\beta$  function, using the vertical emittance measured in the diagnostic section as input to *method 1* probably lead to an underestimation as cross-plane coupling or dispersion effects were not fully corrected in that measurements.

In an attempt to explain the principal mismatches observed in the May 20 and May 28 data sets – for the horizontal dispersion and  $\alpha_x$  Twiss parameter – a set of orthogonal knobs defined for  $D_x$  and  $\alpha_{x,y}$  [14] using the QD0 and QF1 final doublet magnets and QF9, a focusing quadrupole located at a high dispersion point in the upstream part of the chromatic correction section of the final focus section, were used to simulate a correction. It was found that correction could easily be achieved with these knobs, with similar settings in both weeks, implying perhaps some systematic error in the magnetic transport. Trying to reproduce the measured  $\alpha_{x,y}$  Twiss parameters with QD0 and QF1 alone, without using QF9, resulted in values for the horizontal dispersion which were not compatible with the observed ones, indicating that the error that would explain the behavior was not confined to the final doublet magnets.

A set of six matching quadrupole magnets located upstream of the final focus section, intended as part of the  $\beta$  matching procedure of the beam into the final focus section, were also tried to simulate a simultaneous correction of both waist shifts and of the mismatch in  $\beta_x$  and  $\beta_y$  at the IP. The resulting values for these six quadrupole magnets were all found to be within their operational ranges. They were a bit different in each shift, which showed that the betatron matching from the DR probably had changed.

### 5.6.4 References

1. Grishanov B I et al. 2005, Report No. SLAC-R-771.
2. Bambade P. et al. Phys. Rev. ST Accel. Beams. 2010, 13:042801
3. ILC RDR, ILC-Report-2007-001.
4. BAI Sha et al. Phys. Rev. ST Accel. Beams 13, 092804 (2010)
5. T. Shintake, Nucl. Instr. Meth. A311, 453 (1992)
6. T. Yamanaka *et al.*, IEEE NSS08 Conf. Record, 3308 (2008)
7. S. Bai et al., “Optical configurations with variable  $\beta^*$  at different IP locations in ATF2”, ATF-Report 08-05 (2008)
8. Terunuma N., private communication.

9. H. Wiedemann, "Particle Accelerator Physics", Springer, 1999
10. C. Spencer et al., "A project to design and build the magnets for a new test beam line, the ATF2, at KEK", Presented at the 21st International Conference on Magnet Technology October 2009, Accepted for publication in IEEE Trans. Appl. Supercon.
11. I. Agapov, G. A. Blair, M. Woodley, Phys. Rev. ST Accel. Beams 10, 112801 (2007)
12. K. Kubo et al., Proceedings of PAC09, FR1RAC05
13. Y. Honda et al., PHYS. REV. LETT. 92, 054802 (2004)
14. B. Bolzon et al., "Linear collider test facility: Twiss parameter analysis at the IP/Post-IP location of the ATF2 beam line", IPAC2010, THPD077.

## 5.7 Linac Beam Mismatch Modes for Unequal Transverse Tunes

G. H. Rees

ASTeC, Rutherford Appleton Lab, STFC, Chilton, Didcot, Oxon OX11 0QX, UK

Mail to: [ghrees@stfc.ac.uk](mailto:ghrees@stfc.ac.uk)

### 5.7.1 Introduction

Linac bunches have three types of mismatched, envelope oscillation modes [1,2]. If the transverse tunes and emittances are equal, one mode has no longitudinal envelope motion and its pure quadrupole, transverse envelope oscillations have opposite phases. The other two, a high and a low mode, both have longitudinal-transverse coupling and in-phase, transverse envelope motions. High and low modes differ in that longitudinal and transverse envelope motions of the former are in phase, while those of the latter are out of phase. In [2], the mode tunes and the ratios for the three envelope amplitudes are derived approximately in terms of the two zero and two full current tunes.

For unequal transverse tunes, all three modes have longitudinal-transverse coupling, though it is small in the "near" quadrupole mode. Revised equations are derived in terms of the three zero current, and the three, beam current and emittance dependent, tunes. The conditions considered for unequal, zero current transverse tunes,  $\sigma_{y0}/\sigma_{x0} = m$ , are:

Condition	$\sigma_{y0}/\sigma_{x0}$	$\varepsilon_y/\varepsilon_x$	$a_{y0}/a_{x0}$
Transverse equipartitioning	$m$	$1/m$	$1/m$
Equal transverse emittances	$m$	$1$	$1/\sqrt{m}$
Equal transverse amplitudes	$m$	$m$	$1$

Despite the different space charge tune shifts, the mode frequencies and amplitude ratios may be found approximately, for each case, in terms of the zero current ( $\sigma_{y0}$ ,  $\sigma_{x0}$ ,  $\sigma_{z0}$ ) and full current tunes ( $\sigma_y$ ,  $\sigma_x$ ,  $\sigma_z$ ). The analysis follows the assumptions of reference [2], viz:

- the external forces acting on the bunch are linear in  $x$ ,  $y$  and  $z$ , and periodic in  $z$
- the ellipsoidal, bunch shape has semi-axes  $a_x$ ,  $a_y$  and  $a_z$  in the laboratory frame
- the bunch has a uniform charge density, so that space charge forces are linear
- the normalized emittances of the bunch remain constant in the  $x$ ,  $y$  and  $z$  planes

Analysis of [2] is given in an Appendix up to a point where smooth approximations lead to three, linear homogeneous equations for the mismatch modes. These define only stable solutions as all instability information is lost by the approximations. In the case of equal transverse tunes and emittances, equations for envelope mode tunes and amplitude ratios may be approximated and solved directly. When  $\sigma_y \neq \sigma_x$ , however, one equation in [2] has to be modified, and the tunes have then to be found by repeated small corrections. The effects of the non-linearity of the envelope equations are also considered.

### 5.7.2 Case of Equal Transverse Tunes

Mismatch mode equations (I) of the Appendix are solved for the relative mismatches:  $\Delta a_x/a_x = A e^{iks}$ ,  $\Delta a_y/a_y = B e^{iks}$  and  $\Delta a_z/a_z = C e^{iks}$ , where  $Q = kL/2\pi = \sigma/2\pi$  is an envelope mode tune for the periodic cell length,  $L$ . On substituting the ratios into the equations (I), three new linear homogeneous equations are found in terms of  $A$ ,  $B$  and  $C$ . In the case of equal transverse tunes and emittances ( $\sigma_{x0} = \sigma_{y0}$ ,  $\sigma_x = \sigma_y$ ,  $\varepsilon_x = \varepsilon_y$ ,  $a_{x0} = a_{y0}$ ,  $a_x = a_y$ ), the equations (I) become:

$$\begin{aligned}(\sigma_{x0}^2 + 3\sigma_x^2 - \sigma^2) A + (\sigma_{x0}^2 - \sigma_x^2) B + (\sigma_{x0}^2 - \sigma_x^2) C &= 0 \\(\sigma_{x0}^2 - \sigma_x^2) A + (\sigma_{x0}^2 + 3\sigma_x^2 - \sigma^2) B + (\sigma_{x0}^2 - \sigma_x^2) C &= 0 \dots\dots\dots(1) \\(\sigma_{z0}^2 - \sigma_z^2) A + (\sigma_{z0}^2 - \sigma_z^2) B + (\sigma_{z0}^2 + 3\sigma_z^2 - \sigma^2) C &= 0\end{aligned}$$

The equations' determinant is set to zero to find solutions for the envelope tunes,  $\sigma$ :

$$\begin{aligned}(\sigma_{x0}^2 + 3\sigma_x^2 - \sigma^2) [(\sigma_{x0}^2 + 3\sigma_x^2 - \sigma^2)(\sigma_{z0}^2 + 3\sigma_z^2 - \sigma^2) - (\sigma_{z0}^2 - \sigma_z^2)(\sigma_{x0}^2 - \sigma_x^2)] \\+ (\sigma_{x0}^2 - \sigma_x^2)^2 [(\sigma_{z0}^2 - \sigma_z^2) - (\sigma_{z0}^2 + 3\sigma_z^2 - \sigma^2)] + \\(\sigma_{x0}^2 - \sigma_x^2) [(\sigma_{z0}^2 - \sigma_z^2)(\sigma_{x0}^2 - \sigma_x^2) - (\sigma_{z0}^2 - \sigma_z^2)(\sigma_{x0}^2 + 3\sigma_x^2 - \sigma^2)] = 0\end{aligned}$$

$$\text{Thus: } (4\sigma_x^2 - \sigma^2) [(\sigma_{z0}^2 + 3\sigma_z^2 - \sigma^2)(2\sigma_{x0}^2 + 2\sigma_x^2 - \sigma^2) - 2(\sigma_{z0}^2 - \sigma_z^2)(\sigma_{x0}^2 - \sigma_x^2)] = 0 \dots\dots (2)$$

$$\text{One solution is a pure quadrupole mode, with envelope tune: } \sigma = 2\sigma_x = 2\sigma_y \dots\dots\dots (3)$$

The  $z$  independent motion has  $C = 0$ ,  $A = -B$ , and thus out of phase  $\Delta a_x$  and  $\Delta a_y$  motions. The high and the low mode, envelope motion tunes (4) differ from those of reference [2] in having the factor two, instead of one, in the final term under the square root.

$$\begin{aligned}\sigma^4 - \sigma^2(2\sigma_{x0}^2 + 2\sigma_x^2 + \sigma_{z0}^2 + 3\sigma_z^2) + 2(\sigma_{x0}^2 + \sigma_x^2)(\sigma_{z0}^2 + 3\sigma_z^2) - 2(\sigma_{z0}^2 - \sigma_z^2)(\sigma_{x0}^2 - \sigma_x^2) &= 0 \\ \sigma^2 = \sigma_{x0}^2 + \sigma_x^2 + 1/2 (\sigma_{z0}^2 + 3\sigma_z^2) \pm [(\sigma_{x0}^2 + \sigma_x^2 - 1/2 (\sigma_{z0}^2 + 3\sigma_z^2))^2 + 2(\sigma_{x0}^2 - \sigma_x^2)(\sigma_{z0}^2 - \sigma_z^2)]^{1/2} &\dots\dots\dots(4)\end{aligned}$$

It may be seen, from the three, initial equations (1), that when  $C \neq 0$ ,  $A = B$ , and  $C/B$  is:

$$C/B = \sigma^2 - 2(\sigma_{x0}^2 + \sigma_x^2) / (\sigma_{x0}^2 - \sigma_x^2) \dots\dots\dots(5)$$

The high and low coupled modes have positive and negative C/B, respectively. Envelope motions in all three planes are thus in phase for the high mode, while the low mode has a longitudinal oscillation which is out of phase with its in-phase, transverse motions.

As an example, consider:  $\sigma_{z0}/\sigma_{x0} = 1.50$ ,  $\sigma_z/\sigma_{x0} = 1.28$ ,  $\sigma_x/\sigma_{x0} = 0.64$  and  $\sigma_z/\sigma_x = 2.00$ . The tune ratios, for the pure quadrupole mode, the high and the low coupled modes, are:

$$\sigma/\sigma_x \text{ (quadrupole)} = 2.00 \quad \sigma/\sigma_x \text{ (high)} = 4.23 \quad \sigma/\sigma_x \text{ (low)} = 2.55$$

The most and least likely source of halo is the quadrupole and high mode, respectively.

### 5.7.3 Instability for Equal Transverse Tunes

As noted earlier, the smooth approximations result in loss of instability information, with only stable solutions being defined. Instability studies need beam tracking but, it is advisable, before tracking, to avoid a value of  $Q = \sigma/2\pi \approx 0.5$  for the high mode tune. In the example of the previous section, this requires  $Q_x < \approx 0.1182$ , and corresponds, for the zero and the full beam currents, to betatron phase shifts per cell of  $< 66.5^\circ$  and  $42.6^\circ$ , respectively. This does not usually present a serious constraint.

### 5.7.4 Case of Unequal Transverse Tunes

For  $\sigma_y \neq \sigma_x$ , the earlier  $\Delta a_x$  and  $\Delta a_z$  equations (1) remain unchanged, but that for  $\Delta a_y$  is modified as in (6), where  $n_1 = (\sigma_{y0}^2 - \sigma_y^2) / (\sigma_{x0}^2 - \sigma_x^2)$  and  $n_2 = (\sigma_{y0}^2 + 3\sigma_y^2) / (\sigma_{x0}^2 + 3\sigma_x^2)$ . A 3-D, rms, envelope matching code may be used to find  $\sigma_y$ ,  $\sigma_x$ ,  $n_1$  and  $n_2$  values for the linac cell and beam bunches involved. Parameters  $n_1$ ,  $n_2$  depend on  $m$  ( $= \sigma_{y0}/\sigma_{x0}$ ) and also on the beam current and conditions listed in the introduction (transverse equipartitioning, equal transverse emittances or equal transverse amplitudes).

$$\begin{aligned} (\sigma_{x0}^2 + 3\sigma_x^2 - \sigma^2) A + (\sigma_{x0}^2 - \sigma_x^2) B + (\sigma_{x0}^2 - \sigma_x^2) C &= 0 \\ (\sigma_{x0}^2 - \sigma_x^2) A n_1 + ((\sigma_{x0}^2 + 3\sigma_x^2) n_2 - \sigma^2) B + (\sigma_{x0}^2 - \sigma_x^2) C n_1 &= 0 \dots \dots \dots (6) \\ (\sigma_{z0}^2 - \sigma_z^2) A + (\sigma_{z0}^2 - \sigma_z^2) B + (\sigma_{z0}^2 + 3\sigma_z^2 - \sigma^2) C &= 0 \end{aligned}$$

Envelope tunes,  $\sigma$ , are obtained by setting the determinant of the three equations to zero. As  $C$  may  $\neq 0$  in (6), it is seen that all three modes have longitudinal-transverse coupling.

$$\begin{aligned} f(\sigma) = (\sigma_{z0}^2 + 3\sigma_z^2 - \sigma^2) [\sigma^4 - \sigma^2(\sigma_{x0}^2 + 3\sigma_x^2)(n_2 + 1) + n_2(\sigma_{x0}^2 + 3\sigma_x^2)^2 - n_1(\sigma_{x0}^2 - \sigma_x^2)^2] \\ + (\sigma_{z0}^2 - \sigma_z^2)(\sigma_{x0}^2 - \sigma_x^2) [2 n_1(\sigma_{x0}^2 - \sigma_x^2) - (n_1 + n_2)(\sigma_{x0}^2 + 3\sigma_x^2) + (n_1 + 1)\sigma^2] = 0 \dots (7) \end{aligned}$$

Equation (7) has no direct solutions unless  $n_1 = n_2 = 1$ , when it reverts to the equation (2). Estimated roots,  $\sigma_1$ , are corrected repeatedly to  $(\sigma_1 - (f(\sigma_1)/f'(\sigma_1)))$ , with  $f'(\sigma) = df(\sigma)/d\sigma$ , and the initial values assumed for  $\sigma_1$  are the solutions obtained for equal transverse tunes.

$$f'(\sigma) = 2\sigma(\sigma_{z0}^2 + 3\sigma_z^2 - \sigma^2)[2\sigma^2 - (n_2 + 1)(\sigma_{x0}^2 + 3\sigma_x^2)] + 2\sigma[(\sigma_{z0}^2 - \sigma_z^2)(\sigma_{x0}^2 - \sigma_x^2)(n_1 + 1)] \\ - 2\sigma[\sigma^4 - \sigma^2(\sigma_{x0}^2 + 3\sigma_x^2)(n_2 + 1) + n_2(\sigma_{x0}^2 + 3\sigma_x^2)^2 - n_1(\sigma_{x0}^2 - \sigma_x^2)^2] \dots \dots \dots (8)$$

In the example where  $\sigma_{z0}/\sigma_{x0} = 1.50$ ,  $\sigma_z/\sigma_{x0} = 1.28$ ,  $\sigma_x/\sigma_{x0} = 0.64$ , with the mode tunes of  $\sigma/\sigma_x$  (quadrupole) = 2.00,  $\sigma/\sigma_x$  (high) = 4.23 and  $\sigma/\sigma_x$  (low) = 2.55, let  $n_1 = 0.9$ ,  $n_2 = 0.8$ . Revised tune ratios, for the nearly quadrupole and the high and low coupled modes, are:

$$\sigma/\sigma_x \text{ (near quadrupole)} = 1.8484 \quad \sigma/\sigma_x \text{ (high)} = 4.225 \quad \sigma/\sigma_x \text{ (low)} = 2.454$$

### 5.7.5 Case of Unequal Transverse Tunes and Envelope Equation Non-Linearity

The non-linear nature of the envelope equations leads to envelope mode tunes which are functions of the mismatch ratios, A, B and C. The non-linear terms may be expanded in polynomial series, as shown below. The relevant terms are the first and the product of the second and third, so the three examples involve five cubic and four quadratic terms.

$$-(1 + \Delta a_x/a_{x0})^{-3} \approx -1 + 3\Delta a_x/a_{x0} - 6(\Delta a_x/a_{x0})^2 + 10(\Delta a_x/a_{x0})^3 + \dots \\ -(1 + \Delta a_y/a_{y0})^{-1} \approx -1 + \Delta a_y/a_{y0} - (\Delta a_y/a_{y0})^2 + (\Delta a_y/a_{y0})^3 + \dots \dots \dots \\ (1 + \Delta a_z/a_{z0})^{-1} \approx 1 - \Delta a_z/a_{z0} + (\Delta a_z/a_{z0})^2 - (\Delta a_z/a_{z0})^3 + \dots \dots \dots \\ \vdots \\ \cos^3(\sigma s/L) = \frac{1}{2} \cos(\sigma s/L) (1 + \cos(2\sigma s/L)) = \frac{3}{4} \cos(\sigma s/L) + \frac{1}{4} \cos(3\sigma s/L)$$

The cubic terms provide both  $\cos(\sigma s/L)$  and  $\cos(3\sigma s/L)$  components, as shown by the final equation above, while the quadratic terms involve only  $\cos(2\sigma s/L)$ . The former may be included directly in the envelope equations but an asymptotic phase amplitude analysis is required for the latter. Here, the expressions are approximated, with the cubic terms retained but the smaller quadratic terms omitted. The relevant cubic terms are therefore added to the three linear envelope equations (6), of section 1.1.4, to form equations (9).

$$(\sigma_{x0}^2 + 3a^2\sigma_x^2 - \sigma^2) A + (\sigma_{x0}^2 - \sigma_x^2) f^2 B + (\sigma_{x0}^2 - \sigma_x^2) f^2 C = 0 \\ (\sigma_{x0}^2 - \sigma_x^2) e^2 A n_1 + ((\sigma_{x0}^2 + 3b^2\sigma_x^2) m_2 - \sigma^2) B + (\sigma_{x0}^2 - \sigma_x^2) e^2 C n_1 = 0 \dots \dots (9) \\ (\sigma_{z0}^2 - \sigma_z^2) d^2 A + (\sigma_{z0}^2 - \sigma_z^2) d^2 B + (\sigma_{z0}^2 + 3c^2\sigma_z^2 - \sigma^2) C = 0$$

These have been simplified by using the following abbreviated functions of A, B and C:

$$a^2 = 1 + 2\frac{1}{2} A^2 \quad b^2 = 1 + 2\frac{1}{2} B^2 \quad c^2 = 1 + 2\frac{1}{2} C^2 \\ d^2 = 1 + \frac{3}{4} (A^2 + B^2) \quad e^2 = 1 + \frac{3}{4} (A^2 + C^2) \quad f^2 = 1 + \frac{3}{4} (B^2 + C^2)$$



$$\text{Also: } n_1 = (\sigma_{y0}^2 - \sigma_y^2)/(\sigma_{x0}^2 - \sigma_x^2) \quad \text{and} \quad m_2 = (\sigma_{y0}^2 + 3b^2\sigma_y^2)/(\sigma_{x0}^2 + 3b^2\sigma_x^2)$$

Envelope mode tunes are the roots of  $f(\sigma) = 0$ , where  $f(\sigma)$  is the determinant from (9). The  $f(\sigma)$  equation (10) allows computations of tune change for various sizes of mismatch. Initial values assumed for the roots,  $\sigma_1$ , are those found without the non-linear terms, and subsequent roots,  $\sigma_1$ , are corrected repeatedly to  $(\sigma_1 - (f(\sigma_1)/f'(\sigma_1)))$ , with  $f'(\sigma) = df(\sigma)/d\sigma$ .

$$f(\sigma) = (\sigma_{z0}^2 + 3c^2\sigma_z^2 - \sigma^2) [\sigma^4 - \sigma^2((m_2+1)\sigma_{x0}^2 + 3g^2\sigma_x^2) + m_2(\sigma_{x0}^2 + 3a^2\sigma_x^2)(\sigma_{x0}^2 + 3b^2\sigma_x^2) - h^2(\sigma_{x0}^2 - \sigma_x^2)^2] + d^2(\sigma_{z0}^2 - \sigma_z^2)(\sigma_{x0}^2 - \sigma_x^2)[2h^2(\sigma_{x0}^2 - \sigma_x^2) - j^2\sigma_{x0}^2 - 3k^2\sigma_x^2 + j^2\sigma^2] = 0 \dots (10)$$

$$\text{where: } g^2 = a^2 + m_2b^2 \quad h^2 = n_1e^2f^2 \quad j^2 = n_1e^2 + m_2f^2 \quad k^2 = n_1a^2e^2 + m_2b^2f^2$$

### 5.7.6 Inter-Stage Mismatch

Linac stages may appear matched, and yet beam emittances grow and halo increases. The cause may be a too-rapid change of transverse or longitudinal focusing and, to limit this, more matching variables may be used. Thus, a six parameter match may involve the setting of six quadrupole fields and the ramps of cavity phases at the output of one stage and input of the next. Phase ramps tend to give more rapid changes of transverse focusing than the quadrupoles, and sensitivity to the ramps is found by tracking. A few, matched parameter sets may be found, some with smaller beta-function variation than others and proving better in tracking studies. An upgrade for ISIS had three options for an 800 MeV linac design [3]. All used 324 MHz at low energy; two had a 648 MHz transition at 74.6 MeV and one, a 972 MHz transition at 196 MeV. The first two had very small emittance growths but the third, despite apparent matching, had > 50% growths.

A second possible source for mismatch is the errors generated in a 3-D rms envelope matching code. The code first finds input matching parameters for an early lattice cell in a linac stage. Parameters are different for each stage, and are a function of cell focusing, beam energy, current and emittances. Many cells may need to be included ahead of the match point, but effects of emittance change in the cells are not included in current codes. Thus, errors develop progressively along a linac, even for many matching points. Particle tracking has to alternate with matching studies, so that match parameters may include the effects of emittance changes. In future, codes may be improved to include both envelope matching and beam tracking. A third mismatch source is the cavity fields' non-linearity.

An operating linac often exhibits, after mismatch, changes to both the tunes and beam emittances [4, 5]. Thus, even when the zero current transverse tunes are equal, the full current tunes may not be and, if this occurs, the equation (7) gives a better approximation than equation (2) for estimating the tunes of the three coupled envelope modes.

### 5.7.7 Mismatch Mode Features

- The quadrupole mode is affected by longitudinal-transverse coupling if  $\sigma_{y0} \neq \sigma_{x0}$ . The tune alters, and the resonant effects of mismatch differ in the x and y

planes. At increased bunch current, the tune of the mode reduces in proportion to  $\sigma_x$ .

- The high mode tune is little changed when making  $\sigma_{y0} \neq \sigma_{x0}$ . The tune reduces a little in the direction of greater stability at increased bunch current. To escape from an initially unstable region, both transverse tunes have to be reduced.
- The tune of the low coupled mode is reduced when  $\sigma_{y0} < \sigma_{x0}$ , but not by as much as in the case of the pure quadrupole mode. The effects of  $\sigma_{y0} < \sigma_{x0}$  and mismatch have to be assessed by means of particle tracking studies.
- In all linac stages,  $\sigma_{y0}$  and  $\sigma_{x0}$  are reduced as the energy increases, so a sufficient check of instability for the high mode, is over the initial cells of the stage. Beam tracking is required, however, to confirm the predictions.

### 5.7.8 Envelope Modes for an Un-Bunched Beam with Unequal Tunes

In the case of unbunched beams ( $\sigma_{z0} = \sigma_z = 0$ ), the three equations (I) of the Appendix reduce to two, and there is a modified  $(a_x + a_y)^{-1}$  term involved in the space charge forces. After introducing  $n_3 = a_x/(a_x + a_y)$  and  $n_4 = a_y/(a_x + a_y)$ , the revised equations are:

$$\Delta a_x''/a_x + (\sigma_{x0}^2 + 3\sigma_x^2)(\Delta a_x/a_x)/L^2 + (\sigma_{x0}^2 - \sigma_x^2)(n_3(\Delta a_x/a_x) + n_4(\Delta a_y/a_y))/L^2 = 0 \dots\dots(13)$$

$$\Delta a_y''/a_y + (\sigma_{y0}^2 + 3\sigma_y^2)(\Delta a_y/a_y)/L^2 + (\sigma_{y0}^2 - \sigma_y^2)(n_4(\Delta a_y/a_y) + n_3(\Delta a_x/a_x))/L^2 = 0$$

These may be developed into the equation (14), where  $n_1 = (\sigma_{y0}^2 - \sigma_y^2)/(\sigma_{x0}^2 - \sigma_x^2)$  and  $n_2 = (\sigma_{y0}^2 + 3\sigma_y^2)/(\sigma_{x0}^2 + 3\sigma_x^2)$ , as defined previously. The envelope mode tunes are the roots of the equation (14), as given in equation (15):

$$f(\sigma) = \sigma^4 - \sigma^2((n_2+1)(\sigma_{x0}^2 + 3\sigma_x^2) + (n_1n_4 + n_3)(\sigma_{x0}^2 - \sigma_x^2)) + n_2(\sigma_{x0}^2 + 3\sigma_x^2)^2 + (n_1n_4 + n_2n_3)(\sigma_{x0}^2 + 3\sigma_x^2)(\sigma_{x0}^2 - \sigma_x^2) = 0 \dots\dots\dots(14)$$

$$\sigma^2 = \frac{1}{2} ((n_2+1)(\sigma_{x0}^2 + 3\sigma_x^2) + (n_1n_4 + n_3)(\sigma_{x0}^2 - \sigma_x^2)) \pm \frac{1}{2} [(n_1n_4 + n_3)^2(\sigma_{x0}^2 - \sigma_x^2)^2 + (n_2^2 - 2n_2 + 1)(\sigma_{x0}^2 + 3\sigma_x^2)^2 + 2((n_2+1)(n_1n_4 + n_3) - 2(n_1n_4 + n_2n_3))(\sigma_{x0}^2 + 3\sigma_x^2)(\sigma_{x0}^2 - \sigma_x^2)]^{1/2} \dots\dots\dots(15)$$

In the special case of equal transverse tunes and emittances ( $n_1 = n_2 = 1$ ,  $n_3 = n_4 = 1/2$ ), the mode tunes are in agreement with the findings of reference [6] and others:

$$\sigma^2 = 2\sigma_{x0}^2 + 2\sigma_x^2 \quad \sigma^2 = \sigma_{x0}^2 + 3\sigma_x^2$$

### 5.7.9 Appendix: Homogeneous Linear Equations for the Mismatch Modes

Single particle equations of motion in a linac lab frame ( $x, y, z, s$ , & diff. w.r.t.  $s$ ) are:

$$x'' + (k_{x0}^2 - K_x/a_x a_y a_z) x = 0, \quad y'' + (k_{y0}^2 - K_y/a_x a_y a_z) y = 0, \quad z'' + (k_{z0}^2 - K_z/a_x a_y a_z) z = 0$$

where external focusing effects,  $k_{x0}$ ,  $k_{y0}$  and  $k_{z0}$ , vary with  $s$  and the cell period length,  $L$ , and the defocusing effects of the space charge,  $K_x$ ,  $K_y$  and  $K_z$ , are defined as follows:

$$K_i = 3 e I / (4\pi\epsilon_0 m_0 c^2 \beta^2 \gamma^2 f) \int_0^\infty (a_x a_y \gamma a_z dt / 2(a_i^2 + t)) / ((a_x^2 + t)(a_y^2 + t)(a_z^2 + t))^{1/2}$$

for  $i = x, y$  or  $z$ , with  $e$  and  $m_0 c^2$  the ion charge and rest energy,  $I$  and  $f$  the bunch current and repetition rate,  $\epsilon_0$  the permittivity of free space, and  $\beta$  and  $\gamma$  the beam's relativistic factors. A Courant-Snyder transformation into bunched beam envelope equations gives:

$$\begin{aligned} a_x'' + k_{x0}^2 a_x - K_x/a_y a_z - \epsilon_x^2/a_x^3 &= 0 & a_y'' + k_{y0}^2 a_y - K_y/a_x a_z - \epsilon_y^2/a_y^3 &= 0 \\ a_z'' + k_{z0}^2 a_z - K_z/a_x a_y - \epsilon_z^2/a_z^3 &= 0 \end{aligned}$$

Matched beam envelope amplitudes, with period length,  $L$ , are defined by  $a_{x0}$ ,  $a_{y0}$  and  $a_{z0}$ .

$$\text{For a mismatch:} \quad a_x = a_{x0} + \Delta a_x \quad a_y = a_{y0} + \Delta a_y \quad a_z = a_{z0} + \Delta a_z$$

The envelope motion equations for  $\Delta a_x$ ,  $\Delta a_y$  and  $\Delta a_z$  are three, Hill type, linear coupled equations with periodic coefficients, if only small, linear mismatch terms are considered:

$$\begin{aligned} \Delta a_x'' + (k_{x0}^2 + 3\epsilon_x^2/a_{x0}^4) \Delta a_x + (K_x/a_{y0}^2 a_{z0}) \Delta a_y + (K_x/a_{y0} a_{z0}^2) \Delta a_z &= 0 \\ \Delta a_y'' + (K_y/a_{x0}^2 a_{z0}) \Delta a_x + (k_{y0}^2 + 3\epsilon_y^2/a_{y0}^4) \Delta a_y + (K_y/a_{x0} a_{z0}^2) \Delta a_z &= 0 \\ \Delta a_z'' + (K_z/a_{z0}^2 a_{y0}) \Delta a_x + (K_z/a_{z0} a_{y0}^2) \Delta a_y + (k_{z0}^2 + 3\epsilon_z^2/a_{z0}^4) \Delta a_z &= 0 \end{aligned}$$

Smooth, zero and full current tune, approximations for the  $s$ -dependent coefficients are:

$$k_{x0}^2 = \sigma_{x0}^2/L^2, k_{y0}^2 = \sigma_{y0}^2/L^2, k_{z0}^2 = \sigma_{z0}^2/L^2, \epsilon_x^2/a_{x0}^4 = \sigma_x^2/L^2, \epsilon_y^2/a_{y0}^4 = \sigma_y^2/L^2, \epsilon_z^2/a_{z0}^4 = \sigma_z^2/L^2,$$

$$K_x/a_{x0} a_{y0} a_{z0} = (\sigma_{x0}^2 - \sigma_x^2)/L^2, K_y/a_{x0} a_{y0} a_{z0} = (\sigma_{y0}^2 - \sigma_y^2)/L^2, K_z/a_{x0} a_{y0} a_{z0} = (\sigma_{z0}^2 - \sigma_z^2)/L^2$$

The three, mismatch equations are modified by the smooth approximations, as follows:

$$\begin{aligned} \Delta a_x''/a_x + (\sigma_{x0}^2 + 3\sigma_x^2)(\Delta a_x/a_x)/L^2 + (\sigma_{x0}^2 - \sigma_x^2)((\Delta a_y/a_y) + (\Delta a_z/a_z))/L^2 &= 0 \\ \Delta a_y''/a_y + (\sigma_{y0}^2 + 3\sigma_y^2)(\Delta a_y/a_y)/L^2 + (\sigma_{y0}^2 - \sigma_y^2)((\Delta a_x/a_x) + (\Delta a_z/a_z))/L^2 &= 0 \dots (I) \\ \Delta a_z''/a_z + (\sigma_{z0}^2 + 3\sigma_z^2)(\Delta a_z/a_z)/L^2 + (\sigma_{z0}^2 - \sigma_z^2)((\Delta a_x/a_x) + (\Delta a_y/a_y))/L^2 &= 0 \end{aligned}$$

## 5.7.10 References

1. J. J. Barnard and S. M. Lund; Theory of longitudinal beam halo in RF linacs: 1. Core/test particle formation, Proceedings of PAC97, Vancouver, Canada (1997).
2. M. Pabst and K Bongardt, Analytical approximation of the three mismatch modes for bunched beams, ESS, KFA, Jülich, Germany, ESS 97-85-L, August (1997).

3. G. H. Rees, Linac, beam line and ring studies for upgrading of ISIS, Rutherford Appleton Laboratory internal report, STFC, GHR1/ASTec /December (2009).
4. J. Galambos, SNS high power operation; expectations and experience, Proc. of the 46<sup>th</sup> ICFA Beam Dynamics Workshop on High-Intensity and High-Brightness Hadron Beams, HB 2010, Morschach, Switzerland, MOIB01, September (2010).
5. M. Ikegami et al., Beam measurement and simulation at J-PARC linac, Proc. of the 46<sup>th</sup> ICFA Beam Dynamics Workshop on High-Intensity and High-Brightness Hadron Beams, HB 2010, Morschach, Switzerland, THOIA02, September (2010).
6. J. Struckmeier and M. Reiser, Theoretical studies of envelope oscillations and instabilities of mismatched intense charged particle beams in periodic focusing channels, Particle Accelerators, Volume 14, pp. 227-260 (1984).

## 5.8 Reduced Emittance Growth in a Long MEBT Stage of a Linac

G. H. Rees

ASTeC, Rutherford Appleton Lab, STFC, Chilton, Didcot, Oxon OX11 0QX, UK

Mail to: [ghrees@stfc.ac.uk](mailto:ghrees@stfc.ac.uk)

### 5.8.1 Introduction

A MEBT includes choppers and associated beam dumps, beam defining diagnostics, beam halo collimators, and buncher cavities and focusing elements for longitudinal and transverse matching to the following stage. The advantages of a long MEBT are greater space for collimators, diagnostics and choppers, and lower power for the chopper drivers. The disadvantages are the associated growths of longitudinal and transverse emittances of the beam that is injected from an RFQ.

In a long MEBT, three main factors affect the growth of beam emittances and halo:

- the change of the non-linear space charge forces with varying, beam aspect ratios
- the effects of the non-linear fields of the bunchers over the varying bunch lengths
- the particle distribution and parameters of the incoming beam from the RFQ linac

A preferred, transverse focusing design, for providing long drifts and little change of beam aspect ratio, is the use of solenoids and weak triplets. A quadrupole pair transforms beam cross sections from elliptical to circular ahead of two solenoids, which then focus the circular beam into a first long drift region. Next are two, weak focusing, asymmetric quadrupole triplets, separated by a second long drift. The design allows lower chopper fields without loss of un-chopped beam, and produces less longitudinal halo.

Halo arises from space charge forces and the sinusoidal fields of four bunchers, which control the bunch extents. The second buncher (B2) introduces the main non-linear effect and, to cancel it, a field whose amplitude is  $\sim 12.5\%$  that of B2 is used in an anti-phased, adjacent second harmonic cavity. Focusing is retained by a 33% increase of the B2 field. The modified MEBT is then re-matched to the following stage (usually a DTL), using a six parameter matching routine. The low field, second

harmonic cavity proves to be very effective in reducing longitudinal rms emittance growth.

The longitudinal to transverse rms emittance ratio is a key parameter. A typical range is 2:1 to 1:1, and the ends of the range are best avoided, as undesirable tune ratios result in an equipartitioned linac. A low ratio is less demanding for the following DTL, which needs to be designed in conjunction with the MEBT. Even if the longitudinal growth is contained over a long MEBT, transverse growth occurs, so the emittance ratios change. The ratio assumed in an ISIS upgrade study [1] was 1.4 to 1, for the MEBT beam at entry to the DTL. Beam distributions assumed at the MEBT input are 6-D waterbag, with either a uniform or parabolic or Gaussian, local beam density. Distributions do not retain their initial forms over the length of the MEBT, so beam tracking studies are made for all three types of distribution.

### 5.8.2 A 3 MeV, Long MEBT Option for an ISIS Upgrade

One option for a 3 MeV MEBT is given in Figure 1. There are two input quadrupoles, two solenoids, two beam choppers, four, 324 MHz buncher cavities, and two asymmetric, weak focusing triplets. The solenoids focus a round beam into a 1.48 m long drift region, which has the choppers and a large beam dump. There follows a first triplet set, a 1.14 m drift, and a second triplet set, which helps in the matching of a 43 mA beam to the DTL. The bunchers are near the input and output of the solenoids, and at each end of the second drift. They provide beam bunch lengths that are suitable for matching into the DTL. The additional, low field second harmonic cavity is located just after the second buncher.

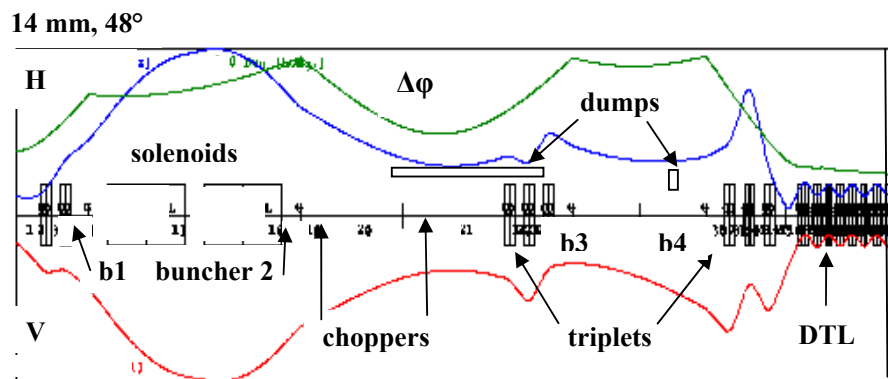


**Figure 1:** Beam amplitudes and components in the proposed, 5.2172 m long MEBT.

Maximum beam amplitudes of 14 mm occur in the two, 0.8 T field solenoids, whose lengths are 0.5134 m. Quadrupoles are all 70 mm long, and adjacent quadrupole spacings are all 60 mm. Diagnostic units, scrapers and a smaller beam dump are installed in the second drift, and the length available for the diagnostics is 0.5 m. The long drifts allow reduced chopper deflecting fields and the loss-less transmission of unchopped beam. The chopper plate voltages are set by the maximum beam emittances, and the pulse repetition rate by the parameters of the ring into which the linac injects. Schematic drawings of the chopper deflections are given in the Figures 2a and 2b.

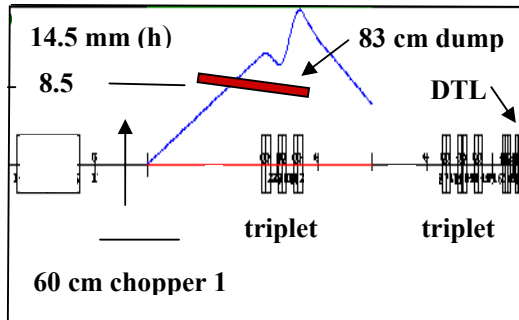


**Figure 2a:** Horizontal “slow” chopper 1.

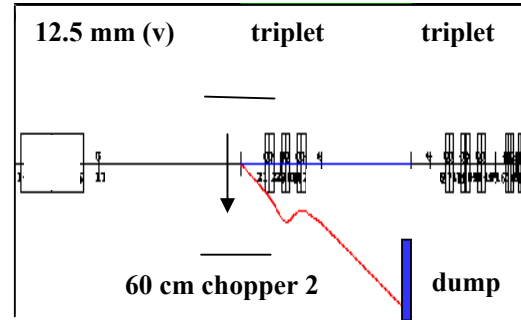


**Figure 2b:** Vertical “fast” chopper 2.

“Slow and fast type” beam choppers are used, as developed at RAL [2]. The initial, “slow type” chopper 1 is between 122 and 722 mm downstream of the second buncher. It deflects beam horizontally, with  $\sim 10$  ns, pulse rise and fall times, leaving three early and three late, partially deflected bunches each pulse. Deflected beam passes to the 0.83 m main beam dump via the vertical, “fast” chopper 2 plates, which extend through the first triplet. Beam is intercepted over the length of the dump for a lower peak heat load. Some partially deflected beam is collected on the main dump, and the rest in the second dump.

The “fast” chopper 2 is pulsed appropriately twice per ring period, with pulses of time duration  $\sim 10$  ns and rise and fall times  $\sim 2.5$  ns. Beam is deflected vertically during the pulses, and the particles that survive the partial horizontal deflection are collected at the second dump, as shown in Figure 2b. The chopper plates are not symmetric about the beam axis but are positioned to allow for the deflections and maximum beam amplitudes. Effective lengths for both choppers are assumed at 90% of their full, 0.6 m lengths.

Plate voltages ( $\pm V$ ) for the two choppers are given by:  $V = \pm (m_0 c^2 / e) (\gamma \beta^2) (d/L) \theta$ , where  $m_0 c^2$  is the  $H^-$  ion rest energy,  $e$  the electronic charge,  $\beta$  or  $\gamma$  the relativistic factors,  $d$  half the plate separation,  $L$  the effective length of the chopper and  $\theta$  its deflection angle. In chopper 1, for a 14.5 mm beam centre deflection needed at the triplet output, the angle  $\theta$  is 10.70 mr. The voltages, assuming  $L = 0.540$  m and  $d = 0.0084$  m, are  $V = \pm 1.0$  kV. In chopper 2, for a 12.2 mm beam centre deflection at the second beam dump position, the angle  $\theta$  is 11.10 mr. The voltages for  $L = 0.540$  m and  $d = 0.0081$  m are  $V = \pm 1.0$  kV.

The two asymmetric triplets provide elliptical beam cross sections, as required for the FODO quadrupole focusing of the following DTL. Quadrupole and buncher cavity field settings depend on RFQ output phase space orientations and beam emittances, and on the acceptances chosen for the DTL. The initial pair of quadrupoles may not be needed if the RFQ beam has similar, upright phase space orientations in the two transverse planes.

### 5.8.3 The Basis of the Need for a Second Harmonic Cavity

The bunch phase extents at the second, third and fourth buncher cavities are  $\pm 46^\circ$ , as seen in Figure 1, so their sinusoidal fields introduce non-linear effects. The major effect is due to the second buncher and, to compensate its non-linearity, an anti-phased,

second harmonic cavity is added in an adjacent, downstream position. The voltages required for the second buncher,  $V_1$ , and the second harmonic cavity,  $\delta V_1$ , are obtained as follows:

$$V = V_1 \sin \phi + \delta V_1 \sin 2\phi = V_1 (1 + 2\delta) \phi + V_1 (1 + 8\delta) \phi^3/6 + \dots$$

$$\delta = -1/8 \quad (\text{for the cubic field components to cancel})$$

$$V_1 = V_0/(1 + 2\delta) = 4V_0/3 \quad (V_0 \text{ is the second buncher's original voltage})$$

Best results are found for  $V_1 \sim 1.29 V_0 = 117.25 \text{ kV}$ ,  $\delta V_1 = 16.75 \text{ kV}$ ,  $\delta = -1/7$ , and the second harmonic cavity 60 mm downstream of the second buncher. The largest field is needed in the fourth b4 buncher, but its voltage of 121.51 kV is marginally lower than its original value. Additional, second harmonic cavities are not required.

#### 5.8.4 Beam Tracking Results for the Modified MEBT

Tracked results for 6-D waterbag, uniform, parabolic and Gaussian input distributions are given below and in Figure 3. The sequences of three numbers are for rms, normalized beam emittances in horizontal, vertical and longitudinal planes, respectively. Units are: ( $\pi$ ) mm mr (transverse), and deg-MeV (longitudinal). The emittances for the 648 MHz, 800 MeV, superconducting SCL3 stage would benefit from improved matching.

6-D Waterbag	Uniform	Parabolic	Gaussian
MEBT in	0.250, 0.250, 0.137	0.249, 0.249, 0.1376	0.245, 0.248, 0.137
MEBT out	0.271, 0.287, 0.135	0.275, 0.305, 0.134	0.282, 0.331, 0.136
DTL4 out	0.282, 0.284, 0.1377	0.293, 0.297, 0.1397	0.321, 0.320, 0.1405
ScL3 out	0.391, 0.332, 0.154 x 2	0.417, 0.360, 0.154 x 2	0.456, 0.422, 0.156 x 2

The results below for no second harmonic buncher show the longitudinal emittance gains:

MEBT in	0.250, 0.250, 0.137	0.250, 0.250, 0.139	0.248, 0.249, 0.137
MEBT out	0.290, 0.300, 0.143	0.290, 0.320, 0.143	0.292, 0.344, 0.144
DTL4 out	0.292, 0.296, 0.1475	0.305, 0.306, 0.148	0.324, 0.331, 0.151
ScL3 out	0.380, 0.351, 0.155 x 2	0.420, 0.390, 0.157 x 2	0.470, 0.480, 0.222 x 2

Uniform, with 2<sup>nd</sup> harmonic cavity

Uniform, without 2<sup>nd</sup> harmonic cavity

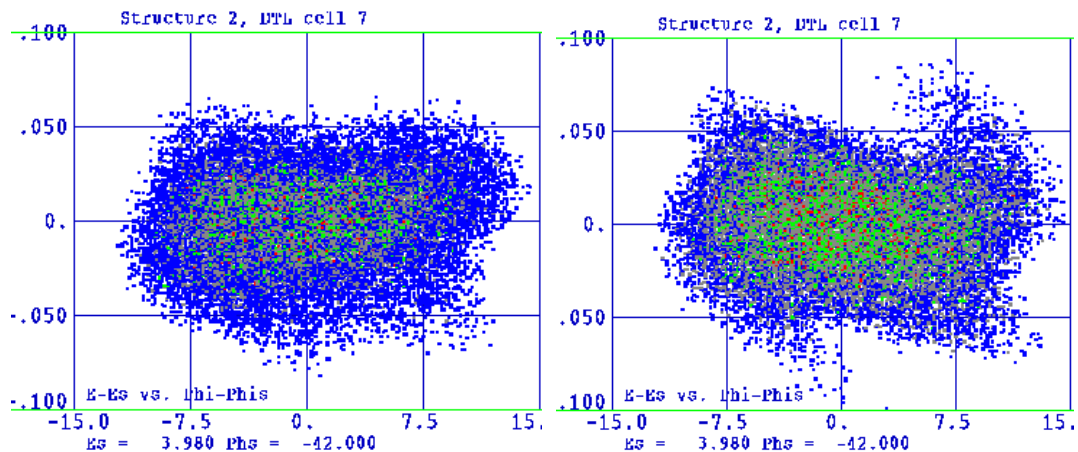


**Figure 3:** Longitudinal phase space plots for the seventh cell of the first DTL tank.

### 5.8.5 References

1. G. H. Rees, Linac, beam line and ring studies for upgrading of ISIS, Rutherford Appleton Laboratory internal report, STFC, GHR1/ASTec /December (2009).
2. M.A. Clarke-Gayther, A fast beam chopper for next generation proton drivers, Proceedings of EPAC'04 (2004).

## 6 Workshop and Conference Reports

### 6.1 X-Band Structures, Beam Dynamics and Sources Workshop (XB-10)

Roger M. Jones, University of Manchester and the Cockcroft Institute, UK  
 Mail to: [roger.jones@manchester.ac.uk](mailto:roger.jones@manchester.ac.uk)

The X-Band (XB-10) mini-ICFA workshop took place at the Cockcroft Institute, Daresbury, UK from the 29<sup>th</sup> November through the 3<sup>rd</sup> December, 2010. This was the second in the series, scheduled to be held every two years, and focusing on consolidating progress over this period. The motivation behind these workshops is to bring together scientists working in the area of linear colliders, light sources and compact industrial and medical linacs, and to capitalize on inherent synergies.

The purpose of this workshop, referred to as XB-10, was to explore a range of RF and beam dynamics issues associated with X-band accelerators. In order to achieve high gradient, room temperature X-band structures are a natural choice. CLIC for example, is now aiming at an accelerating gradient of 100MV/m at 12 GHz. Other accelerators are already in use commercially at X-band for medical cancer treatment and for cargo scanning. It is natural to exploit synergies in these areas. Both fundamental and technological aspects of linacs and drive beams were explored. More than 80 delegates



participated in the workshop. The workshop provided an open forum for delegates to present and discuss their work, and to exchange experiences and ideas.

The following topics were covered:

- Latest CLIC and single-beam (GLC/NLC) optimization of acceleration
- Novel acceleration techniques (hybrid mode, photonic band gap)
- Higher performance acceleration– improved gradient predicting models, exotic input couplers, standing wave versus traveling wave structures, materials, preparation, etc
  - Advanced wakefield and impedance analysis/simulation in accelerating structures
    - Design of couplers (fundamental and HOM)
    - Testing capability at different labs/institutes and likely capacities and schedules
    - Novel RF power sources, high power sources and modulator options based on X-band klystron and other test facilities
      - Test-structure fabrication
      - Plans of labs/ institutes to actively pursue structure development, breakdown theory and experiment, etc.
      - Active and passive overmoded and quasi-optical components
      - Advanced beam diagnostic and feedback techniques (FONT, Laser wire, HOMBPM diagnostics, etc)
      - Drive beam deceleration, wakefield suppression, and extraction structures
      - Measurement and simulation of impedance (stretched wire measurement and intensive simulation techniques)
  - Beam dynamics issues impacting beam quality in colliders and low-energy structures
    - Advanced beam dynamics simulations (parallel processing, particle tracking, emittance, PIC codes, beam breakdown simulation)
    - Industrial linacs (including medical X-sources and cargo scanning compact linacs)
    - Light sources (recent proposed X-band next generation light sources)

Each morning consisted of a series of invited plenary talks, followed by working groups towards the end of the afternoon sessions. The plenary sessions were organised with a focus each day, on linear colliders, light sources and medical/industrial linacs. Four working groups were organised:

Working Group 1: Linear Colliders/Light Sources (Convened by Chris Adolphsen and Chris Christou)

This group reviewed the state of the art in linear colliders and light sources, paying particular attention to the applicability of X-band structures as basic building blocks or as specialised components in accelerators based on different waveband technologies. Future demands for X-band power supplies and accelerating structures were discussed.

Working Group 2: RF Structures (Convened by Walter Wuensch, Sami Tantawi and Roger Jones) High frequency gives fundamental benefits in gradient, peak-power and compactness which is now complimented by a wide range of available designs and operating components. These include accelerating structures, power generating structures and waveguide components. Details of the structures and components, along

with their high-power design criteria and achieved performances, were discussed in this working group

Working Group 3: Beam Dynamics (Convened by Cho Ng and Graeme Burt) This group reviewed state of the art designs of X-structures from a beam dynamics perspective. Linear colliders, light sources, power sources and medical linacs were included in the study. In particular, the influence of short and long-range wakefields on beam dynamics in linear colliders and its impact on fabrication tolerances were discussed. This WG assessed beam dynamics in both accelerating structures and drive beams.

Working Group 4: Industrial/Medical (Convened by Tony Johns and Yasuo Higashi) The group reviewed RF systems for X-band accelerators including high power sources, RF distribution and low-level RF systems. Industrial activity in the field including X-band accelerators for medical and security applications were investigated. The group reviewed the needs of future X-band accelerators and collated views about the R&D on sources, distribution systems and low-level RF systems required to meet those needs.

Tours of the accelerator facilities at the Daresbury laboratory were provided, which included the non-scaling FFAG, EMMA (Electron Machine with Many Applications) and the energy recovery linac, ALICE (Accelerators and Lasers in Combined Experiments). This year, there was a particularly strong participation from delegates interested in the application of X-band technology to light sources. Plenary talks were given from Europe, Japan and the USA, on plans for FEL and compact light sources. This, together with a series of talks on medical application of X-band technology, indicated the recent surge of interest in this area. The workshop closed with a special invited plenary talk given by a distinguished speaker from the SLAC National Accelerator Laboratory, Emeritus Professor Roger Miller. The talk chronicled the initial stages of the 2 mile linac, through to current short medical linacs and also featured the speaker's own graduate work conducted in the 1960s. The talk concluded with a fascinating video demonstrating the first recorded example of beam break up seen on the SLAC linac in the 1960s.

The conference dinner, held in a local castle, included medieval music and the awarding of two student poster prizes. Hirotoishi Masuda, from the University of Tokyo, won the poster prize and Vasim Khan, from the University of Manchester, received the second prize. Financial support, in the form of bursaries, was provided to four students. Selected papers submitted to the XB-10 workshop will be published in a Nuclear Instruments and Methods in Physics Research Section A: Accelerators, Spectrometers, Detectors and Associated Equipment (NIMs A) special issue. Further details on the workshop are available: <http://www.cockcroft.ac.uk/events/XB10/index.html>.

## 7 Recent Doctorial Theses

### 7.1 ILC Physical Design and Key Experimental Study

Dou Wang, IHEP, Chinese Academy of Sciences  
Mail to: [wangdou@ihep.ac.cn](mailto:wangdou@ihep.ac.cn)

**Graduation date:** May 21<sup>st</sup>, 2011

**Supervisor:** Prof. Jie Gao (IHEP), Prof. Q. Qin (IHEP)

*Abstract:*

A revolution has begun in the way we see the universe with the Standard Model. This model gives us new knowledge about the elementary units and their relations in the universe. But it still has some imperfections and challenges. In order to study the spontaneous symmetry breakdown and the origin of mass, discover the new physics beyond the Standard Model, and further to understand the dark matter and dark energy, we need to build a new collider with high energy up to TeV scale. The LHC can discover new phenomena but it can not give precise measurement. All the scientists of the world particle physics have reached a consensus that we need a lepton collider (ILC) as a complementarity of LHC to reveal the new principles of nature.

The LHC has finished and started to commissioning in March 2010. ILC R&D also has started since 2005 under a wide global collaboration after the extensive argumentations and discussions among the particle physics community. Now ILC has entered the Technical Design Phase. From very beginning, Chinese ILC group participated the R&D work and give contributions on physical design and key experimental study.

The studies of this thesis include the parameter choice for ILC, damping ring design and the beam dynamics from the exit of damping ring to the IP. The thesis is mainly divided in to five parts:

First, the thesis discusses the method of ILC physical design (Chapter 2). In this chapter we give a new parameter design for ILC-New Low Charge Parameter -after comparison the RDR design and SB2009 design. Based on this parameter choice study, the thesis discusses four sub-systems in the following chapters which are damping ring (Chapter 3), RTML (Chapter 4), main linac (Chapter 5) and BDS (Chapter 6) respectively. Chapter 3 talks about the ILC 3.2 km damping design, the principles of vertical emittance production and vertical emittance correction in storage rings. Chapter 4 gives a new design of bunch compressors corresponding to the New Low Charge Parameter, introduces the tracking code of the beam dynamics study and also make some simulations on ILC bunch compressors. Chapter 5 discusses the beam dynamics problems in ILC main linac with theoretical method and numerical method. The last chapter makes some studies on ATF2 – a test facility of ILC type BDS. The physical study and experiments will provide valuable experience for ILC future construction.

## 7.2 A Damped and Detuned Accelerating Structure for the Main Linacs of the Compact Linear Collider

Vasim F. Khan, University of Manchester  
Mail to: [roger.jones@manchester.ac.uk](mailto:roger.jones@manchester.ac.uk)

**Graduation date:** April 1<sup>st</sup>, 2011

**Supervisor:** Prof. Roger M. Jones (Univ. of Manchester and the Cockcroft Institute)

### *Abstract:*

Linear colliders are an option for lepton collision at several TeV. The Compact Linear Collider (CLIC) aims at electron and positron collisions at a centre of mass energy of 3 TeV. In CLIC, the main accelerating structures are designed to operate at an X-band frequency of 12GHz with an accelerating gradient of 100MV/m. Two significant issues in linear accelerators that can prevent high gradient being achieved are electrical breakdown and wakefields. The baseline design for the CLIC main linacs relies on a small aperture size to reduce the breakdown probability and a strong damping scheme to suppress the wakefields. The strong damping scheme may have a higher possibility of electrical breakdown. In this thesis an alternative design for the main accelerating structures of CLIC is studied and various aspects of this design are discussed. This design is known as a Damped and Detuned Structure (DDS) which relies on moderate damping and strong detuning of the higher order modes (HOMs). The broad idea of DDS is based upon the Next Linear Collider (NLC) design. The advantages of this design are: well damped wakefields, minimized rf breakdown probability and reduced size of the structure compared to the strong damping design. Procedures necessary to minimize the rf monopole fields and enhance the wakefield suppression are discussed. The rf as well as mechanical designs of a test structure are presented. This unique design forms the basis of this research and allows both the electrical breakdown and beam dynamics constraints to be simultaneously satisfied.

## 8 Forthcoming Beam Dynamics Events

### 8.1 Sixth Workshop on Polarized Positron Beams (POSIPOL 2011)

Following the tradition of holding POSIPOL at hosting laboratory campus, POSIPOL 2011 welcome you to IHEP from August 28-30, 2011, in Beijing, China. POSIPOL workshop started in 2006 at CERN, and becomes a series of annual workshop: POSIPOL 2006 at CERN, POSIPOL 2007 at LAL, POSIPOL 2008 at Hiroshima, POSIPOL 2009 at Lyon, POSIPOL 2010 at KEK.

As the sixth of POSIPOL workshop series, POSIPOL 2011 at IHEP will keep the main features of POSIPOL series, i.e. to couple Linear Collider (ILC+CLIC) aimed polarized positron source R&D efforts to more general polarized positron related community with the aim of advancing polarized positron studies through exchanges and collaborations.

The main goal of this workshop is to achieve required positron beams for linear colliders, but not limited to it, with the main items listed below:

- Polarized gamma ray generation
- High degree Polarized positron generation from compton scattering both ring and linac based
- High degree polarized positron generation from undulator radiation
- Stacking and accumulation of the polarized beam from compton regime
- Polarized beam transport, control and acceleration
- Channelling radiation and applications
- Physics applications of polarized positrons
- Various high intensity positron sources (include conventional)
- For other future colliders (SuperB for example)
- Positron generation target issues
- Physics applications of high quality X-rays and gamma-rays
- Polarimetry at the e+ source
- The positron capture section and the photon collimation
- Review the activities of the “ILC-CLIC e+ generation” working group for all schemes
- Status of the CDR for CLIC and TDR for ILC
- Polarized electron sources

POSIPOL 2011 Chair: Prof. J. Gao, IHEP: [gaoj@ihep.ac.cn](mailto:gaoj@ihep.ac.cn)

Contact:

E-mail: [posipol2011@ihep.ac.cn](mailto:posipol2011@ihep.ac.cn)

POSIPOL 2011 website: <http://posipol2011.ihep.ac.cn/>

## 8.2 Sixth International Accelerator School for Linear Colliders

Barry Barish, Weiren Chou and Vinod Bharadwaj

Mail to: [barish@ligo.caltech.edu](mailto:barish@ligo.caltech.edu), [chou@fnal.gov](mailto:chou@fnal.gov), [vinod@slac.stanford.edu](mailto:vinod@slac.stanford.edu)

We are pleased to announce the Sixth International Accelerator School for Linear Colliders. This school is a continuation of the series of schools started five years ago. The first school was held in 2006 at Sokendai, Hayama, Japan, the second in 2007 at Erice, Sicily, Italy, the third in 2008 at Oakbrook Hills, Illinois, USA, the fourth in 2009 at Huairou, Beijing, China, and the fifth in 2010 at Villars-sur-Ollon, Switzerland. The school is organized by the International Linear Collider (ILC) Global Design Effort (GDE), the Compact Linear Collider (CLIC) and the International Committee for Future Accelerators (ICFA) Beam Dynamics Panel. The school this year will take place at the Asilomar Conference Center, Pacific Grove, California, USA from November 6 to 17, 2011. It is hosted by SLAC and sponsored by a number of funding agencies and institutions around the world including the U.S. Department of Energy (DOE), the U.S. National Science Foundation (NSF), Fermilab, SLAC, Stanford University, TRIUMF,

CERN, DESY, INFN, IN2P3, CEA, CPAN, Oxford University, KEK, IHEP, TIFR and KNU.

We will offer an 11-day program, including an excursion, a site visit and an examination. There will be 8-1/2 days of lectures. The first two days will be an introductory course with an overview of proposed future lepton colliders (ILC, CLIC and the muon collider). This will be followed by two elective courses, one on accelerator physics and the other on RF technology. Both of these will run in parallel for 6 days. Each student is required to take the introductory course and one of the electives. A complete description of the program can be found on the school web site ([www.linearcollider.org/school/2011/](http://www.linearcollider.org/school/2011/)). There will be homework assignments and a final examination but no university credits.

We encourage young physicists (graduate students, post doctoral fellows, junior researchers) to apply. In particular we welcome those physicists who are considering changing to a career in accelerator physics. This school is adopting an in-depth approach. Therefore, former students are welcome to apply if they have a compelling reason to do so. The school will accept a maximum of 70 students from around the world. Students will receive financial aid covering their expenses for attending the school including travel (full or partial). There will be no registration fee. Each applicant should complete the online registration form (which can be found on the school web site) and submit a curriculum vita as well as a letter of recommendation from his/her supervisor (in electronic form, either PDF or MS WORD). The application deadline is June 30, 2011. For more information, please contact: Naomi Nagahashi, SLAC National Accelerator Lab, 2575 Sand Hill Road, Menlo Park, CA 94025, U.S.A., telephone: +1-650-926-2645, fax: +1-650-926-4365, e-mail: [lcschool@slac.stanford.edu](mailto:lcschool@slac.stanford.edu)

#### Organizing Committee

Barry Barish (GDE/Caltech, Chair)  
 Alex Chao (SLAC)  
 Hesheng Chen (IHEP)  
 Weiren Chou (ICFA BD Panel/Fermilab)  
 Paul Grannis (Stony Brook Univ.)  
 In Soo Ko (PAL)  
 Shin-ichi Kurokawa (KEK)  
 Hermann Schmickler (CERN)  
 Nick Walker (DESY)  
 Kaoru Yokoya (KEK)

#### Curriculum Committee

Weiren Chou (Fermilab, Chair)  
 William Barletta (USPAS)  
 Alex Chao (SLAC)  
 Jie Gao (IHEP)  
 Carlo Pagani (INFN/Milano)  
 Hermann Schmickler (CERN)  
 Nobuhiro Terunuma (KEK)  
 Andrzej Wolski (Univ. of Liverpool)  
 Kaoru Yokoya (KEK)

Local Committee

Vinod Bharadwaj (SLAC, Chair)  
 Alex Chao (SLAC)  
 Naomi Nagahashi (SLAC)  
 Nick Arias (SLAC)

**Sixth International Accelerator School for Linear Colliders – Curriculum**  
 (v.2, 04/11/2011)

November 6 – 17, 2011, Asilomar Conference Center, Pacific Grove, California, USA

Daily Schedule

Breakfast	08:00 – 09:00
Morning	09:00 – 12:30, including ½-hour break
Lunch	12:30 – 14:00
Afternoon	14:00 – 17:30, including ½-hour break
Dinner	17:30 – 19:00
Tutorial & homework	19:00 – 22:00

List of Courses (black: required, red and blue: elective)

	Morning	Afternoon	Evening
November 6		<i>Arrival, registration</i>	<i>Reception</i>
November 7	Introduction	ILC	Tutorial & homework
November 8	CLIC	Muon collider	Tutorial & homework
November 9	Joint lecture: Linac basics	Joint lecture: Beam instrumentation	Tutorial & homework
November 10	Course A: Accelerator physics Course B: RF technology	<i>Site visit to SLAC</i>	Tutorial & homework
November 11	Course A: Accelerator physics Course B: RF technology		Tutorial & homework
November 12	Course A: Accelerator physics Course B: RF technology		Tutorial & homework
November 13	Course A: Accelerator physics Course B: RF technology	<i>Excursion</i>	Tutorial & homework
November 14	Course A: Accelerator physics Course B: RF technology		Tutorial & homework
November 15	Course A: Accelerator physics Course B: RF technology		Tutorial & homework
November 16	Course A: Accelerator physics Course B: RF technology	Study time	Study time
November 17	Final exam	<i>Free time</i>	<i>Banquet; Student Award Ceremony</i>
November 18	<i>Departure</i>		

Program

	Monday, November 7	Tuesday, November 8	Wednesday, November 9	Thursday, November 10
Morning 09:00 – 12:30	<p><b>Opening remarks</b></p> <p><b>Lecture 1 – Introduction</b> (3 hrs) <b>Barry Barish</b> (GDE/ Caltech)</p> <ul style="list-style-type: none"> <li>• Tera scale physics</li> <li>• ILC and LHC</li> <li>• Layout of the ILC</li> <li>• Parameter choices &amp; optimization</li> <li>• Other possible future lepton colliders: CLIC and the muon collider</li> <li>• Detectors</li> </ul>	<p><b>Lecture 3 – CLIC</b> (3 hrs)</p> <ul style="list-style-type: none"> <li>• Klystron vs. beam driven acceleration</li> <li>• CLIC layout</li> <li>• Parameter choices &amp; optimization</li> <li>• Driver beam stability</li> <li>• Comparison of the CLIC and ILC</li> <li>• Technical challenges</li> </ul>	<p><b>Joint lecture of Courses A &amp; B: Linac basics</b> (3 hrs)</p>	<p><b>Course A: Accelerator physics</b> <b>Lecture A1 – Linac</b> (9 hrs)</p> <p><b>Course B: RF technology</b> <b>Lecture B1 – Room temperature RF</b> (12 hrs)</p>
Afternoon 14:00 – 17:30	<p><b>Lecture 2 – ILC</b> (3 hrs) <b>Barry Barish</b> (GDE/ Caltech)</p> <ul style="list-style-type: none"> <li>• e- and e+ sources</li> <li>• Bunch compressors and spin rotators</li> <li>• Damping rings</li> <li>• Main linac</li> <li>• Beam delivery system</li> <li>• Civil construction issues</li> </ul>	<p><b>Lecture 14 – Muon collider</b> (3 hrs)</p> <ul style="list-style-type: none"> <li>• Muon collider basics</li> <li>• Machine layout</li> <li>• Major sub-systems</li> <li>• Challenges</li> </ul>	<p><b>Joint lecture of Courses A &amp; B: Beam instrumentation</b> (3 hrs)</p>	<p><b>Excursion</b></p>
Evening 19:00 – 22:00	Tutorial & homework	Tutorial & homework	Tutorial & homework	Tutorial & homework



Program (cont'd)

	Friday, November 11	Saturday, November 12	Sunday, November 13	Monday, November 14
Morning 09:00 – 12:30	<b>Course A: Accelerator physics Lecture A1 – Linac (cont'd)</b>  <b>Course B: RF technology Lecture B1 – Room temperature RF (cont'd)</b>	<b>Course A: Accelerator physics Lecture A2 – Sources (6 hrs)</b>  <b>Course B: RF technology Lecture B1 – Room temperature RF (cont'd)</b>	<b>Course A: Accelerator physics Lecture A3 – Damping rings (12 hrs)</b>  <b>Course B: RF technology Lecture B2 – Superconducting RF (cont'd)</b>	<b>Course A: Accelerator physics Lecture A3 – Damping rings (cont'd)</b>  <b>Course B: RF technology Lecture B2 – Superconducting RF (cont'd)</b>
Afternoon 14:00 – 17:30	<b>Course A: Accelerator physics Lecture A1 – Linac (cont'd)</b>  <b>Course B: RF technology Lecture B1 – Room temperature RF (cont'd)</b>	<b>Course A: Accelerator physics Lecture A2 – Sources (cont'd)</b>  <b>Course B: RF technology Lecture B2 – Superconducting RF (12 hrs)</b>	<b>Excursion</b>	<b>Course A: Accelerator physics Lecture A3 – Damping rings (cont'd)</b>  <b>Course B: RF technology Lecture B2 – Superconducting RF (cont'd)</b>
Evening 19:00 – 22:00	Tutorial & homework	Tutorial & homework	Tutorial & homework	Tutorial & homework
	Tuesday, November 15	Wednesday, November 16	Thursday, November 17	Friday, November 18
Morning 09:00 – 12:30	<b>Course A: Accelerator physics Lecture A3 – Damping rings (cont'd)</b>  <b>Course B: RF technology Lecture B3 – LLRF &amp; high power RF (9 hrs)</b>	<b>Course A: Accelerator physics Lecture A4 – Beam delivery system and beam-beam (cont'd)</b>  <b>Course B: RF technology Lecture B3 – LLRF &amp; high power RF (cont'd)</b>	<b>08:00 – 12:30 Final exam (4.5 hrs)</b>	<b>Departure</b>
Afternoon 14:00 – 17:30	<b>Course A: Accelerator physics Lecture A4 – Beam delivery system and beam-beam (6 hrs)</b>  <b>Course B: RF technology Lecture B3 – LLRF &amp; high power RF (cont'd)</b>	<b>Study time</b>	<i>Free time</i>	
Evening 19:00 – 22:00	Tutorial & homework	Study time	Banquet at 19:00; Student Award Ceremony	

Notes on the Program:

1. There are a total of 11 school days in this year's program, excluding the arrival day (November 6) and the departure day (November 18). The time is divided as follows: 2 days for required courses, 6-1/2 days for elective courses, 1/2 day for excursion, 1/2 day for site visit to SLAC, 1/2 day for study time and a final examination day.
2. The required course consists of four lectures: Introduction, ILC, CLIC and the muon collider. Every student must take this course.
3. There are two elective courses: Course A (the red course) is accelerator physics, Course B (the blue course) is RF technology. They will run in parallel. Each student will choose one of these.
4. The accelerator physics course consists of lectures on four topics: (1) linac, (2) sources, (3) damping rings, and (4) beam delivery system and beam-beam effects.
5. The RF technology course consists of lectures on three topics: (1) room temperature RF, (2) superconducting RF, and (3) LLRF and high power RF.
6. There is a half-day joint lecture on linac basics and another half-day joint lecture on beam instrumentation for all students.
7. There will be homework assignments, but homework is not counted in the grade. There will be a final examination. Some of the exam problems will be taken from variations of the homework assignments. The exam papers will be graded immediately after the exam and results announced in the evening of November 17 at the student award ceremony.
8. There is a tutorial and homework period every evening. It is part of the curriculum and students are required to attend. Lecturers will be available in the evening of their lecture day during this period.
9. Lecturers have been asked to cover the basics as well as possible. Their teaching material will be made available online to the students well ahead of time (a few weeks prior to the school). Students are strongly encouraged to study this material prior to the beginning of the school.
10. Lecturers of the elective courses are required to provide lecture syllabus as soon as possible in order to help students make their selection.
11. All lecturers are responsible for the design of homework and exam problems as well as the answer sheet. They are also responsible for grading the exams.
12. The award ceremony will honor the top (~10) students based on their exam scores.

### **8.3 Workshop on Accelerators for Heavy Ion Inertial Fusion (HIF2011)**

The Workshop on Accelerators for Heavy Ion Inertial Fusion will be held at Lawrence Berkeley National Laboratory May 23-26, 2011. Registration is now open, and the instructions are given below.

The purpose of the Workshop is to review the status of Heavy Ion Fusion (HIF) Research, and to identify the most promising areas of research. The Workshop will bring together experts in these areas:

- Fusion target physics
- Ion sources
- RF accelerators (including linacs, synchrotrons, storage rings, cyclotrons)
- Induction accelerators
- Superconducting magnets
- Chamber and chamber-driver interface
- Technology development (e.g.: insulators, high-voltage pulsed power, RF systems, vacuum systems, accelerator alignment and non-intercepting beam diagnostics)

The structure of the Workshop will be plenary sessions to review the state of the art in HIF, followed by parallel working groups, and conclude with a plenary session to review the status and needed future developments. This Workshop will be in the spirit of the early Heavy Ion Fusion Workshops, which will include participants from many accelerator labs.

We plan to produce a scientific report to document the results of the Workshop.

The content and timing of this Workshop is significant for several reasons:

- There is renewed interest in the development of energy solutions that can provide carbon-free, base-load electricity.
- The U.S. National Academies of Sciences and Engineering are sponsoring a review of the prospects for inertial confinement fusion energy systems. This will include various driver systems, including heavy-ion accelerators. Presentations commenced early in 2011.  
[http://sites.nationalacademies.org/BPA/BPA\\_058425](http://sites.nationalacademies.org/BPA/BPA_058425)
- The National Ignition Facility has commenced its campaign of ignition experiments. These are likely to stimulate interest in inertial fusion energy systems. <https://lasers.llnl.gov/>

We are pleased with the timing and the release of the report from the symposium “Accelerators for America’s Future.” It convincingly shows the potential of particle accelerators in many fields. The section on Accelerators and the Environment includes heavy ion inertial fusion. The report is available at

<http://www.acceleratorsamerica.org/>

#### Registration:

1. Register for the meeting at: <http://www.regonline.com/HIF11>. The registration fee is \$350 (\$100 for students). The registration fees will increase after April 4.
2. If you need accommodations, book your hotel directly with the Berkeley Guest House at Lawrence Berkeley National Laboratory by calling [510-495-8000](tel:510-495-8000).  
Mention “HIF ‘11” to get the group rate.

The room rate is \$100/night (single occupancy) or \$110/night (double occupancy). No tax is charged and coffee, tea and light refreshments are available in the Guest House lounge.

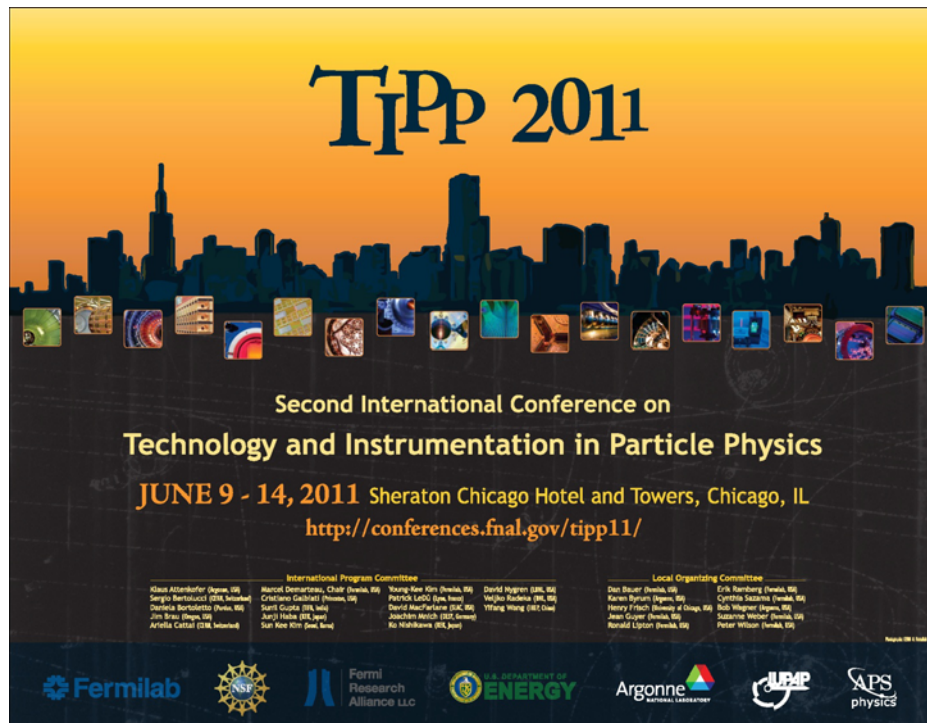
Please register and book your hotel room as soon as possible. May is a busy month for the Berkeley Guest House. We have reserved a block of rooms from Sunday May 22 through Thursday May 26.

The Workshop will include a working dinner on Tuesday evening, May 24.

Contact:

Peter Seidl (LBNL), Organizing Committee (chair) -- [paseidl@lbl.gov](mailto:paseidl@lbl.gov)  
 John Barnard (LLNL), Organizing Committee -- [jjbarnard@lbl.gov](mailto:jjbarnard@lbl.gov)  
 Jan Hennessey, Conference Services -- [JKHennessey@lbl.gov](mailto:JKHennessey@lbl.gov)  
 Lynn Heimbucher, Assistant -- [lcheimbucher@lbl.gov](mailto:lcheimbucher@lbl.gov)

## 8.4 Second International Conference on Technology and Instrumentation in Particle Physics (TIPP 2011)



The poster for TIPP 2011 features a silhouette of the Chicago skyline against a yellow and orange gradient sky. Below the skyline is a row of small, colorful icons representing various particle physics experiments and technologies. The main text on the poster reads: "TIPP 2011", "Second International Conference on Technology and Instrumentation in Particle Physics", "JUNE 9 - 14, 2011 Sheraton Chicago Hotel and Towers, Chicago, IL", and "http://conferences.fnal.gov/tipp11/". At the bottom, there are logos for Fermilab, Fermi Research Alliance LLC, U.S. DEPARTMENT OF ENERGY, Argonne NATIONAL LABORATORY, LBNL, and APS physics. A list of committee members is also provided.

**TIPP 2011**

Second International Conference on  
**Technology and Instrumentation in Particle Physics**

**JUNE 9 - 14, 2011** Sheraton Chicago Hotel and Towers, Chicago, IL  
<http://conferences.fnal.gov/tipp11/>

**International Program Committee**

Klaus Aldenhoff (Argonne, US)	Marcel Demarteau, Chair (Fermilab, US)	Young-Kee Kim (Fermilab, US)	David Hyginen (LBNL, US)
Sergio Bertolucci (BNL, Switzerland)	Christiano Dall'Oli (Fermilab, US)	Patrick LeDuc (Fermilab, US)	Hajime Kubota (Fermilab, US)
Diego Borsoi (Fermilab, US)	Sunil Gupta (BNL, India)	David MacFarlane (SLAC, US)	Wang Meng (MIT, China)
Jim East (Fermilab, US)	Junji Harada (JAEA, Japan)	Joscha Schmies (BNL, Germany)	
Archie Costantini (BNL, Switzerland)	Sun-Kee Kim (JAEA, Japan)	Bo Wolden (BNL, USA)	

**Local Organizing Committee**

Dan Bauer (Fermilab, US)	Erik Rosenberg (Fermilab, US)
Ramon Bystrom (Fermilab, US)	Christina Steinhilber (Fermilab, US)
Henry Frisch (Fermilab, US)	Ruth Wagner (Fermilab, US)
Jean Guillet (Fermilab, US)	Suzanne Hoesler (Fermilab, US)
Donald Lippert (Fermilab, US)	Peter Wilson (Fermilab, US)

Fermilab    Fermi Research Alliance LLC    U.S. DEPARTMENT OF ENERGY    Argonne NATIONAL LABORATORY    LBNL    APS physics

In frame of the *Technology and Instrumentation in Particle Physics TIPP 2011* conference, the working track on “**Machine Detector Interface and Beam Instrumentation**” is looking for your participation! We will discuss about beam instrumentation and machine detector interface diagnostics, e.g. beam position and profile monitors, emittance measurements, background simulations and accelerator control systems, etc. Please note that the abstract submission deadline has been extended to April 15, 2011. Please also note, the TIPP proceedings with your contribution will be published as special issue of NIM. You find further details under: <http://conferences.fnal.gov/tipp11/>

Contact:

Manfred Wendt, TIPP2011 convener MDI & BI, [manfred@fnal.gov](mailto:manfred@fnal.gov)

## 8.5 15<sup>th</sup> International Conference on RF Superconductivity (SRF2011)

We'd like to welcome you to attend the 15th International Conference on RF Superconductivity to take place on July 25-30, 2011 in downtown Chicago. Our goal is to continue in the tradition of the 14 previous conferences and provide a lively forum for SRF scientists, engineers, students and industrial partners to present and discuss the latest developments in the science and technology of superconducting RF for particle accelerators. Please visit the conference website <http://conferences.fnal.gov/srf2011/> where details are available and additional updates will be posted.

Important dates are as follows:

Registration Open - January 1, 2011

Abstract Submission Deadline - May 1, 2011

Early Registration Ends - April 4, 2011

Registration must be paid by April 4, 2011 to avail the early registration discount.

Important Announcement - Non-US citizens wishing to attend either the tutorials or the laboratory tour at Argonne must fill out the foreign national questionnaire form as soon as possible. (This requirement includes permanent residents). This form can be found at

[http://conferences.fnal.gov/srf2011/ANL\\_FV.html](http://conferences.fnal.gov/srf2011/ANL_FV.html).

For more information on foreign visitors to ANL, go to

[http://conferences.fnal.gov/srf2011/ANL\\_FV.html](http://conferences.fnal.gov/srf2011/ANL_FV.html)

Conference co-chairs:

Mike Kelly, Argonne National Laboratory, [kelly@phy.anl.gov](mailto:kelly@phy.anl.gov)

Bob Kephart, Fermilab, [Kephart@fnal.gov](mailto:Kephart@fnal.gov)

## 8.6 13<sup>th</sup> International Conference on Accelerator and Large Experimental Physics Control Systems (ICALEPCS 2011)

The 13<sup>th</sup> ICALEPCS conference, hosted by the European Synchrotron Radiation Facility (ESRF, [www.esrf.eu](http://www.esrf.eu)), will be held from the 10th to the 14th of October 2011 in Grenoble, France.

ICALEPCS (<http://www.icalepcs.org>) is a series of biennial conferences that rotates between three major areas of the world: America (including North, Central and South America), Asia (including Oceania) and Europe (including Russia, the Near East and Africa) and is well established as the largest conference dedicated to control systems for accelerators and large experiments in physics.

The high standard that has been reached by the conference is widely recognised. The conference series is endorsed by the European Physics Society/Experimental Physics Control Systems (EPS/EPCS); the Institute of Electrical and Electronics Engineers (IEEE); the Nuclear and Plasma Science Society (NPSS); the French Society of Physics (SFP Interdivision Physique des Accelérateurs et Technologies Associées); the Physical Society of Japan (JPS); the Association of Asia Pacific Physical Societies (AAPPS).

We are pleased to invite all those involved worldwide in the field of controls and those interested in following the latest trends in control systems for accelerators and experimental physics systems, large and small (particle accelerators, particle detectors, telescopes and nuclear fusion facilities, etc.). Please visit our home page for details:

<http://icalepcs2011.esrf.eu>

Abstract submission will be available from 1st February 2011 via the SPMS (login <https://oraweb.cern.ch/pls/icalepcs2011/profile.html>). You are invited to submit your abstract before 1st April 2011.

CALEPCS 2011 Local Organizing Committee:

Andy Gotz (Conference Chairman)

Jean-Michel Chaize (Scientific Programme Chairman)

Marie Robichon (Proceedings Editor)

## **9 Announcements of the Beam Dynamics Panel**

### **9.1 ICFA Beam Dynamics Newsletter**

#### **9.1.1 Aim of the Newsletter**

The ICFA Beam Dynamics Newsletter is intended as a channel for describing unsolved problems and highlighting important ongoing works, and not as a substitute for journal articles and conference proceedings that usually describe completed work. It is published by the ICFA Beam Dynamics Panel, one of whose missions is to encourage international collaboration in beam dynamics.

Normally it is published every April, August and December. The deadlines are 15 March, 15 July and 15 November, respectively.

#### **Categories of Articles**

The categories of articles in the newsletter are the following:

1. Announcements from the panel.
2. Reports of beam dynamics activity of a group.
3. Reports on workshops, meetings and other events related to beam dynamics.
4. Announcements of future beam dynamics-related international workshops and meetings.
5. Those who want to use newsletter to announce their workshops are welcome to do so. Articles should typically fit within half a page and include descriptions of the subject, date, place, Web site and other contact information.
6. Review of beam dynamics problems: This is a place to bring attention to

unsolved problems and should not be used to report completed work. Clear and short highlights on the problem are encouraged.

7. Letters to the editor: a forum open to everyone. Anybody can express his/her opinion on the beam dynamics and related activities, by sending it to one of the editors. The editors reserve the right to reject contributions they judge to be inappropriate, although they have rarely had cause to do so.

The editors may request an article following a recommendation by panel members. However anyone who wishes to submit an article is strongly encouraged to contact any Beam Dynamics Panel member before starting to write.

### 9.1.2 How to Prepare a Manuscript

Before starting to write, authors should download the template in Microsoft Word format from the Beam Dynamics Panel web site:

<http://www-bd.fnal.gov/icfabd/news.html>

It will be much easier to guarantee acceptance of the article if the template is used and the instructions included in it are respected. The template and instructions are expected to evolve with time so please make sure always to use the latest versions.

The final Microsoft Word file should be sent to one of the editors, preferably the issue editor, by email.

The editors regret that LaTeX files can no longer be accepted: a majority of contributors now prefer Word and we simply do not have the resources to make the conversions that would be needed. Contributions received in LaTeX will now be returned to the authors for re-formatting.

In cases where an article is composed entirely of straightforward prose (no equations, figures, tables, special symbols, etc.) contributions received in the form of plain text files may be accepted at the discretion of the issue editor.

Each article should include the title, authors' names, affiliations and e-mail addresses.

### 9.1.3 Distribution

A complete archive of issues of this newsletter from 1995 to the latest issue is available at

<http://icfa-usa.jlab.org/archive/newsletter.shtml>.

This is now intended as the primary method of distribution of the newsletter.

Readers are encouraged to sign-up for electronic mailing list to ensure that they will hear immediately when a new issue is published.

The Panel's Web site provides access to the Newsletters, information about future and past workshops, and other information useful to accelerator physicists. There are links to pages of information of local interest for each of the three ICFA areas.

Printed copies of the ICFA Beam Dynamics Newsletters are also distributed (generally some time after the Web edition appears) through the following distributors:

Weiren Chou	<a href="mailto:chou@fnal.gov">chou@fnal.gov</a>	North and South Americas
Rainer Wanzenberg	<a href="mailto:rainer.wanzenberg@desy.de">rainer.wanzenberg@desy.de</a>	Europe <sup>++</sup> and Africa
Susumu Kamada	<a href="mailto:susumu.kamada@kek.jp">susumu.kamada@kek.jp</a>	Asia <sup>**</sup> and Pacific

<sup>++</sup> Including former Soviet Union.

<sup>\*\*</sup> For Mainland China, Jiu-Qing Wang ([wangjq@mail.ihep.ac.cn](mailto:wangjq@mail.ihep.ac.cn)) takes care of the distribution with Ms. Su Ping, Secretariat of PASC, P.O. Box 918, Beijing 100039, China.

To keep costs down (remember that the Panel has no budget of its own) readers are encouraged to use the Web as much as possible. In particular, if you receive a paper copy that you no longer require, please inform the appropriate distributor.

#### 9.1.4 Regular Correspondents

The Beam Dynamics Newsletter particularly encourages contributions from smaller institutions and countries where the accelerator physics community is small. Since it is impossible for the editors and panel members to survey all beam dynamics activity worldwide, we have some Regular Correspondents. They are expected to find interesting activities and appropriate persons to report them and/or report them by themselves. We hope that we will have a “compact and complete” list covering all over the world eventually. The present Regular Correspondents are as follows:

Liu Lin	<a href="mailto:Liu@lnls.br">Liu@lnls.br</a>	LNLS, Brazil
Sameen Ahmed Khan	<a href="mailto:Rohelakan@yahoo.com">Rohelakan@yahoo.com</a>	SCOT, Oman
Jacob Rodnizki	<a href="mailto:Jacob.Rodnizki@gmail.com">Jacob.Rodnizki@gmail.com</a>	Soreq NRC, Israel
Rohan Dowd	<a href="mailto:Rohan.Dowd@synchrotron.org.au">Rohan.Dowd@synchrotron.org.au</a>	Australian Synchrotron

We are calling for more volunteers as Regular Correspondents.



## 9.2 ICFA Beam Dynamics Panel Members

<b>Name</b>	<b>eMail</b>	<b>Institution</b>
Rick Baartman	<a href="mailto:baartman@lin12.triumf.ca">baartman@lin12.triumf.ca</a>	TRIUMF, 4004 Wesbrook Mall, Vancouver, BC, V6T 2A3, Canada
Marica Biagini	<a href="mailto:marica.biagini@lnf.infn.it">marica.biagini@lnf.infn.it</a>	LNF-INFN, Via E. Fermi 40, Frascati 00044, Italy
Yunhai Cai	<a href="mailto:yunhai@slac.stanford.edu">yunhai@slac.stanford.edu</a>	SLAC, 2575 Sand Hill Road, MS 26, Menlo Park, CA 94025, U.S.A.
Swapn Chattopadhyay	<a href="mailto:swapan@cockcroft.ac.uk">swapan@cockcroft.ac.uk</a>	The Cockcroft Institute, Daresbury, Warrington WA4 4AD, U.K.
Weiren Chou (Chair)	<a href="mailto:chou@fnal.gov">chou@fnal.gov</a>	Fermilab, P.O. Box 500, Batavia, IL 60510, U.S.A.
Wolfram Fischer	<a href="mailto:wfisher@bnl.gov">wfisher@bnl.gov</a>	Brookhaven National Laboratory, Bldg. 911B, Upton, NY 11973, U.S.A.
Yoshihiro Funakoshi	<a href="mailto:yoshihiro.funakoshi@kek.jp">yoshihiro.funakoshi@kek.jp</a>	KEK, 1-1 Oho, Tsukuba-shi, Ibaraki-ken, 305-0801, Japan
Miguel Furman	<a href="mailto:mafurman@lbl.gov">mafurman@lbl.gov</a>	Center for Beam Physics, LBL, 1 Cyclotron Road, Berkeley, CA 94720-8211, U.S.A.
Jie Gao	<a href="mailto:gaoj@ihep.ac.cn">gaoj@ihep.ac.cn</a>	Institute for High Energy Physics, P.O. Box 918, Beijing 100049, China
Ajay Ghodke	<a href="mailto:ghodke@cat.ernet.in">ghodke@cat.ernet.in</a>	RRCAT, ADL Bldg. Indore, Madhya Pradesh, 452 013, India
Ingo Hofmann	<a href="mailto:i.hofmann@gsi.de">i.hofmann@gsi.de</a>	High Current Beam Physics, GSI Darmstadt, Planckstr. 1, 64291 Darmstadt, Germany
Sergey Ivanov	<a href="mailto:sergey.ivanov@ihep.ru">sergey.ivanov@ihep.ru</a>	Institute for High Energy Physics, Protvino, Moscow Region, 142281 Russia
In Soo Ko	<a href="mailto:isko@postech.ac.kr">isko@postech.ac.kr</a>	Pohang Accelerator Lab, San 31, Hyoja-Dong, Pohang 790-784, South Korea
Alessandra Lombardi	<a href="mailto:alessandra.lombardi@cern.ch">alessandra.lombardi@cern.ch</a>	CERN, CH-1211, Geneva 23, Switzerland
Yoshiharu Mori	<a href="mailto:mori@kl.rii.kyoto-u.ac.jp">mori@kl.rii.kyoto-u.ac.jp</a>	Research Reactor Inst., Kyoto Univ. Kumatori, Osaka, 590-0494, Japan
George Neil	<a href="mailto:neil@jlab.org">neil@jlab.org</a>	TJNAF, 12000 Jefferson Ave., Suite 21, Newport News, VA 23606, U.S.A.
Toshiyuki Okugi	<a href="mailto:toshiyuki.okugi@kek.jp">toshiyuki.okugi@kek.jp</a>	KEK, 1-1 Oho, Tsukuba-shi, Ibaraki-ken, 305-0801, Japan
Mark Palmer	<a href="mailto:mark.palmer@cornell.edu">mark.palmer@cornell.edu</a>	Wilson Laboratory, Cornell University, Ithaca, NY 14853-8001, USA
Chris Prior	<a href="mailto:c.r.prior@rl.ac.uk">c.r.prior@rl.ac.uk</a>	ASTeC Intense Beams Group, STFC RAL, Chilton, Didcot, Oxon OX11 0QX, U.K.
Yuri Shatunov	<a href="mailto:yu.m.shatunov@inp.nsk.ru">yu.m.shatunov@inp.nsk.ru</a>	Acad. Lavrentiev, prospect 11, 630090 Novosibirsk, Russia
Jiu-Qing Wang	<a href="mailto:wangjq@mail.ihep.av.cn">wangjq@mail.ihep.av.cn</a>	Institute for High Energy Physics, P.O. Box 918, 9-1, Beijing 100049, China
Rainer Wanzenberg	<a href="mailto:rainer.wanzenberg@desy.de">rainer.wanzenberg@desy.de</a>	DESY, Notkestrasse 85, 22603 Hamburg, Germany

*The views expressed in this newsletter do not necessarily coincide with those of the editors.  
The individual authors are responsible for their text.*